SYNTHESIS AND CHARACTERIZATION OF Ni_3AL-BASED HARD AND PROTECTIVE COATINGS

A thesis submitted to the

UPES

For the Award of

Doctor of Philosophy

in

Mechanical Engineering

BY

Sunil Kumar Tiwari

November 2023

SUPERVISOR

Dr. Amit Kumar Chawla

Mechanical Cluster

School of Advanced Engineering

UPES

Dehradun-248007: Uttarakhand, India

SYNTHESIS AND CHARACTERIZATION OF Ni_3AL-BASED HARD AND PROTECTIVE COATINGS

A thesis submitted to the
UPES

For the Award of
Doctor of Philosophy
in
Mechanical Engineering

BY

Sunil Kumar Tiwari

(SAP- 500080560)

November 2023

Internal Supervisor

Dr. Amit Kumar Chawla
Sr. Associate Professor
Applied Science Cluster
UPES

Mechanical Cluster
School of Advanced Engineering
UPES
Dehradun-248007: Uttarakhand, India

Nov. 2023

DECLARATION

I hereby declare that the Ph.D. thesis entitled "**Synthesis and characterization of Ni_3Al-based hard and protective coatings**" in partial fulfillment of the award of the degree of Doctor of Philosophy submitted to Mechanical Cluster, School of Advanced Engineering, UPES, Energy Acres, Dehradun, Uttarakhand, India is a verified and authentic record of my own research conducted out under the supervision of:

1. **Dr. Amit Kumar Chawla**; Senior Associate Professor, Applied Science Cluster, UPES, Energy Acres, Dehradun, India

I declare that this work has not been submitted anywhere else for any part-time or full-time award for a diploma or degree program to the best of my knowledge. Additionally, this work doesn't contain any previously published results or material by any person except where the due acknowledgment and references have been mentioned in the text.

Sunil Kumar Tiwari
Doctoral Research Fellow

Nov. 2023

THESIS COMPLETION CERTIFICATE

This is to certify that the Ph.D. thesis entitled "**Synthesis and characterization of Ni_3Al-based hard and protective coatings**" submitted by SUNIL KUMAR TIWARI (SAP ID: 500080560) in partial fulfillment of the award of the degree of Doctor of Philosophy to Mechanical Cluster, School of Advanced Engineering, UPES, Energy Acres, Dehradun, Uttarakhand has been carried out under my supervision and guidance.

It is certified that any part of the work including the synopsis and results has not been submitted anywhere else for the award of any other part-time or full-time diploma or degree program to any other university.

Dr. Amit Kumar Chawla
Sr. Associate Professor, Applied Science Cluster
UPES, Dehradun, India

ABSTRACT

The demand for advanced engineered coatings in past decades has intensified in several industries including machining, aerospace, marine, nuclear industries and construction industries where hardness and protection in terms of corrosion and oxidation resistance properties are crucial. For the last five decades, the protection of the parent material in particular for enhancing their life and performance in extreme operating conditions has been given by depositing hard and protective coatings over them. These hard coatings provide resistance against local permanent deformations like dents, scratches and wear and are mostly used in tribological applications. The protection of the specimen is given in terms of making them corrosion and oxidation-resistant. These hard and protective coatings have been synthesized by several chemical and vapor deposition techniques such as plasma spraying, electroplating, thermal evaporation, magnetron sputtering, spin coating, electrolyte deposition, etc. However, to meet the demand for high-temperature applications of bulk and coating materials, researchers have shown their interest in Ni-based coatings. In particular, Ni_3Al-based coatings have proved themselves a better candidate for high-temperature applications because of their extraordinary corrosion resistance and oxidation resistance properties. Moreover, these coatings have also shown enhanced mechanical and tribological properties along with excellent creep and fatigue properties.

The main objective of the present work was to synthesize the Ni_3Al-based hard coatings which protect the parent specimen from oxidation attacks at high temperatures. Ni_3Al-based coatings were deposited on Silicon (110) and Ni-superalloy (Inconel -718) in alloy form. The evolution of microstructure, mechanical properties, and oxidation-resistant properties of Ni_3Al coatings as a result of variation in substrate temperature, Ni enrichment, and doping of the Ni_3Al matrix with Cr and Zr in alloy form has been investigated. The chapter-wise summary of the thesis is given below:

Chapter 1: shows the evolution of thin films as a potential material that meets several industrial demands. The different deposition techniques,

their properties, and the area of applications have been discussed briefly. Additionally, the chapter shows the motivation of the present work including the objectives of the research.

Chapter 2 displays the techniques used for the synthesis and characterization of the Ni_3Al-based coatings studied in the present work. **Section 2.1** shows a brief description of the synthesis of thin films via different CVD and PVD methods. It includes the discussion about the nucleation at the first stage followed by its growth to deposit thin films by different growth modes. The section also covers the principle of working and major components of DC/RF magnetron sputtering used to synthesize Ni_3Al-based coatings in this research. **Section 2.2** illustrates the characterization tools and techniques used to study the microstructure, mechanical and oxidation-resistant properties of thin films. It includes the working and principle of X-ray diffraction to study the evolution of different phases, Field emission scanning electron microscopy (FE-SEM) to study the microstructure, atomic force microscopy to study the surface morphology, drop shape analyzer (DSA) to evaluate the hydrophobic properties of the film, nanoindentation to evaluate the hardness, young's modulus and adhesion strength of the film and the substrate and oxidation test setup to perform oxidation test at high temperatures.

Chapter 3 reflects the synthesis of Ni_3Al-based alloy coating at different substrate temperatures using DC magnetron sputtering. The chapter includes four subsections. **Subsection 3.1.1** reflects the basic introduction about the existence and need of hard coatings and how Ni_3Al-based coatings prove themselves a better candidate for industrial applications. **Subsection 3.1.2** shows the parameters of synthesizing Ni_3Al-based alloy coating where the substrate temperature was varied to deposit four samples on the silicon substrate. The films were deposited at room temperature, 200℃, 400℃ and 600℃. The deposited films were characterized for the evolution of phase, microstructure, surface topography, contact angle, and mechanical properties using XRD, FESEM, AFM, DSA, and nanoindentation respectively. The results of the tests have been shown in **subsection 3.1.3** It is observed that the Ni_3Al film shows the preferred orientation of (111) whose intensity increases

with increase in the substrate temperature up to 400℃ beyond which it decreases with the evolution of a new peak of Al (111). The results of FE-SEM show that the film deposited at 400℃ possesses fine and compactly packed microstructure whereas the film deposited at 600℃ possesses a higher percentage of porosity. Simultaneously the hardness and Young's modulus of the film increases with an increase in the substrate temperature up to 400℃ beyond which it falls abruptly. **Section 3.1.4** shows the conclusion of the work which reflects that the alloy Ni_3Al film deposited at 400℃ possesses the best microstructural and mechanical properties. The highest hardness and Young's modulus of 12.8 ± 0.8 GPa and (205 ± 15) GPa have been achieved respectively.

Chapter 4 shows the synthesis and characterization of Ni_3Al and Ni-rich Ni_3Al films using DC magnetron sputtering. This chapter consists of four subsections. **Subsection 4.1.1** shows the introduction of the evolution of transition metal-based hard coatings and how the demand for Ni-based coatings came into the picture when the high-temperature application was targeted. It also shows the advancement done so far in the fabrication of NiAl and Ni_3Al-based protective coatings. **Subsection 4.1.2** demonstrates the synthesis of Ni_3Al and Ni-rich Ni_3Al coatings using DC magnetron sputtering and co-sputtering respectively. The films were deposited on silicon substrates at a substrate temperature of 400℃ where the power to Ni target was increased to vary the concentration of Ni in Ni_3Al films via co-sputtering. The evolution of phase, microstructure and surface properties were characterized using XRD, FE-SEM and AFM respectively. The wetting properties of the deposited alloy films were characterized using DSA whereas nanoindentation was used to evaluate the hardness and Young's modulus of the films. The results of the work are presented in **subsection 4.1.3**. The results of the XRD show that the deposited films show the preferred orientation of Ni_3Al (111) which is also in accord with the ordered $L1_2$ structure of Ni_3Al. It is also observed that there is an evolution of the XRD peak of Ni_5Al (113) when the concentration of Ni is increased in the host Ni_3Al matrix. The results of EDS confirm that the concentration of Ni in the alloy film increases with increase in

DC power to the Ni target. The results of nanoindentation showed that the Ni_3Al film showed the maximum hardness and Young's modulus of 12.8 ± 0.8 GPa and 205.3 ± 17 GPa respectively. It is observed that the mechanical properties decrease with an increase in Ni concentration in the Ni_3Al matrix. The conclusion of the study is shown in **subchapter 4.1.4**.

Chapter 5 shows the synthesis and characterization of doped Ni_3Al alloy films. This chapter consists of two major sections. **Section 5.1** shows the synthesis and characterization of Cr-doped Ni_3Al alloy films whereas **section 5.2** shows the demonstrated results of Zr-doped Ni_3Al alloy films. **Subsection 5.1.1** shows the introduction of the need for Ni and Ni_3Al-based coatings and brings out the importance of these coatings for applications at high temperatures. The parameters of synthesis of these coatings using DC magnetron co-sputtering are explained in **subsection 5.1.2**. It also explains how the deposited coatings were characterized for microstructural and mechanical properties. The results of the test have been explained and discussed in **section 5.1.3**. The results of XRD show that the Cr-Ni_3Al films possess prominent peaks of Ni_3Al (111) followed by Ni_3Al (200) and Ni_3Al (220). However, the evidence of the Cr is not seen in any of the XRD spectra of Cr-Ni_3Al films. The results of FE-SEM show that the grain size of the Cr-Ni_3Al films increases with increase in the Cr concentration which leads to the increase in porosity and surface roughness. The subsection also reflects the results of nanoindentation performed at room temperature. It is observed that the hardness and Young's modulus of the Cr-Ni_3Al films decrease with increase in the Cr concentration in the host Ni_3Al film. **Subsection 5.1.4** shows the conclusion part of the work which reflects the maximum hardness (~ 12.7 GPa) and Young's modulus (~ 206 GPa) obtained for pure Ni_3Al films without doping with Cr. **Subchapter 5.2.2** shows the synthesis of Zr-Ni_3Al films followed by characterization to analyze their microstructural and mechanical properties. The experiment and characterization techniques were common to **subchapter 5.1.2** except for the change in target material. In this subsection, the Zr target was used in place of Cr for co-sputtering. **Subsection 5.1.3** reflects the discussion of the obtained results. The results of XRD show a shift in the XRD peak towards the lower angle as a result of the increase in Zr

content in the host Ni_3Al matrix. The enrichment of Zr in Ni_3Al leads to increase in grain size of the film and thus the porosity and surface roughness of the film increased simultaneously as studied from FE-SEM and AFM images. The results of nanoindentation show that the hardness and Young's modulus decrease with an increase in Zr content in the Ni_3Al film. The maximum value of hardness and Young's modulus has been reported as 12.8 ± 0.8 GPa and 205 ± 15 GPa respectively for 0 W Zr- Ni_3Al films in **subsection 5.2.4**.

Chapter 6 brings about the synthesis and characterization of microstructural, mechanical (adhesive strength), and high-temperature oxidation-resistant properties of doped Ni_3Al films. Two major sections namely **section 6.1** and **section 6.2** reflect the study of Cr-doped Ni_3Al and Zr-doped Ni_3Al coatings on Ni superalloy (Inconel-718). **Subsection 6.1.1** brings about a brief introduction to the application of Ni superalloys along with their high-temperature stable and oxidation-resistant properties. It also includes how the use of thin film coating over the base Ni superalloy improves the oxidation-resistant properties and life of the parent specimen. **Subsection 6.1.2** shows the parameters of synthesizing Cr-Ni_3Al coatings over Inconel-718 substrate using magnetron-co-sputtering at the substrate temperature of 400℃ followed by characterization tools and parameters for studying microstructural, adhesion, and high-temperature oxidation-resistant properties. The results of the test are mentioned in **subsection 6.1.3**. The results of XRD show a shift in the XRD peak towards the lower angle as a result of the increase in Cr content in the Ni_3Al matrix. However, it is observed that the grain size of the film decreases resulting a decrease in percentage of porosity and surface roughness of the film. Additionally, the film doped with 30 W Cr in Ni_3Al shows the best adhesive strength between the film and substrate. The deposited films were exposed to high temperatures of 900℃, 1000℃, and 1100℃ in the split furnace for the oxidation test. The conclusion **subsection 6.1.4** shows that the film deposited with 30 W Cr in Ni_3Al shows the best oxidation-resistant properties at 900℃. It also explains that the oxidation-resistant property of Cr-Ni_3Al films increase with increase in the Cr concentration in the Ni_3Al matrix. The parameters of depositing Zr-Ni_3Al

films over the Inconel-718 substrate are shown in **subsection 6.2.2**. All the parameters of deposition and characterization were common to **subsection 6.1.2** except the use of the Zr target in place of the Cr target for co-sputtering. **Subsection 6.2.3** shows the result part that reflects the microstructural enhancement of the Zr-Ni_3Al due to decreased grain size which leads to decrease in the surface roughness of the film. Simultaneously it is observed that the adhesive strength and the oxidation-resistant properties of Zr-Ni_3Al films increase with increase in the Zr content in the Ni_3Al matrix. The conclusion **subsection 6.2.4** shows that the Ni_3Al film doped with 30 W Zr exhibits the best result in terms of high-temperature oxidation-resistant properties when exposed to 900℃. However, it was found that the Ni_3Al films doped with 30 W Cr has showed the best oxidation-resistant properties.

The thesis ends with presenting the conclusion and future scope of the studies.

ACKNOWLEDGMENTS

Wisdom is not a product of schooling but,
of the lifelong attempt to acquire it-

-Albert Einstein

I feel immense pleasure in expressing my sincere and profound gratitude to my thesis supervisor Dr. Amit Kumar Chawla whose guidance and inspiring vision helped me in carrying out my research work. Dr. Chawla's commitment to my academic and professional development has been truly remarkable. His insightful feedback, encouragement, and valuable insights have played a pivotal role in shaping the direction of my research and ensuring its quality. His ability to provide constructive criticism and thoughtful guidance has been invaluable, pushing me to strive for excellence. I also want to acknowledge the patience and accessibility Dr. Chawla has demonstrated throughout my doctoral journey. He was always available to address my queries and concerns, offering timely and meaningful advice that helped me overcome challenges and make progress.

I wish to extend my sincere gratitude to my esteemed mentors, Prof. Devesh Kumar Avasthi and Dr. Vikas Saxena, for their invaluable contributions to my doctoral research. Their guidance, unwavering support, and ingenious ideas have been the cornerstone of my academic journey. Prof. Devesh Kumar Avasthi and Dr. Vikas Saxena have consistently provided me with invaluable suggestions and insightful recommendations that have enriched the quality and scope of my research. Their mentorship has been a source of inspiration, motivating me to strive for excellence at every step of my thesis work.

I express my sincere thanks to Dr. Paritosh Dubey, Dr. Vipin Chawla, Dr. Neha Sardana, and Dr. Sanjeev Kumar Dubey for their tremendous help in learning the interpretation of several results obtained during my research. Their expertise and willingness to share their knowledge have been crucial in unraveling the complexities of my study and making sense of the data and

findings. I consider myself fortunate to have had the privilege of working alongside such esteemed professionals, and their guidance will undoubtedly leave a lasting impact on my academic and professional journey.

Next, I would like to express my profound appreciation to my parents for their unwavering support throughout my academic journey. Their constant encouragement and unshakeable belief in my abilities were instrumental in enabling me to successfully complete my research within the designated timeframe. Their love and motivation have been a driving force, and I am deeply grateful for their sacrifices and dedication.

I am also immensely thankful to my wife, Rinku Tiwari, whose prayers, flexibility, and selfless sacrifices were the cornerstone of my perseverance. Her unwavering support sustained me through the challenges, and I am profoundly grateful for her presence in my life.

In addition, I would like to acknowledge the blessings and guidance I received from my teachers, seniors, and colleagues. Their collective support has been invaluable in helping me navigate each step of this research journey, ultimately allowing me to achieve my study's goals.

I wish to express my deep gratitude to my beloved and well-wisher Dr. Jitendra Kumar Pandey for his love and belief in me and the way he has been motivating me for the research. I want to thank the entire team at R&D, UPES, and, in particular, Dr. Devesh Kumar Avasthi, Dr. Pankaj Kumar Thakur, Dr. Anil Sinha, Dr. S.M. Tauseef and Dr. Ashish Mathur for their unwavering belief in my research and for providing the crucial financial support that sustained my journey. I can't forget to thank Mr. Yogesh Kumar Sharma, Mr. Arjun Rana, and the entire team of SRE at UPES who were always one step ahead to help throughout this journey.

I would also like to extend my heartfelt thanks to my dedicated colleagues, Mr. Akula Umamaheswara Rao, Ms. Archana Singh Kharb, and Ms. Avantika Chauhan, for their remarkable assistance and unwavering support, which significantly enriched my research experience.

Furthermore, I'm grateful for the exceptional lab support provided by Mr. Charu Pant and Mr. Prakash Bobde throughout my tenure. Your

contributions have been instrumental in the successful completion of my Ph.D. thesis, and I am deeply appreciative of your belief, support, and assistance.

At last, I would like to extend my heartfelt gratitude to some exceptional individuals who have played a significant role in my academic journey.

Firstly, I am deeply thankful to Dr. Sharad Mehra, Chairman of UPES, Dr. Sunil rai, Chancellor, UPES and Dr. Ram Sharma, Vice-Chancellor, UPES, for their unwavering belief in my potential and for providing the essential infrastructure that allowed me to conduct my research at UPES.

I must also express my appreciation to Mr. Manish Madan, Dr. Atri Nautiyal, Mr. Mohit Miyan, Mr. Sachin Rana, Dr. Nishant Mishra, Mr. Anant Prakash Mishra, Mr. Anil, and Mr. Bijendra for offering me a platform to engage in cultural activities and sports, which served as a mental anchor throughout my academic pursuits.

Lastly, my heartfelt thanks go out to my brothers Manish Kumar Tiwari and Anish Kumar Tiwari and to my numerous friends including Vivek Kumar Singh, Manoj Kumar, Kaushal Kumar Pankaj, Vaibhav Nanaware who, despite their busy schedules, shared their valuable suggestions and advice, enriching my academic journey. Your support and belief in me have been invaluable, and I am truly grateful for the contributions of each one of you to my academic and personal growth. Finally, I would like to express my gratitude to Mr. Rajeev Attri, Chief Librarian, for his invaluable assistance in tirelessly helping me with the formatting of my thesis, regardless of the time or day, through email and calls.

Sunil Kumar Tiwari

Doctoral Research Fellow

TABLE OF CONTENTS

SN	Contents			Page No
Declaration				i
Thesis completion certificate				ii
Abstract				iii
Acknowledgments				ix
Table of contents				xii
List of abbreviation				xvi
List of figures				xix
List of tables				xxvii
CHAPTER 1. Introduction				1
1.1	Evolution and importance of thin films			2
1.2	Hard coatings			3
	1.2.1	Need and importance of hard coatings		3
	1.2.2	Deposition method of hard coatings		4
		1.2.2.1	Chemical vapor deposition method	4
		1.2.2.2	Physical vapor deposition method	5
		1.2.2.3	Literature survey	6
1.3	Ni_3Al-based thin films			12
	1.3.1	Ni_3Al-based films in alloy and multilayer forms		14
1.4	Mechanical properties of Ni_3Al-based thin films			15
1.5	Tribological properties of Ni_3Al-based thin films			17
1.6	Application of Ni_3Al-based thin films			19
1.7	Motivation of present work			20
	1.7.1	Why Ni_3Al based coatings are chosen		20
	1.7.2	Objectives of the research		22
CHAPTER 2. Experimental and characterization techniques				23
2.1	Synthesis of thin films			24

	2.1.1	Magnetron sputtering for deposition of Ni_3Al films		26
	2.1.2	Parameters of deposition		30
2.2	Characterization techniques			31
	2.2.1	X-Ray diffraction technique		31
	2.2.2	FE-SEM and EDS analysis		35
	2.2.3	Atomic force microscopy		37
	2.2.4	Contact angle measurements		40
	2.2.5	Nano indentation technique		42
		2.2.5.1	Hardness and Young's modulus	44
		2.2.5.2	Adhesion between film and substrate	45
	2.2.6	Oxidation resistance test		45
CHAPTER 3. Synthesis and characterization of DC-sputtered Ni_3Al alloy films at different substrate temperatures				48
3.1	DC magnetron sputtered Ni_3Al alloy films at different substrate temperatures			49
	3.1.1	Introduction		49
	3.1.2	Experimental details		51
		3.1.2.1	Synthesis of Ni_3Al alloy films	51
		3.1.2.2	Characterization details	52
	3.1.3	Results and discussion		53
	3.14	Conclusion		64
CHAPTER 4. Synthesis and characterization of DC-co-sputtered Ni_3Al alloy and Ni-rich Ni_3Al films				65
4.1	DC magnetron co-sputtered Ni-rich Ni_3Al films			66
	4.1.1	Introduction		66
	4.1.2	Experimental details		68
		4.1.2.1	Synthesis of Ni_3Al and Ni-rich Ni_3Al films	68
		4.1.2.2	Characterization details	70
	4.1.3	Results and discussion		70

	4.1.4	Conclusion		80
CHAPTER 5. Synthesis and characterization of DC-co-sputtered doped Ni_3Al films				81
5.1	DC magnetron co-sputtered Cr-Ni_3Al films			82
	5.1.1	Introduction		82
	5.1.2	Experimental details		84
		5.1.2.1	Synthesis of Cr-Ni_3Al films	84
		5.1.2.2	Characterization details	85
	5.1.3	Results and discussion		86
	5.1.4	Conclusion		97
5.2	DC magnetron co-sputtered Zr-Ni_3Al films			98
	5.2.1	Introduction		98
	5.2.2	Experimental details		98
		5.2.2.1	Synthesis of Zr-Ni_3Al films	98
		5.2.2.2	Characterization details	99
	5.2.3	Results and discussion		99
	5.2.4	Conclusion		110
CHAPTER 6. Synthesis and characterization of oxidation-resistant properties of DC-co-sputtered doped Ni_3Al films				112
6.1	DC magnetron co-sputtered Cr-Ni_3Al films			113
	6.1.1	Introduction		113
	6.1.2	Experimental details		115
		6.1.2.1	Synthesis of Ni_3Al and Cr-Ni_3Al films	115
		6.1.2.2	Characterization details	116
	6.1.3	Results and discussion		117
	6.1.4	Conclusion		133
6.2	DC magnetron co-sputtered Zr-Ni_3Al films			135
	6.2.1	Introduction		135
	6.2.2	Experimental details		136

		6.2.2.1	Synthesis of Ni_3Al and Zr-Ni_3Al films	136
		6.2.2.2	Characterization details	136
	6.2.3	Results and discussion		136
	6.2.4	Conclusion		153
Conclusion and future prospect				155
References				160
List of publications				188
Similarity index				189

LIST OF ABBREVIATION

1	AC	Alternating current
2	AFM	Atomic force microscopy
3	BCC	Body-centered cubic
4	CAE	Cathodic arc evaporation
5	CAD	Cathodic arc deposition
6	CVD	Chemical vapor deposition
7	DC	Direct current
8	DSA	Drop shape analyzer
9	EC	Electrodeposition coating
10	EDS	Energy dispersive spectroscopy
11	ELD	Electrolytic deposition coating
12	FCC	Face centered cubic
13	FESEM	Field emission scanning electron microscopy
14	FWHM	Full width at half maxima
15	HCP	Hexagonal close pack
16	HVOF	High-velocity oxy-fuel
17	MAO	Micro arc oxidation
18	MEMS	Micro-electromechanical systems
19	MFC	Mass flow controller
20	PLD	Pulsed laser deposition
21	PVD	Physical vapor deposition

22	RF	Radiofrequency
23	RMS	Root mean square
24	RT	Room temperature
25	SCCM	Standard cubic centimeter per minute
26	SEM	Scanning electron microscopy
27	XRD	X-Ray diffraction
28	Al	Aluminum
29	B	Boron
30	Cr	Chromium
31	CrN	Chromium nitride
32	Cu	Copper
33	E	Young’s modulus
34	H	Hardness
35	Ni	Nickel
36	Nb	Niobium
37	Pd	Palladium
38	TaN	Tantalum nitride
39	Ti	Titanium
40	Ti-Si-N	Titanium silicon nitride
41	TiN	Titanium nitride
42	VN	Vanadium nitride
43	WN	Tungsten nitride
44	Zr	Zirconium

45	ZrN	Zirconium nitride
46	W	Tungsten
47	Å	Angstrom
48	at%	Atomic percent
49	cm	Centimeter
50	eV	Electron volt
51	GPa	Gega pascal
52	keV	Kilo electron volt
53	kW	Kilowatt
54	Mbar	Millibar
55	mm	Multimeter
56	mN	Milli newton
57	MPa	Mega Pascal
58	nm	Nanometers
59	µl	Micron liter
60	µm	Micron meter
61	W	Watt
62	wt%	Weight percent
63	2D	Two dimensions
64	3D	Three dimensions
65	℃	Degree Celsius

LIST OF FIGURES

Figure No	Caption	Page No
Figure 1.1	Different PVD and CVD techniques used to deposit hard coatings	6
Figure 1.2	Application of Ti, Ni and other transition metal-based thin films	13
Figure 1.3	Areas of application of Ni_3Al based hard and protective coatings	19
Figure 1.4	Variation in mechanical properties at different deposition parameters	21
Figure 1.5	Variation in oxidation properties due to different composition of dopants and parameters of synthesis	22
Figure 2.1	Free energy diagram for the formation of the nucleus with a critical radius	25
Figure 2.2	Growth modes of thin films	26
Figure 2.3	Schematic diagram of sputtering gun and placement of permanent magnets	27
Figure 2.4	Schematic diagram of the magnetron sputtering system	28
Figure 2.5	DC magnetron sputtering system used in the present work	29
Figure 2.6	Schematic diagram of X-ray diffractometer	34

Figure 2.7	X-ray diffraction **(a)** XRD (Bruker D8 ADVANCE ECO) **(b)** GI-XRD (Empyrean Panalytical)	34
Figure 2.8	Schematic diagram of Scanning electron microscopy	36
Figure 2.9	Field emission scanning electron microscopy used in present work	37
Figure 2.10	Schematic diagram of atomic force microscopy **(a)** operation of AFM **(b)** Contact mode AFM **(c)** Tapping mode AFM **(d)** non-contact mode AFM	38
Figure 2.11	Atomic force microscopy with contact mode of scanning	40
Figure 2.12	Schematic diagram of drop shape analyzer	41
Figure 2.13	Water drop shape analyzer used to measure the contact angle at static state	42
Figure 2.14	Nanoindentation setup used to evaluate the mechanical properties of the deposited films	43
Figure 2.15	Required setup for the oxidation test (a) front view of split furnace (b) side view of split furnace (c) Weighing balance	46
Figure 3.1	XRD spectra of Ni_3Al films deposited at different substrate temperatures	54
Figure 3.2	EDS results of Ni_3Al films deposited at different substrate temperatures (a) RT (b) 200℃ (c) 400℃ (d) 600℃	55
Figure 3.3	SEM images of Ni_3Al films deposited at different temperatures (a) RT (b) 200℃ (c) 400℃ (d) 600℃	56

Figure 3.4	Porosity in Ni_3Al films deposited at different substrate temperatures	57
Figure 3.5	2D AFM image of Ni_3Al films deposited at different substrate temperatures (a) RT (b) 200℃ (c) 400℃ (d) 600℃	58
Figure 3.6	3D AFM image of Ni_3Al films deposited at different substrate temperatures (a) RT (b) 200℃ (c) 400℃ (d) 600℃	59
Figure 3.7	Contact angles of the films deposited at different substrate temperatures (a) RT (b) 200℃ (c) 400℃ (d) 600℃	60
Figure 3.8	Load versus displacement curve of Ni_3Al film deposited at different substrate temperatures	61
Figure 3.9	Variation in hardness and Young's modulus as a function of substrate temperature	62
Figure 4.1	XRD spectra of Ni_3Al and Ni-rich Ni_3Al films	71
Figure 4.2	EDS results (a) 0 W Ni (b) 25 W Ni (c) 50 W Ni (d) 100 W Ni	72
Figure 4.3	Cross-sectional thickness (a) 0 W Ni (b) 25 W Ni (c) 50 W Ni (d) 100 W Ni	73
Figure 4.4	Microstructure of Ni_3Al and Ni-rich Ni_3Al films (a) 0 W Ni (b) 25 W Ni (c) 50 W Ni (d) 100 W Ni	74
Figure 4.5	Evolution of porosity with respect to sputtering power to Ni target	74
Figure 4.6	2D AFM images of Ni_3Al and Ni-rich Ni_3Al films	75

	(a) 0 W Ni (b) 25 W Ni (c) 50 W Ni (d) 100 W Ni	
Figure 4.7	3D AFM images of Ni_3Al and Ni-rich Ni_3Al films (a) 0 W Ni (b) 25 W Ni (c) 50 W Ni (d) 100 W Ni	76
Figure 4.8	Contact angle between water droplet and Ni_3Al surface (a) 0 W Ni (b) 25 W Ni (c) 50 W Ni (d) 100 W Ni	77
Figure 4.9	Load versus displacement curve of Ni_3Al and Ni-rich Ni_3Al films	78
Figure 4.10	Evolution of hardness and Young's modulus of Ni_3Al and Ni-rich Ni_3Al films	79
Figure 5.1	XRD spectra of Ni_3Al and Cr-Ni_3Al alloy films	87
Figure 5.2	FESEM images of Cr-Ni_3Al films (a) 0 W Cr (b) 10 W Cr (c) 20 W Cr (d) 30 W Cr (e) 40 W Cr	88
Figure 5.3	Evolution of porosity with respect to sputtering power to Cr target	89
Figure 5.4	Distribution of grains in Cr-Ni_3Al coatings	90
Figure 5.5	2D AFM images of Cr-Ni_3Al films (a) 0 W Cr (b) 10 W Cr (c) 20 W Cr (d) 30 W Cr (e) 40 W Cr	91
Figure 5.6	3D AFM images of Cr-Ni_3Al films (a) 0 W Cr (b) 10 W Cr (c) 20 W Cr (d) 30 W Cr (e) 40 W Cr	92
Figure 5.7	Contact angles of Ni_3Al and Cr-Ni_3Al films	93
Figure 5.8	Hardness and Young's modulus of Cr-Ni_3Al films as a function of power to Cr target	94
Figure 5.9	Hall-Petch relationship in Ni_3Al and Cr-Ni_3Al films	95

Figure 5.10	Load versus displacement graph of Cr-Ni_3Al films	96
Figure 5.11	XRD spectra of Ni_3Al and Zr-Ni_3Al alloy films	100
Figure 5.12	Peak shift in Zr-Ni_3Al films as a function of power to Zr target	100
Figure 5.13	FESEM images of Zr-Ni_3Al films (a) 0 W Zr (b) 10 W Zr (c) 20 W Zr (d) 30 W Zr (e) 40 W Zr	101
Figure 5.14	Evolution of porosity as a function of Zr enrichment in Ni_3Al alloy films.	102
Figure 5.15	Distribution of grains in Ni_3Al and Zr-Ni_3Al coatings	103
Figure 5.16	2D AFM images of Zr-Ni_3Al films (a) 0 W Zr (b) 10 W Zr (c) 20 W Zr (d) 30 W Cr (e) 40 W Zr	104
Figure 5.17	3D AFM images of Zr-Ni_3Al films (a) 0 W Zr (b) 10 W Zr (c) 20 W Zr (d) 30 W Cr (e) 40 W Zr	105
Figure 5.18	Contact angles of Zr-Ni_3Al films as a function of Zr enrichment	106
Figure 5.19	Hardness and Young's modulus of Zr-Ni_3Al films as a function of power to Zr target	108
Figure 5.20	Hall-Petch relationship in Ni_3Al and Zr-Ni_3Al films	109
Figure 5.21	Load versus displacement graph of Zr-Ni_3Al films	110
Figure 6.1	XRD Spectra of substrate, Ni_3Al and Cr-Ni_3Al films	119
Figure 6.2	Peak shift in the prominent peak (111) of XRD Spectra of Ni_3Al and Cr-Ni_3Al films	119

Figure 6.3 (a)	XRD spectra of the oxidized substrate, Ni_3Al and Cr-Ni_3Al films oxidized at 900 ℃	120
Figure 6.3 (b)	XRD spectra of the oxidized substrate, Ni_3Al and Cr-Ni_3Al films oxidized at 1000 ℃	120
Figure 6.3 (c)	XRD spectra of the oxidized substrate, Ni_3Al and Cr-Ni_3Al films oxidized at 1000 ℃	121
Figure 6.4	FESEM images of Cr-Ni_3Al films **(a)** 0 W Cr **(b)** 10 W Cr **(c)** 20 W Cr **(d)** 30 W Cr	122
Figure 6.5	Cross-sectional thickness of deposited films **(a)** 0 W Cr **(b)** 10 W Cr **(c)** 20 W Cr **(d)** 30 W Cr	122
Figure 6.6	FESEM images of oxidized samples at 900℃ **(a)** Substrate **(b)** 0 W Cr **(c)** 10 W Cr **(d)** 20 W Cr **(c)** 30 W Cr	123
Figure 6.7	FESEM images of oxidized samples at 1000℃ **(a)** Substrate **(b)** 0 W Cr **(c)** 10 W Cr **(d)** 20 W Cr **(e)** 30 W Cr	124
Figure 6.8	FESEM images of oxidized samples at 1100℃ **(a)** Substrate **(b)** 0 W Cr **(c)** 10 W Cr **(d)** 20 W Cr **(e)** 30 W Cr	125
Figure 6.9	3D AFM images of substrate as-deposited Cr-Ni_3Al films (a) Substrate (b) 0 W Cr (c) 10 W Cr (d) 20 W Cr (e) 30 W Cr	127
Figure 6.10	3D AFM images of Substrate, Ni_3Al and Cr-Ni_3Al films oxidized at different temperatures	128
Figure 6.11	Relationship between normal load and friction coefficient of the substrate, Ni_3Al and Cr-Ni_3Al	129

	films	
Figure 6.12	Weight gain/area versus number of cycles **(a)** Cr-Ni_3Al oxidized at 900℃ **(b)** Cr-Ni_3Al oxidized at 1000℃ **(c)** Cr-Ni_3Al oxidized at 1100℃	130
Figure 6.13	Parabolic characteristics of oxidation kinetics **(a)** Cr-Ni_3Al oxidized at 900℃ **(b)** Cr-Ni_3Al oxidized at 1000℃ **(c)** Cr-Ni_3Al oxidized at 1100℃	132
Figure 6.14	Parabolic characteristics of oxidation kinetics **(a)** Cr-Ni_3Al oxidized at 1100℃ up to 10 cycles **(b)** Cr-Ni_3Al oxidized at 1100℃ from 11 to 30 cycles.	132
Figure 6.15	XRD Spectra of as-deposited Ni_3Al and Zr-Ni_3Al films	137
Figure 6.16	Peak shift in the prominent peak (111) of XRD Spectra of Ni_3Al and Zr-Ni_3Al films	138
Figure 6.17 (a)	XRD spectra of Ni_3Al and Zr-Ni_3Al films oxidized at 900℃	139
Figure 6.17 (b)	XRD spectra of Ni_3Al and Zr-Ni_3Al films oxidized at 1000℃	140
Figure 6.17 (c)	XRD spectra of Ni_3Al and Zr-Ni_3Al films oxidized at 1100℃	140
Figure 6.18	FESEM images of Zr-Ni_3Al films **(a)** 0 W Zr **(b)** 10 W Zr **(c)** 20 W Zr **(d)** 30 W Zr	141
Figure 6.19	Cross-sectional thickness of deposited films **(a)** 0 W Zr **(b)** 10 W Zr **(c)** 20 W Zr **(d)** 30 W Zr	142
Figure 6.20	FESEM images of oxidized samples at 900℃ **(a)** Substrate **(b)** 0 W Zr **(c)** 10 W Zr **(d)** 20 W Zr **(e)** 30	143

	W Zr	
Figure 6.21	FESEM images of oxidized samples at 1000℃ **(a)** Substrate **(b)** 0 W Zr **(c)** 10 W Zr **(d)** 20 W Zr **(e)** 30 W Zr	144
Figure 6.22	FESEM images of oxidized samples at 1100℃ **(a)** Substrate **(b)** 0 W Zr **(c)** 10 W Zr **(d)** 20 W Zr **(e)** 30 W Zr	145
Figure 6.23	3D AFM images of as-deposited Zr-Ni_3Al films (a) 0 W Zr (b) 10 W Zr (c) 20 W Zr (d) 30 W Zr	146
Figure 6.24	3D AFM images of Substrate, Ni_3Al and Zr-Ni_3Al films oxidized at different temperatures	147
Figure 6.25	Relationship between normal load and friction coefficient of the substrate, Ni_3Al and Zr-Ni_3Al films	149
Figure 6.26	Weight gain/area versus number of cycles **(a)** Zr-Ni_3Al oxidized at 900℃ **(b)** Zr-Ni_3Al oxidized at 1000℃ **(c)** Zr-Ni_3Al oxidized at 1100℃	150
Figure 6.27	Parabolic characteristics of oxidation kinetics **(a)** Zr-Ni_3Al oxidized at 900℃ **(b)** Zr-Ni_3Al oxidized at 1000℃ **(c)** Zr-Ni_3Al oxidized at 1100℃	152
Figure 6.28	Parabolic characteristics of oxidation kinetics **(a)** Zr-Ni_3Al oxidized at 1100℃ up to 10 cycles **(b)** Zr-Ni_3Al oxidized at 1100℃ from 11 to 30 cycles.	152

LIST OF TABLES

Table No	Caption	Page No
Table 1.1	Literature survey showing the methodology opted by researchers to deposit hard coatings	6
Table 1.2	Properties of alloy and multi-layered Ni_3Al films	15
Table 1.3	Mechanical properties of Ni_3Al-based coatings	16
Table 3.1	Sputtering parameters for depositing Ni_3Al alloy films	52
Table 3.2	Calculated parameters of Ni_3Al films deposited at different substrate temperatures	55
Table 4.1	Sputtering parameters for depositing Ni_3Al and Ni-rich Ni_3Al films	69
Table 4.2	Calculated parameters of Ni_3Al and Ni-rich Ni_3Al films	72
Table 5.1	Sputtering parameters for depositing Cr-Ni_3Al films with variation in Cr content	85
Table 5.2	Calculated parameters of Cr-Ni_3Al coatings as a function of Cr enrichment	87
Table 5.3	Sputtering parameters for depositing Zr-Ni_3Al films with variation in Zr content	99
Table 5.4	Calculated parameters of Zr-Ni_3Al coatings as a function of Zr enrichment	104
Table 6.1	Elemental composition of INCONEL-718	116

Table 6.2	Sputtering parameters for depositing Zr-Ni_3Al films with variation in Zr content	116
Table 6.3	Calculated grain size, porosity, surface roughness and microstrain in Cr-Ni_3Al films	121
Table 6.4	EDS results of substrate and Cr-Ni_3Al films oxidized at different temperatures	126
Table 6.5	Surface roughness of oxidized Ni_3Al and Cr-Ni_3Al films	127
Table 6.6	Parabolic rate constant of substrate and deposited Cr-Ni_3Al films	133
Table 6.7	Sputtering parameters for depositing Zr-Ni_3Al films with variation in Zr content	136
Table 6.8	Calculated grain size, porosity, surface roughness and microstrain in Zr-Ni_3Al films	141
Table 6.9	EDS results of substrate and Zr-Ni_3Al films oxidized at different temperatures	145
Table 6.10	Surface roughness of oxidized Ni_3Al and Zr-Ni_3Al films	148
Table 6.11	Parabolic rate constant of substrate and deposited Zr-Ni_3Al films	153
Table 7.1	Hardness, Young's modulus, and oxidation-resistant properties of Ni_3Al-based coating with respect to varying sputtering parameters	156

CHAPTER 1

INTRODUCTION

1.1 EVOLUTION AND IMPORTANCE OF THIN FILM

The demand for materials for different applications including the harsh conditions was fulfilled by the raw and bulk materials during the 15th century [1]. However, the way of joining similar metals with an interfacial layer of thin films has been reported back to 3400 before Christ followed by electroplating in few centuries after the death of Christ. Some of the scientists, Issac Newton, Robert Boyle, and Robert Hooke studied the interfacial patterns of the color spectrum and oil films in early 1660 after the death of Christ [2]. Several scientists and research groups studied and understood the importance and role of thin films after the development of vacuum technology [1]–[3]. The evolution of vacuum technology with the development of thin film deposition techniques helped researchers and scientists invent and develop several instruments and engineering technologies [4]. The invention of the barometer in 1640, the mechanical energy was transformed into electrical energy in 1663, use of storage devices in the 1700 century, and the evolution of batteries to covert energy, etc. are the gifts of the evolution of thin film deposition technologies [1]. The technology of developing different kinds of thin films has a long mesmerizing history with its roots being spread from the early 20th century till date.

Thin films are a layer of materials whose thickness lies between a few angstroms to a few millimeters. These thin films belong to a part of advanced materials group that are used in several industries like, optics, radar technology, defense and marine industries, nuclear industries, electronics and microchips, power and energy sectors, aerospace and automobile industries, etc. Thin films are capable of protecting the parent material (substrate) in even harsh conditions and also contributes in the improvement of the properties, reliability and durability of specimen. The increased demand for thin films for their use in different conditions and environments resulted in the development of different classes of coatings and deposition techniques. Depending upon their different use, several kinds of thin films have been developed over the years with extraordinary properties. Hard, brittle and wear-resistant thin films have been used in automobile and machinery industries, hydrophobic and

transparent coatings have been used in power industries, heat-resistant, corrosion and oxidation-resistant coating have been used in marine, defense and aerospace industries, antibacterial, corrosion resistant coatings have been used in medical industries and so on. In last five decades researchers have developed several kinds of coatings which are used in medical, aerospace, marine, defense, power, energy and electronic industries etc. The development of thin films serves as a key material which shows its importance in tailoring the properties of materials according to the need. They are used to develop several technological advancements which gives flexibility in the use of materials[5]–[7].

1.2 HARD COATINGS

The name “Hard coatings” is given to a family of thin films which are able to protect the parent material (substrate) from the permanent deformation due to local indents, scratch and wear. These hard coatings are capable of giving protection to the substrates against wear, abrasion and corrosion attacks that enhances the life of parent material and also enhances the desired properties [8], [9].

1.2.1 Need and importance of hard coatings

With increase in demand of the functional requirements of the material, hard coatings have been generally used in automobile industries, machine shop for enhancing tool strength, aerospace industries, wear resistant applications of automobile industries and so on [10]. Apart from enhancing the wear properties and hardness of the specimen, hard coatings also give protection to the material against corrosion and oxidation attacks. They also possess lubricity and resist wear and abrasion during friction and help enhancing the life of the parent material [11], [12]. Researchers have used different transition metal-based nitrides and carbides coatings that have revealed resistant properties against wear with enhanced hardness in aggressive environments. Transition metal-based coatings have been broadly explored and used for their high hardness and resistance to wear. Additionally, they have proved their candidacy in protecting the parent material from oxidation and corrosion

attacks in extreme conditions. The family of hard Transition metal binary and ternary nitride thin films of Titanium, Tungsten, Tantalum, Silicon and Chromium etc. have found their broad application in cutting tool and machine shops, automobile sectors and aerospace applications [13]–[16].

Hard coatings of titanium are used in chip fabrication industries, electromechanical systems and bioimplants at large scale [17] [18]. Vanadium and chromium nitride thin films possess exceptional resistance against wear which makes them suitable for fabricating engine parts, gears and bearings. [19], [20]. These hard coatings have demonstrated enhanced mechanical properties with robust resistance against oxidation and corrosion attacks but they have failed to endure these properties at extreme elevated temperatures [21], [22].

1.2.2 Deposition method of hard coatings

There are several ways to enhance the hardness of the material and thin films. In case of metallic materials, surface modification, heat treatment, incorporation of reinforcing materials to parent material to fabricate composites, nano hard coatings, etc. are responsible for increasing the hardness of the material. Reinforcing materials used in such cases are nitrides and carbides of metals and nonmetals, carbon-rich nanomaterials, etc. [23]. The use of metallic materials on a large scale in automobile industries, aerospace industries, and marine industries has led to the rise in demand for hard and corrosion-resistant coating materials. Several researchers have worked on increasing the hardness of the material following the deposition or coating technique as the common one. Hard coating involves depositing a thin layer of hard material on the specimen that shields it from the adverse effects of environmental exposures. [24]. There are two major hard coating deposition techniques opted by researchers namely Chemical vapor deposition technique (CVD) and physical vapor deposition technique (PVD).

1.2.2.1 Chemical vapor deposition method

CVD includes use of gaseous precursor which is introduced in reaction chamber to form coatings at 950–1150℃. In other words, CVD is a process in

which gaseous compound is condensed on a substrate to form solid coating layer [25]. In this process, the precursors used reacts with the surface of substrate resulting in deposition of thin and thick layers in the presence of inert gas [26]. Generally, the stable gases used in the process are $TiCl_4$, BCl_3 and $AlCl_3$. CVD can produce coatings with high thickness, at high power whereas it results in residual stresses in coatings and surface roughness and there is requirement of high pressure and temperature which is major disadvantage of this process[26] [27]. This technique has the ability to modify the optical, mechanical, electrical, and corrosion resistance properties of the substrate [28]. This technique can be used to produce coating on large surface area as the development of the film can be on either side based on fulfilment of precursors [24].

1.2.2.2 Physical vapor deposition method

All the deposition methods which use solid precursor materials (commonly known as targets) come under the class of Physical Vapor Deposition (PVD). During the process, a solid target is converted into gaseous state either by evaporation or by impact processes which is cooled on the substrate resulting in uniform deposition [29]. Thermal and kinetic activation of film growth is the major requirement when compared to CVD.

The purpose of use of PVD is to achieve good properties like high hardness, anti-corrosion property, wear resistance properties, adjustable tribological and mechanical properties. Conversely, the requirement of high vacuum is a key challenge to be achieved [30]. In PVD based deposition, very fine grain size and microcrystalline structure are achieved with enhancement in adhesion which results in improving the surface roughness and corrosion resistance properties [31]. Finer grains also increase the wear resistance of hard coated material [32]. The performance of the hard coatings is affected by several factors such as chemical composition, stoichiometry, impurities, microcrystalline structure imperfection, orientation, inert gases atmosphere, characteristics of targets etc. The properties of hard coatings can be précised during the deposition process [33]. **Figure 1.1** represents some of the PVD

and CVD methods used for depositing thin films on different kinds of substrates [24].

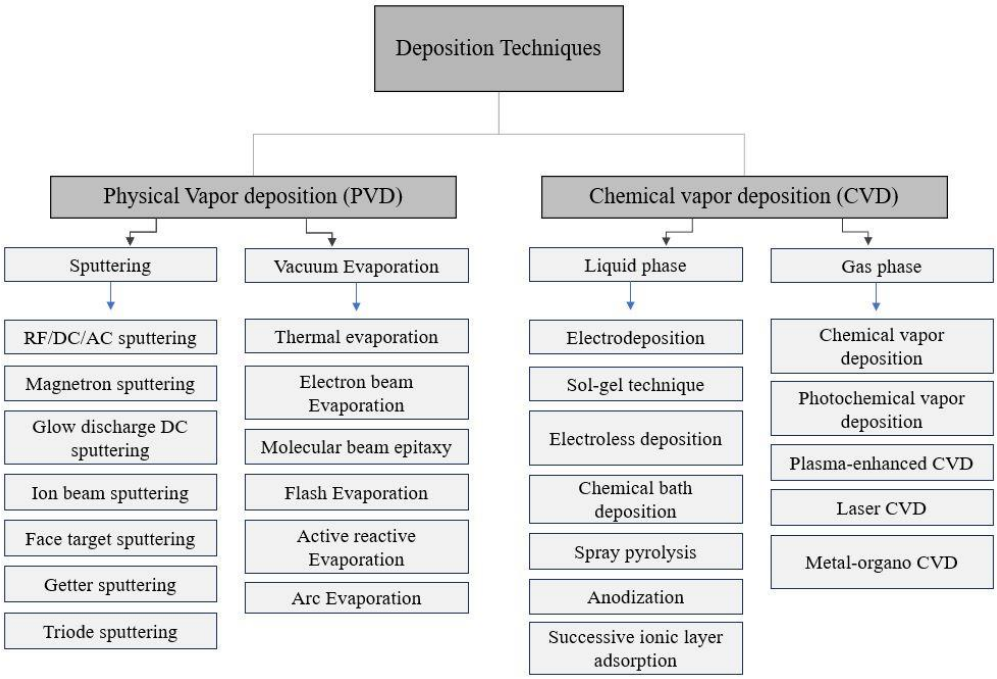

Figure 1.1: Different PVD and CVD techniques used to deposit hard coatings

1.2.2.3 Literature survey

A short overview of different deposition method which is used to deposit hard coatings along with the target elements, substrate material, coating thickness, mechanical and tribological properties that are observed by different researchers are mentioned in **table 1.1**:

Table 1.1: Literature survey showing the methodology opted by researchers to deposit hard coatings

Authors	Methodology	Targets/ coatings	Substrate	Major Findings
Gharavi *et al.*,(2018) [34]	Reactive Magnetron Sputtering	Cr (In presence of argon and nitrogen gas mixture)	Sapphire	• Prepared coated surface showed the hardness of H=18.9±0.5 GPa • Oxidation resistant up to 400°C
Ou *et al.*, (2000) [35]	Deep oscillation magnetron	TiAlSi	AISI 304L stainless steel	• Enhancement in voltage caused in reduction in grain size.

	sputtering	**(**argon and N_2 mixture)		• Maximum hardness of ~ 42.4 GPA and Young's modulus of 495 GPa was obtained. • TiAlSiN coatings with high hardness possessed uniform distribution of refined grains which brings out in lowering the rate of wear.
Yadav *et al.,* (2000) [36]	Magnetron sputtering	TiSiBC (In presence of argon)	SS- 304 sheets	• Three coatings with different thickness of 10 µm, 15 µm, and 20 µm were fabricated • With increase in film thickness, grain size and microhardness improved
Santecchia *et al.,* (2019) [37]	Physical vapor deposition (PVD)	AlTiCrN and a superlattice (nanolayered) CrN/NbN	High speed tool steel (S600)	• Tribotest was conducted ar rrom temperature and 700℃ • AlTiCrN coating exhibited the best response under the ambient tribo-test while the coating was removed from the substrate at high temperature • CrN/NbN films were moderately pilled off from the substrate at room temperature and showed vilest performance at elevated temperature.
Hauert *et al.,* (2000) [38]	-	Al_2O_3, TiCN, TiC, TiAlN, TiN, CrN,	-	• Alloying of a coating during deposition, while maintaining the deposit as a single phase, shows the possibility of changing most of the properties of the coatings.
PalDey *et al.,* (2003) [39]	Sputtering and CAM (cathodic arc method)	(Al, Ti)-N	HSS, cermet & Cemented carbide	• Resistance to wear, hot hardness, oxidation and thermal stability of tool is improved using Ti-Al-N coatings and make them useful for machining in dry conditions. • Resistance against oxidation is enhanced by doping with Cr and Y • Resistance against wear is improved by incorporating Zr, B, V in the matrix

				whereas addition of Si enhances the hardness
Sundar *et al.*, (2010) [40]	Novel laser/sol-gel method	TiAlN	Steel	• Thin film of 16 µm was deposited • These coatings can be used for repairing purposes. • Enhanced coating/substrate adhesion strength was achieved due to the precipitation of Ti-Al-N grains into the substrate.
Li *et al.*, (2013) [41]	Arc evaporation system	Cr–Al–N & Ti–Al–N	Al_2O_3 CNMG12 0408 and SEET123 inserts	• Individual alloy and multilayer films of CrAlN and TiAlN have been prepared. • Enhanced hardness of ~38.2 GPa was attained for multilayered TiAlN/CrAlN films having bilayers of 15 nm. • The resistance to oxidation enhanced when ratio of CrAlN increased with respect to bilayer. • The results of oxidation test shows that the formation of oxide layers on CrAl-N and TiAlN/CrAlN_2 coatings.
Bukhaiti *et al.*, (2014) [42]	Industrial magnetron sputtering (DC-mode) (MF- pulsed mode	Multilayer coatings of [Ti/TiAlN/TiAlCN]5	Tool steel	• Ti/TiAlN/TiAlCN multilayer coated sample showed low coefficient of friction (~0.28) which is almost three times lower than uncoated sample. • The modulus of elasticity of the fabricated films was matched to that of the substrate. • Rate of wear was found to be increased with increase in load and velocity.
Long *et al.*, (2014) [43]	Cathodic arc evaporation (CAE)	Cr0.3Al0.7N and Ti0.5Al0.5N	Silicon nitride cutting inserts	• Because of the smaller grain size, Ti0.5Al0.5N showed comparatively higher hardness. • The durability and performance of the coated inserts was enhanced by

				two times. However, it was found to be better when coated with Ti0.5Al0.5N
Reddy *et al.*, (2015) [44]	Pulsed RF magnetron sputtering technique	Alumina	Stainless steel-304	• The i_{corr} values of alumina coated SS304 substrate was much superior than i_{corr} of the uncoated substrate. • DC sputtered films exhibited improved resistance to corrosion as compared to RF sputtered films. • The corrosive atmosphere didn't show any considerable differences in the microstructure and surface properties of the coating.
Joshi *et al.*, (2015) [5]	Reactive DC magnetron sputtering	Ti-Nb	AISI SS-304	• Hardness of the film improved with increase in N_2 flow. • XRD spectra reveal the existence of NbN, Nb_2N_3 and TiN phases.
Mishra *et al.*, (2016) [7]	DC magnetron sputtering	Al-Si-N	Si, SS-304 and Glass	• The synthesized film showed the hardness values of ~30GPa and modulus of ~300GPa.
Mikula *et al.*, (2016) [45]	Reactive magnetron co-sputtering	TiAl and Nb (in Ar+N2 environment)	WC/Co & Si (100)	• The deposited TiAl-based thin films showed hardness and modulus of ~32.5 GPA and modulus ~442 GPa. It was observed that the doping of the Nb in TiAl matrix decreased the hardness to the range of ~ 28 to 31 GPa.
Komarov *et al.*, (2016) [46]	Magnetron sputtering	TiN and TiAlN (In the existence of Ar and N_2 gas flow)	Armco-iron and AISI 304 steel substrates	• Hardening of the substrate using nitrocarburization increases the hardness of the film by 7 times.
Paskvale *et al.*, (2016) [47]	Magnetron sputtering	Ti, TiAl and Cr	Tool steel AISI D2 (high carbon high	• The presence of MoS_2 contributes in depressing the wear rate by the fraction of ten.

			chromium)	
Almotairi *et al.*, (2016) [48]	Electroplating	Cr	Annealed 416 stainless steel bars	• The adhesive strength between the Cr layer and the substrate enhanced whereas the residual stress increased with rise in the film thickness.
Kong *et al.*, (2016) [49]	Unbalanced magnetron sputtering (Ar+ plasma)	Cr, CrTi and CrAl	Si Wafer (100)	• CrAlN gives better protection against to substrate as compared to CrN thin films.
Sui *et al.*, (2017) [50]	Reactive magnetron sputtering	TiAlN/CrN coatings	cemented carbide and Silicon (100)	• The deposited films showed the maximum hardness of ~25 GPa which decreased simultaneously to its minimum of 18.1 GPa with increase in bilayer periods.
Ch. Sateesh Kumar, Saroj Kumar Patel (2017) [51]	CAE	AlTiN and AlCrN	Ceramic inserts	• TiAlSiN/TiSiN/TiAlN coating displayed higher hardness.
Kaushal *et al.*, (2017) [52]	Cladding	Ni-SiC claddings	SS-304	• The highest microhardness of ~1025 HV was attained at the top layer while 32 times better wear properties were achieved as compared to the single layer of cladding.
Gong *et al.*, (2017) [53]	Cathode arc evaporation (CAE)	TiAlN and AlCrN	Carbide grade, WC-2TiC-3Co-3Ni-1Mo	• Results reflected that the friction coefficient of AlCrN film was lower as compared to TiAlN film whereas and thus possess better wear resistance
Vettivel *et al.*, (2017) [54]	Cathodic arc deposition (CAD)	TiN, TiAlN and AlCrN	SS-304	• Use of the coatings helped in decreasing the wear rate of the substrate and also reflected better hardness than SS-304. However, TiN films have shown the best hardness and wear resistant properties as compared to other two

				films.
He *et al.*, (2018) [55]	Magnetron sputtering	Ti & Ni (In atmosphere of N_2)	Si (100) and AISI 304	• The grain size of the deposited films was observed as ~8-9 nm • Hardness and modulus decreased with increase in bilayer periods
Mahato *et al.*, (2018) [56]	DC magnetron sputtering	TiSiB-CN & TiSiB-C	Stainless Steel 304	• The rate of wear in coated SS 304 was very less in comparison to uncoated SS 304. • The hardness of the coated and uncoated substrates was observed as ~27 GPa and 4 GPa whereas the obtained modulus was 320 GPa and 130 GPa respectively
Szala *et al.*, (2019) [57]	DC-Magnetron sputtering	AlTi-N &TiAl-N	SS 304	• The adhesion strength between the substrate and deposited films increased. • Resistance to erosion in AlTi-N films caused by cavitation increased by one third of TiAl-N films which was almost ten times higher than the substrate.
Abdallah *et al.*, (2019) [58]	DC magnetron sputtering	TiN and TiAlVN (Ti6Al4 V)	SS304, Carbon and Silicon (100)	• The hardness of the film enhanced with rise in the adhesive strength between Al and V which also contributed in enhancing the corrosion resistant properties.
Romero *et al.*, (2019) [59]	DC magnetron sputtering	TiAlTaN - (TiAlN/TaN)	AISI M2 steel substrates	• 48:52 ratio of TiAlTaN & TiAlN/TaN showed hardness of ~29 GPa.
Alyones *et al.*, (2019) [60]	DC magnetron sputtering	CrN	Silicon (100) and stainless steel (SS 304)	• CrN films deposited at a pressure of 4 mtorr reflected the best resistance to corrosion along with highest hardness of ~29 GPa.
Fryska *et al.*, (2019) [61]	Reactive magnetron sputtering	Chromium nitride/chromium and	(SS 304)	• The change in N_2 content in S-phase varies the hardness of the film

		chromium nitride/S-phase		
Wang *et al.*, (2020) [62]	Plating technique (arc ion)	CrN and CrCN	316L SS and silicon wafers (001)	• It was found that CrN/CrCN possess better hardness and toughness as compared to CrN monolayer. • Additionally, the Cr-C bond contributes in increasing the lubrication property.
Kazlauskas *et al.*, (2020) [63]	Physical vapor deposition	CrN and TiAlN	WC-Co	• It was found that the hardness of the substrate increased from ~18 GPa to ~19.4 GPa when coated with CrN and it reached to 30.8 GPA when coated with TiAlN.
Awan *et al.*, (2020) [64]	Physical vapor deposition (PVD)	Ti/TiN	SS 304	• The substrates coated with Ti/TiN films were able to protect the material from corrosion attacks but the films with 8 layers of Ti showed the best results. • Additionally, the best resistance to wear was showed by TiN films.
Mejía V *et al.*, (2020) [65]	DC Magnetron sputtering	TiAlN (Ag,Cu)	AISI 420 stainless steel	• Deposited TiAlN and TiAlN (Ag, Cu) films resulted in protecting the substrate from oxidation attacks.
Kevin *et al.*, (2020) [66]	Spraying process	Cr_3C_2–NiCr	SS316 stainless steel	• The coated substrate reflected better erosion and corrosion resistant properties as compared to bare substrate.

1.3 Ni_3Al-BASED THIN FILM

With increase in demand of materials to be used at high temperatures, researchers have synthesized different types of transition metal-based coatings especially Ti and Ni-based thin films that can sustain high temperatures for refractory purposes. Additionally, these coatings are capable of withstanding the elevated temperatures for their use in turbine vanes, automobile and jet

engines, aerospace productions, and nuclear industries. Some of the major applications of these coatings have been shown in **figure 1.2**. Ni-based coatings, especially the group of aluminides like NiAl, $NiAl_3$, Ni_3Al, Ni_5Al and Ni_9Al have been generally considered as they possess tremendous resistance to oxidation at elevated temperatures without losing their strength. [67]–[69].

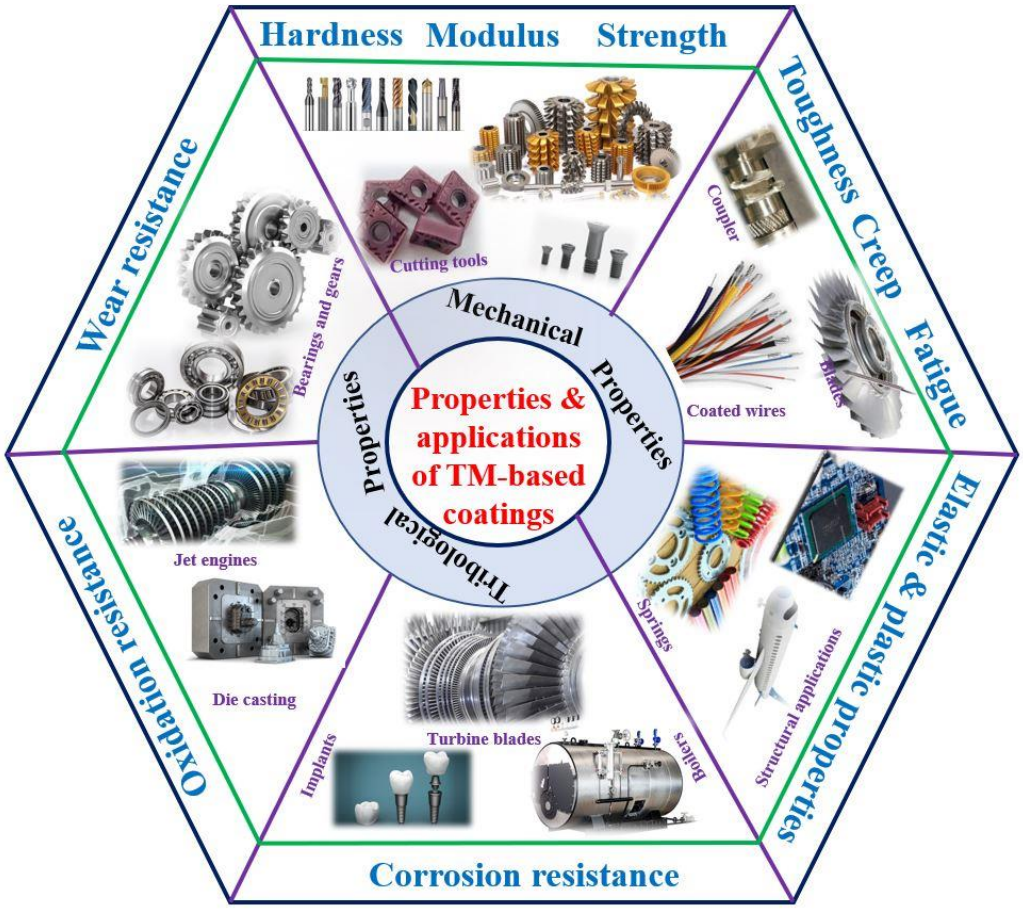

Figure 1.2: Application of Ti, Ni and other transition metal-based thin films

Ni_3Al coatings are polycrystalline intermetallic FCC structured aluminides having lattice constant of nearly ~0.3570 nm which form ordered $L1_2$ structure when deposited or treated beyond 300℃ [70]. Ni_3Al-based thin films show outstanding resistance to oxidation and corrosion at high temperatures that also preserves the structural integrity of the materials [67], [71], [72]. The feasting and interdiffusion of aluminum from the Ni_3Al surface when exposed to elevated temperature par to 900℃, lead to the dilapidation of the coating

resulting in the evolution of pores at the interface. Amongst all the class of aluminides, Ni_3Al has been proven as the best candidate for their application at elevated temperatures as it possesses excellent resistance to oxidation and corrosion in extreme situations [73], [74]. The Ni_3Al coating also gives excellent resistance to fatigue and creep failure and hence can be used in turbine blades and aero engines [75]. Along with the high temperature stability, Ni_3Al is able to perform well in extreme conditions where materials fail due to creep and fatigue [76]. Several researchers have deposited Ni_3Al-based coatings using different deposition techniques by varying the deposition parameters. Some of the research groups have also deposited these films in multilayer and alloy forms to understand the change in structural integrity of the films which helps in altering the tribological and mechanical properties when used at ambient and elevated temperatures [77]–[79].

1.3.1 Ni_3Al-based films in alloy and multilayer forms

Ni_3Al-based thin coatings have been fabricated for applications at high temperatures. These films are also capable of showing enhanced tribological and mechanical properties. The alloy form of Ni_3Al based coatings is achieved by either depositing the Ni and Al together or by depositing the Ni_3Al directly in the alloy form using CVD and PVD techniques. Moreover, different kind of dopants have been used in alloy or multilayer form to alter their properties. In case of PVD, the Ni_3Al (in composition of the ratio 75:25) and dopants are continuously deposited together to obtain alloy form of Ni_3Al coatings whereas a different layer of Ni_3Al and dopant material is deposited layer by layer to form multilayer Ni_3Al coatings [80]–[85]. The properties of Ni_3Al films in alloy form and multilayer form also depends upon the nature and concentration of the dopant used where as the number and thickness of individual layers plays a crucial part in altering the properties of multilayered Ni_3Al coatings. Xing *et al.,* [86] deposited alloy Ni_3Al and Ni_3Al/Cr in multilayer form to examine the properties of the deposited coatings. They observed that the multilayer Ni_3Al/Cr films showed better oxidation resistant properties than Ni_3Al alloy coatings. Boni *et al.,* [87] enriched Ni_3Al with Ni in multilayer form and compared the results with alloy Ni_3Al films and bulk

Ni_3Al. It was observed that the Ni/Ni_3Al coatings reflected low hardness when compared to alloy Ni_3Al films which showed the highest hardness of nearly 13.5 GPa. R Banerjee [88] deposited alloy Ni_3Al films at different substrate temperature starting from ambient temperature to 400℃ and proclaimed that Ni_3Al alloy film synthesized at 400℃ exhibited the highest hardness of nearly 8 GPa. Some of the results of the Ni_3Al films in alloy and multilayer form have been mentioned in **table 1.2**.

Table 1.2: Properties of alloy and multi layered Ni_3Al films

Matrix material	Properties
Ni_3Al & Ni_3Al/W [89]	• The rise in concentration of tungsten in Ni_3Al matrix increases the hardness • Hardness of Ni_3Al alloy film decreased when annealed after synthesis whereas it increased for W-Ni_3Al films and that with 12 at% of W in Ni_3Al.
Ni_3Al and Ni_3Al/Cr [86]	• Hardness decreased and modulus increased when thin layer of Cr was inserted between Ni_3Al layers. • Oxidation resistance properties improved. • Ni_3Al/Cr showed enhanced plasticity and toughness than Ni_3Al alloy film
Ni-Ni_3Al and W-Ni_3Al [68]	• Increase in content of tungsten in the host matrix refines the crystallite size • The deposited coating possesses thermally stable microstructure. • 12 at % of W in host Ni_3Al matrix showed the hardness of ~15.6 GPa
Ni_3Al/ MoS_2 [81]	• MoS_2 resulted in enhancing the hardness. • • The deposited coating possesses low frictional coefficient and reflected the property of self-lubrication. • Adhesion strength between the substrate and coating was enhanced.
Ni_3Al/ Cu & MoS_2 [82]	• Microhardness of 320 HV was achieved. • The deposited film showed resistance to wear in dry sliding conditions at ambient temperature. • Adhesion strength of the coating was improved.

1.4 MECHANICAL PROPERTIES OF Ni_3Al -BASED THIN FILMS

Ni_3Al-based coatings are intermetallic compound with FCC structure which possess a wide range of mechanical characteristics that makes them a suitable candidate for application in automobile, aerospace, MEMS, marine and defense applications. The mechanical properties of Ni_3Al coatings have been

generally evaluated in terms of their hardness, Young's modulus and adhesion strength at ambient and high temperatures. According to literature, Ni_3Al films shows a hardness of ~4 to 8 GPa whereas the modulus varies between ~120 to 250 GPa. Several research groups have deposited Ni_3Al-based coating by varying the deposition parameters and use of different dopants. As a result, they improved the hardness of the film up to ~12 to 17 GPa whereas the modulus between ~220 to 280 GPa has been achieved [87]. The adhesive characteristics of the film lies upon the surface quality and features of the substrate material and type of coating deposited on the surface for particular applications. The adhesive strength of the coatings becomes important as the deposited films should not peel off from the surface of the substrate when used in engineering components. Mishra *et al.*,[90] deposited Ni3Al films over Superni 75 & 718 and Superfer 800H using plasma spraying technique. It was found that the deposited coating possessed the adhesion strength of 17.6 MPa. Additionally, some research group showed that the Ni_3Al-based coatings also possess high resistance to fracture and creep [91]. Some of the results reflecting the mechanical properties of Ni_3Al-based coatings is indexed in **table 1.3**.

Table 1.3: Mechanical properties of Ni_3Al-based coatings

Authors	Coating and substrate	Hardness	Young's modulus
Boni *et al.*, (1995) [92]	Ni_3Al over Silicon using sputtering	• For Ni_3Al bulk - 9.3 ± 0.5 GPa • For alloy Ni_3Al - 13.5 ± 0.3 GPa • For Ni/Ni_3Al (5 nm layer thickness) - 12.1 ± 0.2 GPa • For Ni/Ni_3Al (2.5 nm layer thickness) – 11.8 ± 0.1 GPa	NA
Ng *et al.*, (1998) [93]	Ni_3Al over nickel substrates	• As deposited Ni_3Al films-max 310 HV • Ni_3Al annealed at 300℃ for 2 hours – 345 HV • Ni_3Al annealed at 700℃ for 2 hours – 490 HV	NA
Tixier *et al.*, (1998) [87]	Ni_3Al/Ni multilayers over Silicon	• For bulk Ni_3Al – 9.3 ± 0.5 GPa • For Ni_3Al/Ni with different layer thickness – 11.9 ± 0.6 GPa to 17.5 ± 0.4 GPa	For Ni_3Al/Ni with different layer thickness – 256.2 ± 5.7 GPa to 288.5 ± 7.5 GPa

Meng *et al.*, (2000) [94]	Ni/Ni_3Al over silicon	• ~ 3.5 to 5 GPa	NA
Xu *et al.*, (2000) [95]	Ni_3Al over silicon using PLD	• For as deposited Ni_3Al with increase in indentation loading hardness varies simultaneously between 830 HV to 1000 HV • For Ni_3Al annealed at 1073 K for 1 hour and with increase in indentation load hardness varies simultaneously between 1050 HV to 1025	NA
Banerjee *et al.*, (2003) [96]	Ni-25 Al alloy thin films and Ni/Ni_3Al multilayers over Si using sputtering	• Film deposited at 200℃ - ~ 7.3 GPa • Coatings fabricated at 400℃ - ~6.5 GPa • Film deposited at 45℃ - 2 GPa to 6 GPa with increasing indentation load	Films deposited at 45℃, 200℃ and 400℃ shows the moduli of 180 GPa, 200 GPa and 200 GPa respectively.
Rajarshi Banerjee (2006) [97]	Ni_3Al over silicon using sputtering	• For Ni_3Al Fabricated at 45℃ 5 m torr pressure – 5 GPa • For Ni_3Al fabricated at 45℃ and 25 m torr pressure – 9.4 GPa • For Ni_3Al fabricated at 200℃ and 5 m torr pressure – 7.9 GPa	NA
Fedorischeva *et al.*, (2007) [98]	Ni_3Al over si at different temperature	• As deposited Ni_3Al- 5.61 GPa • Ni_3Al with ion beam treatment 6.99 GPa	NA
Xing *et al.*, (2013) [86]	Ni_3Al and Ni_3Al-Cr over Si	• Hardness of Ni_3Al film – 8.4 GPa • Hardness of Cr/Ni_3Al films – 8.0 GPa	Modulus of Ni_3Al films – 191.4 GPa Modulus of Cr/Ni_3Al films – 219.2 GPa
Azarmi *et al.*, (2014) [99]	Ni-Ni_3Al using cold spraying	• Hardness in the range of ~413.2 to 427.5 HV was achieved for cold sprayed Ni-Ni_3Al composites	NA
Kornienko *et al.*, (2015) [69]	Ni_3Al using plasma spraying	• Microhardness in the range of ~579 to 675 HV was found with variation in regimes during deposition	NA

1.5 TRIBOLOGICAL PROPERTIES OF Ni_3Al -BASED THIN FILMS

The tribological property of Ni_3Al-based coatings deals with the study of its wear resistant properties, behavior of acting frictional forces and lubrication when two surfaces come in contact. Additionally, the tribological properties

deals with the abrasion, corrosion and oxidation resistant properties when exposed to extreme environments. One of the significant advantages of using Ni_3Al-based coating is that it exhibits low coefficient of friction which minimized the wear rate and make them useful for their applications in MEMS and cutting tools because of high wear and abrasion resistant properties. Ni_3Al films also acts as solid lubricant which helps in improving their wear resistant properties even at high temperatures. Additionally, these films found their applications at elevated temperatures as they exhibit extraordinary corrosion and oxidation resistant properties [67], [71], [72]. This is because of the formation of protective layers of Al_2O_3 and NiO that protects the parent materials (substrates) from being drastically oxidized. Mirzaaghaei *et al.*,[82] presented that the Ni_3Al films doped with MoS2 exhibits self-lubrication features and also shows low frictional coefficient when deposited on steel substrates. Xing *et al.*,[86] used DC magnetron sputtering to deposit multilayered and alloy Ni_3Al films on superalloy. They observed better oxidation resistant properties of multilayered films when compared to alloy films. It was also observed that the addition of chromium layer in the host Ni_3Al reduced the rate of oxidation of the films. Meng *et al.*,[94] used magnetron co-sputtering to fabricate multilayers of Ni-Ni_3Al coatings over silicon substrate. They observed the formation of Al_2O_3 layer on the surface of the coating during deposition at high temperature and annealing because of the oxidation of aluminum. These developed layers acts as a protecting layer and prevents the material from being drastically oxidized. Mishra *et al.*,[90] investigated the properties of Ni_3Al coatings deposited on superalloys using plasma spray technique. The results showed that the films were oxidized after 10 cycles (1 cycle is equal to 100 hours) when exposed to coal power plant and their kinetics was investigated using weight gain measurements. The oxidized coatings persist protective layers which contributes in increasing the life and durability of the substrate and film. Some research group showed that Ni_3Al-based coatings are capable of protecting the materials from oxidation and corrosion attacks. however, several research and attempts are being done to improve these properties even in harsh environments at elevated temperatures [86], [89].

1.6 APPLICATIONS OF Ni_3Al -BASED THIN FILMS

Ni_3Al intermetallic compound in form of thin films has a wide area of applications because of its remarkable tribological and mechanical properties. Moreover, its extraordinary corrosion and oxidation resistant properties makes it a suitable candidate for its application at high temperatures. The enhanced mechanical properties of these films allow them to be used in cutting tools for woodshops and machine shops whereas because of their wear resistant properties, they are used in aerospace machineries, MEMS, and data storage devices [86]. They can also be used in the automobile industries for making engine parts and automobile components. These films possess enhanced corrosion resistant properties which makes them a suitable candidate for their use in medical devices and electronic gadgets. Moreover, their extraordinary and unparallel oxidation resistant properties make them worthy for different scale of applications at ambient and high temperatures.

These Ni_3Al-based coatings can be used in boilers, heat exchangers and blades of gas turbine [89], [96]. Additionally, they are used in making the combustion components, seals and bearings, and vanes of gas turbines and parts of automobiles and aerospace industries. The areas of application of hard and protective Ni_3Al based coatings are shown in **figure 1.3.**

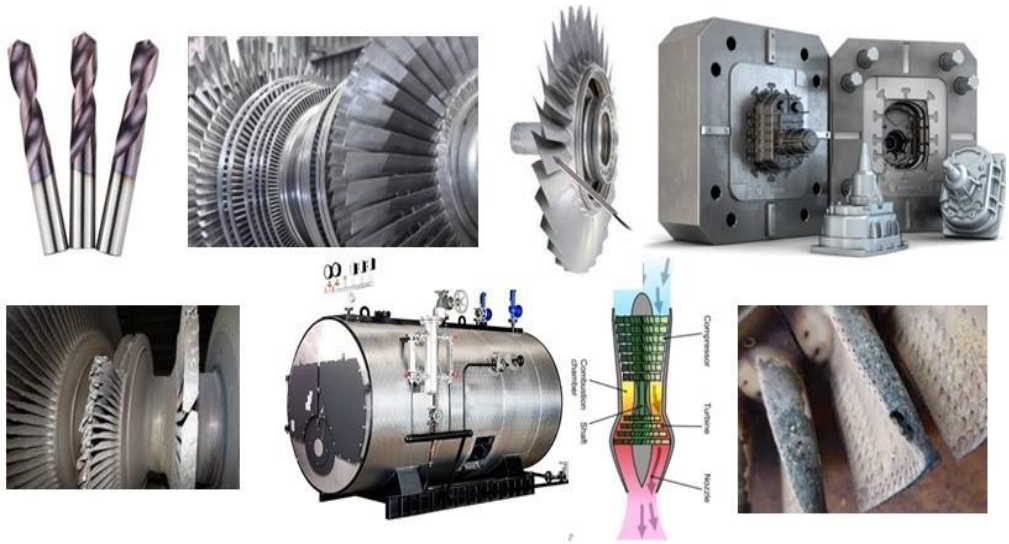

Figure 1.3: Areas of application of Ni_3Al based hard and protective coatings

1.7 MOTIVATION OF PRESENT WORK

The prime motivation of the study starts with the need and application of hard and wear resistant coatings for industrial applications. Moreover, the demand of materials in thin film state for high temperature application draw the attention towards the coating materials that possess remarkable properties against oxidation and corrosion. The idea of using Ni-based coatings particularly Ni_3Al- based intermetallic compound coatings came after looking at the necessity of coatings for their use in gas-turbine components and blades, aerospace & defense industries.

1.7.1 Why Ni_3Al-based coatings are chosen

Over the last few decades, Nickel based thin films especially Ni_3Al intermetallic compound films have been recognized as a promising and competent candidate for their use at elevated temperatures as they possess extraordinary tribological and mechanical properties where resistance to oxidation and corrosion is the significant one. Some of the key facts about the fabrication and results of Ni_3Al coatings have been presented in **figure 1.4 and 1.5.**

- Nickel aluminide thin films especially the Ni_3Al are thermally stable and reflect good mechanical and tribological properties. These films have shown better corrosion and oxidation resistance properties even at high temperatures.
- RF/DC magnetron sputtered Ni_3Al-based coating is generally homogeneous with less contamination. Magnetron sputtering is capable of depositing these films at different substrate temperatures and in both alloy and multilayer forms.
- Synthesis of Ni_3Al films in multilayered arrangement with incorporation of Ni layers has shown improved tribological and mechanical properties than alloy form.
- The strength and properties of Ni_3Al based coatings are influenced by the use of dopants like Cr, W, Zr, Ni, MoS_2 etc.

- The microstructural arrangements of grains are influenced by the heat treatment (generally annealing) method after fabrication which modifies the properties of the synthesized coatings.
- The fabrication of Ni_3Al coatings over the heated substrate par to ~300°C or the annealing of the film after their fabrication contributes in the evolution of ordered $L1_2$ phase of Ni_3Al which is responsible for increasing the hardness of the film regardless of the Hall-Petch grain size theory.

Very limited research in the area of Ni_3Al based coating is reported in the literature where the optimization of sputtering pressure, substrate temperature, concentration of dopant is still to be explored.

There are some results which imitates the consequence of heat treatment on the properties of these coatings but still there is a huge gap in identifying the range of the treatment temperatures and time.

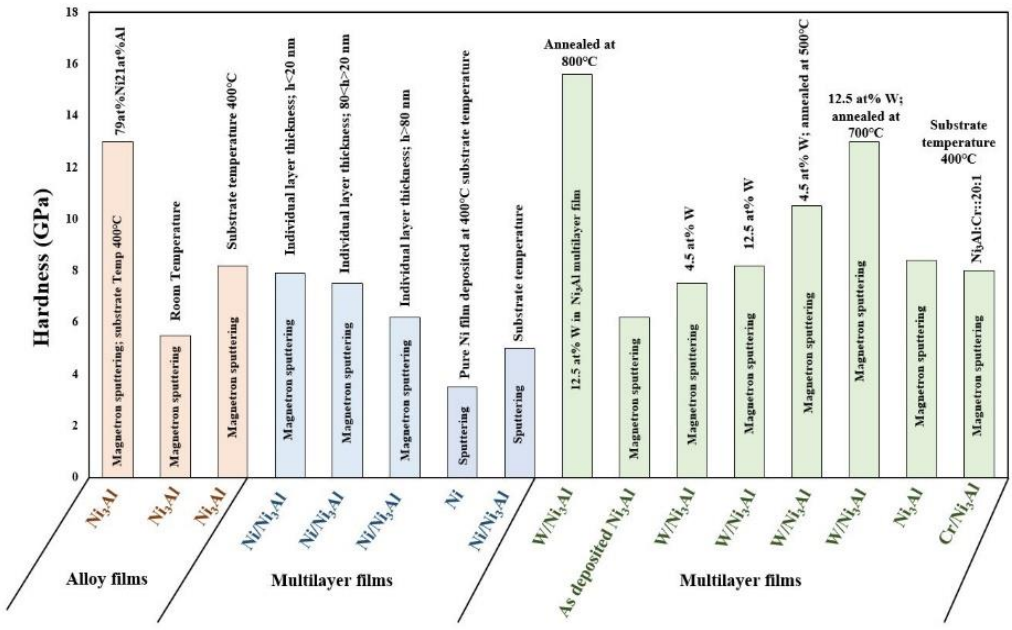

Figure 1.4: Variation in mechanical properties at different deposition parameters [68], [89], [100]–[103]

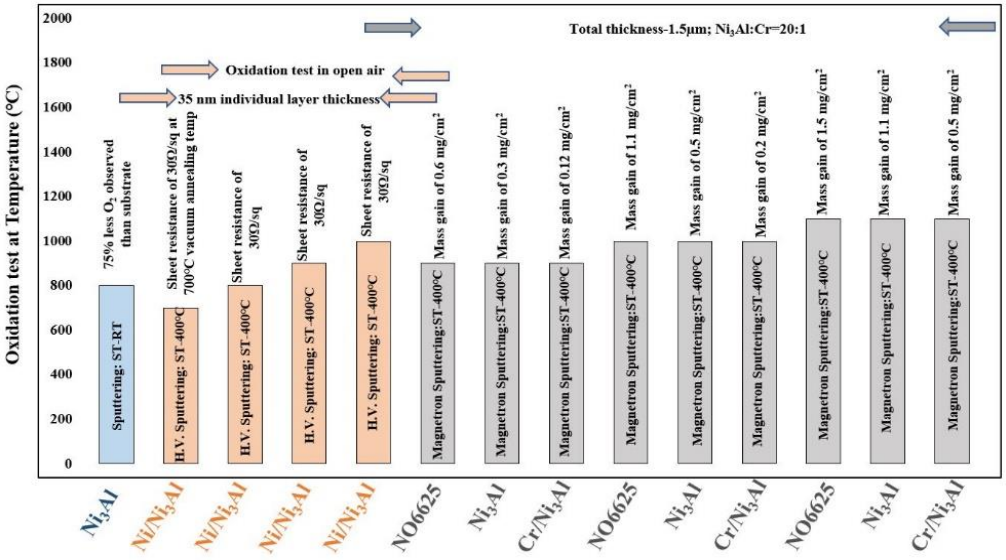

Figure 1.5: Variation in oxidation properties due to different composition of dopants and parameters of synthesis [86], [93], [104]

1.7.2 Objectives of the research

The objectives of the research work have been mentioned below:

1. Synthesis of Ni_3Al-based coatings via magnetron sputtering.
2. Characterization of phase and composition of Ni_3Al-based coatings.
3. Characterization of synthesized coatings for hardness, adhesion and oxidation.
4. Comparison of Ni_3Al-based coatings synthesized at different parameters.

CHAPTER 2

EXPERIMENTAL AND CHARACTERIZATION TECHNIQUES

2.1 SYNTHESIS OF THIN FILMS

Thin films are a class of materials that are generally measured in terms of their thickness. The thickness of thin films typically ranges between a few angstroms (Å) to multimeters (mm) [105]–[107]. The deposition of thin film over a substrate generally consists of two steps; nucleation and film growth. In any kind of deposition technique either in CVD or PVD etc. [108], [109], nucleation is a process where the group of atoms from the vapor or solution come together to form a nucleus which governs the formation of the new phase. The formation of nuclei uniformly over the parent surface is called homogeneous nucleation while structural inhomogeneities reflect heterogeneous nucleation like dislocations and grain boundaries [110]–[112]. While studying the case of the liquid phase, the formation of heterogeneous nucleation is easy because of the presence of a nucleating surface but the formation of homogeneous nucleation is considered thermodynamically by observing the total free energy of the particle**. Figure 2.1** shows the diagram explaining the possibilities of the existence of the nucleus with respect to the free energy.

The total free energy of the spherical-shaped particle of diameter "r" is given by **equation 2.1.**

$$\Delta G = 4\pi r^2\gamma + \frac{4}{3}\pi r^2 \Delta G_v \qquad \textit{Equation 2.1}$$

$$\Delta G_v = -K_B T \ln(s)\,/v \qquad \textit{Equation 2.2}$$

To form a stable nucleus, the maximum free energy a nucleus transit is calculated by d ΔG /dr = 0 which gives a critical free energy and critical radius of the particle as shown in **equation 2.3** and **equation 2.4** which shows that the formed particle can survive in the solution if it achieves the critical free energy to achieve its critical size or it will redissolve [113].

$$\Delta G_{critical} = \frac{4}{3}\pi\gamma r_{critical} = \Delta G_{critical}(homo) \qquad \textit{Equation 2.3}$$

$$r_{critical} = -\frac{2\gamma}{\Delta G_v} = \frac{2\gamma v}{K_B T \ln(s)} \qquad \textit{Equation 2.4}$$

Where r and γ is represents the radius and surface energy of the particle, ΔG_v and ΔG represents energy of bulk crystal and total free energy, S is the supersaturation of the solution, T is temperature, K_B is Boltzmann's constant.

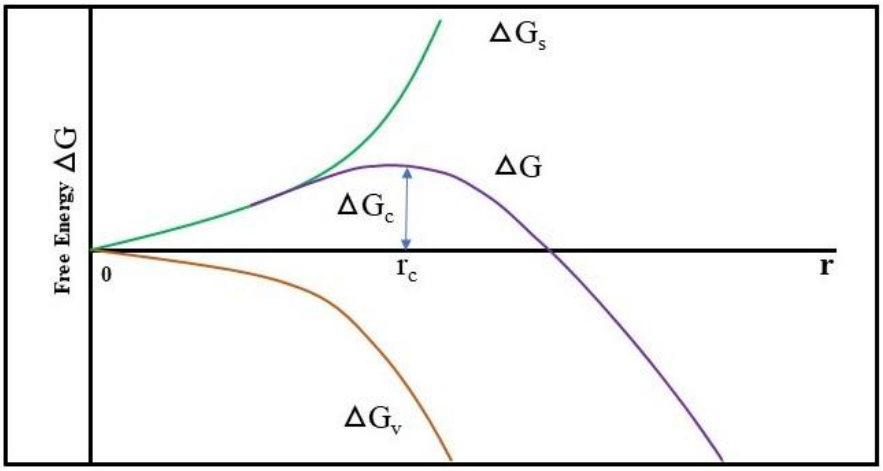

Figure 2.1: Free energy diagram for the formation of the nucleus with a critical radius

Once the formation of nucleation is stable and homogeneous, their growth can be observed due to their coalescence in various ways which finally end up with the formation of thin coatings [114], [115]. The process involved in the growth mechanism of thin films are shown in **figure 2.2**.

(a) **Layer by layer growth:** This process is also called as Frank-Vander Merwe growth mode. The interaction strength between the substrate and the atoms of the material to be deposited is higher as compared to the interaction strength between two neighboring atoms. This results in the growth of a new layer over the deposited layer.

(b) **Island growth:** This process is also named as Volmer-Weber growth mode. In this case the interaction strength between the consecutive atoms to be are higher as compared to the interaction strength between the atoms and substrate. This results in the clustering of the atoms which take a shape of island. The coalescence of these island results in the formation of thin films.

(c) **Layer by layer plus island growth**: This growth is also termed as Stranski-Krastanov growth mode in which the growth starts with the

formation of layers followed by the clustering of atoms resulting in the formation of islands. The coalescence of the atoms in layer and island forms the coatings.

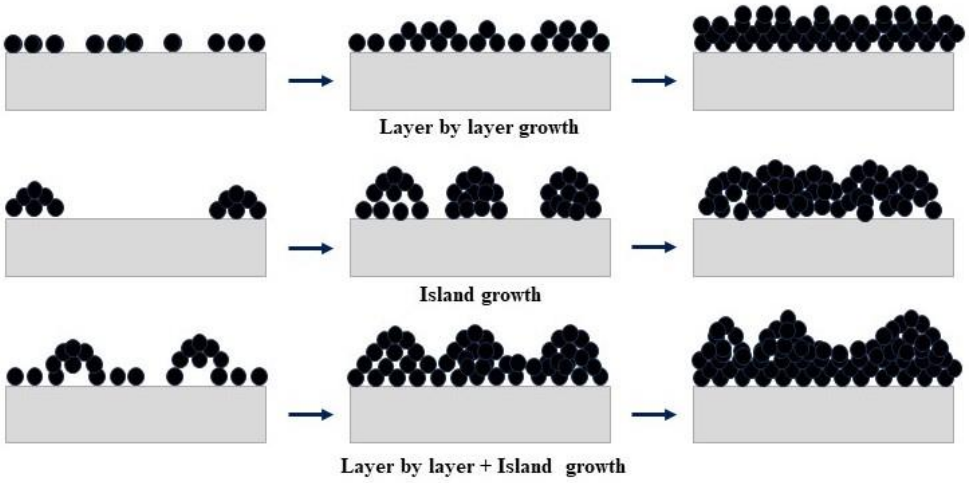

Figure 2.2: Growth modes of thin films

2.1.1 Magnetron sputtering for deposition of Ni_3Al films

Magnetron sputtering is a thin film deposition technique that comes under the broad category of physical vapor deposition technique. In this technique, the solid target material is bombarded using high-energetic ions which results in the sputtering of atoms from the surface of the target [116]–[119]. The sputtered atoms are confined in a radial direction towards the substrates in the form of stable plasma which is then condensed on the surface of the substrate in the form of thin films. The confinement of the plasma in the radial direction is provided by the permanent magnets which are placed in a circular geometry behind the target material in the sputtering gun as shown in **figure 2.3**.

A large variety of materials can be deposited over any substrate using this technology. DC magnetron sputtering is used to deposit the metallic conducting material (alloy or compounds of conductor or semiconductor) whereas to deposit nonconducting material Radio frequency (RF) sputtering is used. This is because the non-conducting target is charged due to the deficit of conductive routes for the flow of electrons which further leads to the formation of unstable plasma. However, in the case of radio frequency power supply, there is a continuous alteration of AC current which helps in

preventing the charge buildup at the surface of non-conducting target material and thus enables the formation of stable plasma. **Figure 2.4** displays the schematic diagram of the magnetron sputtering and its major equipment. The major components of the magnetron sputtering setup are:

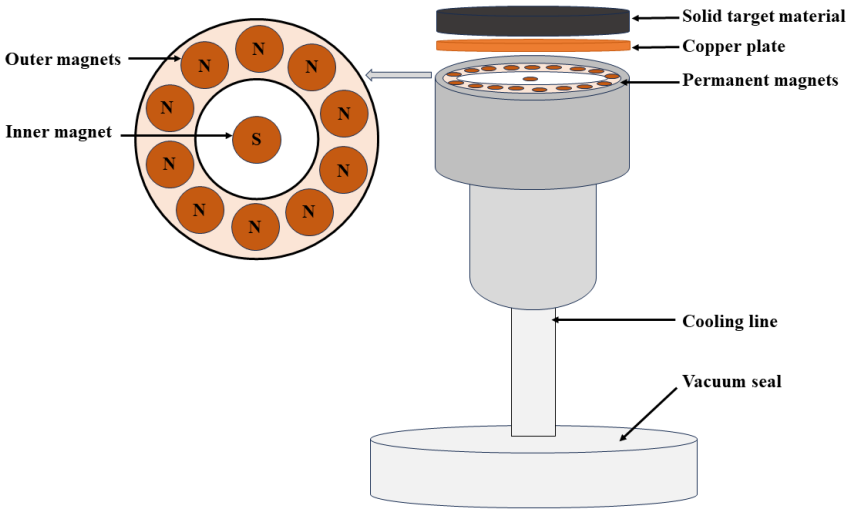

Figure 2.3: Schematic diagram of sputtering gun and placement of permanent magnets

(a) ***Vacuum chamber:*** The vacuum chamber is designed with a specific material (generally steel) in such a way that it reaches the required low pressure in a short duration of time. The entire magnetron sputtering process takes place inside the vacuum chamber to eliminate the possibility of contamination during the deposition.

(b) ***Rotary and Turbopump:*** The vacuum chamber is evacuated with the help of a turbo pump attached to the rotary pump before sputtering. This helps in removing the contaminants and impurities from the chamber before sputtering and maintains the actual required sputtering pressure during the deposition.

(c) ***Vacuum gauges:*** Low-pressure gauges (Pirani gauge) and high-pressure gauges (Penning gauge) are generally used to monitor the pressure inside the vacuum chamber.

(d) ***Thermocouple:*** It is used to measure the substrate temperature inside the vacuum chamber.

(e) ***Sputtering guns:*** Sputtering guns are the arms of the sputtering process. The solid target material is clamped to the sputtering gun which helps to sputter the atom from the surface of the target when the power is supplied.

(f) ***Mass flow controller:*** It is used to supply a specific amount of the sputtering gas which gets ionized inside the vacuum chamber and sputters the target material.

(g) ***Power supply (DC/RF):*** Depending upon the nature of the target material, the DC/RF power is supplied to the sputtering which creates a voltage difference between the cathode (target) and anode (substrate) generating an electric field that allows the ions to bombard the target and thus sputtering occurs.

(h) ***Substrate and substrate holder:*** The substrate is a material over which the film is to be deposited. The substrates are clamped to the rotating substrate holder which is equipped with the heating facility.

(i) ***Target material:*** It is a solid material in the form of a circular disc of a few millimeters which is clamped in sputtering guns. This is the material that undergoes bombardment and is sputtered off and deposited in the form of thin films over the substrates.

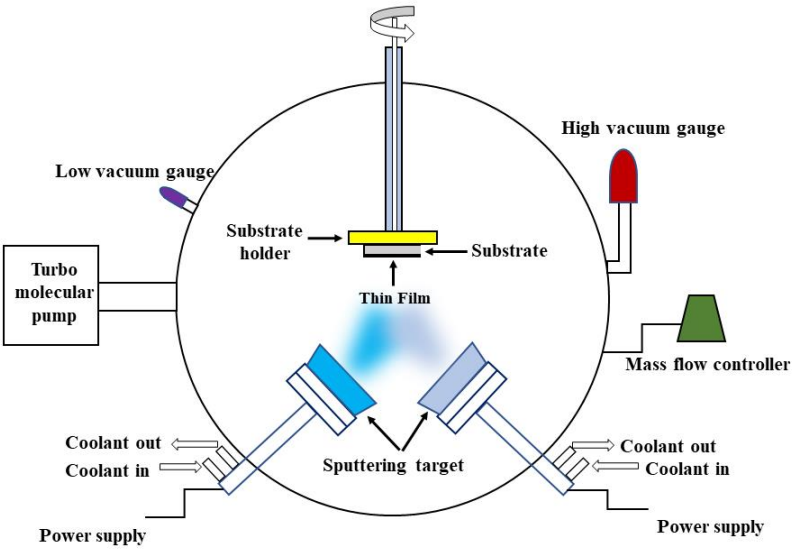

Figure 2.4: Schematic diagram of the magnetron sputtering system

Another way of depositing over the surface is reactive magnetron sputtering. This process is similar to magnetron sputtering except for the use of processed

sputtering gas. In reactive magnetron sputtering, a reactive gas is passed in the vacuum chamber which ionizes because of the difference in voltage between anode and cathode and thus bombards the target material which sputters off the surface of the target. The reactive gas can be used in single or sometimes they are used in ratio with the noble gases (Ar or He). The reactive magnetron is capable of depositing several kinds of nitrides, carbides, oxides and oxynitrides like TiN, CrN, B_4C, SiC, MgO, SiO_2, CuO, TiON, SiN_xO_y etc.

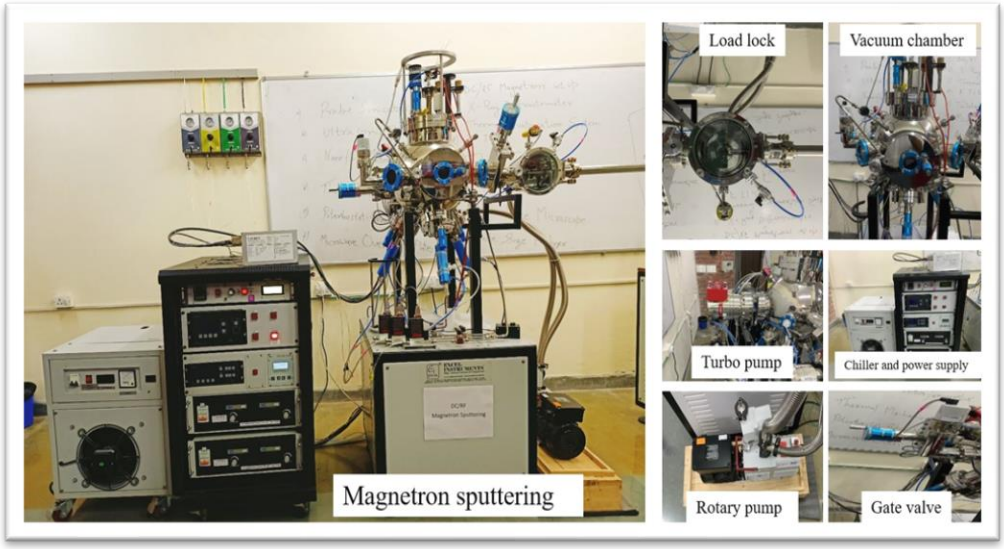

Figure 2.5: DC magnetron sputtering system used in the present work

Figure 2.5 displays the actual setup of the magnetron sputtering used in the present work. The setup is equipped with three sputtering guns with the flexibility of 1-inch and 2-inch diameter targets clamping facility, three mass flow controllers, a substrate heater (coil type), a chiller, a load lock with magnetic arm, and both DC and RF power supply systems. The chamber is initially evacuated at a pressure of ~10^{-6} mbar using a turbo pump backed with a rotary pump. The desired amount of sputtering gas (noble or reactive gas) is allowed to pass inside the chamber with the help of mass flow controllers (MFC) and the chamber pressure is maintained with the gate valve of the turbo pump. The cleaned substrates are clamped to the substrate holder either by the use of clamping pins or silver paste and the holder is rotated between the desired speed of $0 \leq 30$ rpm. There is also a provision to heat the substrate up to 800℃. Additionally, the distance between the substrate and the targets can

be adjusted between 10 cm to 15 cm. Two DC power supply system (1 kW) and 1 RF power supply system (300 W) is available with the magnetron sputtering setup. A pre-sputtering is done to eliminate the impurities and contaminants from the surface of the target followed by the actual sputtering for the desired period of time. Once the deposition is over, the heated substrate is cooled in the chamber itself followed by venting the chamber using nitrogen gas.

2.1.2 Parameters of deposition

In order to deposit the films in multilayer or alloy form, there are several sputtering and deposition parameters that can be optimized to achieve better results. Some of the parameters have been discussed below [120], [121]:

(a) ***DC/RF power supply:*** DC and RF power supply is given to the sputtering guns as per the requirement and nature (conductive/nonconductive) of the target material. Additionally, it has been reported that RF sputtering is a controlled way of deposition that produces thin films with good microstructure whereas the rate of deposition is higher in DC sputtering.

(b) ***Sputtering gas pressure:*** Sputtering gas pressure has a vital role in altering the microstructural integrity of the deposited films and thus their properties. It influences the microstructure, uniformity and thickness of the film. It is reported that the film deposited at low pressure results in a low rate of depositio. However, in case of higher pressure in reactive magnetron sputtering, the rate of chemical reaction increases which further affects the microstructure and properties of the deposited films.

(c) ***Sputtering gas used:*** The type of sputtering gas (noble/reactive) and its purity highly influence the properties of thin films. The type and the volume of the noble gas inserted in the chamber for deposition have a high impact on the microstructure, adhesion, crystallinity and the amount of stress induced in the film. In the case of reactive gas flow, the microstructure, and composition of the film are highly influenced which results in altering the properties of the film.

(d) ***Substrate temperature:*** The variation in substrate temperature generally affects the microstructure, adhesion and crystallinity of the deposited

coatings as higher substrate temperature gives additional time for the rearrangement of atoms which results in producing smooth surfaces and thus reduced surface roughness, but in some case the agglomeration of crystallites results in the formation of larger grains which increases the surface roughness of the film. There can also be the development of stresses in the films due to adatom diffusion. It also alters the morphological properties of the deposited coatings.

(e) ***Substrate target distance:*** The variation in substrate target distance during deposition has a great impact on the rate of deposition, the uniformity in deposition and thus the film thickness. The high rate of deposition and the enhancement in film thickness due to the small substrate target distance also affect the grain growth and thus the microstructure of the coatings.

(f) ***Substrates and targets:*** The use of different solid targets with different power supplies alters the chemical composition of the deposited film whereas the use of different substrates for a similar coating alters the grain growth because of a mismatch in lattice parameters and thus affects the phase formation and the microstructure of the film.

(g) ***Sputtering power:*** Sputtering rate and the film thickness is the major component which is generally affected by alteration in the sputtering power. Additionally, it has a great impact on the surface properties (surface roughness) and microstructure of the coatings.

(h) ***Deposition time:*** It generally influences the variation in thickness of the deposited coatings. Higher deposition time results in higher film thickness and vice versa. Moreover, it also affects the evolution of phases, crystallinity and the type and amount of stress induced in the film

(i) ***Fixed, rotating or tilt angle deposition:*** The way of placing the substrates to the substrate holder also influences the uniformity and crystallinity of the coatings. The rotating substrate holder results in a homogeneous deposition of the film whereas the tilted substrate positioning helps in varying the film thickness over the same substrate.

2.2 Characterization techniques

2.2.1 X-Ray diffraction technique

X-Ray diffraction is a nondestructive powerful and multipurpose analytical method that is used to disclose the information about the formation of phases, crystallographic structure, crystallite size, strain, lattice parameters, defects and stress etc. of a crystalline material [122], [123]. The method of characterization is employed over different kind of bulk solid materials, power materials and thin films etc. Particularly in the case of thin films, XRD can reveal the crystallographic structure of the film in the thickness range of very few angstroms (Å) to millimeters.

X-rays are similar to the electromagnetic radiations of light with comparatively shorter wavelengths. They are generally produced by two different processes namely acceleration and fluorescence. The X-ray is generated by a method called Bremsstrahlung radiation. Electrons are accelerated to high energy levels and are directed towards the target of heavy metals to produce X-rays. The circulation of relativistic electrons under magnetic field within electron storage rings also leads to the acceleration of electrons known as synchrotron radiation. In case of fluorescence, the target material experiences a core shell ionization by incident electrons where the electron of the outer shell fills the vacancy of the inner shell causing the generation of X-ray. The process of XRD mainly relies on the constructive interference of crystalline specimen and the monochromatic X-rays [124]. When the X-rays of wavelength (~1.5 Å) is subjected towards the crystalline sample to be tested at specific angle (theta), it undergoes diffraction which upon constructive or destructive interference liable upon the path variance reveals the crystallographic information of the sample. The constructive interference of X-rays generates diffraction peaks in the spectrum which relates the angle of incidence, wavelength and the inter-planar spacing of the crystalline material. The formulated equation for the constructive interference was given by W.L Bragg as shown in **Equation 2.5** [125], [126]**.**

$$n\lambda = 2d_{(hkl)} \sin\theta \qquad \textbf{\textit{Equation 2.5}}$$

Where *n* is the maximum order of diffraction, λ is wavelength, *d* is inter-planer spacing and Θ is Bragg's angle (between incident ray and plane).

The diffraction pattern consists of the two major components namely the peak position (theta) and peak intensity. These two parameters are used to investigate and analyze the information about the phase formed, size and shape of unit cell and the crystallize size of the material. The crystallite size of the material can be calculated using Scherrer formula shown in **equation 2.6** [127]–[130]. To find the accurate broadening in the XRD peak it is always suggested to subtract the instrumental line width from the observed line width.

$$\frac{0.9\lambda}{B\cos\theta} \qquad \textit{Equation 2.6}$$

Where, D is the crystallite size, λ is wavelength of the target material, B is the full width at half maxima (FWHM) and Θ is Bragg's angle

Figure 2.6 shows the schematic diagram of the X-ray diffractometer. The three major components of the XRD diffractometer are the X-ray tube, the specimen and the detector. The filament is heated in the X-ray tube which generates electron that further bombards with the target material when the voltage is supplied. The X-rays are produced when the electrons of high energy repudiate the electrons of the inner shell of the target. However, 99 percent of the kinetic energy of the electron are converted into heat when they bombard with the target material resulting in the formation of X-ray with remaining 1 %. The produced X-ray consists of the several components prominently K_α and K_β. K_β consists of a shorter wavelength as compared to K_α and are filtered out using the absorbing film. Furthermore, K_α consists of two components $K_{\alpha1}$ and $K_{\alpha2}$. $K_{\alpha1}$ has a small wavelength as compared to $K_{\alpha2}$ but it shows intensity twice than $K_{\alpha2}$. Since the both the components of K_α shows almost same values of wavelength, the average of the two is used to produce the result. The constructive interference occurs when the geometry of the X-ray encroaching the sample to be tested satisfies the Bragg's lay stated in **equation 2.5**, resulting in the formation of XRD spectra which shows a relation between the intensity and position (two theta) of the XRD peak. **Figure 2.7** shows the actual powder XRD (Bruker D8 ADVANCE ECO) and GI-XRD (Empyrean Panalytical) used in the present work. In both the setup copper has been used as a target material with Cu K_α = 1.54 Å.

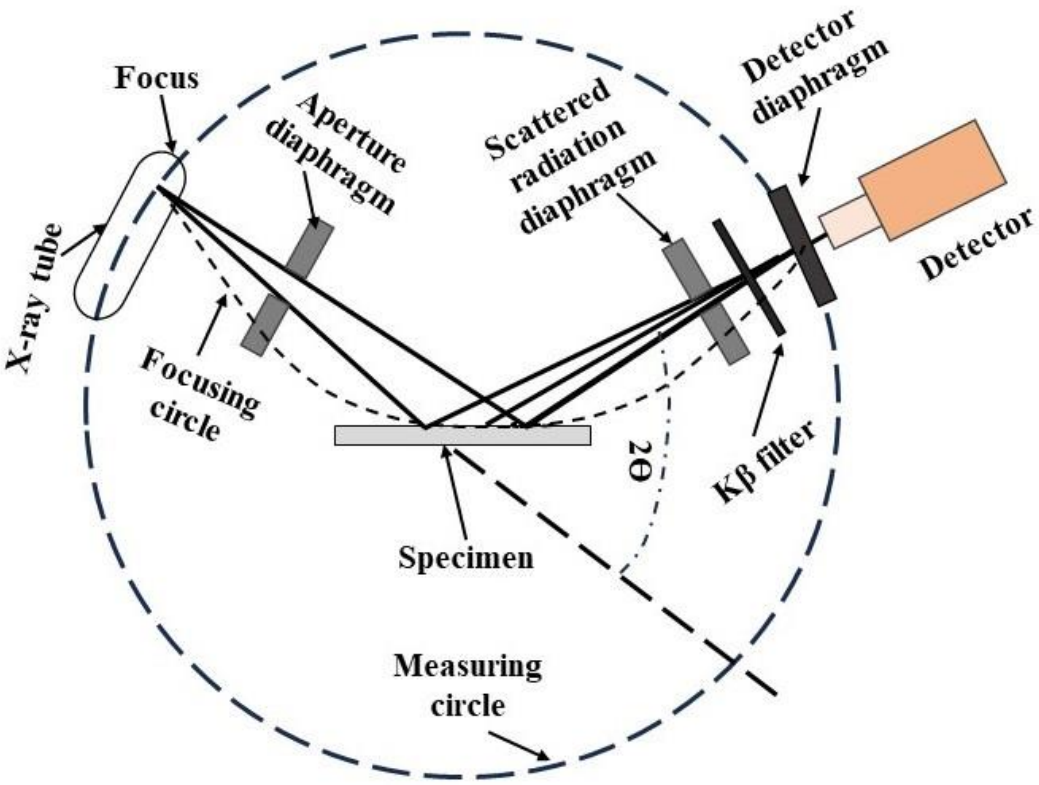

Figure 2.6: Schematic diagram of X-ray diffractometer

Figure 2.7: X-ray diffraction **(a)** XRD (Bruker D8 ADVANCE ECO) **(b)** GI-XRD (Empyrean Panalytical)

2.2.2 FE-SEM and EDS analysis

Scanning Electron microscopy (SEM) is a prevailing imaging method that scans the surface of the specimen by focusing the electron beams over it and reveal the information about the microstructure, orientation and surface morphology and of the materials [131], [132]. This technique is capable of producing the three-dimensional images of the specimen at high resolution with higher magnification. The technology also offers the secondary and backscattered imaging where Energy dispersive spectroscopy (EDS) detector can be used for the analysis of the chemical composition of the material. In order to generate the electrons in SEM, the filament of Tungsten (W) or Lanthanum hexaboride (LaB_6) are used as they exhibit low vapor pressure and high melting point as compared to other metals. However, in case of Field Emission Scanning Electron Microscope (FE-SEM), high voltage is applied between the cathode and anode plate which results in generation of high electric field at the tip of emitter (tungsten) which results in the emission of electron using the field emission due to tunneling effect. The technology of FESEM is able to produce the image of specimen at higher resolution (~ 2 nm) which is multiple times better than the conventional SEM results. The work function of the element (tungsten) is generally affected by the absorbed gases therefore, a high vacuum is required to scan the surface using FE-SEM. Additionally, the low pressure inside the chamber benefits in reducing the scattering of electron and maintains the required mean free path for the better imaging. A schematic diagram of field emission electron microscopy displayed in **figure 2.8**.

The electron beams (having energy ~ few hundred eV to 50 keV) is released from the sharp filament of single crystal tungsten attached in the emission electron gun as a result of strong electric field. The sharp tip of the filament allows to emit the a very focused beam of electrons (primary beam of electrons) using field emission. The electron beam passes through the series of lenses in a controlled manner and are focused across the surface of the specimen to be characterized. The scan coils within the objective lens creates the magnetic field because of the variation in the voltage formed by the scan

generator. The produced magnetic field deflects the electron beam in a point-by-point manner of scanning over the specimen called as a raster scan. As a result of interaction of the beam of electrons with the sample, various signals including secondary and backscattered electrons, diffracted backscattered electrons, photons, and visible lights with generation of heat is produced. The secondary electrons are detected to obtain and analyze the surface structure and morphology of the specimen whereas the backscattered electrons are used to define the composition in contrast. The orientation of the structure can be studied by the use of diffracted backscattered electron.

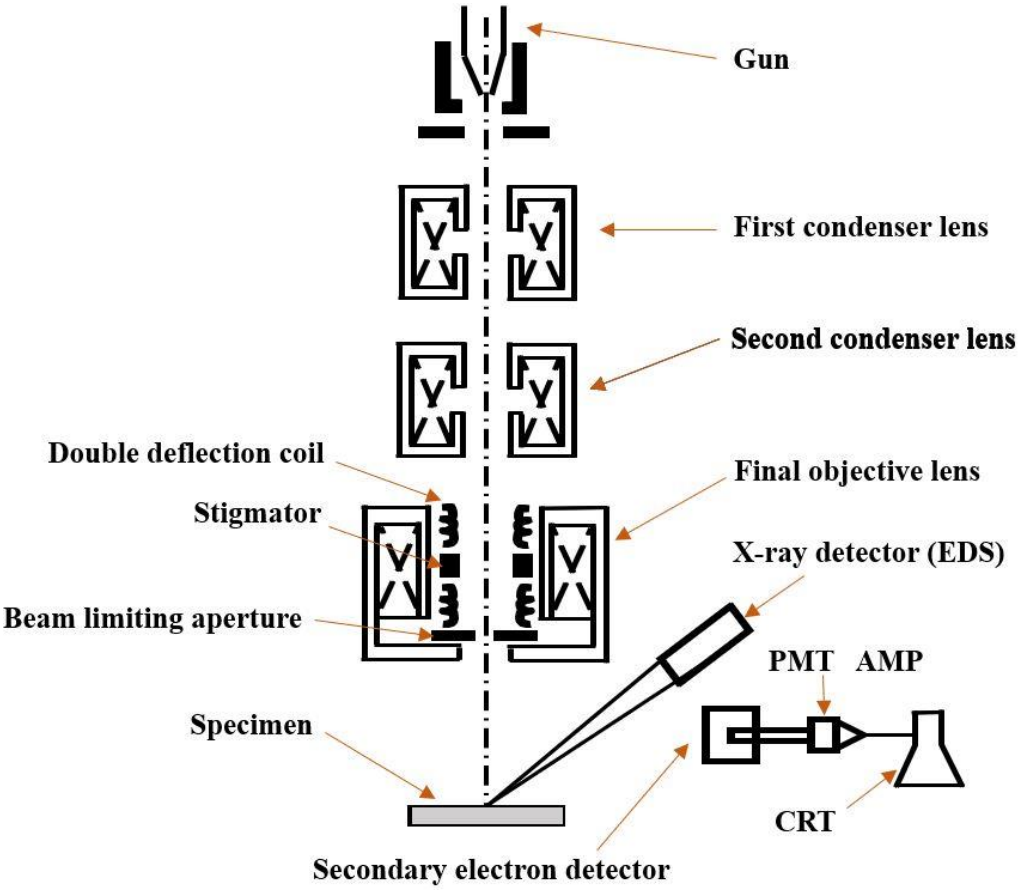

Figure 2.8: Schematic diagram of Scanning electron microscopy

It is recommended that the specimen used in FE-SEM for studying its microstructure and morphology should be conductive in nature. In case of nonconductive surfaces, the charge is accumulated on the surface of the specimen which further distorts the beam of electrons making it difficult to obtain better results. The non conducting specimen are generally prepared

before analyzing through FE-SEM. A thin layer of conducting surface either of gold or carbon is deposited over the insulating sample before the test. The advantage of the conducting surface is that it helps in emitting the significant amount of secondary and backscattered electrons. The FE-SEM (Nova NanoSEM 450, FEI) setup used in thin study has been shown in **figure 2.9**.

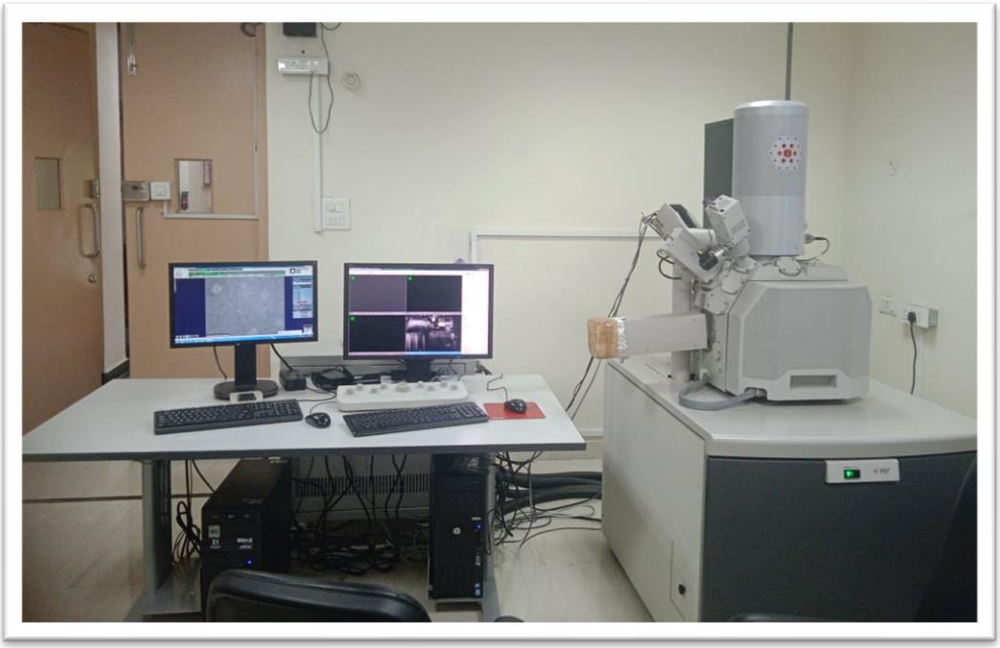

Figure 2.9: Field emission scanning electron microscopy used in present work

The energy dispersive spectroscopy (EDS) was attached to the FE-SEM setup which was used to study the composition of the material [133]–[135]. The EDS detector attached in the setup detects the X-rays which are emitted from the specimen as a result of bombarding with the beam of primary electrons. The results are generated in the form of spectra where the peaks show the energy levels of the element. The peaks showing the energy levels are unique for the individual element of the periodic table. The disparity in the intensity of the peak demonstrates the concentration of the particular element in the specimen.

2.2.3 Atomic force microscopy

Atomic force microscopy is an imaging technique that helps in studying the surface properties of the specimen in terms of surface morphology along with the mechanical properties [136]–[138]. This technique is capable of producing

three dimensional images of high resolution (~ 0.01 nm) without using the electromagnetic radiations, beam of electrons or high vacuum chambers. Moreover, this technique is used in open air environment either at ambient temperature or high temperatures. The process of atomic force microscopy involves the consideration of Vander walls force, electrostatic forces and constant forces acting between the specimen and the tip of the cantilever probe of AFM setup. **Figure 2.10** shows the schematic diagram of AFM.

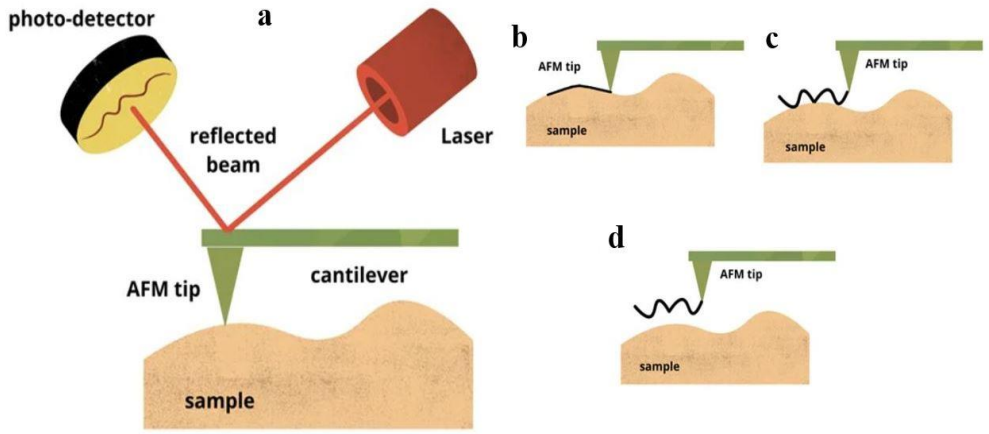

Figure 2.10: Schematic diagram of atomic force microscopy **(a)** operation of AFM **(b)** Contact mode AFM **(c)** Tapping mode AFM **(d)** non-contact mode AFM

The setup of AFM consists of the sample stand, the cantilever with sharp tip probe, photo probe and a detector. The radius of the tip of the probe is in few nanometers which is made up of silicon or silicon nitride. The basis working of the AFM involves the approaching of the tip of the probe to the surface of the sample at its atomic level interactions followed by the focusing of the laser at the tip of the probe. Photo detector detects the beam reflected from the surface of the sample. When the probe is brought over the surface of the specimen, it bends or twist because of the acting forces between the specimen and the probe which further varies the ratio of the reflected laser beam detected by the photodetector. The change in the intensity of the reflected beam recorded over the photodetector is converted into the respective voltage which behaves as a feedback signal and helps in maintaining the persistent height or constant force over the specimen. The feedback signal is

continuously monitored by the feedback loop that adjusts the height of the cantilever tip over the specimen by comparing to the user defined set values. In order to obtain the constant and stable operation, the gap between the surface and the probe tip is kept constant (minimum) by either mounting the specimen or probe at a piezoelectric element which constantly maintains the height and force in Z direction. The cantilever probe is then moved in X-Y direction in raster pattern to scan the desired area of the specimen which as a result gives the surface topography and amplitude of the asperities on the specimen with high resolution. In order to scan the surface of the specimen the cantilever probe of the AFM can be moved in either of the three modes namely, contact mode, non-contact mode or tapping mode.

The principle behind the contact mode of scanning is that the cantilever tip is brought in contact with the surface of the specimen where the force and deflection are maintained constantly. When the cantilever probe scans the surface in X-Y direction, then the force is maintained by the deflection of the probe which is further used to generate the data of surface topography. In case of non-contact mode of scanning, the cantilever probe is not is physical contact with the surface of the specimen. However, the probe is kept at a distance of few angstroms above the surface of the specimen to be scanned. In this instance, the tip of the probe vibrates over the specimen at the frequency close to the resonance frequency. As prove approaches towards the surface of the specimen, the amplitude of vibration changes because of the existence of interaction forces at the surface. This variation in the oscillation is used to generate the surface topography of the material. In case of tapping mode of scanning using AFM, the probe of the cantilever intermittently taps the surface to be scanned. It is a combination of both contact and non-contact modes of scanning. In this process, the cantilever probe of the setup oscillates near the resonance frequency while coming near to the surface of the specimen using piezoelectric crystal. During each cycle of oscillation, the probe of the cantilever approaches the surface and lifts back again resulting in variation of amplitude and phase. The change is the oscillation during tapping are carefully monitored to evaluate the height and force between the surface and tip and the

feedback voltage generated against it are converted into surface imaging. **Figure 2.11** shows the actual atomic force microscope used during this work. The test was performed at ambient temperature in contact mode of scanning.

Figure 2.11: Atomic force microscopy with contact mode of scanning

2.2.4 Contact angle measurements

The contact angle measurements are performed to analyze the wettability of a surface using different liquids and vapor. The measurement can be done either in static conditions or dynamic conditions depending upon the requirement of the surface to be tested. **Figure 2.12** reflects the schematic illustration of the drop shape analyzer to measure the contact angle between the surface and liquid [139], [140]. The setup consists of a backlight camera, the light source, the sample stage, the dispensing unit and the software installed in the computer. The measurement of the contact angle is important to predict the hydrophobic or hydrophilic property of the specimen whereas it is also employed to measure the surface energy of the specimen. The basic working of the drop shape analyzer (DSA) is started with dropping a small amount of liquid (let us say water) over the surface in a controlled way using dispensing

source. When the liquid falls on the surface of the material, it creates a contact line between the water droplet and the surface of the specimen. the light is allowed to fall in a horizontal direction passing through the water droplet whereas the shape of the water on the surface of the specimen is captured by the camera installed in the setup at the opposite side of the light source. The profile of the water droplet is measured by the software installed in the computer which calculates the angle between the water droplet and the surface of the specimen in both the left and right direction. The experiment is repeated for several times and the average values of contact angle obtained from the repeated experiments are evaluated to understand the hydrophilic and hydrophobic property of the surface. In general, the angle obtained below 100° shows the hydrophilic nature of the material and the angle above the 100° shows the hydrophobic nature. Moreover, the angle above the 150° is explained in terms of superhydrophobic nature of the surface.

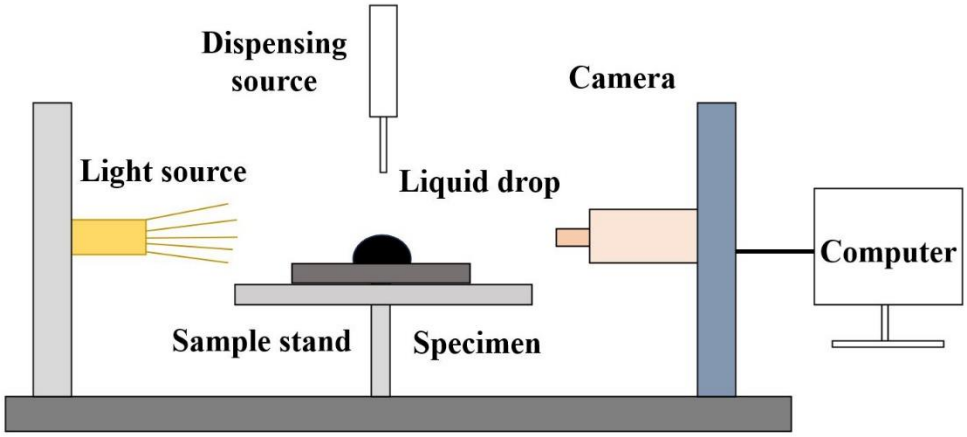

Figure 2.12: Schematic diagram of drop shape analyzer

The contact angle (Θ) measurements of a surface quantify the results using the Young's equation [141]–[143]. According to the Young's theory, the contact angle measurement shows an equilibrium with the given system of Vapor liquid and solid at a specific pressure and temperature. However, a hysteresis in contact angle is observed in range of maximum to minimum contact angle in practical situations. Thermodynamically, the equilibrium state is described considering the three phases of solid (S) liquid (L) and vapor (G) phases. The Young's equation used to define the equilibrium of contact angle using the three phases is shown in **equation 2.7.**

$$\gamma_{SG} - \gamma_{SL} - \gamma_{LG} \cos\theta_c = 0 \qquad \textit{Equation 2.7}$$

Where, γ_{SG} is solid vapor interfacial energy, γ_{SL} is solid liquid interfacial energy γ_{LG} is liquid vapor interfacial energy and Θ_C is contact angle. **Figure 2.13** shows the drop shape analyzer used to measure the contact angle between the deposited film and distilled water. The test was conducted at ambient temperature and pressure in static state conditions.

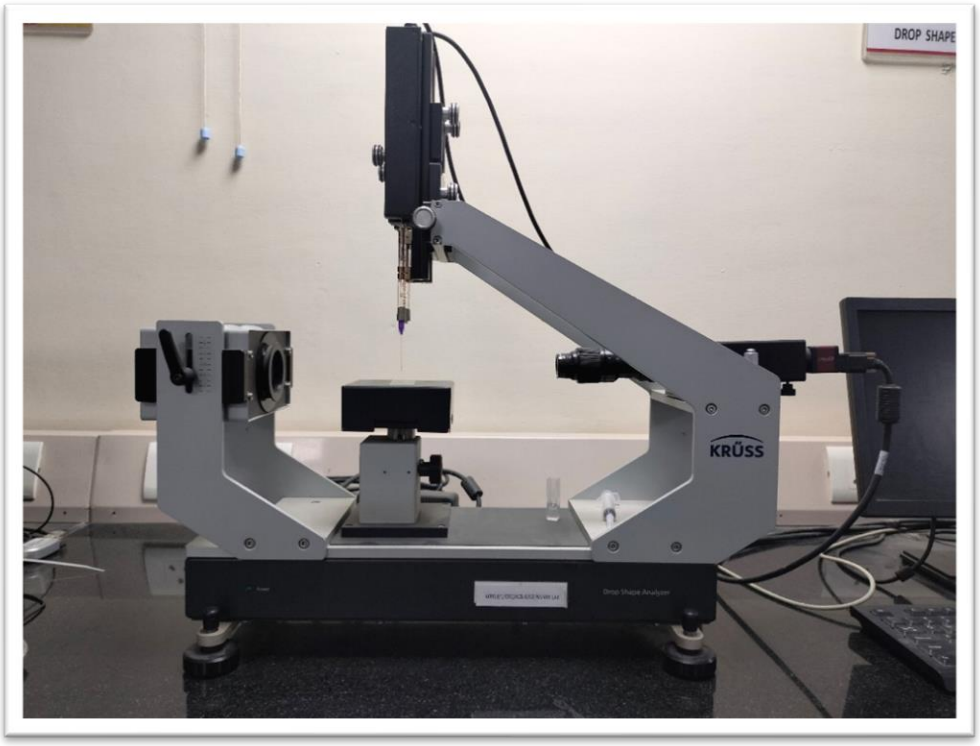

Figure 2.13: Water drop shape analyzer used to measure the contact angle at static state

2.2.5 Nano indentation technique

Nanoindentation is a characterization technique which is used to investigate the mechanical properties of the materials at nano level. The major requirement of nanoindentation is the preparation of the specimen with better surface roughness. The test can be performed either at ambient temperature or the high temperature. The sample is indented linearly with a tip of indenter at a particular known force and held for a specific time (dwell time) and then drawn back linearly. During this process a curve between the applied load and displacement of penetration is recorded which is further evaluated to analyze the mechanical properties of the specimen [144], [145]. In case of the material

where a thin film is deposited over the substrate, it is recommended not to penetrate beyond the $1/10^{th}$ of the total thickness of the deposited coating to evade the so-called substrate effect. The results of nanoindentation can be used to study the mechanical properties of the material like hardness, Young's modulus, adhesion etc. This technique is also used to measure the wear properties which explains the ductile and brittle behavior of the wide range of specimen including metals, polymers and ceramics. In this study nano indenter (Hysitron) used to evaluate the hardness, Young's modulus and adhesion of the coatings over the surface is shown in **figure 2.14**.

Figure 2.14: Nanoindentation setup used to evaluate the mechanical properties of the deposited films

The setup consists of the two major components namely the indenter and the microscope. The microscope is used to analyze the surface before and after the test. The surface to be indented is determined by looking into the microscope and then indentation is made. The dimension of the indent is analyzed by

looking into the microscope after the test. In case of smaller dimension of the imprint of indentation, the atomic force microscope attached in the setup is used to see and measure the dimensions. Overall, the process of nanoindentation consists of finalizing the area to be indented followed by indenting the surface with pyramid shaped diamond Berkovich tip and finally analyzing the imprints of indents using optical or atomic force microscope. The test is generally performed in two modes namely depth control nanoindentation and load control nanoindentation. In case of depth control process over a substrate of thin film, a depth less than or equivalent to $1/10^{th}$ of the total thickness of the coating is penetrated using the Berkovich tip and a corresponding depth versus load graph is plotted and analyzed to measure the properties whereas in case of load control process, a gradual increasing load is applied by the indenter over the surface till it reached the maximum desired load resulting in a depth versus load graph.

2.2.5.1 Hardness and Young's modulus

Hardness (H) of a material is a surface property which is defined as its ability to resist the local permanent deformation against the local forces applied on the specimen due to indentation scratch or wear etc. whereas the Young's modulus is defined as the ability of a material to resist the local stretching or compression. Nanoindentation performed in either of the load control or depth control process reveals the mechanical properties of the specimen. In order to calculate these properties of the material, it is recommended to perform several indentations at different spots of the material and the average value should be considered as the actual value of modulus and hardness. The calculation of the modulus and hardness using nanoindentation is explained by the Oliver and Pharr technique [144], [146]. The two major components used to evaluate the modulus and hardness of the specimen are the applied load and the depth of penetration. In case of thin film, the stiffness is calculated using unloading curve (slope of the curve) of the nanoindentation which is related to the geometry of the indenter and the elastic modulus. The modulus of elasticity of the material can be evaluated using **equation 2.8**. Simultaneously, the hardness of the film is calculated using **equation 2.9**.

$$E = (1 - v^2) \times (\frac{S}{A}) \qquad \textit{Equation 2.8}$$

Where, E denotes the elastic modulus of the film, υ is the poisons ratio, S denotes contact stiffness (calculated from the slope of the unloading curve), A is the area of indentation.

$$H = \frac{P_{max}}{A_c} \qquad \textit{Equation 2.9}$$

Where, H is the hardness of the film, P_{max} is the maximum applied load and A_c denotes the area of contact.

2.2.5.2 Adhesion between film and substrate

The adhesion between the coating and substrate defines the strength through which the deposited film is bonded with the substrate material. Adhesion strength of the coating with the substrate can be calculated using the nanoindentation method. In order to investigate the adhesion strength of the material (thin film), a scratch test is performed using the Berkovich tip of nano indenter. A constant or progressive normal load is applied to indent the film whereas a lateral displacement is made to make a scratch over the surface of the desired length. Simultaneously, lateral displacement, the lateral and normal force increases continuously which reaches a critical point where the film is delaminated. The maximum load at which the film delaminates is called the critical load [147]–[149]. The adhesive strength of the coating is calculated using **equation 2.10**.

$$\sigma = \frac{P_c}{A} \qquad \textit{Equation 2.10}$$

Where, σ denotes adhesion strength of the film, P_c shows maximum critical load of delamination and A is the contact area

2.2.6 Oxidation resistance test

Oxidation is a process of continuous loss of electrons from the parent material. It can also be defined as the reaction in which a material reacts with the oxygen which leads to a permanent physical or chemical change that further deteriorates or corrode the material. Oxidation can occur at ambient or high

temperature depending upon the nature of environment of exposure/use. In order to prevent the material from oxidation, the technology of thin film coatings over the parent material is used which protects the parent material from the oxidation attacks in the extreme situations [150], [151]. The advantage of using thin film coating over the specimen is that the deposited coating behaves as a blockade between the environmental conditions and the parent material which minimizes the interaction of oxygen to the substrate (parent material). However, the selection of the adherent coating with oxidation resistant property is critical. Moreover, the microstructure, thickness, adhesion strength, thermal stability, and chemical stability of the coating material plays a vital role in protecting the parent material from being oxidized at ambient and high temperature. However, the rate of oxidation at elevated temperature is very high as compared to the room temperature [152], [153]. In this study, the oxidation resistant properties of the deposited films over the Ni superalloy (Inconel-718) have been studied at high temperatures of 900℃, 1000℃ and 1100℃. For the purpose, Split furnace (City Instruments, India) has been used for heating the deposited film over the superalloy in open air environment followed by cooling at room temperatures. The mass change of the cooled samples was further measured using weighing balance (Sartorius) at ambient temperature. **Figure 2.15** shows the split furnace and weighing balance used in the experiment.

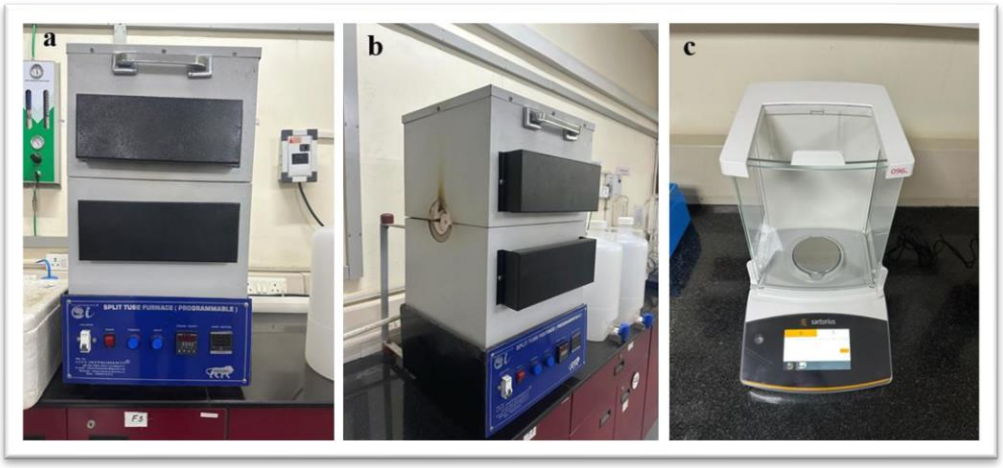

Figure 2.15: Required setup for the oxidation test **(a)** front view of split furnace **(b)** side view of split furnace **(c)** Weighing balance

The steps of the high temperature oxidation test have been mentioned below:

1. The bare sample, and the coated samples were placed in a ceramic boat and kept in the split furnace at temperatures of 900℃, 1000℃ and 1100℃ separately.
2. The samples were heated at the specific temperature for 1 hour and then cooled in air for 30 minutes.
3. The weight of the cooled samples was measured using the weighing balance at room temperature and then they were again exposed to the high temperature following the step 1.
4. The above three steps were repeated 30 times to complete 30 cycles of oxidation test.
5. The oxidation-kinetics were calculated using the logarithmic and parabolic law of oxidation.
6. The change in phase and the evolution of the microstructure and surface topography before and after the oxidation test was compared and analyzed.

CHAPTER 3

SYNTHESIS AND CHARACTERIZATION OF DC-SPUTTERED Ni_3Al ALLOY FILMS DEPOSITED AT DIFFERENT SUBSTRATE TEMPERATURES

3.1 DC MAGNETRON SPUTTERED Ni_3Al ALLOY FILMS AT DIFFERENT SUBSTRATE TEMPERATURES

In this chapter, the microstructural and mechanical properties of Ni_3Al alloy films have been studied. These films have been deposited via DC-Magnetron sputtering at different substrate temperatures to understand the effect of substrate temperature on the microstructure and mechanical properties of the films. The identification of phase, the evolution of microstructure, surface properties and topography, the elemental composition of the film, contact angle measurements, and mechanical properties of the deposited films have been characterized using XRD, FE-SEM, AFM, EDS, DSA, and nanoindentation respectively at room temperature.

3.1.1 INTRODUCTION

Hard and super-hard coatings have been in demand in the automobile, aerospace and marine industries for the last two decades [154]–[156]. In order to fulfill the requirement in terms of mechanical and tribological properties several metal-based coatings were developed by researchers using CVD and PVD methods [157]–[159]. Different types of single-layer and multilayer coatings of transition metal nitrides and carbides like CrN, TiN, TiC, SiN, SiC, WN, WC, VN, etc. were deposited [156], [160]–[163]. These coatings were deposited in the form of binary and ternary alloys also [156], [164]–[166]. However, these coatings were able to meet the demand of machining industries in terms of required mechanical and tribological properties along with corrosion and oxidation resistance properties, but they lack in performance and durability when exposed to a high-temperature environment of ~900 - 1100℃ [167], [168]. In order to maintain the thermal stability and performance of transition metal-based coatings, several researchers have doped transition metal coatings with Nickel, zirconium and titanium superalloys [158], [169], [170]. The evolution of Nickel-based alloy coatings came into existence when synthesizing materials for high-temperature structural applications was a challenge. These coatings are capable of protecting the material even at elevated temperatures of ~900 - 1000℃. Additionally, they enhance the life of the parent material by maintaining

microstructural and thermal stability without losing a lot in the properties [86], [91], [171]. In particular, Nickel aluminides like NiAl and Ni_3Al have shown excellent thermal stability with resistance to creep and fatigue, enhanced mechanical and tribological properties and excellent corrosion and oxidation resistance properties [76], [89], [98], [103]. These properties of Ni_3Al-based coatings make them a suitable candidate for application in semiconductor, automobile, aerospace, marine and nuclear industries [172]–[174]. Ni_3Al-based coatings are face-centered intermetallic compounds having lattice constant of 0.3570 nm. These coatings with $L1_2$ structure are generally hard and brittle as compared to disordered Ni_3Al FCC structure [94], [175].

It has been reported that the properties of Ni_3Al-based coatings are majorly influenced by their microstructure and chemical compositions [98]. In order to achieve better properties, several researchers have altered the processing parameters as well as used different dopants in the Ni_3Al matrix. Moreover, the Ni_3Al films have been deposited in the form of single-layer and multilayer with the incorporation of different dopants [97], [103], [176]. Zhang *et al.*,[89] deposited tungsten (W) doped Ni_3Al films on Si substrate at ambient temperature using magnetron sputtering. The coatings were further heat treated (annealed) at 500℃ and 700℃. They found that the film doped with 12.5at% W in Ni_3Al film resulted in grain refinement and thus enhanced the hardness by 355% when annealed at 700℃. While depositing the films via Magnetron sputtering, several researchers have altered the influencing sputtering parameters like sputtering pressure, film thickness, gas flow rate (sccm) and substrate temperature. Meng *et al.*,[94] fabricated pure Ni, alloy Ni_3Al and Ni/Ni_3Al multilayer films via magnetron sputtering at a substrate temperature of 400℃. They found that pure Ni and alloy Ni_3Al single-layer coatings showed a hardness of 3.5 GPa and 5 GPa respectively while the multilayer of Ni/Ni_3Al showed enhanced hardness as compared to pure Ni and alloy Ni_3Al films. They also claimed that the hardness value of Ni/Ni_3Al films increased as a result of the increase in indentation depth because of the so-called substrate effect. Xu *et al.*,[91] studied the effect of Ni_3Al in Ni/Ni_3Al multilayer when deposited at ambient temperature using magnetron sputtering. They found that the films were synthesized in a sandwich structure where

layers of Ni and Ni_3Al showed FCC and $L1_2$ structure respectively. They also found the multilayers of Ni and Ni_3Al showed strong and coherent bonds as a lattice mismatch of 1.3% was observed when Ni_3Al was deposited on the Ni layer and Ni on Ni_3Al layer. Moreover, they found that the hardness of the multilayered coatings enhanced because the Ni_3Al layer is hard as compared to the Ni layer in the intermetallic state. Xing *et al.*,[86] studied the effect of introducing the Cr layer on mechanical and oxidation resistance properties of Cr/Ni_3Al multilayer coatings deposited via magnetron sputtering. To compare the results, a single layer of Cr/Ni_3Al alloy films was also synthesized at the same sputtering parameters. Both the films were deposited over NO6625 at a substrate temperature of 400℃. They found that with incorporation of Cr in Ni_3Al matrix, the hardness increased whereas the Young's modulus decreased. They claimed that the multilayer Cr/Ni_3Al films showed better mechanical properties as compared to single-layered film. However, results revealed that both the films were thermally stable and were capable of protecting the substrate from being drastically oxidized even at an elevated temperature of 1100℃. Several studies have been made by researchers on the fabrication of Ni_3Al based thin films for studying their properties at ambient and high temperatures [177]–[180]. To attain the required properties, sputtering parameters as well as several dopants have been incorporated in alloy and multilayer forms. However, very limited literature has been reported about the effect of substrate temperature on the microstructural stability and properties of the alloy Ni_3Al films. This work presents the effect of substrate temperature on microstructural and mechanical properties of alloy Ni_3Al films deposited by DC magnetron sputtering.

3.1.2 EXPERIMENTAL DETAILS

3.1.2.1 Synthesis of Ni_3Al alloy films

Ni_3Al alloy films were deposited on Silicon (100) using DC magnetron sputtering. A custom-built steel vacuum chamber of 14" diameter (Excel Instruments, Mumbai) equipped with 3 sputtering guns was used for the deposition. Ni_3Al films in alloy form were deposited at different substrate temperatures namely: Room temperature (RT), 200℃, 400℃ and 600℃. In

order to deposit the film, Ni_3Al alloy target (purity 99.95%, Testbourne Ltd, UK) of 5 mm thickness and 2 inches diameter was used. The target was fixed to the DC-powered sputtering gun at a constant distance of 15 cm from the substrates. In order to ensure the homogeneous thickness of the film throughout the substrate, the holder given a speed of 15 rotations per minute. Prior to deposition, the substrates were first cleaned with acetone and air dried whereas, base pressure of $3x10^{-6}$ mbar was achieved after evacuating the chamber. In order to sputter and deposit Ni_3Al alloy films, argon gas of 99.999% purity (30 sccm using MFC) was inserted in the vacuum chamber and the sputtering pressure of $3x10^{-2}$ mbar mbar was maintained and prudently monitored throughout the deposition. A pre-sputtering of 10 minutes was performed to clean the surface of the target whereas the actual deposition was carried out for 60 minutes. All the sputtering parameters other than the substrate temperature were kept constant throughout the set of experiments. The parameters of deposition have been mentioned in **table 3.1.**

Table 3.1: Sputtering parameters for depositing Ni_3Al alloy films

Targets	Ni_3Al
Substrates	Silicon (100)
Base pressure	3×10^{-6} mbar
Sputtering gas	Argon (30 sccm)
Sputtering pressure	3×10^{-2} mbar
Sputtering power	250 W DC
Substrate temperature	**RT, 200°C, 400°C & 600°C**
Deposition time	60 minutes

3.1.2.2 Characterization details

X-ray diffraction studies were performed on Bruker D8 ADVANCE ECO (CuKα=1.54Å) at ambient temperature to identify the phases formed in the films. Field emission scanning electron microscopy (FE-SEM, Zeiss Gemini) equipped with energy dispersive spectroscopy (EDS) was used to characterize the microstructure and chemical composition of the films. In order to study the

surface topography and to evaluate the surface properties of the deposited films, an atomic force microscope (Naio AFM, Nanosurf, Switzerland) was used at room temperature. The assessment of the coating's wettability in terms of contact angle measurements was conducted using a Drop shape analyzer (DSA 100, Krůss GmbH, Germany) in static conditions. In order to evaluate and calculate the contact angles between water and the surface of synthesized films, 0.5 µl of water droplets were dropped at ten different places on the surface of the coated substrate and the nearer value to the average was considered. The profile of the water droplet and the contact angle between the water droplets and surface were measured and calculated with the help of a backlight and the camera installed in the instrument. A load control nanoindentation (XP, Agilent, USA) test was performed on Ni_3Al coatings synthesized at different substrate temperatures to evaluate their mechanical properties. Before nanoindentation, tip and microscopic calibration were done to confirm the proper positioning and contact area of the tip to the deposited surface. To perform the nanoindentation for calculating the modulus and hardness of the alloy coating, a poisons ratio of 0.25 was considered at a strain rate of $0.05s^{-1}$ whereas the frequency of 45 Hz was set constant all over the test at the harmonic displacement of 2 nm. The average load of 9.5 mN was applied to examine the mechanical properties of all the synthesized films. Mechanical properties in terms of modulus and hardness were calculated using the inbuilt software in the system based on Oliver and Pharr method.

3.1.3 RESULTS AND DISCUSSION

Figure 3.1 shows the XRD spectra of Ni_3Al films deposited at different substrate temperatures. Two major diffraction peaks were observed at 44.13° and 51.3°. These peaks correspond to (111) and (200) planes of orders $L1_2$ face-centered cubic structure respectively. From the figure, it is observed that the intensity of both the major peaks (44.13° and 51.3°) increased with increase in substrate temperature up to 400°C. On further increase in substrate temperature to 600°C, the intensities of Ni_3Al (111) decreased whereas the Ni_3Al (200) peak disappeared. This could be the result of the decline in the preferred orientation and crystallinity of the deposited film. Moreover, the

diffraction peak at 51.3° disappears when the substrate temperature is increased up to 600℃ and there is the evolution of a new diffraction peak at 38° which corresponds to the Al (111) plane. Coherently diffracting crystallite size (d_{XRD}) was calculated using the Scherrer equation (equation 3.1) from the integral width of diffraction lines after correction of instrumental branding and background subtraction as mentioned in **table 3.2**.

$$d = 0.9\lambda/\beta cos\theta \qquad (3.1)$$

Where d denotes crystallite size, λ denotes X-ray wavelength (1.54Å), β denotes full width at half maxima (FWHM) of most dominant XRD peak, and θ is Bragg's angle.

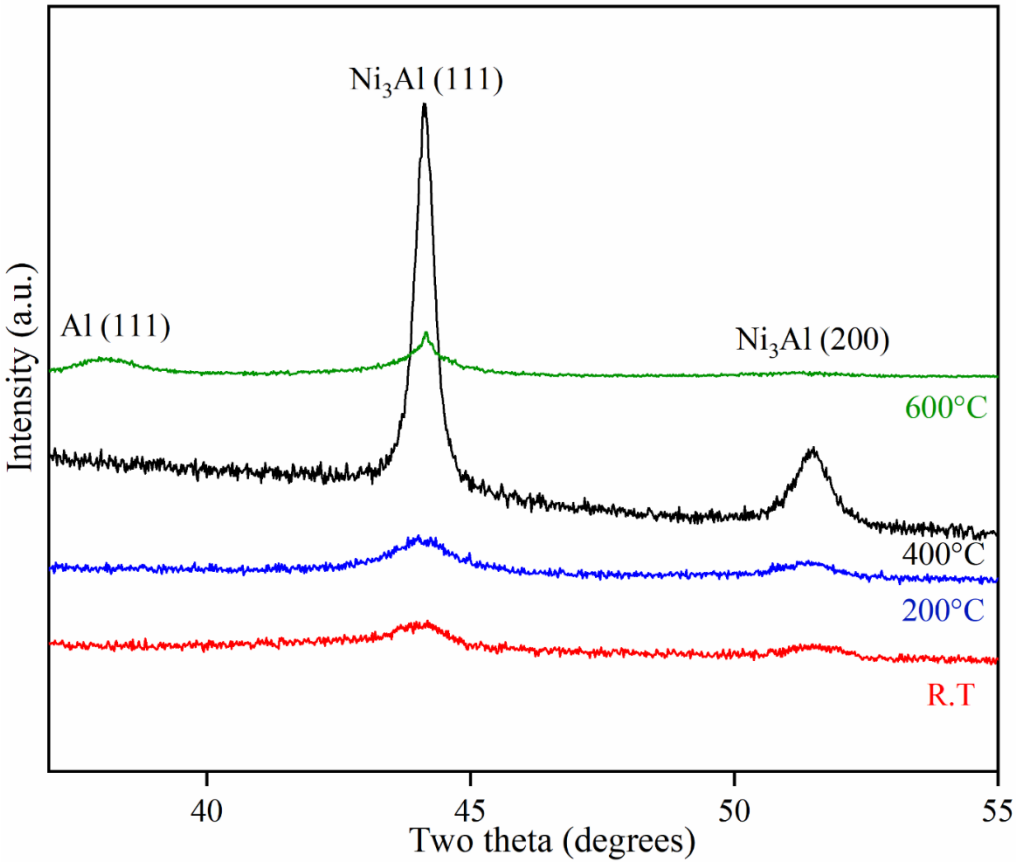

Figure 3.1: XRD spectra of Ni_3Al films deposited at different substrate temperatures

From the results, it is observed that the crystallite size of Ni_3Al films increases with increase in the substrate temperature. This is because of the higher kinetic energy of the atoms at high temperatures that promotes the atomic diffusion

resulting in the growth of crystallites. The minimum and maximum crystallite size of 13.16 ± 0.60 nm and 28.88 ± 1.50 nm have been calculated for film deposited at RT and 600℃ respectively.

The elemental composition of the deposited films has been characterized using Energy dispersive spectroscopy (EDS) as shown in **figure 3.2.** It can be seen that, the atomic percentage of Ni and Al in Ni_3Al films synthesized at different substrate temperatures is almost in the ratio of 75:25 **(table 3.2)**.

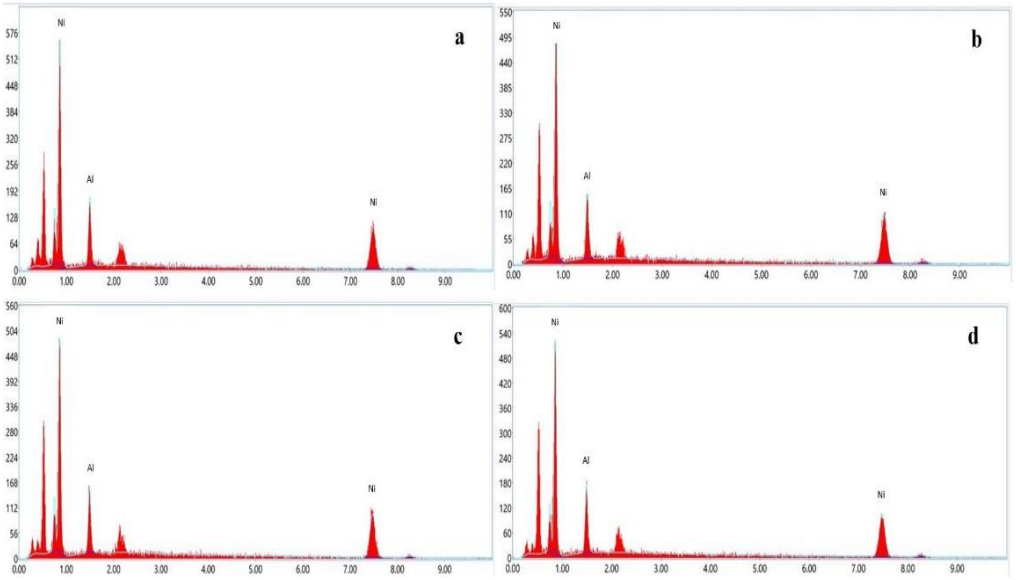

Figure 3.2: EDS results of Ni_3Al films deposited at different substrate temperatures **(a)** RT **(b)** 200℃ **(c)** 400℃ **(d)** 600℃

Table 3.2: Calculated parameters of Ni_3Al films deposited at different substrate temperatures

S N	Sample's name	Substrate temperature (℃)	EDS results (at%)		Surface roughness (nm)	Crystallite Size (nm)	Grain size (nm)	Porosity (%)
			Al	Ni				
1	RT	RT	74.16	25.84	4.61 ± 0.5	13.16 ± 0.60	89.5 ± 1.0	11.71 ± 1.0
2	200℃	200	74.61	25.39	6.44 ± 0.6	14.21 ± 0.80	88.7 ± 1.0	13.50 ± 1.0
3	400℃	400	75.23	24.77	7.30 ± 0.5	18.27 ± 1.00	82.6 ± 1.0	10.00 ± 0.5
4	600℃	600	74.83	25.17	14.64 ± 0.8	28.88 ± 1.50	73.0 ± 1.0	21.06 ± 1.5

Figure 3.3 shows the microstructure of the coatings synthesized at different substrate temperatures. It is observed that the film deposited at room temperature exhibits a closely packed microstructure. However, the presence of agglomerated and overlapped grains is clearly visible. With increase in substrate temperature, the grain size of the coating reduced with the evolution of pores. The Ni_3Al coating synthesized at substrate temperature of 400°C showed the formation of equisized grains resulting in the formation of homogeneous microstructure with less percentage of pores. Furthermore, the coating synthesized at 600°C reflected an inhomogeneous distribution of grains with degraded microstructure resulting in the highest percentage of porosity.

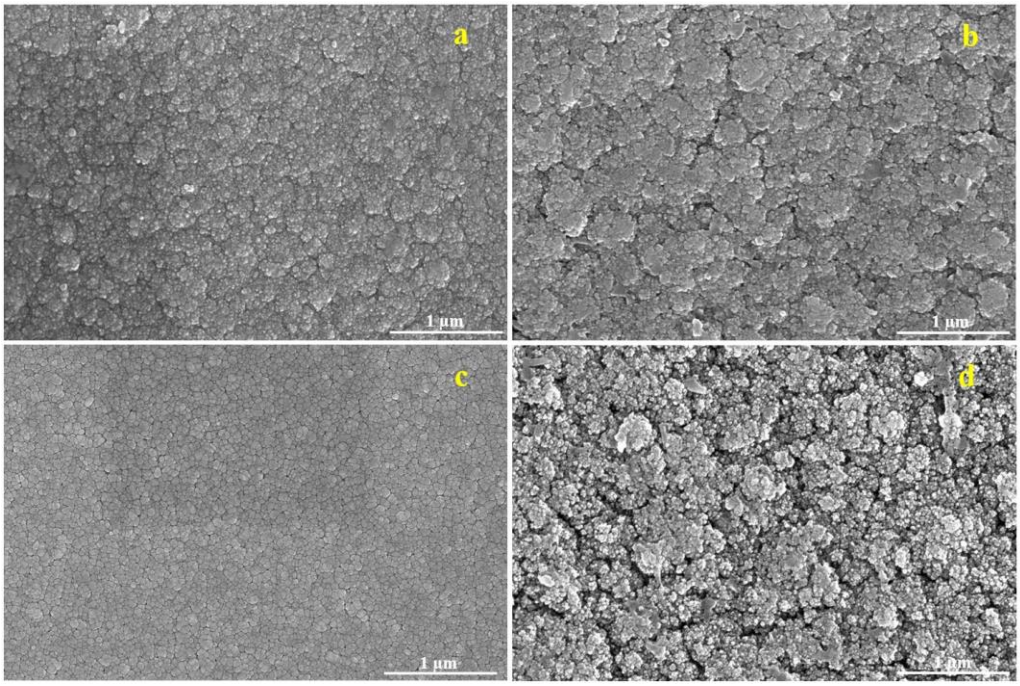

Figure 3.3: SEM images of Ni_3Al films deposited at different temperatures **(a)** RT **(b)** 200°C **(c)** 400°C **(d)** 600°C

Image J software was used to calculate the grain size and percentage of porosity in the film from FESEM images. A unit area of 1 x 1 µm was selected to perform the test. The average value of grain size and percentage porosity was calculated by performing the test at 10 different places of FESEM images. The results of the test confirmed that the maximum and minimum grain size of 89.5 ± 1.0 nm and 73 ± 1.0 nm were shown by the coating deposited at RT and

600℃ respectively. Moreover, the film deposited at 400℃ showed the minimum percentage of pores (10 ± 0.5) while the maximum percentage of pores (21.06 ± 1.5) is shown by the film deposited at 600℃ **(figure 3.4).** The results of the grain size and percentage of pores in Ni_3Al coatings synthesized at different substrate temperatures have been indexed in **table 3.2**.

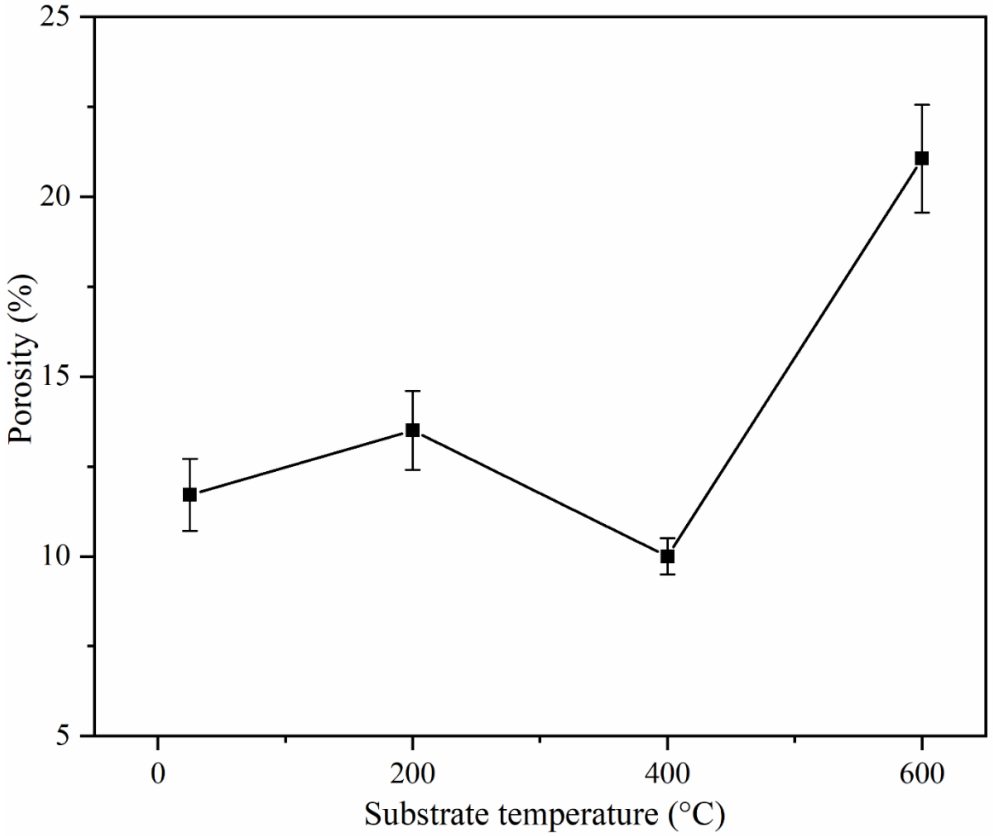

Figure 3.4: Porosity in Ni_3Al films deposited at different substrate temperatures

Atomic force microscope was used to study and evaluate the surface morphology and surface roughness of the deposited coatings. The cantilever probe of AFM scanned the area of 12.5 x 12.5 μm to reveal the structure and arrangement of nano asperities whereas the average value of the surface roughness was obtained using the inbuilt software in the setup by scanning the surface in the area of 50 x 50 μm^2 at ten different places of the deposited films. **Figure 3.5** and **figure 3.6** display the 2D and 3D AFM images of the Ni_3Al coatings synthesized at various substrate temperatures.

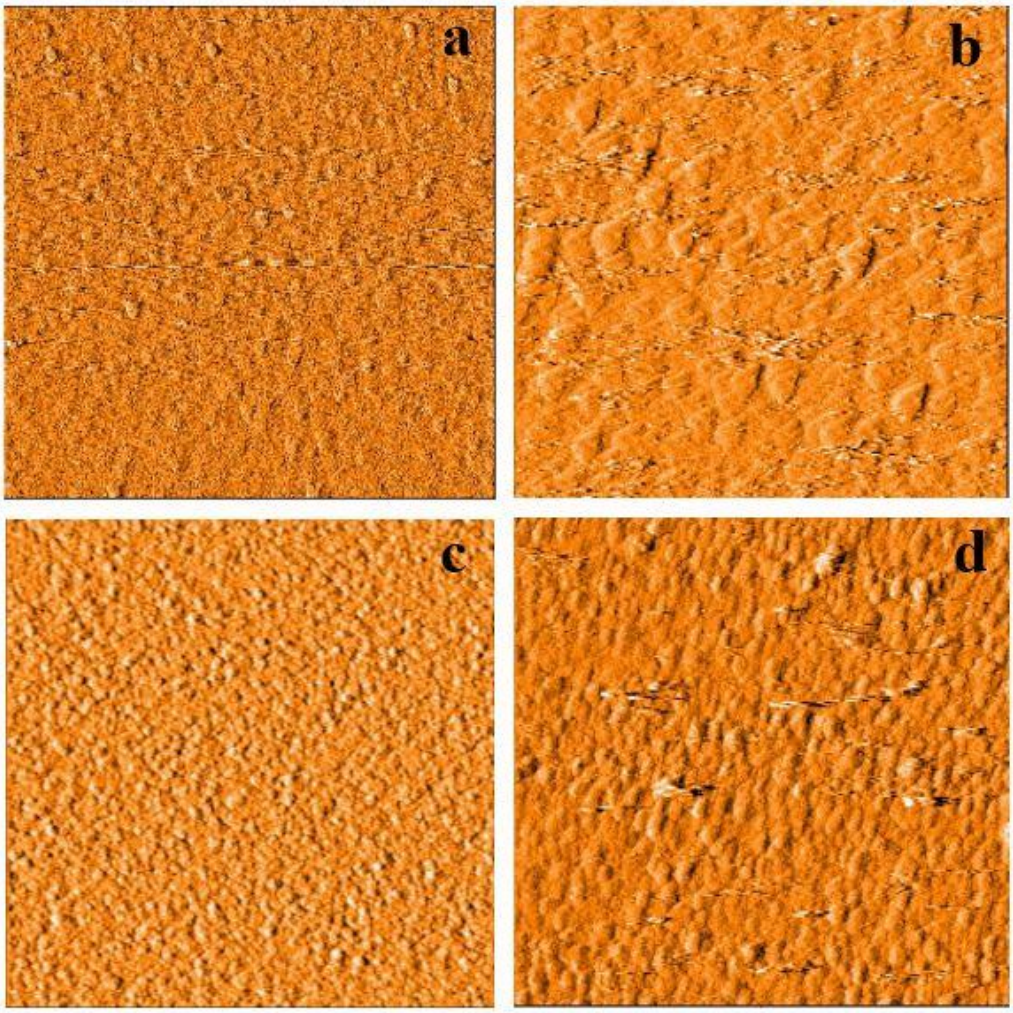

Figure 3.5: 2D AFM image of Ni_3Al films deposited at different substrate temperatures **(a)** RT **(b)** 200℃ **(c)** 400℃ **(d)** 600℃

The 2D images of Ni_3Al films synthesized at RT and 200℃ showed a triangular structure which overlapped each other resulting in the formation of hills and valley of less height and depth respectively. However, the formation of globular and spheroidal structures is observed when the film is deposited at 400℃. The higher number of spheroidal domes-like structure is the evidence of the formation of sharp closely packed sharp asperities. Furthermore, the alloy film deposited at 600℃ has shown the triangular dent-like structure forming the hills and valleys of maximum heights and depth. From the 3D AFM images, it is seen that all the deposited films possess dome-like hilly structures. However, it is found that, the coating synthesized at RT and 200℃ have evenly distributed dome-like wide structures as compared to the film

deposited at 400℃ and 600℃. Very sharp hill-like structures can be seen in the film deposited at 400℃. It can be seen that the height of the asperities (dome-like structure) increases with increase in the substrate temperature. This results in increase in surface roughness of the film. However, the total number of asperities are less in the coating deposited at 600℃ but the size of height, width and depth of the hills and valleys are greater as compared to the rest of the films resulting higher surface roughness. The results of roughness of the coatings synthesized at various substrate temperature have been mentioned in **table 3.2.**

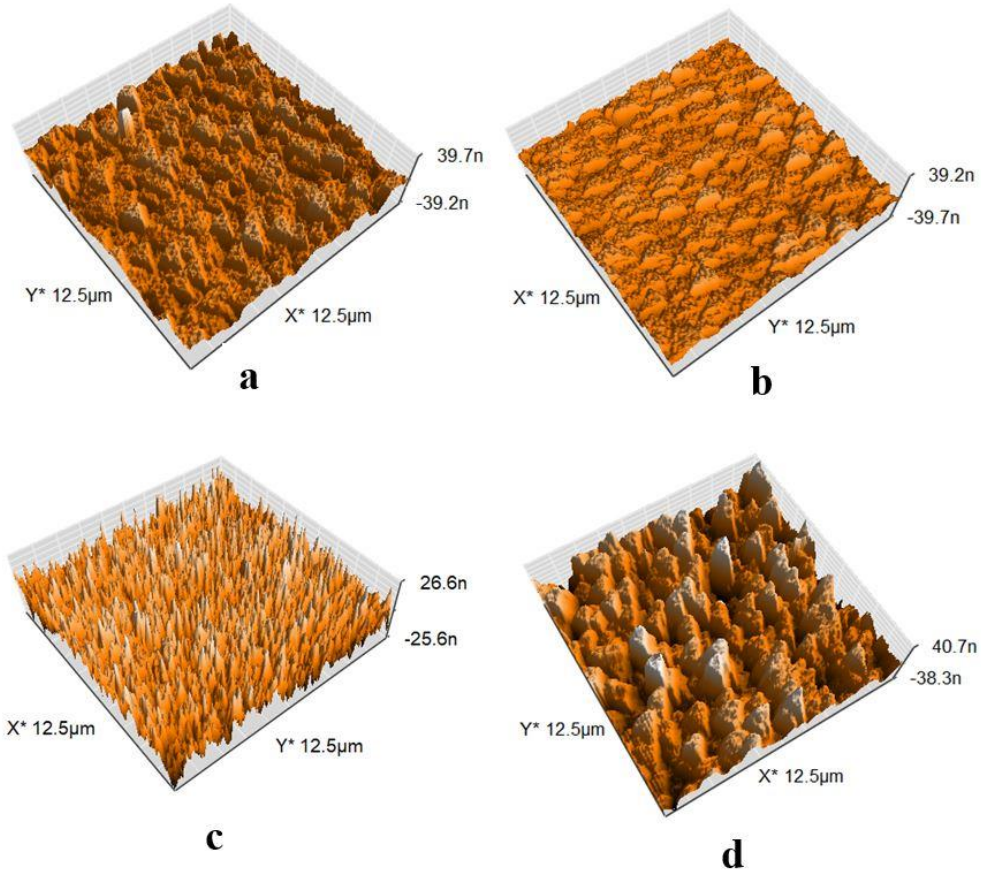

Figure 3.6: 3D AFM image of Ni_3Al films deposited at different substrate temperatures **(a)** RT **(b)** 200℃ **(c)** 400℃ **(d)** 600℃

The wettability of Ni_3Al alloy films deposited at different substrate temperatures has been studied and investigated in terms of contact angle measurements as shown in **figure 3.7**. From the figure, From the figure, it is observed that there is no substantial variation in water contact angles when the

coatings were deposited at RT, 200°C and 400°C. The higher contact angles of the films deposited at RT and 200°C is due to the existence of nano asperities in the film which helps in trapping the air inside them and reduces the solid-liquid interaction of water droplets and deposited coating. The surface topography of the coating deposited at substrate temperature of 400°C possesses hill like sharp nano asperities which are not capable of trapping much air as compared to the films deposited at RT and 200°C. This results in slight decrease in water contact angle of the film as compared to that of RT and 200°C. However, the value of the contact angle falls suddenly when the coating is synthesized at substrate temperature of 600°C. This could be the result of the non-homogeneous surface roughness of the film as a result of the generation of porosity as shown in the FESEM image.

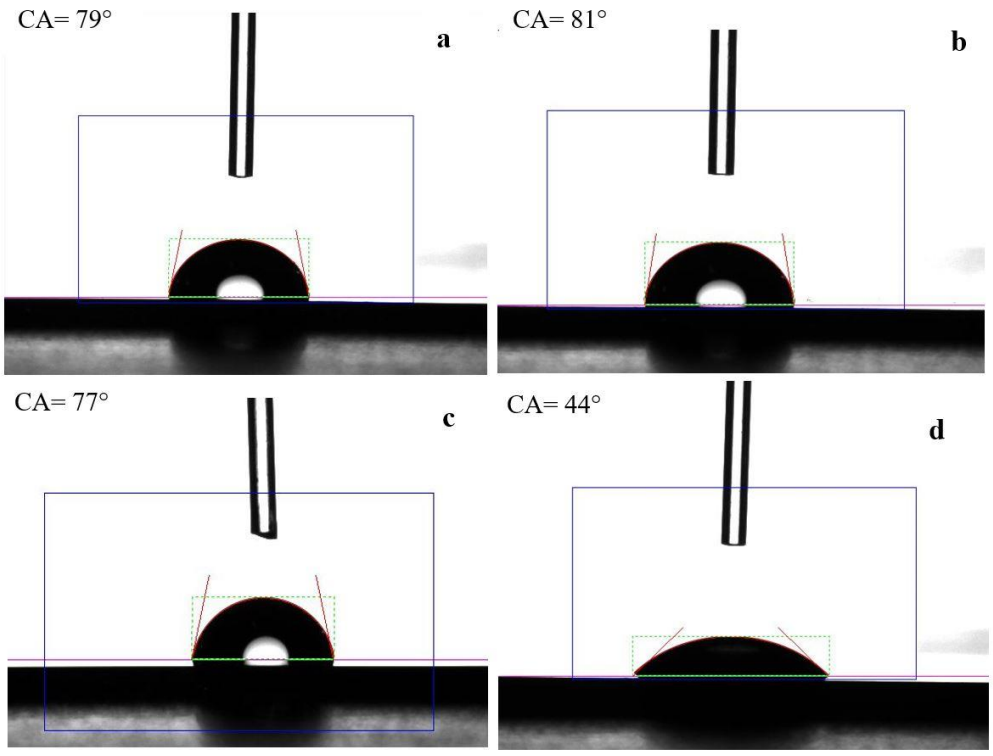

Figure 3.7: Contact angles of the films deposited at different substrate temperatures **(a)** RT **(b)** 200°C **(c)** 400°C **(d)** 600°C

To evaluate the modulus and hardness of the coating, a load control nanoindentation ($1/10^{th}$ of the thickness of the film) was performed at room temperature. An average load of ~9.5 mN was applied during the test. The

load versus displacement curve has been plotted in **figure 3.8.** From the figure it can be observed that all the synthesized coatings undergo both elastic and plastic deformation during the loading of nanoindentation whereas only elastic deformation is observed during the unloading period. It can also be seen that the coating synthesized at room temperature and 200℃ shows the similar trend during loading and unloading resulting in almost the same values of mechanical properties whereas the film deposited at 400℃ shows less plasticity during loading and unloading as compared to the other deposited films at lower substrate temperatures. This implies that the film deposited at 400℃ is comparatively harder than the former two films. Nanoindentation performed on the film deposited at 600℃ revealed that the film gets softened resulting in more deformation as compared to other films and thus decreased hardness. This could be the result of the presence of the highest percentage of pores in the film.

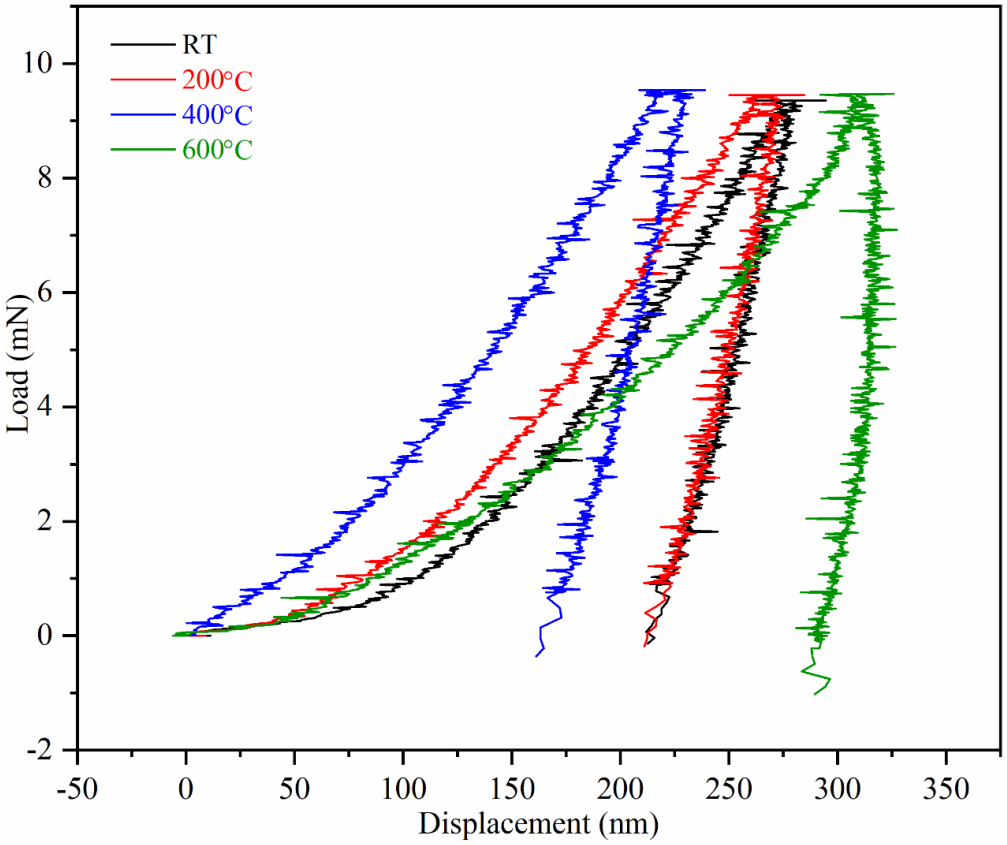

Figure 3.8: Load versus displacement curve of Ni_3Al film deposited at different substrate temperatures

The results of hardness and Young's modulus calculated as a result of nanoindentation have been shown in **figure 3.9.** From the figure, it can be observed that the hardness of alloy Ni_3Al films enhances with increase in the substrate temperature up to 400°C beyond which it declined. The results of Young's modulus have followed almost the same trend as that of hardness.

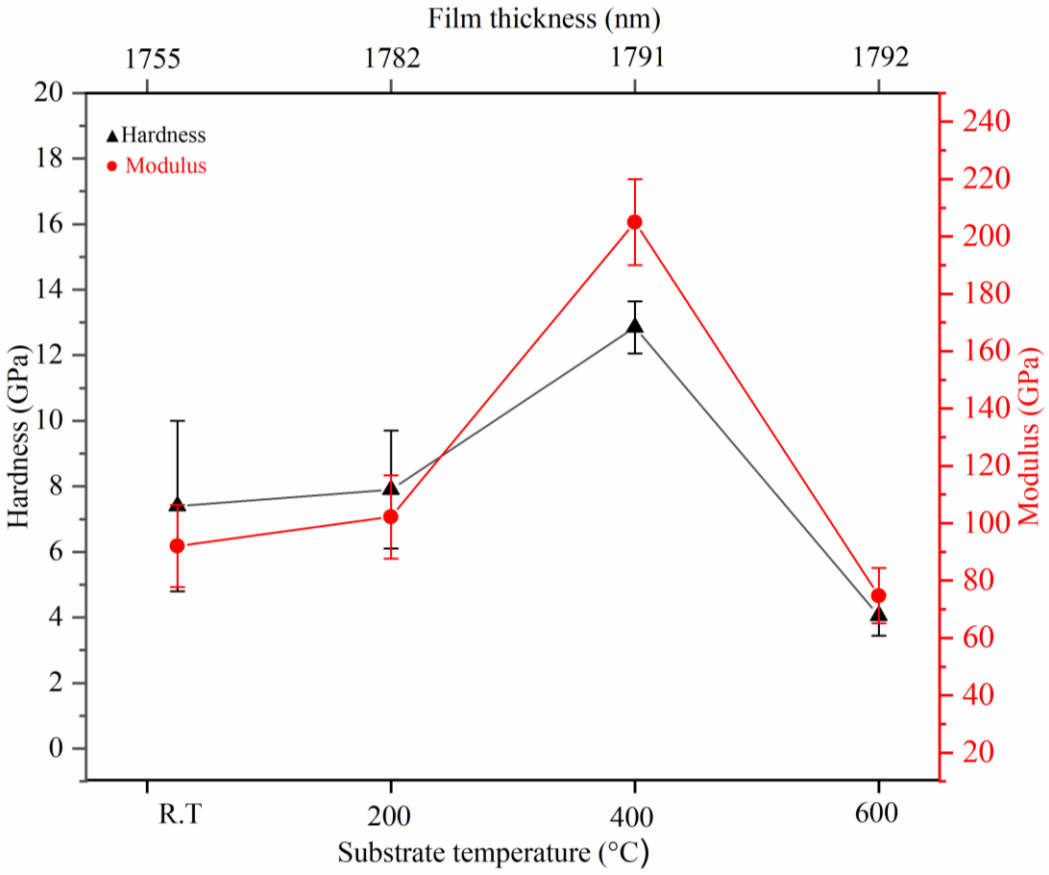

Figure 3.9: Variation in hardness and Young's modulus as a function of substrate temperature

The reports in literature shows that the properties of the Ni_3Al films are influenced by the parameters like chemical composition, microstructure, grain size, surface morphology and topography, sputtering pressure and post-deposition treatments [93], [177].

Some of the research groups have also deliberated the impact of substrate temperature on the properties of Ni_3Al coatings. Rajarshi Banerjee [97] synthesized Ni_3Al films on silicon substrates at two substrate temperature of 400°C and ambient temperature using magnetron sputtering. He found that

film deposited at elevated temperature showed $L1_2$ structure while the film deposited at room temperature showed FCC structure. The researcher proclaimed that the ordered $L1_2$ structure formed in the coating deposited at 400℃ has led to the enhancement in hardness of the coating when compared with the coating deposited at ambient temperature.

Researchers have also showed that the Ni_3Al film sustains its microstructural and thermal stability when deposited at elevated substrate temperature. However, a decline in lattice constant is also observed as a result of enhancement in substrate temperature during deposition [181]–[183].

In our case, the grain size of the film continuously decreased when the deposition was done at higher substrate temperatures. The deposited alloy films showed a continuous and subsequent enhancement in the hardness and modulus up to the substrate temperature of 400℃ following the classical Hall-Petch relationship. Moreover, the formation of chemically ordered $L1_2$ FCC structure **(Figure 3.1)** contributed to enhancing the mechanical properties of the coatings. [97]. The Ni_3Al coating deposited at substrate temperature of 600℃ showed the minimum hardness and Young's modulus of (4.06 ± 0.61) GPa and (74.76 ± 9.63) GPa respectively. The reason for this could be the formation of high percentage of pores in the film. The maximum and minimum hardness of (12.8 ± 0.8) GPa and (4.06 ± 0.61) GPa have been achieved for the film deposited at 400℃ and 600℃ respectively.

The evolution of modulus epitomizes almost the same drift as represented by nano hardness. The highest modulus of (205 ± 15) GPa and lowest modulus of (74.76 ± 9.63) GPa have been achieved for the film deposited at 400℃ and 600℃ respectively. Furthermore, the drop in intensity of Ni_3Al phase and the appearance of Al (111) as shown in **figure 3.1** is evident that the preferred orientation of Ni_3Al in the film is influenced by the evolution of the Al (111) phase which resulted in diminishing the mechanical properties of the coating. The obtained value of hardness (12 ± 2.8) is greater than the values achieved and reported so far in the literature for alloy Ni_3Al films where indentation is made up to $1/10^{th}$ of the film thickness.

3.1.4 CONCLUSION

Ni_3Al coatings were synthesized on Silicon substrate via DC magnetron sputtering at various substrate temperatures. From XRD spectra, it is found that all the films possessed the preferred orientation of (111) whereas a broad peak of Al (111) is perceived when the coating is deposited at 600℃. It was investigated that, the crystallite size of the coating increased whereas the grain size decreased simultaneously with increase in deposition temperature. Moreover, the increase in the percentage of pores is also observed due to the rise in the substrate temperature. This resulted in enhancing the surface roughness of the coating. Maximum porosity (21.06 ± 1.5 %) and surface roughness (14.64 ± 0.80) have been calculated for the film deposited at 600℃. The investigation of water contact angle measurements revealed that the film deposited at 200℃ showed the maximum contact angle of 81°. However, there is insignificant variation in values of contact angles when the film is deposited at RT, 200℃ and 400℃. The smallest value of water contact angle is perceived for the coating synthesized at substrate temperature of 600℃ because of the presence of the largest percentage of pores. Ni_3Al alloy film deposited at 400℃ has shown the maximum value of hardness (12.8 ± 0.8) GPa and Young's modulus (205 ± 15) GPa.

CHAPTER 4

SYNTHESIS AND CHARACTERIZATION OF DC-CO-SPUTTERED Ni_3Al AND Ni-RICH Ni_3Al FILMS

4.1 DC MAGNETRON CO-SPUTTERED Ni-RICH Ni_3Al FILMS

In this chapter, the synthesis and characterization of Ni_3Al and Ni-rich Ni_3Al films have been explored in detail. These alloy films have been deposited on silicon substrates using DC-Magnetron sputtering and co-sputtering respectively at substrate temperatures of 400℃. The effect of Ni enrichment on the evolution of phases, microstructure, surface topography, mechanical, and hydrophobic properties of Ni-rich Ni_3Al alloy films has been studied in detail using, XRD, FESEM, AFM, nanoindentation and Drop shape analyzer respectively.

4.1.1 INTRODUCTION

Nickel-based superalloys and nickel-based intermetallic alloys have been broadly researched and used in structural applications at high temperatures [89], [184], [185]. They are capable of resisting thermal instability, oxidation and hot corrosion properties [101], [177], [179]. Different phases of the Ni-Al system while depositing them as a thin film has also resulted in increasing the mechanical and tribological properties of these aluminides. Therefore, the Ni-Al-based thin films have been proven as a better candidate for high-temperature applications as well as in MEMS and integrated circuits [88], [186]–[188]. Over the last few decades, researchers have studied to improve their properties by altering the composition of these aluminides as well as by using different dopants. These intermetallic alloys are being used in structural applications of aerospace, marine, nuclear and defense industries because of their excellent tribological properties [98], [189], [190].. To enhance the hardness of thin films, different kinds of CVD and PVD methods have been used to deposit transition metal nitrides, oxides and carbides. Researchers have deposited several transition metal-based thin films with enhanced modulus and hardness like, CrN, TiN, Ti-Si-N, WN, TaN, VN etc.[154], [170], [191]–[193] These transition metal-based nitrides have shown a hardness of ~25 to 40 GPa at room temperature [194]–[197]. However, these coatings were not able to perform similarly at elevated temperatures. Along with enhanced mechanical properties, Ni-based thin films have resulted in enhancing the corrosion and oxidation resistance properties at elevated temperatures of ~900 - 1100℃ [75],

[86], [103], [186], [189], [190], [198]. Ni-Al-based coating has shown better thermal, and microstructural stability at high temperatures resulting in resistance to corrosion, oxidation, creep and fatigue [199]–[202]. Among the different aluminides of Ni-Al-based coatings, Ni_3Al has resulted better in terms of enhancement in mechanical and tribological properties. Ni_3Al is a polycrystalline intermetallic FCC compound that shows $L1_2$ structure which continues up to solidus temperature and has a lattice constant of 0.3570 nm. Several researchers have deposited Ni_3Al thin films in alloy form and multilayer forms with the incorporation of different dopants to study their properties. It has been reported that Ni_3Al is brittle at room temperature but the incorporation of Boron in Ni_3Al has resulted in an increase in its ductility [203]. However, Ni_3Al is good oxidation and corrosion-resistant film at high temperatures but the addition of Zirconium and hafnium has resulted in a further increase in corrosion and oxidation resistance properties along with high-temperature strength and creep resistance [198]. Swygenhoven *et al.*,[92] used DC magnetron sputtering to synthesize Ni_3Al film in alloy and multilayer form on Si substrate. The thickness of alloy Ni_3Al was 400 nm while multilayers were deposited with an individual thickness of 2.5 nm and 5 nm. they performed nanoindentation to investigate the mechanical properties of Ni_3Al films. They observed that the alloy film showed a hardness of ~13.5 GPa while multilayer Ni_3Al films Ni_3Al/Ni (5 nm individual thickness) and Ni_3Al/Ni (2.5 nm individual thickness) exhibited a hardness of ~12 GPa and 11.8 GPa respectively. The decrease in hardness of the multilayer Ni_3Al films was reported as a result of the increased Ni concentration in the film. Tixier *et al.*, [87] also deliberated the significance of multilayers coatings on the mechanical properties of Ni/Ni_3Al thin coatings. They deposited the multilayer films on Si substrate at ambient temperature using DC magnetron sputtering. The maximum hardness achieved was ~17.5 GPa which is almost 88% greater than that of the bulk Ni_3Al polycrystalline compound. It has been investigated that the hardness of the multilayer films is coherent with the Hall-Petch equation for $\Lambda > 100$Å. With further decrease in Λ the grain size of the deposited coating reached a limited value which contributed in decreasing the hardness of the film. Meng *et al.*, [94] synthesized Ni/Ni_3Al coatings on Si

substrate using DC magnetron sputtering at substrate temperature of 400℃. They fabricated three categories of Ni/Ni_3Al films with total number of multilayers of 4, 8 and 12. They measured the hardness of the film with respect to the variation in indentation depth. They found that the hardness of the multilayer films increased with increasing the indentation depth while performing nanoindentation. Considering the substrate effect beyond the indentation depth of $1/10^{th}$ of the total coating thickness, they found a maximum hardness of ~4.3 to 4.8 GPa. Huang *et al.*, [175] examined the effect of long-range ordering on the mechanical properties of Ni_3Al films. They deposited Ni_3Al films on Si substrate using electron beam co-evaporation of Ni and Al with thicknesses of 170 nm and 300 nm. In order to ensure good adhesion between the substrate and Ni_3Al films, Chromium (Cr) of 12 nm was deposited on the Si substrate. They found that the $L1_2$-ordered Ni_3Al films have shown better hardness as compared to disordered FCC structures. It was also found that the film with lesser film thickness (170 nm) showed better modulus and hardness as compared to the film of 300 nm thickness. They found that the hardness of the coating increases with increase in indentation depth because of so called substrate effect as the SiO_2 layer on the Si substrate is harder than the intermetallic Ni_3Al compound film. Many researchers have studied the impact of Ni enrichment in Ni_3Al films on its mechanical and tribological properties. However, they have synthesized Ni_3Al films in multilayer forms but the synthesis and characterization of Ni-rich Ni_3Al films in alloy form is still to be explored and understood. This research presents the synthesis of Ni_3Al and Ni-rich Ni_3Al-based alloy thin films and the effect of Ni enrichment in the Ni_3Al matrix on microstructural and mechanical properties.

4.1.2 EXPERIMENTAL DETAILS

4.1.2.1 Synthesis of Ni_3Al and Ni-rich Ni_3Al films

Ni_3Al and Ni-rich Ni_3Al alloy coatings were deposited on Silicon (100) substrates using DC magnetron sputtering and co-sputtering respectively. The films were deposited at the substrate temperature of 400℃ in a customized steel vacuum chamber of 14” diameter (Excel Instruments, Mumbai) equipped

with three sputtering guns. In order to deposit Ni_3Al and Ni-rich Ni_3Al alloy films, both the Ni_3Al target (99.95% purity) and Ni target (99.99% purity) of 5 mm thickness and 2 inches diameter were used. Prior to deposition, the substrates were cleaned using acetone followed by drying in open air. The substrates were clamped in rotating substrate holder whereas the sputtering guns were placed at 120° apart from each other. During the deposition process, the substrate holder was rotated with speed of 15 rotations per minute to ensure the homogeneous deposition of the films. The vacuum chamber was primarily evacuated to a pressure of 3×10^{-6} mbar to eradicate the contaminants from the chamber and chamber walls. Argon gas (99.99% purity) was inserted in the vacuum chamber and the sputtering pressure was maintained at 3×10^{-2} mbar during deposition. Sputtering targets were pre-sputtered for 5 minutes in order to remove the contaminants from the surface of the targets and the actual deposition was carried out for 60 minutes. In order to deposit Ni_3Al film, a continuous DC power of 250 W was supplied to the Ni_3Al alloy target whereas the power to the Ni target was varied as 25 W, 50 W and 100 W for co-sputtering to deposit Ni-rich Ni_3Al films namely 0 W Ni, 25 W Ni, 50 W Ni and 100 W Ni. During each set of experiments, the processed gas flow, substrate temperature and the pressure inside the vacuum chamber were carefully monitored. The sputtering parameters used during the deposition of Ni_3Al and Ni-rich Ni_3Al films are shown in **table 4.1**

Table 4.1: Sputtering parameters for depositing Ni_3Al and Ni-rich Ni_3Al films

Targets	Ni_3Al & Ni
Substrates	Silicon (100)
Base pressure	3×10^{-6} mbar
Sputtering gas	Argon (30 sccm)
Sputtering pressure	3×10^{-2} mbar
Sputtering power (Ni_3Al)	250 W DC
Sputtering power (Ni)	**0 W, 25 W, 50 W & 100 W DC**
Substrate temperature	400°C
Deposition time	60 minutes

4.1.2.2 Characterization details

X-ray diffraction was performed on Bruker D8 ADVANCE ECO (CuKα = 1.54Å) at room temperature to investigate the different phases formed in the Ni_3Al and Ni-rich Ni_3Al alloy films. The microstructure of the deposited films was characterized by FE-SEM (Zeiss Gemini) whereas the surface topography was analyzed using atomic force microscopy (NaioAFM, Nanosurf, Switzerland) at ambient temperature. The elemental composition of the alloy coatings was characterized using Energy dispersive spectroscopy equipped with FE-SEM. The hydrophobic property of Ni_3Al and Ni-rich Ni_3Al films has been studied and evaluated in terms of contact angle measurements. The test was performed in on drop shape analyzer setup (DSA 100, Krůss GmbH, Germany) in the static condition in open air at ambient temperature. In order to evaluate the wettability of the film, water droplets of 0.5 µl were dropped at 10 different places on the surfaces of the deposited films. The profile and average contact angle between the water droplets and the deposited surfaces were calculated using the backlight camera and inbuilt software in the set up respectively. A load control nanoindentation (XP, Agilent, USA) was carried out to characterize the mechanical properties of the deposited coatings. Prior to the test, microscopic and tip calibration was done in order to ensure the proper positioning of the tip to the surface contact area of the deposited films. Poison's ratio of 0.25 at a displacement rate of $0.05s^{-1}$ was considered whereas a constant frequency of 45 Hz at a harmonic displacement of 2 nm was maintained right through the nanoindentation test. The inbuilt software in the nano-indenter based on the Oliver and Pharr technique was used to calculate the modulus and hardness of the coatings. An average load of 9.5 mN was applied at 20 different spots of the sample to evaluate the average values of modulus and hardness.

4.1.3 RESULTS AND DISCUSSION

XRD spectra of pure Ni_3Al films and Ni-rich Ni_3Al films have been shown in **figure 4.1.** Two major peaks of Ni_3Al corresponding to face-centered cubic structure of the (111) and (200) plane is observed at 44.1° and 51.3° respectively. These XRD peaks also correspond to the $L1_2$ structure of Ni_3Al

films. From the figure, it can be observed that the intensity of the XRD peak at 44.1° increases with Ni enrichment up to 25 W but beyond 25 W it decreases. This could be the result of the stresses present in the film due to the increase in thickness. This may also be due to decrease in crystallinity and preferred orientation of the Ni_3Al (111) plane along with the evolution of new phase of Ni_9Al (012) and Ni_5Al (113) at 33.3° and 62° respectively. It can be observed that the diffraction peak of Ni_9Al disappears when enriched with 100 W Ni resulting in the evolution of the broad diffraction peak of Ni.

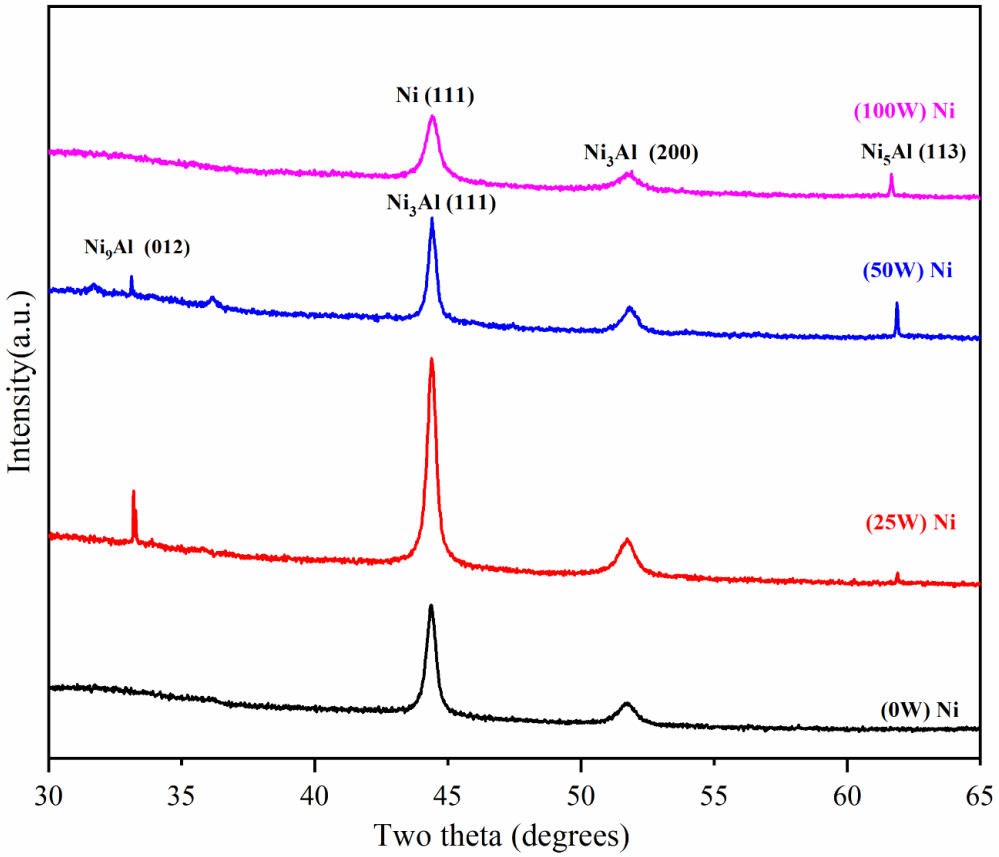

Figure 4.1: XRD spectra of Ni_3Al and Ni-rich Ni_3Al films

The average crystallite size (d_{XRD}) of the synthesized alloy films was calculated from the Scherrer equation **(equation 3.1, chapter 3)** using the integral width of the diffraction lines after the subtraction of correction for instrumental broadening [100]. The crystallite size of Ni_3Al and Ni-rich Ni_3Al alloy films has been shown in **table 4.2.** The results showed that there is a continuous and subsequent decrease in the crystallite size as the concentration of Ni increases in the host Ni_3Al matrix. The existence of higher concentration

of Ni in Ni_3Al coatings suppresses the crystallization during the co-sputtering process resulting in decrease of crystallite size of the Ni-rich Ni_3Al films. The maximum and minimum crystallite size of 18±1.5 nm and 8.0±0.5 nm has been observed for 0 W Ni and 100 W Ni respectively.

Table 4.2: Calculated parameters of Ni_3Al and Ni-rich Ni_3Al films

SN	Sample	EDS results (at%)		Film thickness (nm)	Surface roughness (nm)	Crystallite Size (nm)	Grain size (nm)	Porosity (%)
		Al	Ni					
1	0 W Ni	20.8	79.2	1667	7.3 ± 0.5	18 ± 1.5	82 ± 1.0	10.77 ± 1.5
2	25 W Ni	16.4	83.6	1742	8.8 ± 0.5	17 ± 1.5	91 ± 1.5	12.81 ± 1.5
3	50 W Ni	14.9	85.1	2618	9.1 ± 0.5	15 ± 1.2	98 ± 1.5	18.12 ± 1.8
4	100 W Ni	13.3	86.7	3170	32.3 ± 1.5	8 ± 0.5	NA	39.07 ± 1.5

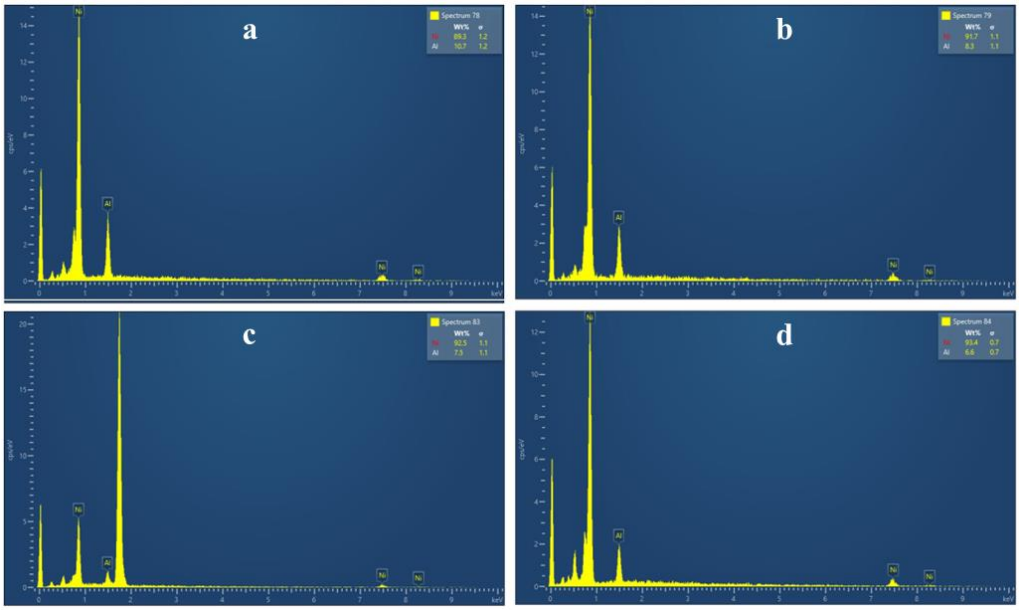

Figure 4.2: EDS results **(a)** 0 W Ni **(b)** 25 W Ni **(c)** 50 W Ni **(d)** 100 W Ni

Figure 4.2 shows the results of EDS. From the figure it is seen that the concentration of Ni increases when the DC power to Ni target increases simultaneously. This resulted in continuous and subsequent increases in the thickness of the coatings. **figure 4.3** displays the cross-sectional FESEM images of the deposited coatings. The cross-sectional view of Ni_3Al films

showed a closely packed columnar grain. However, a non-homogeneity in columnar grain structure is found when Ni_3Al film is enriched with 100 W Ni. The concentration [Ni (at %) and Al (at %)] and the thickness of the Ni_3Al and Ni-rich Ni_3Al films have been indexed in **table 4.2**.

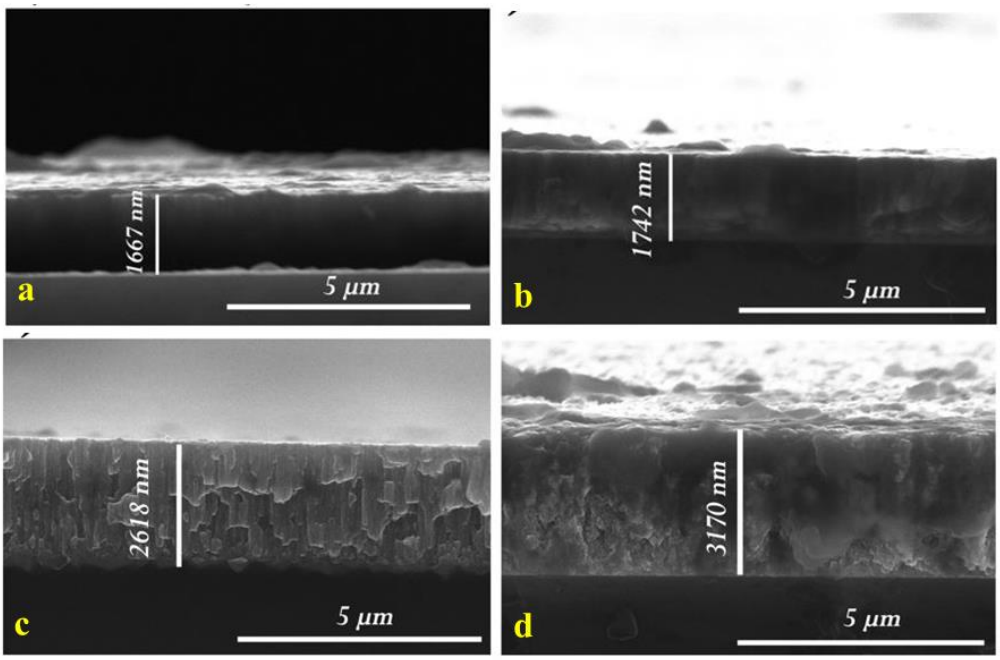

Figure 4.3: Cross-sectional FESEM images of the samples **(a)** 0 W Ni **(b)** 25 W Ni **(c)** 50 W Ni **(d)** 100 W Ni

The microstructure of Ni_3Al and Ni-rich Ni_3Al films is shown in **figure 4.4**. From the figure, it can be seen that the 0 W Ni consists of densely packed microstructure which reflects a smooth and homogeneous structure of the coating. With rise in Ni content in host Ni_3Al up to 25 W Ni, the enlargement of grains is observed as a result of the clustering of crystallites which further contributes to evolution of porosity resulting in inhomogeneity in the microstructure. Furthermore, the Ni_3Al films enriched with 50 W Ni, resulted in the spheroidization of grains resulting in the generation of higher percentage of pores. The film enriched with 100 W Ni has shown the maximum percentage of pores with degraded microstructure. This could be the result of deterioration of the grains and grain boundaries. The percentage of pores and grain size of Ni_3Al and Ni-rich Ni_3Al films has been calculated using Image J software. For this purpose, the FESEM images have been used in the software. The variation in porosity (%) as a result of increase in Ni

content in the Ni_3Al matrix is shown in **figure 4.5**. The minimum and maximum grain size of 82 ± 1.0 nm and 98.0 ± 1.5 nm has been found for 0 W Ni and 50 W Ni samples respectively. However, it was hard to identify the size of grains in Ni_3Al film enriched with 100 W Ni.

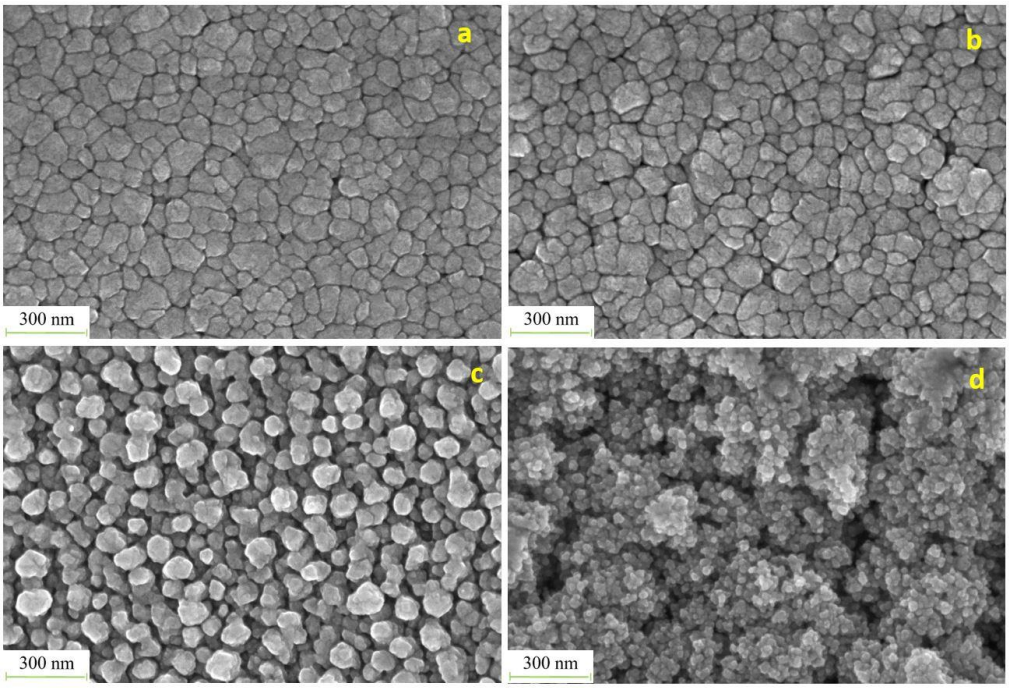

Figure 4.4: Microstructure of Ni_3Al and Ni-rich Ni_3Al films **(a)** 0 W Ni **(b)** 25 W Ni **(c)** 50 W Ni **(d)** 100 W Ni

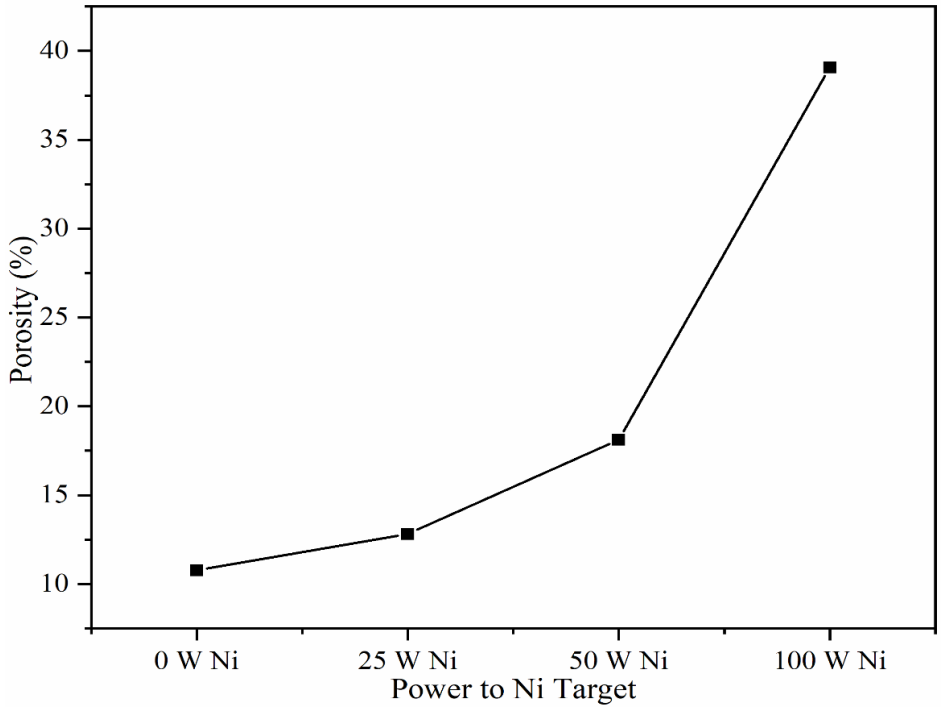

Figure 4.5: Evolution of porosity with respect to sputtering power to Ni target

The surface topography of the deposited Ni_3Al and Ni-rich Ni_3Al film was characterized and studied using atomic force microscopy (Naio AFM, Nanosurf, Switzerland) in the scanned area of 5 x 5 μm^2. However, to calculate the surface roughness of the films, an area of 50 x 50 μm^2 was scanned at ten different places of the coatings. **Figure 4.6** and **figure 4.7** show the 2D and 3D AFM images of the surfaces of deposited films respectively.

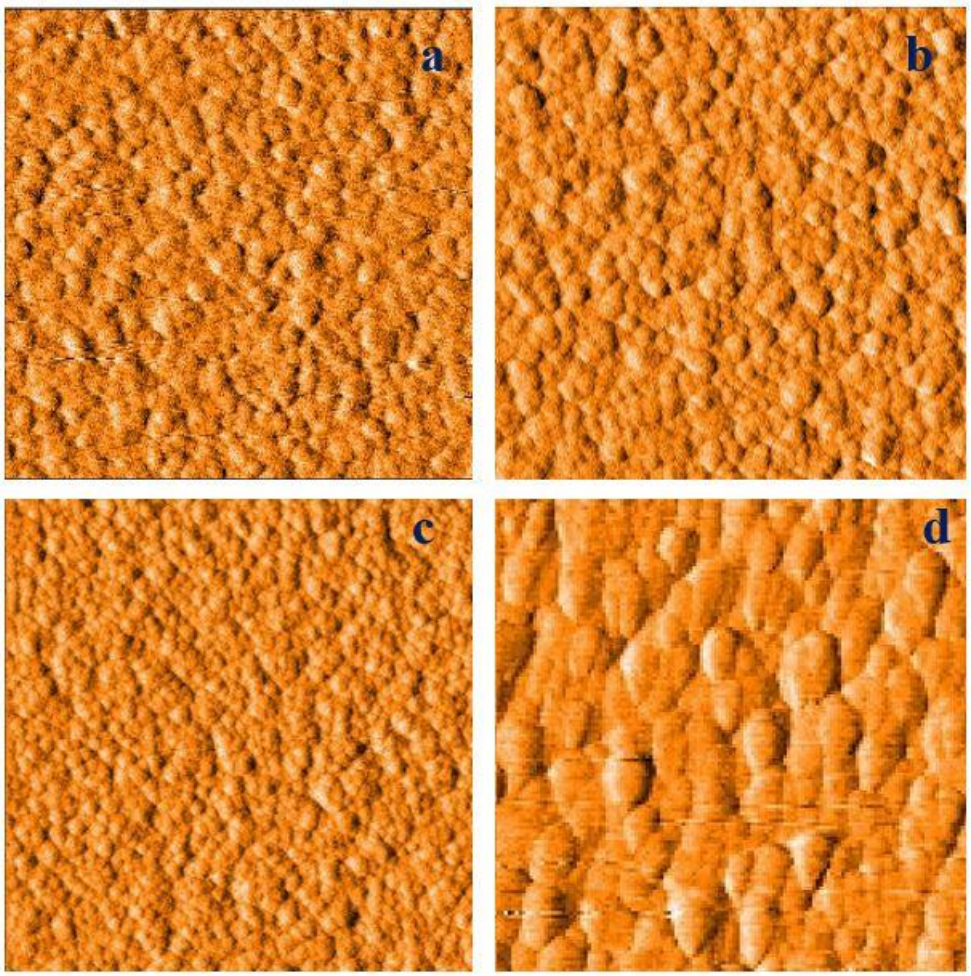

Figure 4.6: 2D AFM images of Ni_3Al and Ni-rich Ni_3Al films **(a)** 0 W Ni **(b)** 25 W Ni **(c)** 50 W Ni **(d)** 100 W Ni

The 2D image of 0 W Ni and 25 W Ni shows almost a similar kind of globular and spheroidal structure. These structures became smaller in size when enriched with 50 W Ni representing a larger number of inhomogeneous spheroidal structures. However, the evolution of oval shaped patches and structures of even larger size are observed when the Ni_3Al matrix is enriched with 100 W Ni. From the figure, it can be observed that the coating

synthesized with 0 W Ni, 25 W Ni and 50 W Ni possess dome-like hilly structural asperities with almost smooth and similar surfaces. The film with 100 W Ni enrichment showed asperities of larger sizes. This could be the result of the presence of the Ni_5Al phase whose crystallite size influences the grain growth of Ni_3Al resulting in the generation of higher percentage of pores. Therefore, the surface roughness of the Ni_3Al films enriched with 100 W Ni changes and degraded abruptly after 50 W of DC power supply to the Ni target.

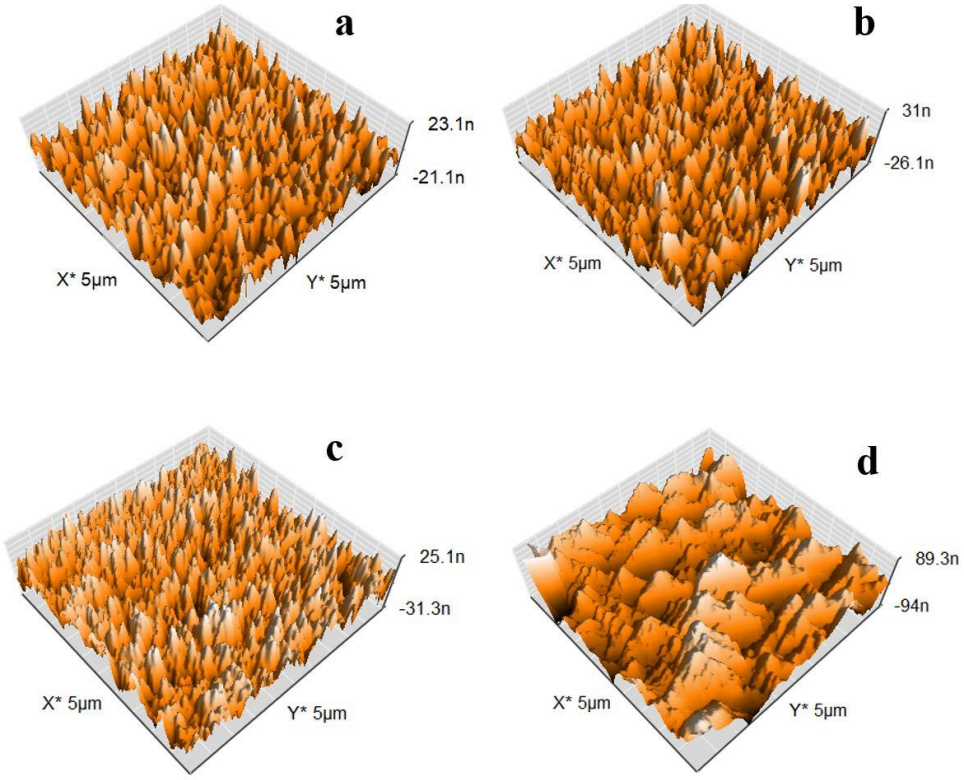

Figure 4.7: 3D AFM images of Ni_3Al and Ni-rich Ni_3Al films **(a)** 0 W Ni **(b)** 25 W Ni **(c)** 50 W Ni **(d)** 100 W Ni

The hydrophobic property of Ni_3Al and Ni-rich Ni_3Al films has been studied and evaluated in terms of contact angle measurements. **Figure 4.8** shows the results of water contact angles for all the deposited Ni_3Al and Ni-rich Ni_3Al films. From the figure, it is observed that the pure Ni_3Al film showed a contact angle of 75° which further increased with increase in the concentration of Ni in Ni_3Al films. The maximum contact angle of ~107° is observed in the case when Ni_3Al is enriched with 50 W Ni which decreases to ~43° when enriched with 100 W Ni. It is reported that wettability is inversely

proportional to the hydrophobic properties [204], thus we can say that the Ni_3Al film with 25 W and 50 W Ni are hydrophobic whereas the film with 100 W Ni is hydrophilic in nature. Moreover, the surface roughness of the film is the influencing factor that alter the wettability of the film. In our case it is observed that the hydrophobic property of the coating increases with increase in homogeneous surface roughness of the film up to 50 W Ni enrichment. This could be the result of trapping of air inside the asperities of the surfaces up to 50 W Ni which reduces the surface interaction of water with the deposited surfaces resulting in water spheroidization leading to increase in contact angles and thus hydrophobic properties. However, with increase in higher surface roughness of film with 100 W Ni, the contact angle decreases abruptly. In the case of Ni_3Al with 100 W Ni, the size of asperities is larger as compared to other surfaces which allows the water droplets to move inside resulting in increasing the surface interaction of water and deposited surface that leads to decrease in contact angles. Moreover, it has been reported that the presence of Ni_5Al and Ni phases in host Ni_3Al matrix lower the contact angles of the Ni_3Al film which is observed in 100 W Ni sample **(figure 4.1)**.

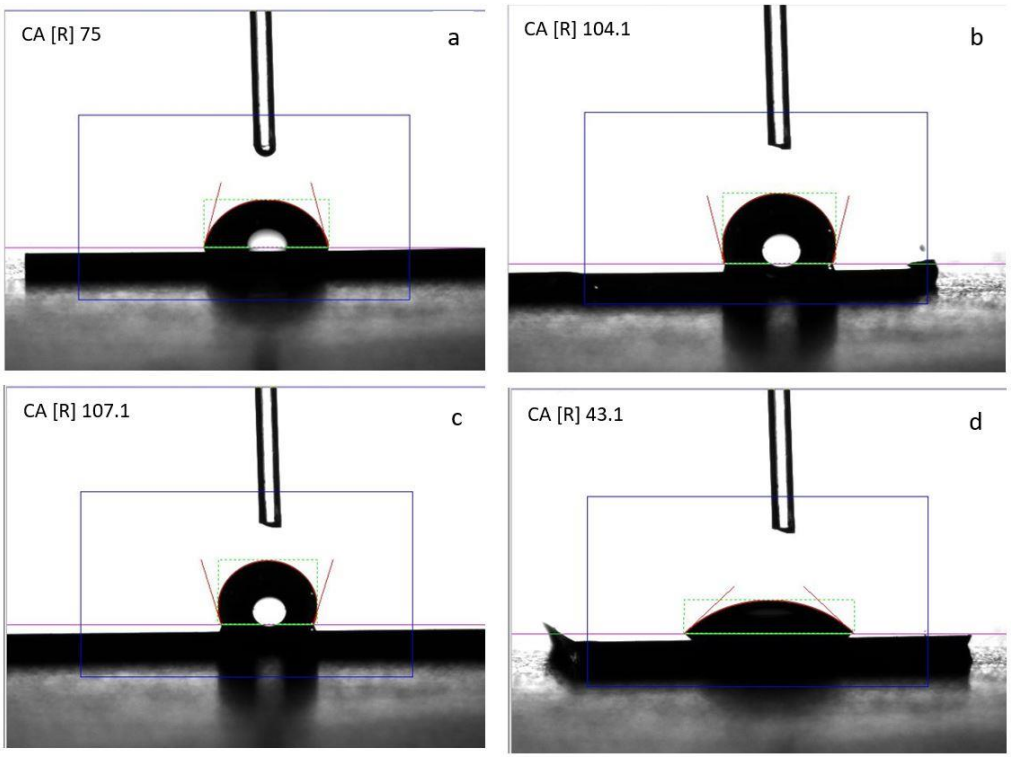

Figure 4.8: Contact angle between water droplet and Ni_3Al surface **(a)** 0 W Ni **(b)** 25 W Ni **(c)** 50 W Ni **(d)** 100 W Ni

To investigate the mechanical properties of Ni_3Al and Ni-rich Ni_3Al films, a load control nanoindentation (XP, Agilent, USA; at CSIR NML, India) was performed on Silicon substrates. An average recorded load of 9.5 mN was applied to penetrate the Berkovich tip up not beyond $1/10^{th}$ of the total film thickness to eliminate the so-called substrate effect on mechanical properties. The test was performed in open air at ambient temperature. The load versus displacement data as a result of indentation inside the deposited film has been plotted in **figure 4.9.** From the figure it can be observed that at an average load of 9.5 mN, the displacement as a result of penetration increases with increase in Ni concentration in the alloy film. Moreover, it can be observed that the Ni_3Al and Ni-rich Ni_3Al films showed both plastic and elastic deformation while loading whereas only elastic deformation is observed during unloading. This clearly evident that the Ni_3Al films enriched with Ni get softened resulting in decrease in hardness as shown in **figure 4.10**. The maximum displacement in terms of plasticity is observed in Ni_3Al film enriched with 100 W Ni resulting in the degradation of modulus and hardness values.

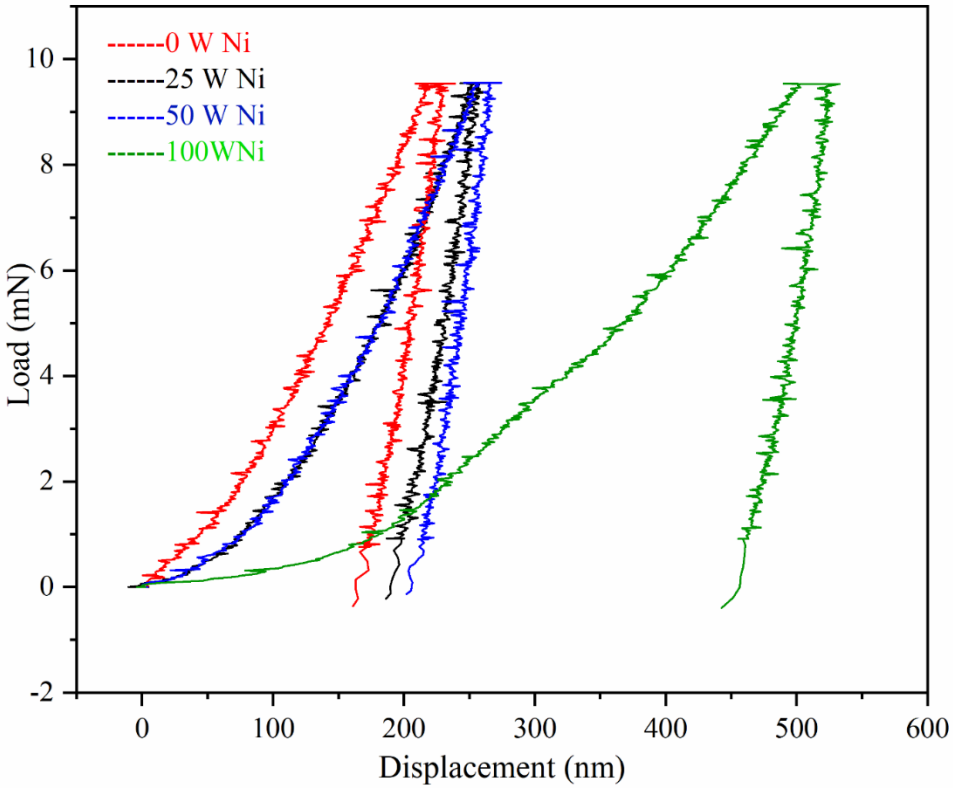

Figure 4.9: Load versus displacement curve of Ni_3Al and Ni-rich Ni_3Al films

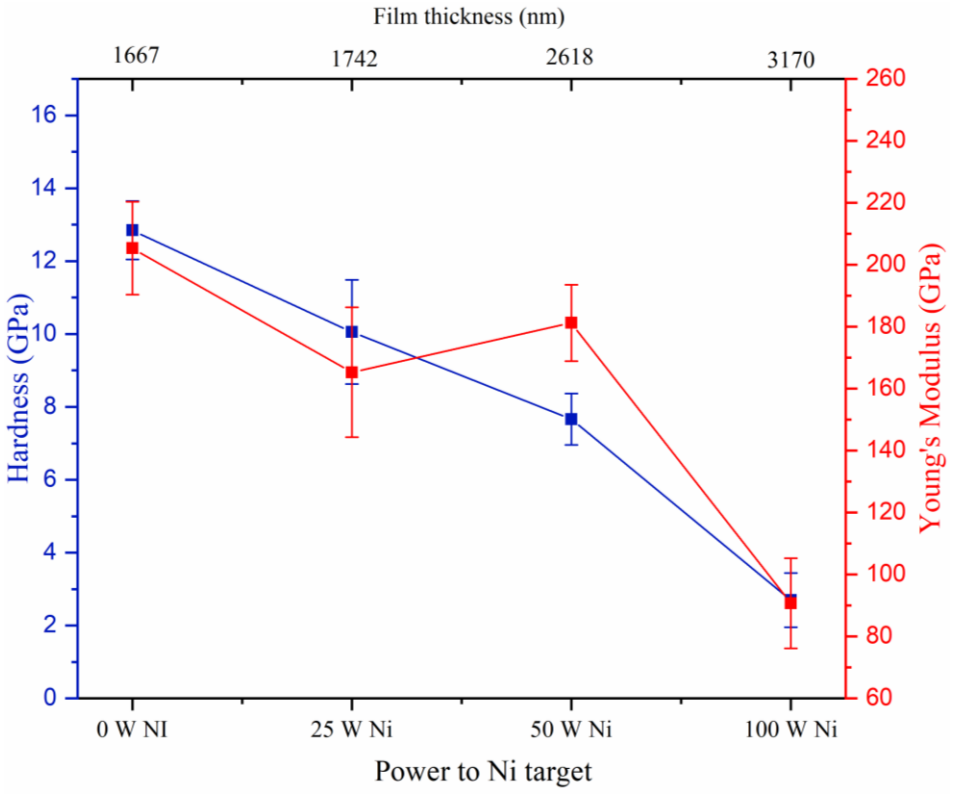

Figure 4.10: Evolution of hardness and Young's modulus of Ni_3Al and Ni-rich Ni_3Al films

It has been reported in the literature that there are several factors along with chemical composition that influence the mechanical and tribological properties of Ni_3Al-based thin films. Several researchers have fabricated Ni_3Al and Ni-rich Ni_3Al films in multi-layer and alloy forms and have found that the phases formed, number of layers deposited, post deposition heat treatments as well as the depth of indentation affects the modulus and hardness of the coating [205]. In our case, it is observed that the grain size (calculated from FE-SEM images using Image J software) of Ni-rich Ni_3Al film increases with increase in Ni concentration in the host Ni_3Al film resulting in the evolution of pores due to the agglomeration of grains which contributed to the overall degradation of modulus and hardness of the coating. Moreover, Nickel is ductile in nature and its grains and grain boundaries are weaker and softer as compared to pure Ni_3Al films. This led to the film softening due to increase in Ni concentration resulting in decrement in modulus and hardness of Ni_3Al films. The maximum value of hardness and Young's modulus of 12.8 ± 0.8 GPa and 205.3 ± 17

GPa respectively have been observed for pure Ni_3Al film i.e., 0 W Ni while the minimum hardness and Young's modulus of 2.6 ± 0.75 GPa and 90.70 ± 14.55 GPa respectively has been observed for the Ni rich Ni_3Al film with 100 W Ni.

4.1.4 CONCLUSION

Ni_3Al and Ni-rich Ni_3Al films have been synthesized on Si substrates at substrate temperature of 400℃ using DC magnetron sputtering and co-sputtering respectively. XRD spectra of the films showed that the film has a preferred orientation of Ni_3Al (111) up to 50 W Ni enrichment. Moreover, the evolution of the Ni_5Al phase has been observed at 62° when the pure Ni_3Al film was enriched with Ni concentration. The rise in sputtering power to the Ni cathode target resulted in increasing the concentration of Ni and the thickness of Ni_3Al films. It also contributed towards decreasing the subsequent crystallite size which resulted in the evolution of pores in 100 W Ni sample. The measurements of water contact angles revealed that the hydrophobic properties of the films increase with Ni enrichment up to 50 W Ni. Further enrichment of Ni concentration in the film (at 100 W Ni) resulted in a sudden fall in contact angles. This is because of the evolution of Ni and Ni_5Al phased along with the generation of larger percentage of pores. The highest values of hardness and Young's modulus of 12.8 ± 0.8 GPa and 205.3 ± 17 GPa respectively have been calculated for pure Ni_3Al films with elemental composition of 79.2 at% Ni and 20.8 at% Al. The values of hardness and Young's modulus decreases with increase in Ni content in Ni_3Al films. The least values of hardness and Young's modulus of 2.6 ± 0.75 GPa and 90.70 ± 14.55 GPa respectively has been observed for the film enriched with 100 W Ni enrichment.

CHAPTER 5

SYNTHESIS AND CHARACTERIZATION OF DC-CO-SPUTTERED DOPED Ni_3Al FILMS

5.1 DC MAGNETRON CO-SPUTTERED Cr- Ni_3Al FILMS

In this section, the evolution of phases, microstructure and mechanical properties of Cr-Ni_3Al alloy films have been discussed. Cr-Ni_3Al alloy films were deposited on Silicon substrates using DC sputtering and co-sputtering processes. The films were deposited at a substrate temperature of 400℃. The effect of varying the DC power to the Cr target on the concentration and properties of the films has been investigated and discussed. The evolution of phases, microstructure, surface topography, mechanical properties and hydrophobic properties have been investigated using XRD, FESEM, AFM, nanoindentation and drop shape analyzer respectively.

5.1.1 INTRODUCTION

Over the past two decades, transition metal-based thin films have been synthesized and characterized by several research groups for high-temperature applications [206], [207]. These coatings have shown excellent mechanical and tribological properties at ambient and elevated temperatures [208]–[210]. Moreover, some of the transition metal nitride coatings like CrN, TiN, WN, etc. and Ni and Ti-based coatings have shown enhanced properties in terms of corrosion and oxidation resistance along with microstructural stability [21], [211], [212]. Looking into the demand for high-temperature structural applications, researchers have fabricated, Nickel and Nickel superalloy-based coating because of their high thermal stability [22], [93]. In the last decade, the demand for enhanced surface properties and strength like hardness and wear resistance in semiconductor, microelectronics and machining industries spurred the advancement in the coatings with enhanced mechanical and tribological properties along with high-temperature stability [86]. In particular, Ni_3Al-based intermetallic compound coatings with excellent properties like, creep and fatigue resistance, thermal stability, high stiffness and high melting point make them a potential candidate for high-temperature applications like gas turbine blades, jet engines, aerospace and nuclear industries [101], [200], [213]–[216]. Moreover, doping of transition metals like W, Cr, Pd, and B in Ni_3Al films in alloy or multilayer forms also alter their properties and mechanical behavior at ambient and high temperature [89], [217], [218].

Alloying Ni_3Al intermetallic with Fe has increased mechanical properties whereas it has resulted in improving high-temperature strength when doped with zirconium (Zr) because of solid solution hardening [219]. It has been reported that Boron doped in Ni_3Al films, extensively occupies the Al sites, or the element which is a substitute for both Al and Ni is ductilized by Boron resulting in increasing the overall ductility of the film [220]. While synthesizing Ni_3Al-based coatings, phase formation and microstructure have a great impact on mechanical and tribological properties. It has been reported that with an increase in crystallite size, the hardness generally decreases and vice versa following the Hall-Petch but in some cases, inverse Hall-Petch results have been observed [89], [103], [184]. In literature, it has been found that, despite increasing the crystallite and grain size of the film, mechanical and tribological properties have increased. This has been perceived because of the formation of ordered $L1_2$ preferred orientation of Ni_3Al films which contributes to increasing the hardness of the film [86], [97]. There are several factors affecting the properties and microstructure of Ni_3Al films while depositing via magnetron sputtering. Sputtering process parameters like sputtering pressure and substrate temperature influence grain growth, refinement and rearrangement which results in altering the properties of the film. Moreover, post-deposition heat treatment also contributes to varying the properties of the Ni_3Al films. Swygenhoven *et al.,* [92] deposited Ni_3Al alloy and Ni/Ni_3Al multilayer films on Si substrate via DC magnetron sputtering. They found that the alloy films exhibited a maximum hardness of ~13 GPa whereas the Ni/Ni_3Al with an individual layer thickness of 5 nm and 2.5 nm exhibited a hardness of ~ 12 GPa and 11.8 GPa respectively. Ng *et al.,* [93] deposited Ni_3Al films onto the Ni substrate using the multi-target system by putting the Ni and Al sheets glued together on a thin circular metal sheet and with casted alloy Ni_3Al targets also via sputtering. The results of microhardness revealed that the as-deposited film and the film annealed at 300℃ showed almost the same hardness whereas the maximum hardness was shown by the film annealed at 700℃. They also found a continuous fall in hardness as a result of an increase in indentation depth. Xing *et al.,* [86] in their research to synthesize Ni_3Al and Ni_3Al/Cr multilayer films found that the

hardness of Ni_3Al/Cr decreased as compared to single-layered Ni_3Al films whereas Young's modulus increased. They also found that both the Single-layered and multilayered films were able to prevent the substrate from being drastically oxidized at an elevated temperature of 900℃ whereas the toughness of multilayer films was increased. Zhang *et al.,* [89] found that the hardness of Ni_3Al films doped with ultra-thin Cr layers in multilayer form increased with an increase in Cr content and annealing temperature. In their further research while synthesizing Ni/Ni_3Al multilayer films, with different individual layer thicknesses of Ni and Ni_3Al (layer thickness h<100 and h=160) they found that the Ni/Ni_3Al film showed the preferred orientation of (111) texture. It is seen that with decreasing individual layer thickness, there appears a peak broadening in the XRD spectrum reflecting a decrease in the crystallite size of the film. Results of nanoindentation showed that the hardness of the annealed films was low as compared to as-deposited Ni/Ni_3Al films which further decreased with an increase in the individual layer thickness of Ni and Ni_3Al [103]. In our previous research **(Chapter 4)**, alloy Ni_3Al coatings were synthesized on Si substrate via DC magnetron sputtering [100] where the hardness of ~13 GPa was achieved. Enriching the film further with Ni via Co-sputtering process, it was observed that the modulus and hardness of the film decreased simultaneously with the evolution of cracks and pores. Several research groups have studied the properties and behavior of Ni_3Al-based films at ambient and high temperatures. However, very limited research is available in the literature related to alloy deposition particularly using dopants in alloy form. The present work reports the effect of Cr enrichment in Ni_3Al films in alloy form on its microstructural and mechanical properties for their application in microelectronic devices, molding industries and aerospace industries.

5.1.2 EXPERIMENTAL DETAILS

5.1.2.1 Synthesis of Cr-Ni_3Al films

Cr-Ni_3Al alloy films were deposited on Si (100) substrates via co-sputtering at a substrate temperature of 400 ℃ in a custom-designed vacuum chamber. Alloy target of Ni_3Al (2-inch diameter and 5 mm thickness; 99.99% purity)

and Cr target (2-inch diameter and 5 mm thickness; 99.99% purity) was placed in DC-powered sputtering guns placed at 120° apart from each other. Si substrates were cleaned with acetone and then dried in the air before clamping to the substrate holder. The substrate holder was rotated at a speed of 15 rpm to ensure the homogeneous deposition of the film over the substrates. The sputtering chamber was evacuated at a base pressure of 3×10^{-6} while the substrates were kept at a temperature of 400 ℃. Argon (99.999% purity) as a processed gas (30 sccm) was inserted in the chamber and the pressure during sputter deposition was kept constant at 3×10^{-2} mbar. DC power of 250 W was supplied to the Ni_3Al target to deposit Ni_3Al film (namely 0 W Cr). To vary the concentration of Cr in Ni_3Al films, the power supply to Cr target was varied from 10 W to 40 W in steps of 10 W to deposit Cr-Ni_3Al alloy films namely 10 W Cr; 20 W Cr; 30 W Cr and 40 W Cr. Prior to deposition, pre-sputtering of 5 minutes was done on both the targets to remove the impurity from the surface of the targets whereas the actual sputtering was done for a duration of one hour. Other than the DC power to the Cr target, all the sputtering parameters were kept constant for all depositions. The sputtering parameters for synthesizing the Cr-Ni_3Al films have been shown in **table 5.1.**

Table 5.1: Sputtering parameters for depositing Cr-Ni_3Al films with variation in Cr content

Targets	Cr & Ni_3Al
Substrates	Silicon (100)
Base pressure	3×10^{-6} mbar
Sputtering gas	Argon (30 sccm)
Sputtering pressure	3×10^{-2} mbar
Sputtering power (Ni_3Al)	250 W DC
Sputtering power (Cr)	**0 W, 10 W, 20 W, 30 W & 40 W DC**
Substrate temperature	400℃
Deposition time	60 minutes

5.1.2.2 Characterization details

Grazing angle X-ray diffraction (Empyrean Panalytical), was used to detect the phases of Ni_3Al-based films using CuKα = 1.54Å at ambient temperature. The microstructure and surface topography of the films were characterized by FE-SEM (Zeiss Gemini) and atomic force microscopy (NaioAFM, Nanosurf, Switzerland). The elemental composition of Cr in Ni_3Al films was characterized using Energy dispersive spectroscopy equipped with FE-SEM. In order to measure the contact angle to study the hydrophobic properties of the films, a drop shape analysis experiment (DSA 100, Krüss GmbH, Germany) was performed in the similar way as explained in **section 3.1.2.2**. Quasi-static nanoindentation (nano DMA, Hysitron Inc Minneapolis USA, TI-900) was performed to investigate the hardness and Young's modulus of Ni_3Al and Cr-Ni_3Al coatings. The depth control nanoindentation test was performed at ambient temperature with a strain rate of 0.05^{-1} calibrated at a poison ratio of 0.25. The average depth of penetration during the nanoindentation test was 100 nm and kept constant throughout the set of experiments. The mechanical property in terms of modulus and hardness was calculated using Oliver and Pharr's technique by the inbuilt software in the nanoindentation setup. A total of 20 indents were made using a Berkovich diamond tip to calculate the average value of modulus and hardness.

5.1.3 RESULT AND DISCUSSION

XRD patterns of Cr-Ni_3Al alloy coatings with different concentrations of Cr in alloy form are shown in **figure 5.1**. It can be seen that the Ni_3Al film (0 W Cr) displays a preferred (111) orientation at 44.13° followed by low-intensity diffraction peaks of (200) and (220) planes at 51.3° and 75.2° of face-centered cubic structure respectively. These diffraction peaks are also in accord with the standard intermetallic $L1_2$ diffraction peaks of Ni_3Al. XRD patterns of Cr-Ni_3Al films do not display any evidential diffraction peaks of Cr. This may be attributed to the substitution of Ni by Cr atoms from the host Ni_3Al lattice structure which causes the strain to induce in the film [86], [220]. When Cr replaces Ni atoms of the host Ni_3Al lattice structure, it gives rise to the tensile residual stress. The value of strain in Ni_3Al and Cr-Ni_3Al calculated from the

prominent peak of XRD spectra using equation 5.1 [221] is shown in **table 5.2**.

$$\epsilon = \beta/4tan\Theta \qquad \textit{Equation 5.1}$$

Where ϵ is microstrain, β is FWHM, Θ is Bragg's angle

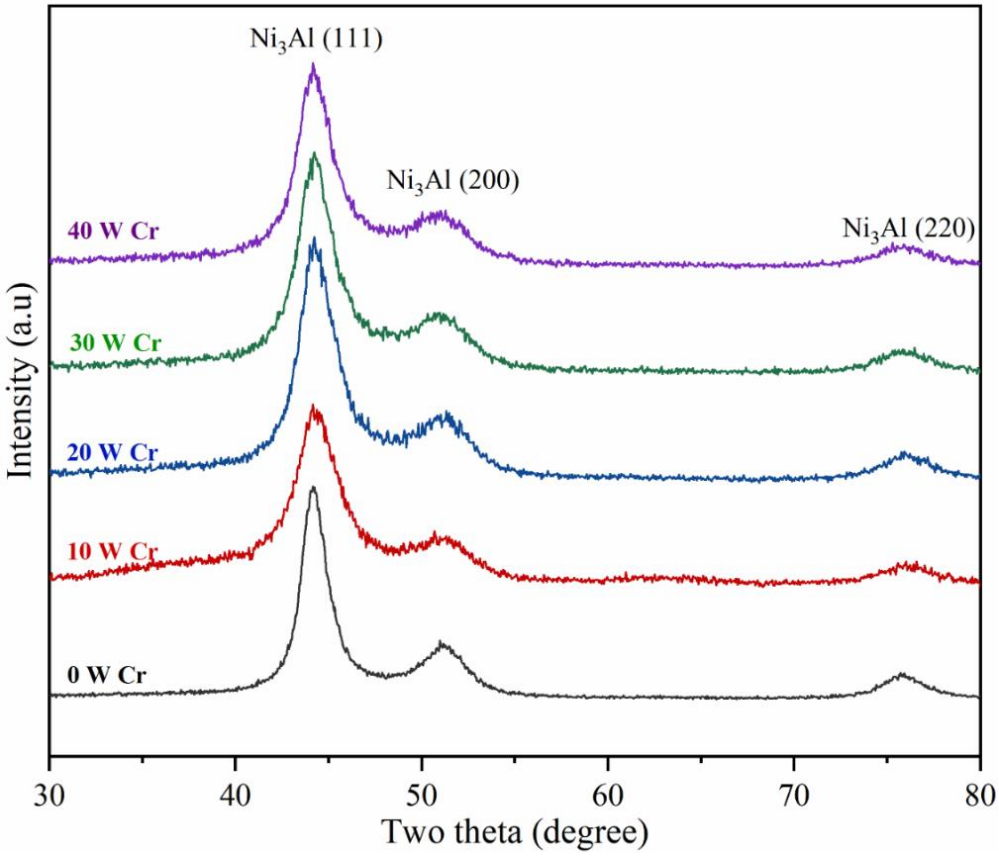

Figure 5.1: XRD spectra of Ni_3Al and Cr-Ni_3Al alloy films

Table 5.2: Calculated parameters of Cr-Ni_3Al coatings as a function of Cr enrichment

SN	Sample	Cr (at%)	Crystallite Size (nm)	Grain size (nm)	Surface roughness (nm)	Contact angle (degree)	Porosity (%)	Strain
1.	0 W Cr	0.00	19.3 ± 0.5	91 ± 2.5	7.5 ± 0.23	75.5 ± 1.0	10.34	0.0195
2.	10 W Cr	1.07	18.2 ± 0.5	110 ± 2.5	9.4 ± 0.27	98.4 ± 1.0	11.50	0.0213
3.	20 W Cr	2.25	17.9 ± 0.5	139 ± 4.0	11.9 ± 0.42	111.9 ± 1.0	11.69	0.0229
4.	30 W Cr	5.71	17.8 ± 0.5	166 ± 5.0	12.6 ± 0.63	112.5 ± 1.0	12.52	0.0244
5.	40 W Cr	7.34	17.2 ± 0.5	195 ± 5.0	14.8 ± 0.71	115.9 ± 1.5	14.05	0.0269

The microstructure of Cr-Ni_3Al is characterized using FESEM as shown in **figure 5.2**. From the figure it can be seen that 0 W Cr-Ni_3Al film exhibits fine, equisized and densely packed consolidated grains reflecting smooth and homogeneous microstructure while in 10 W Cr-Ni_3Al film, there is the evolution of coarser grains and pores resulting in inhomogeneous microstructure. A simultaneous increase in porosity is observed with a further increase in the Cr content (up to 40 W Cr) in the host Ni_3Al film. This could be the result of the agglomeration of crystallites resulting in grain growth which later contributes to deteriorating the arrangements of grains and grain boundaries.

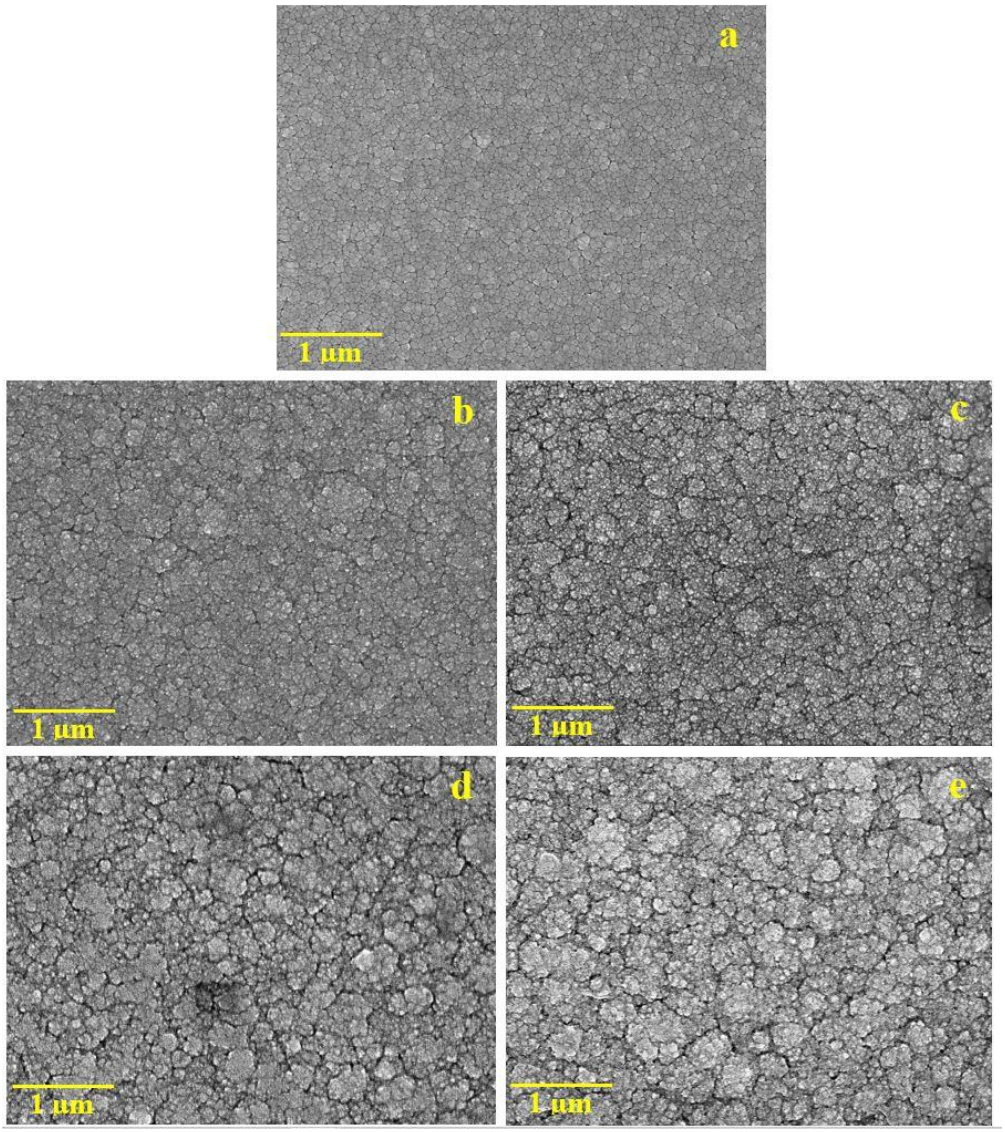

Figure 5.2: FESEM images of Cr-Ni_3Al films **(a)** 0 W Cr **(b)** 10 W Cr **(c)** 20 W Cr **(d)** 30 W Cr **(e)** 40 W Cr

Image j software is used to calculate the percentage of porosity in the film using the SEM images of the Cr-Ni_3Al films [222]. Results revealed that 0 W Cr-Ni_3Al films exhibited minimum percentage of pores (10.3%) whereas 40 W Cr-Ni_3Al films showed the maximum percentage of pores (14%) in the film as shown in **figure 5.3.**

Furthermore, the grain size of the deposited coatings has also been computed using Image J software. For this purpose, we have used the FE-SEM images. The distribution of grain size in Ni_3Al and Cr-Ni_3Al films has been shown in **figure 5.4.** From the figure it is observed that 10 W Cr-Ni_3Al reflects the homogeneous distribution of smaller grains with an average grain size of 91 ± 2.5 nm. With increase in Cr content in the film, the distribution of grains becomes inhomogeneous as a result of grain coarsening which continues up to 40 W Cr enrichment in the film. The minimum and maximum grain size of 91 ± 2.5 and 195 ± 5.0 nm has been observed for 10 W Cr-Ni_3Al and 40 W Cr-Ni_3Al film respectively [222].

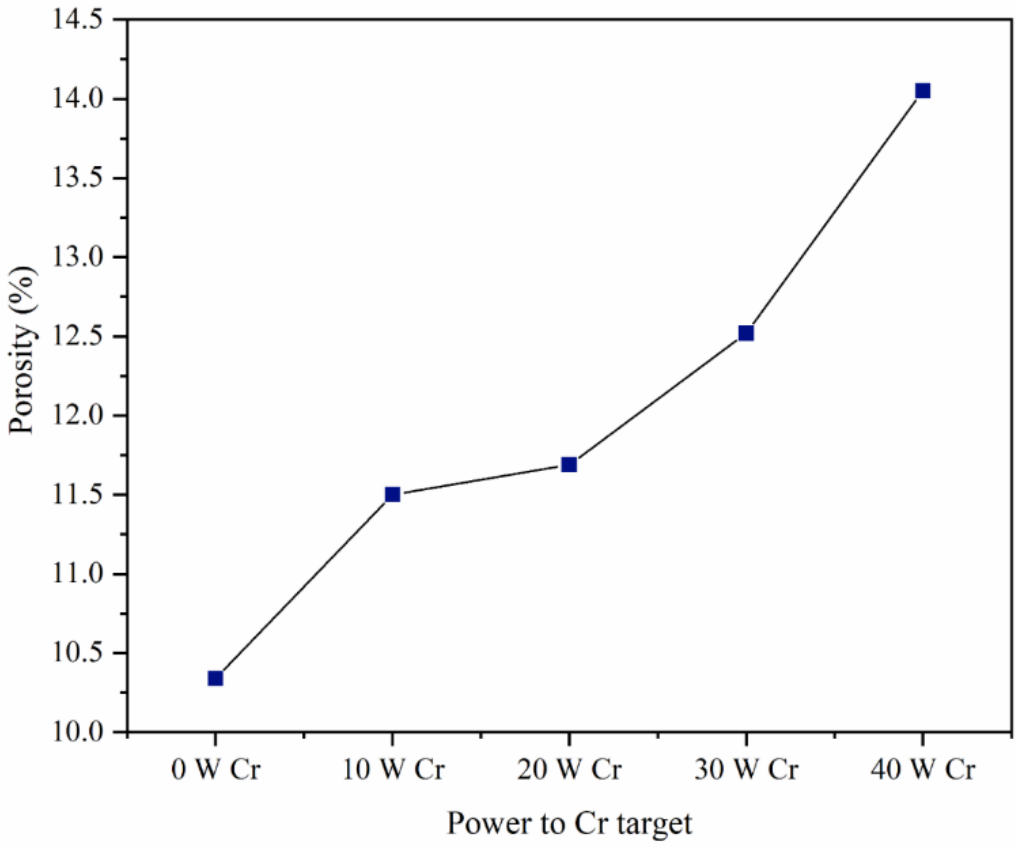

Figure 5.3: Evolution of porosity with respect to sputtering power to Cr target

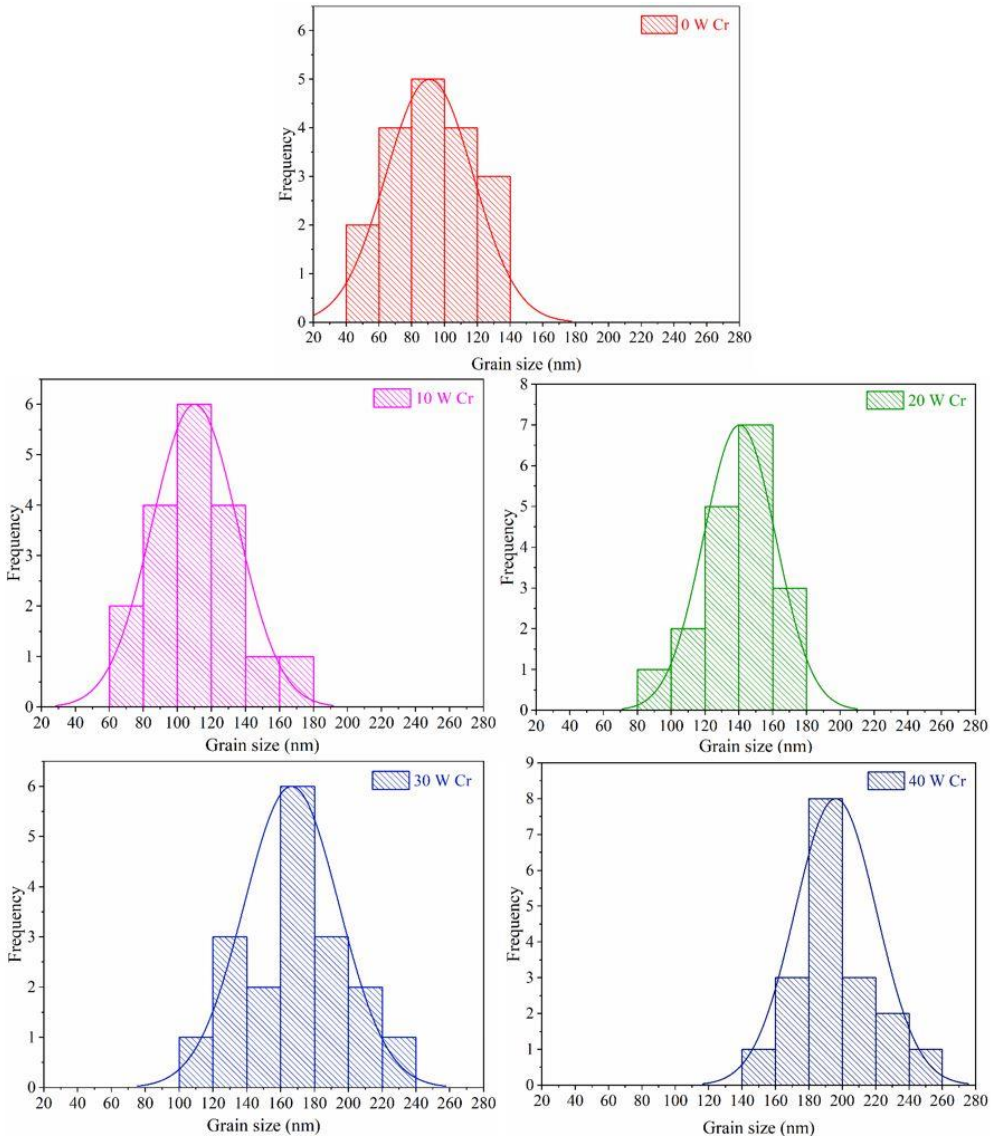

Figure 5.4: Distribution of grains in Cr-Ni_3Al coatings

The surface topography of deposited alloy coatings has been examined and explored using atomic force microscopy. The cantilever probe of AFM scanned an area of 5 x 5 μm^2 to reveal information about the surface asperities of the coatings. However, to calculate the average surface roughness (rms) of the film, the area of 50 x 50 μm^2 was scanned at 10 different spots. **Figure 5.5 and figure 5.6** displays the 2D and 3D AFM images of Cr-Ni_3Al films.

From the **figure 5.5 (a)**, it can be observed that the Ni_3Al film with 0 W Cr exhibits small granular like structure which are closely packed to each other whereas the corresponding 3D image of 0 W Cr shown in **figure 5.6 (a)** reflects a high frequency of fine, thin and sharp hill-type structured nano

asperities. A subsequent and continuous increase in a granular shaped structures in 2D images of AFM is seen because of the increase in Cr concentration in Ni_3Al films **[Figure 5.5, (b), (c), (d)].** The corresponding 3D images of AFM show dome like broad asperities with distorted structures in Cr-Ni_3Al coatings as a result of increase in Cr content **[Figure 5.6, (b), (c), (d)]**. This led to an increase in surface roughness and also an increase in void fraction. The surface roughness (rms) of the deposited films calculated using AFM has been reported in **table 5.2**. The minimum and maximum surface roughness of 7.5 nm and 14.8 nm has been observed for 0 W Cr-Ni_3Al and 40 W Cr-Ni_3Al films respectively.

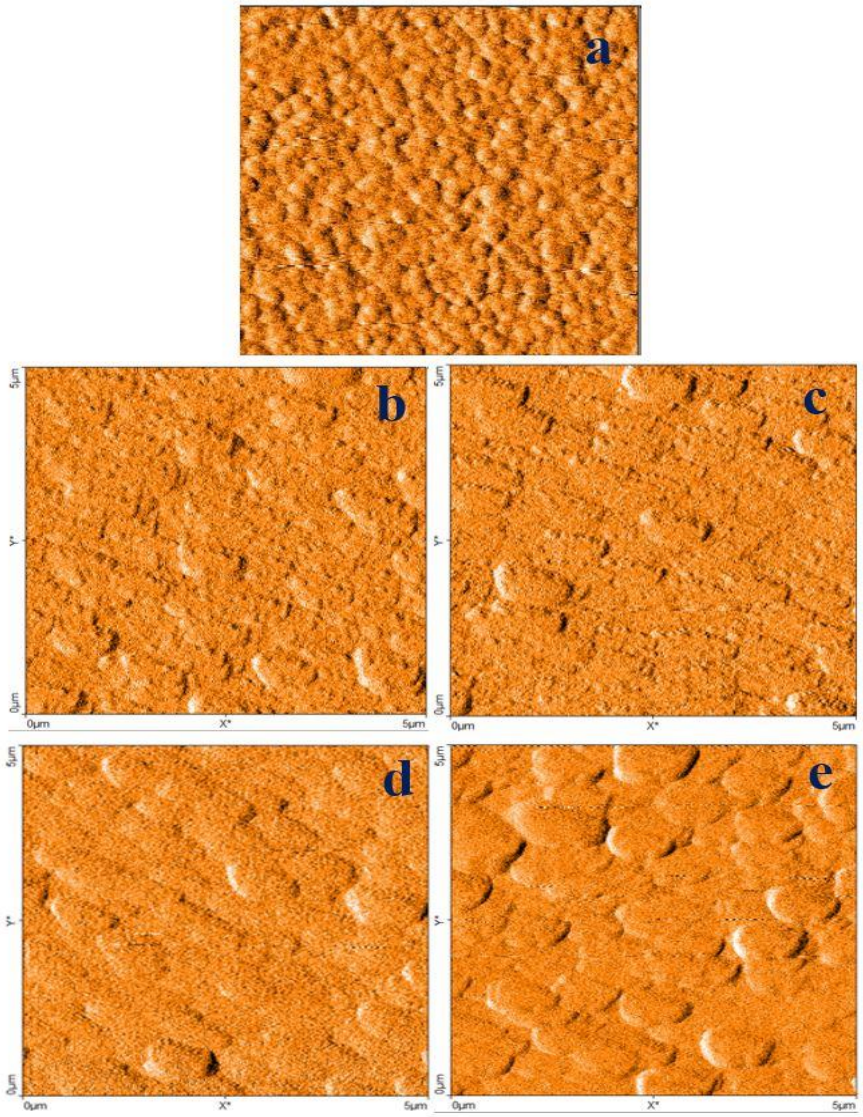

Figure 5.5: 2D AFM images of Cr-Ni_3Al films **(a)** 0 W Cr **(b)** 10 W Cr **(c)** 20 W Cr **(d)** 30 W Cr **(e)** 40 W Cr

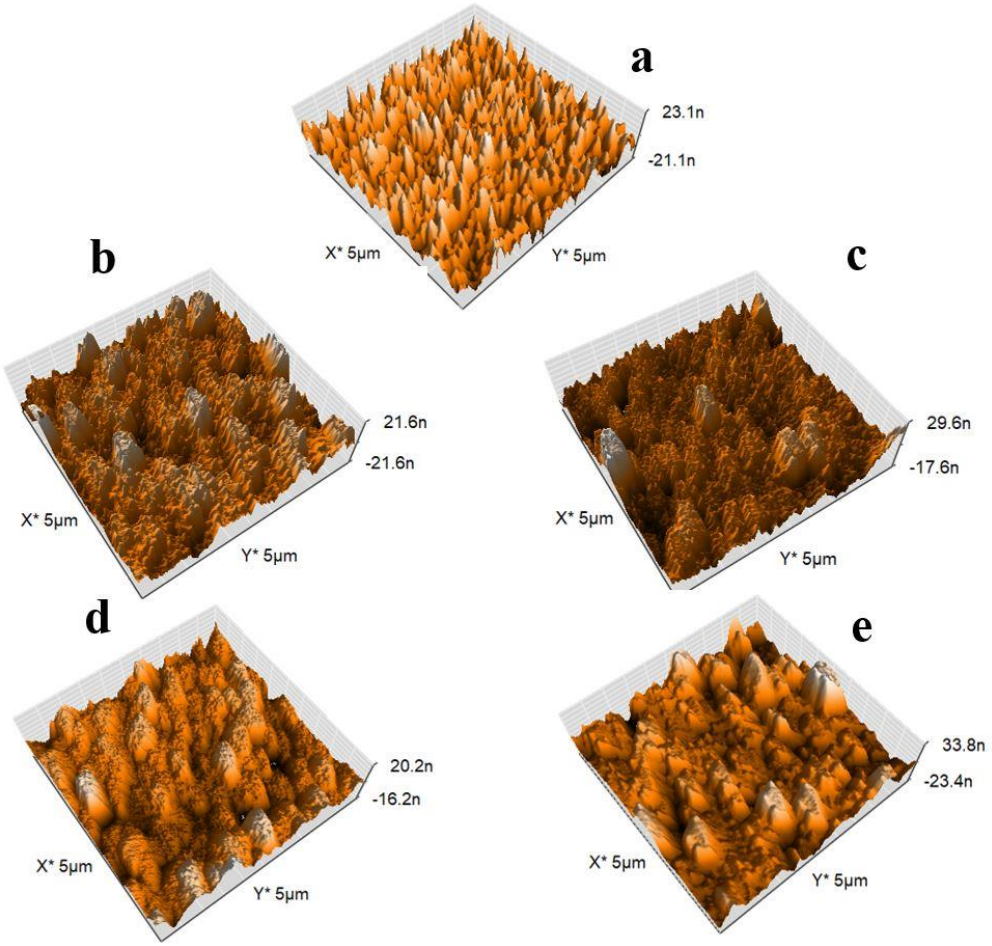

Figure 5.6: 3D AFM images of Cr-Ni_3Al films **(a)** 0 W Cr **(b)** 10 W Cr **(c)** 20 W Cr **(d)** 30 W Cr **(e)** 40 W Cr

Contact angle measurements have been performed and examined on a drop shape analyzer at ambient temperature. In order to study the hydrophobic property of the film, the contact angle has been measured between water droplets and the deposited surface with different concentrations of Cr in steady state as displayed in **figure 5.7.** Results showed that the contact angle improves simultaneously with increase in Cr concentration in Ni_3Al film. This is because of the subsequent rise in the surface roughness of the coating with Cr enrichment as indexed in **table 5.2.** With rise in the surface roughness of the coating, there is increase in void fraction too. These available voids between the nano-asperities of the surface help in trapping air that decreases the surface contact area between water and deposited films and thus increases the hydrophobic property of the film (wettability is decreased)

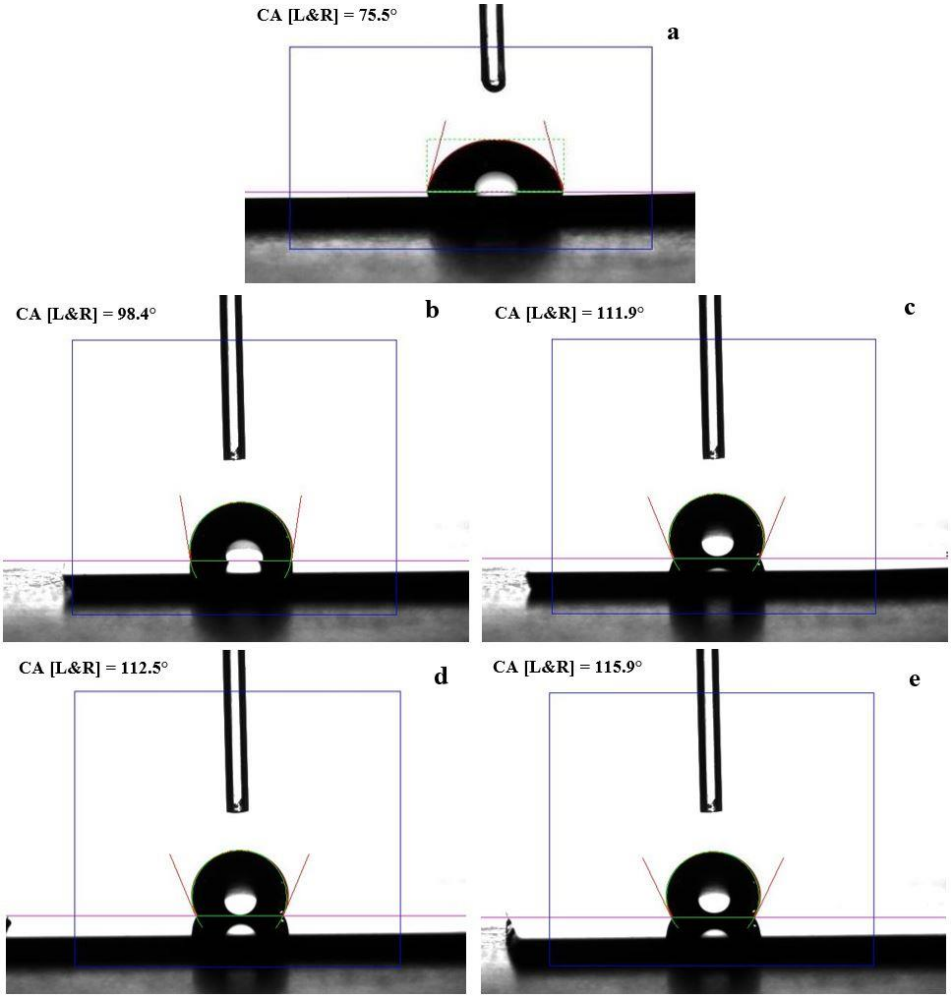

Figure 5.7: Contact angles of Ni_3Al and Cr-Ni_3Al films **(a)** 0 W Cr **(b)** 10 W Cr **(c)** 20 W Cr **(d)** 30 W Cr **(e)** 40 W Cr

It has been reported in the literature that increase in surface roughness increases the hydrophobic property of the film up to a limit [100]. From the results of AFM, it can be seen that there is a sudden increase in surface roughness of 10 W Cr-Ni_3Al films (7.5 nm to 9.4 nm) which lead to a dramatic rise in water contact angle too. However, the marginal difference in surface roughness of 20 W Cr-Ni_3Al and 30 W Cr-Ni_3Al (11.9 nm to 12.6 nm) has reflected a small degree of variation in contact angle. The lowest and highest contact angle of 75.5° and 115.9° has been found for 0 W Cr-Ni_3Al and 40 W Cr-Ni_3Al coatings respectively. Mechanical properties of Cr-Ni_3Al have been investigated in terms of modulus and nano hardness. Depth-control Quasi-static nanoindentation was used to investigate and analyze the results of mechanical properties at ambient temperature. The results of modulus and hardness have been plotted in **figure 5.8.**

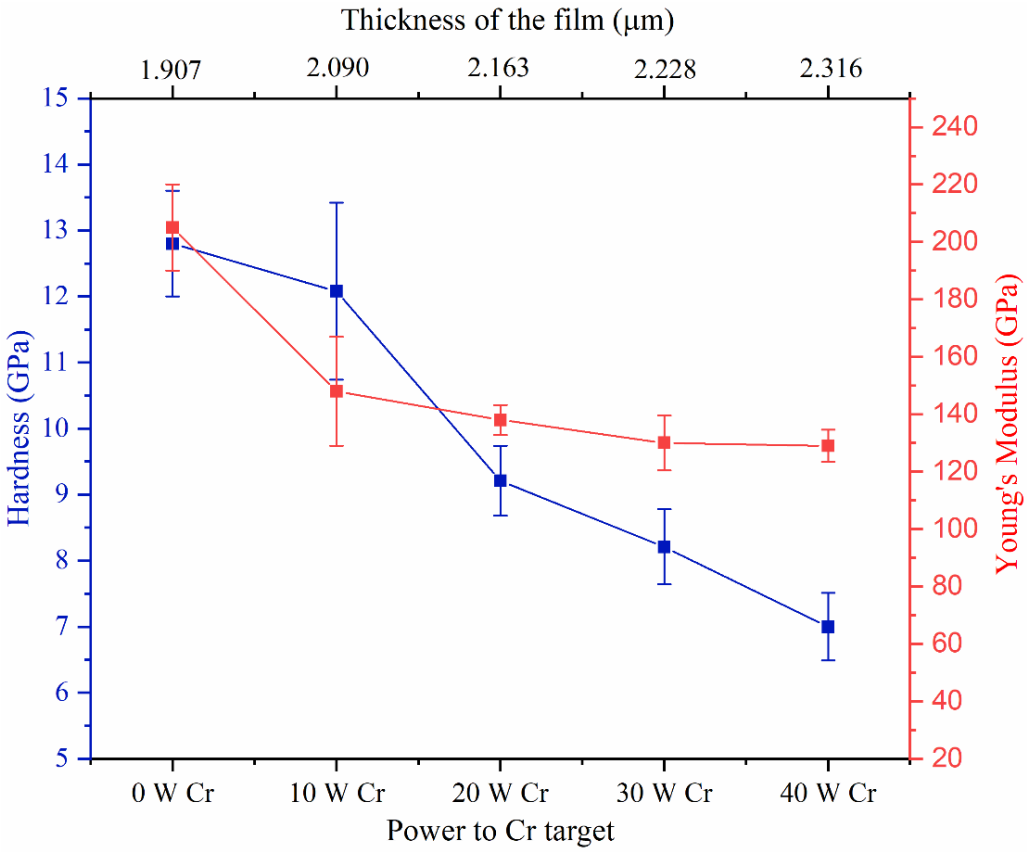

Figure 5.8: Hardness and Young's modulus of Cr-Ni_3Al films as a function of power to Cr target

From the figure, it is found that the hardness of the film decreases with rise in power to Cr target. This is because of the rise in Cr content in host Ni_3Al film which led to an increase in the overall film thickness that further contributes to agglomeration of crystallites resulting in grain size enlargement. Furthermore, the larger grains contribute to the generation of large volume of pores **(table 5.2)** which led to the degradation of the microstructure of the film. **Figure 5.9** shows the summarized result of hardness versus inverse square root of the grain size. From the figure, it can be observed that the hardness of the film is directly proportional to the inverse square root of grain size obeying the classical Hall-Petch relation. This is evident that the hardness of the film declines with enhancement in grain size following the dislocation pileup model [223], [224]. The films with smaller grain sizes consists of large volumes of grain boundaries which resist the dislocation movement across the boundaries and are piled up near the grain boundaries resulting enhancement

in hardness [221], [225]. Moreover, the value of R^2 is very close to 1 (R^2 = 0.974) which suggests that the regression line fits the data well resulting in a high value of H-P coefficient [slope = 184.04615 ± 17.34491 GPa ($nm^{1/2}$)]. It is also reported in literature that the hardness of the film increases with rise in H-P coefficient [80], [224]. In our case, however, the value of the H-P coefficient is higher, but the presence of cracks and pores in the films degrades the microstructure resulting in the evolution of hardness in the range of ~7 GPa to 12.7 GPa.

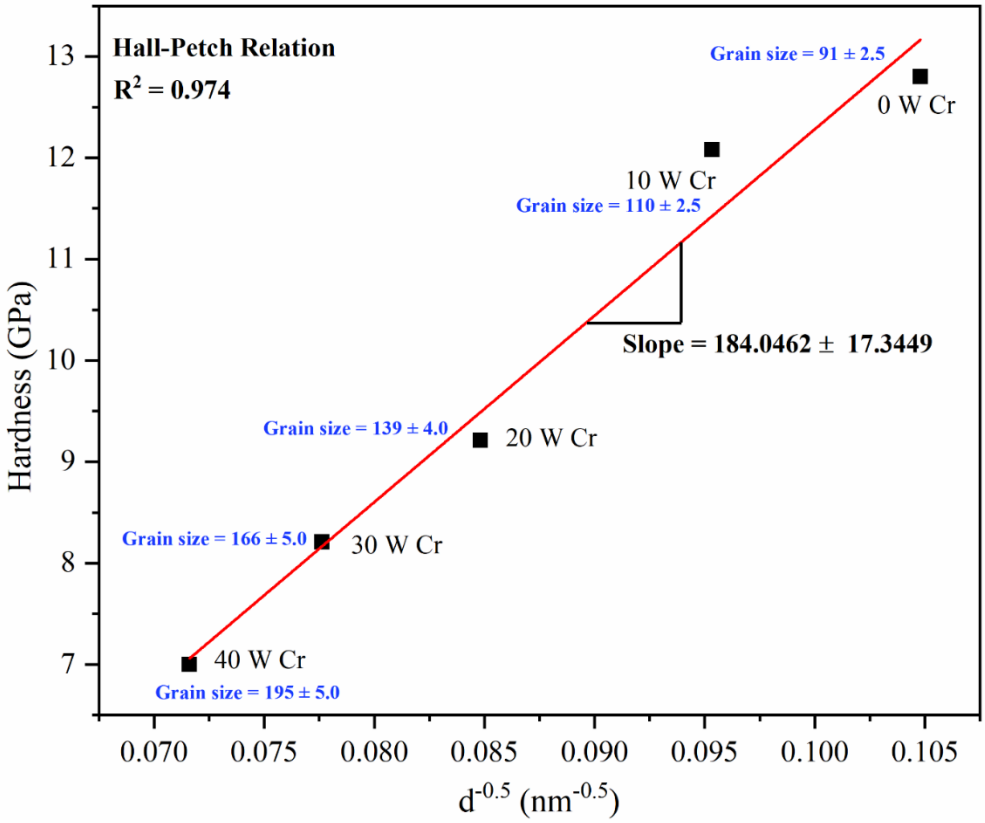

Figure 5.9: Hall-Petch relationship in Ni_3Al and Cr-Ni_3Al films

It has also been reported that the variation in hardness as a function of grain size is compensated by the chemical ordering of FCC Ni_3Al film (formation of thermodynamic equilibrium Ni_3Al $L1_2$ phase) which says that, due to the enhancement in grain size, the hardness of the coating increases if the ordered equilibrium $L1_2$ Ni_3Al phase is formed in nanocrystalline films [97], [103], [226]. In our case, the XRD Spectrum of Ni_3Al film (0 W Cr) showed a prominent peak of Ni_3Al (111) at 44.13° which is also in accord with the standard intermetallic $L1_2$ structure contributing in enhancing the hardness of

the film. However, the existence of the pores in Cr-Ni_3Al films contributes in lowering the hardness of the alloy Cr-Ni_3Al films. The evolution in Young's modulus also shows the same trend as reflected by the nano-hardness curve.

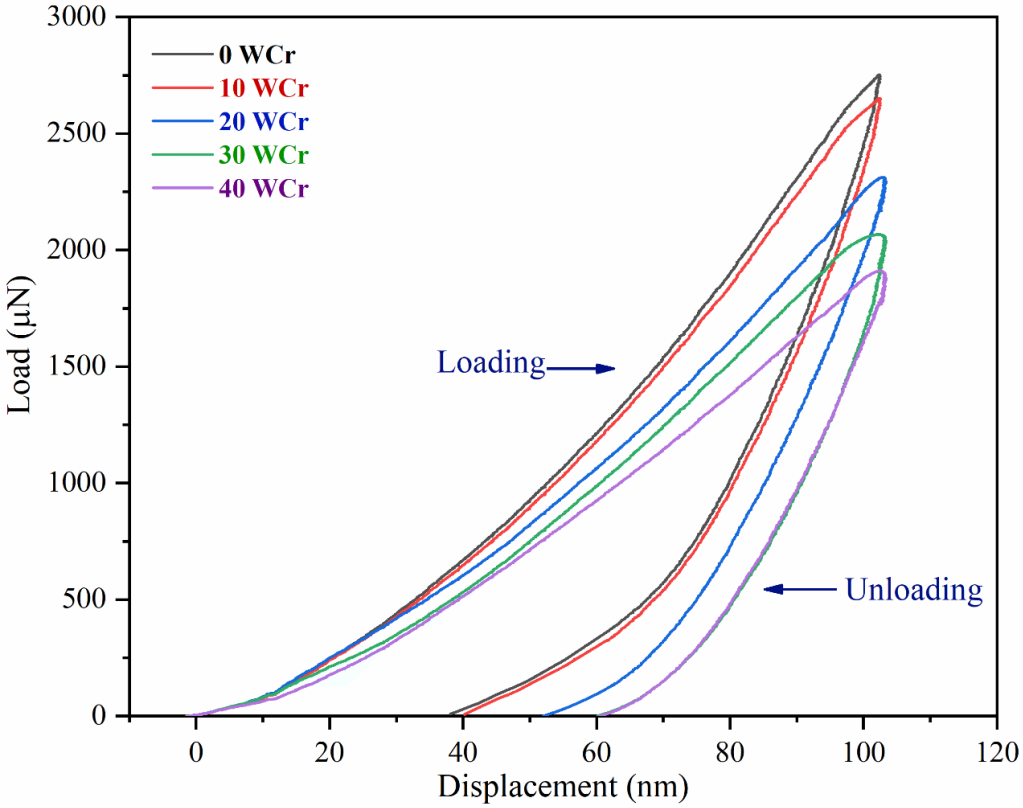

Figure 5.10: Load versus displacement graph of Cr-Ni_3Al films

Figure 5.10 reflects the load versus depth curve as a function of Cr enrichment in Ni_3Al alloy films. A maximum load (P_{max}) of 2.8 mN is recorded during depth control nanoindentations. From the figure it is seen that the synthesized coating showed both elastic and plastic deformation during loading whereas only elastic deformation has been observed during unloading. Moreover, 0 W and 10 W Cr-Ni_3Al samples reflected almost the same permanent deformation depth of ~38 nm and ~40 nm respectively whereas 20 W Cr-Ni_3Al samples showed a permanent deformation depth of ~46 nm. The maximum permanent deformation depth of 60 nm is observed for both 30 W Cr-Ni_3Al and 40 W Cr-Ni_3Al films. This shows that 0 W Cr and 10 W Cr possess a better rate of elastic recovery as compared to 20 W Cr, 30 W Cr and 40 W Cr films.

Xing *et al.,* (2013) [86] also found similar results in terms of a decrease in hardness when they synthesized Cr/Ni_3Al multilayer films. It has been reported that the Ni_3Al films in multilayer forms when enriched with Nickel have reflected a hardness in the range of ~4.5 to 8 GPa [104], [172], [184], [227]. Some studies based on doped Ni_3Al with transition metals in multilayer forms followed by heat treatment have shown an increase in the hardness beyond 8 GPa [89], [97], [103]. In our case, the maximum and minimum hardness of (12.7 ± 0.8 GPa) and (7.0 ± 0.5 GPa) has been observed for 0 W Cr-Ni_3Al and 40 W Cr-Ni_3Al alloy films whereas the maximum and minimum Young's modulus of (203 ± 15 GPa) and (129 ± 5.6 GPa) has been observed for 0 W Cr-Ni_3Al and 40 W Cr-Ni_3Al respectively. The enhanced mechanical properties of deposited Ni_3Al-based coatings make them a suitable candidate for their application in scratch resistant connectors, slider and other components of electronic devices and molding dies.

5.1.4 CONCLUSION

Ni_3Al and Cr-Ni_3Al alloy films with variations in Cr concentration have been synthesized via DC magnetron sputtering. The microstructure, phase, and mechanical properties of the deposited coatings have been studied. XRD patterns of Ni_3Al and Cr-Ni_3Al alloy films have reflected a preferred orientation of the (111) plane followed by low intensity peak of (200) and (220). However, no evidence of Cr in diffraction peak of Cr-Ni_3Al films has been observed upon enriching the host Ni_3Al film with Cr. The rise in sputtering power to the Cr target resulted in enriching the Cr content in the films which led to the evolution of microcracks resulting in degradation of the surface roughness. The maximum percentage of porosity (14%) has been observed in 40 W Cr-Ni_3Al films with highest surface roughness of 14.80 ± 0.71 nm. 0 W Cr-Ni_3Al alloy film has shown the highest value of hardness (12.7 ± 0.8 GPa) and Young's modulus (203 ± 15 GPa) that decreases with increase in Cr content. Contact angle measurements reveal that Cr-Ni3Al films are hydrophilic in nature but converts to hydrophobic with increase in Cr content in the samples. The maximum contact angle of 115.9° is observed for 40 W Cr-Ni_3Al films.

5.2 DC MAGNETRON CO-SPUTTERED Zr-Ni_3Al FILMS

*In this section, the properties of Zr-Ni_3Al alloy films have been investigated using the same characterization techniques discussed in section **5.1**.*

5.2.1 INTRODUCTION

Ni_3Al in bulk and thin film state have been investigated by several researchers to study their mechanical, tribological, and high temperature oxidation resistant properties. It has been reported that the Ni_3Al based thin films are able to prevent the substrate from being drastically oxidized at elevated temperature of ~900- 1100°C. However, the polycrystalline Ni_3Al-based coatings possess brittle behavior at room temperature which hinders their practical applications at ambient temperature [78], [228]. In order to overcome the problem, several research groups have doped Ni_3Al with Boron (B) and found that the ductility of the polycrystalline material increased by ~35% [78], [228], [229]. Li *et al.*, found that the incorporation of Zirconium (Zr) in bulk Ni_3Al also contributes in increasing the ductility of the host Ni_3Al intermetallic compound whereas Yavorska *et al.*, reported enhancement in oxidation resistance properties of Ni_3Al films when enriched with Zr [230]. Very limited research has been reported in literature highlighting the mechanical properties of intermetallic Ni_3Al compound specially in case of alloy thin films. This work reflects the synthesis and characterization of microstructural and mechanical properties of Ni_3Al films enriched with Zr in alloy form.

5.2.2 EXPERIMENTAL DETAILS

5.2.2.1 Synthesis of Zr-Ni_3Al films

Ni_3Al and Zr-Ni_3Al films were deposited on Silicon (100) substrate using DC magnetron sputtering and co-sputtering process respectively. All the sputtering process were kept common as discussed in section **5.1.2.1** except the use of Zr target at the place of Cr to synthesize the Zr-Ni_3Al films namely 0 W Zr, 10 W Zr, 20 W Zr, 30 W Zr and 40 W Zr. The parameters of deposition of Zr-Ni_3Al films have been indexed in **table 5.3**.

Table 5.3: Sputtering parameters for depositing Zr-Ni_3Al films with variation in Zr content

Targets	Zr & Ni_3Al
Substrates	Silicon (100)
Base pressure	3×10^{-6} mbar
Sputtering gas	Argon (30 sccm)
Sputtering pressure	3×10^{-2} mbar
Sputtering power (Ni_3Al)	250 W DC
Sputtering power (Zr)	**0 W, 10 W, 20 W, 30 W & 40 W DC**
Substrate temperature	400℃
Deposition time	60 minutes

5.2.2.2 Characterization details

The deposited Ni_3Al and Zr-Ni_3Al films were characterized to study the evolution of phase, the surface morphology, surface topography and mechanical properties. The characterization techniques and testing parameters used were same as discussed in **section 5.1.2.2**

5.2.3 RESULTS AND DISCUSSION

Figure 5.11 illustrates the XRD spectra of Ni_3Al and Zr-Ni_3Al films deposited with different concentration of Zr. From the figure, it can be observed that the Ni_3Al and Zr-Ni_3Al films display a preferred orientation of (111) plane at 44.13° followed by low intensity XRD peak at 51.5° (200) and 75.1° (220) of FCC structure. The XRD peak at 44.13° also corresponds to the standard $L1_2$ intermetallic phase of Ni_3Al. XRD spectra of Zr-Ni_3Al films don't reflect any evidential diffraction peak of Zr. However, a shift towards a lower angle in (111), (200) and (220) planes is observed as a result of Zr enrichment in the host Ni_3Al film (**figure 5.12**) which leads to the generation of micro strain as larger sized Zr replaces the smaller sized Ni in the Ni_3Al matrix. A continuous and subsequent shift towards the lower degree of angle is evident from the films enriched with Zr and this results in deteriorating the $L1_2$ phase of the host Ni_3Al films.

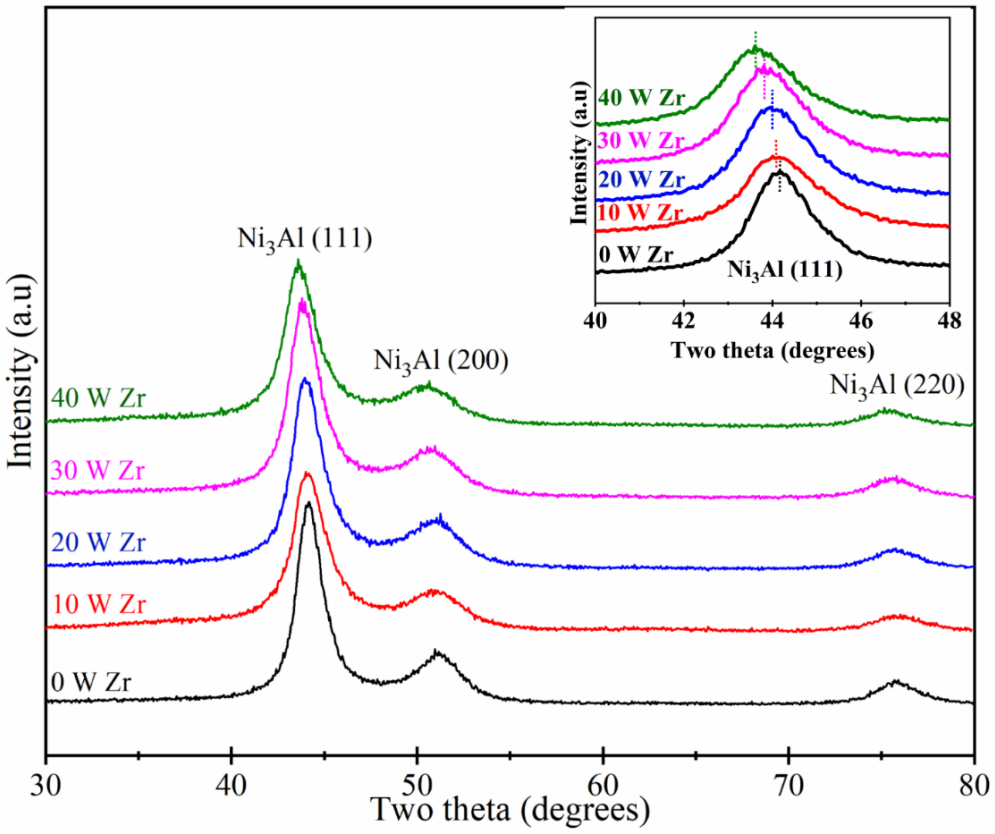

Figure 5.11: XRD spectra of Ni_3Al and Zr-Ni_3Al alloy films

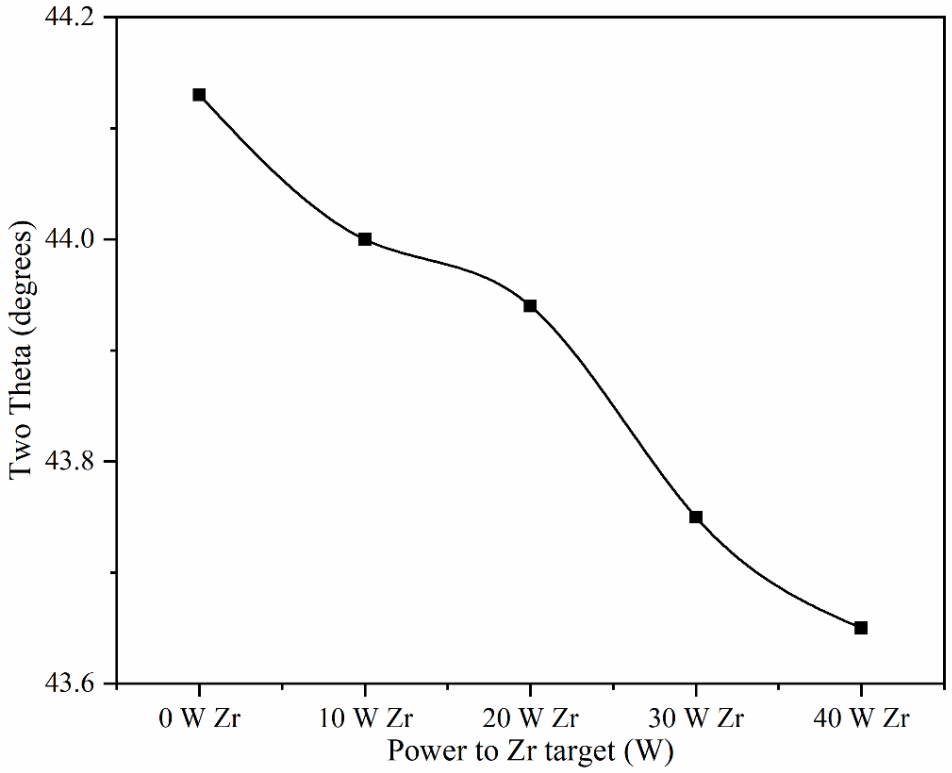

Figure 5.12: Peak shift in Zr-Ni_3Al films as a function of power to Zr target

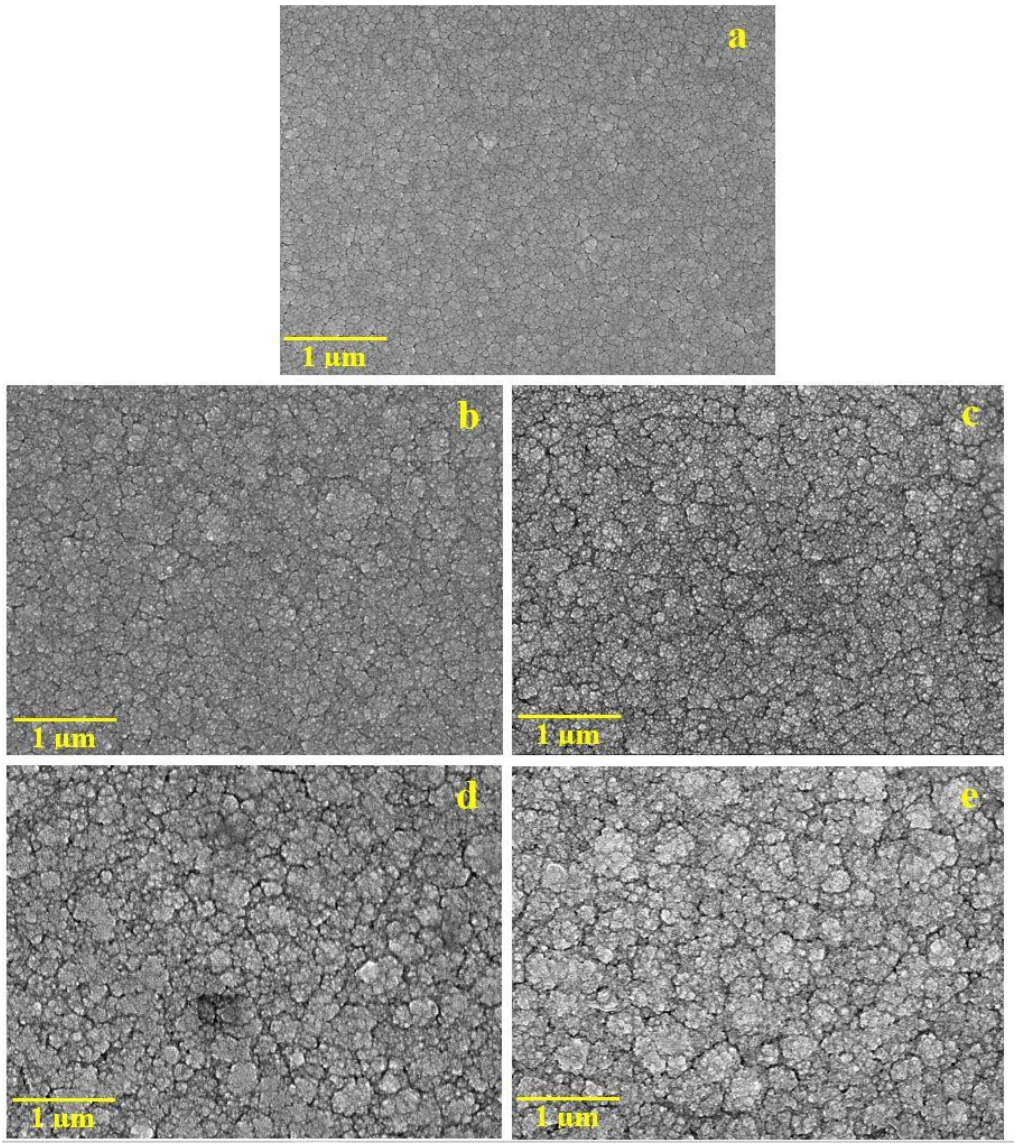

Figure 5.13: FESEM images of Zr-Ni_3Al films **(a)** 0 W Zr **(b)** 10 W Zr **(c)** 20 W Zr **(d)** 30 W Zr **(e)** 40 W Zr

Figure 5.13 represents the microstructure of Zr-Ni_3Al films characterized using FESEM. It can be seen that the Ni_3Al film without addition of Zr (0 W Zr), shows circular equisized and closely packed grains resulting in making the coated surface smooth and homogeneous. However, the doping of Zr in Ni_3Al coatings contributes to to the generation of coarse grains as a result of agglomeration of crystallites. Furthermore, a continuous and subsequent increase in percentage of pores is also observed with Zr enrichment. This could be the result of the thermal mismatch between the substrate and the

coating or due the presence of residual stress generated during the deposition [231], [232]. Furthermore, the enhancement in grain size not only degraded the arrangements of grains and grain boundaries but also lead to the generation of pores which propagates across the deposited surface. It is observed that the incorporation of Zr in host Ni_3Al has affected the grain enlargement kinetics which led to the grain growth with globular structure.

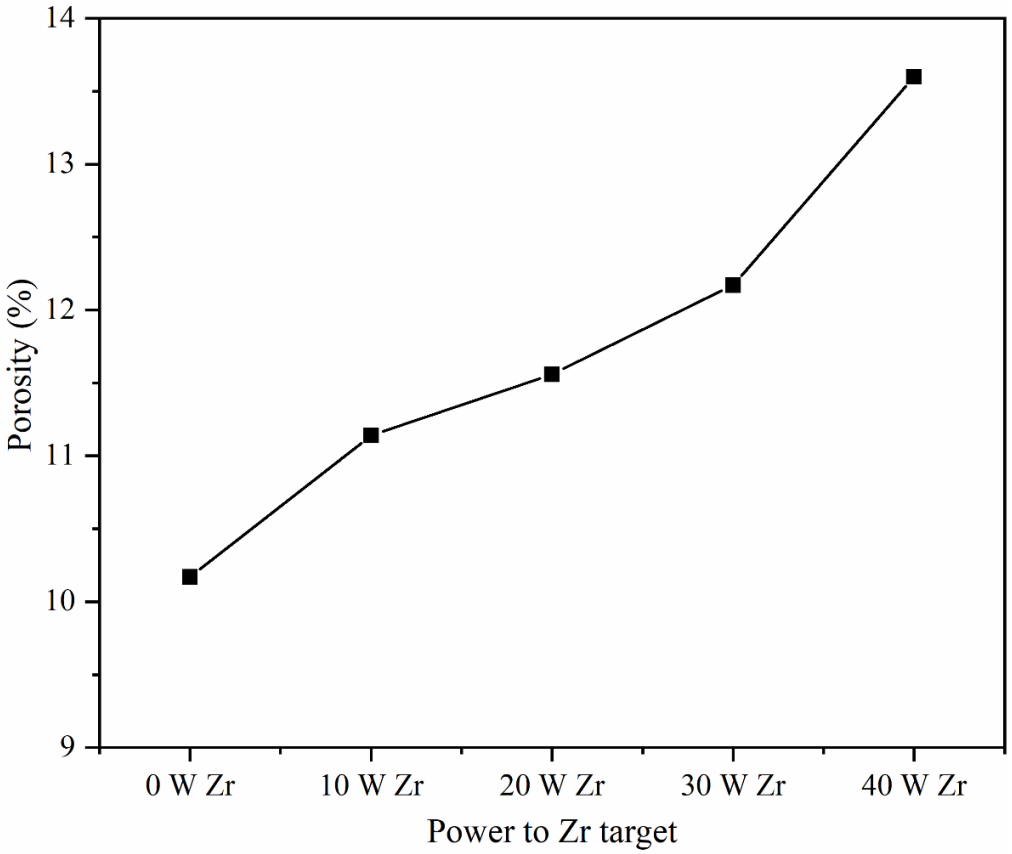

Figure 5.14: Evolution of porosity as a function of Zr enrichment in Ni_3Al alloy films.

Image J software has been used to calculate the size of grains and percentage of pores present in Ni_3Al and Zr-Ni_3Al films. For the purpose, FESEM image of the deposited films have been used in the software. **Figure 5.** illustrates the evolution of porosity with respect to the rise in power to the Zr target while depositing the alloy films. 0 W Zr film shows denser microstructure resulting in the generation of minimum percentage of pores (10.17%) whereas the film with 40 W Zr has shown the larger grains with maximum percentage of pores

(13.6%). Results of grain size and grain distribution measurements revealed that the film deposited with 0 W Zr possessed the homogeneously distributed smaller sized grains as shown in **figure 5.15**. The grain size of the films increases with increase in Zr content. Furthermore, an inhomogeneity in the grain distribution can be seen when enriched with Zr content up to 40 W Zr. The average minimum and maximum grain size of the films has been calculated as 90 ± 2.0 nm and 190 ± 2.5 nm for 0 W Zr and 40 W Zr respectively. The continuous increase in Zr content and grain size of the film as result of increase in sputtering power to Zr target has been indexed in **table 5.4**.

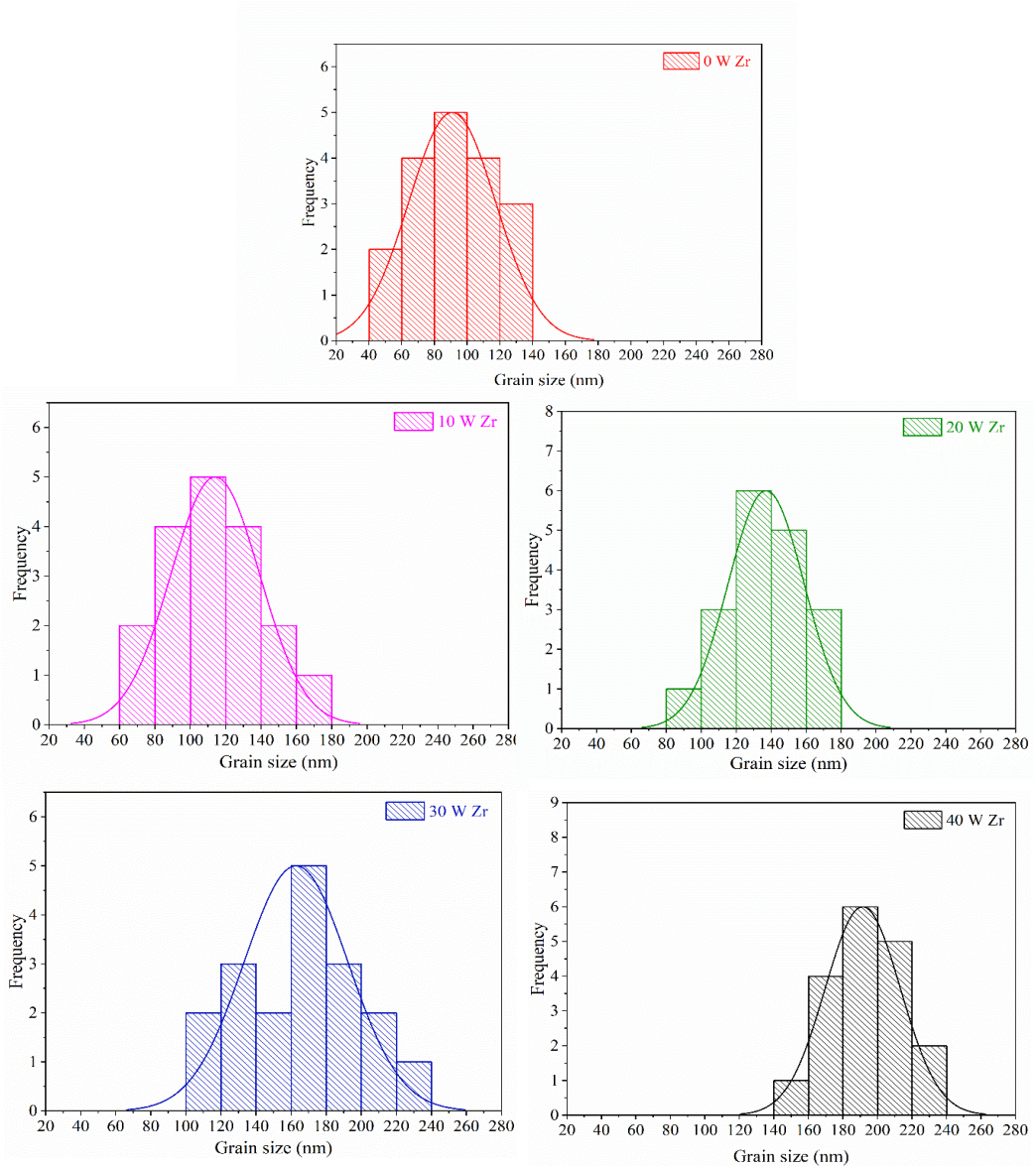

Figure 5.15: Distribution of grains in Ni_3Al and Zr-Ni_3Al coatings

Table 5.4: Calculated parameters of Zr-Ni_3Al coatings as a function of Zr enrichment

SN	Sample	Zr (at%)	Lattice constant (nm)	Grain size (nm)	Surface roughness (nm)	Contact angle (degree)	Porosity (%)	Strain
1.	0 W Zr	0.0	0.3552	90 ± 2.0	7.2 ± 0.5	75 ± 1.5	10.17	0.01956
2.	10 W Zr	0.65	0.3561	114 ± 2.0	8.4 ± 0.5	88 ± 1.5	11.14	0.02332
3.	20 W Zr	1.02	0.3566	137 ± 2.5	9.1 ± 0.5	95.9 ± 1.0	11.56	0.02401
4.	30 W Zr	1.2	0.3581	161 ± 2.5	11.3 ± 1.0	99.1 ± 1.0	12.12	0.02510
5.	40 W Zr	1.51	0.3589	190 ± 2.5	13.6 ± 1.0	101.7 ± 1.0	13.6	0.02680

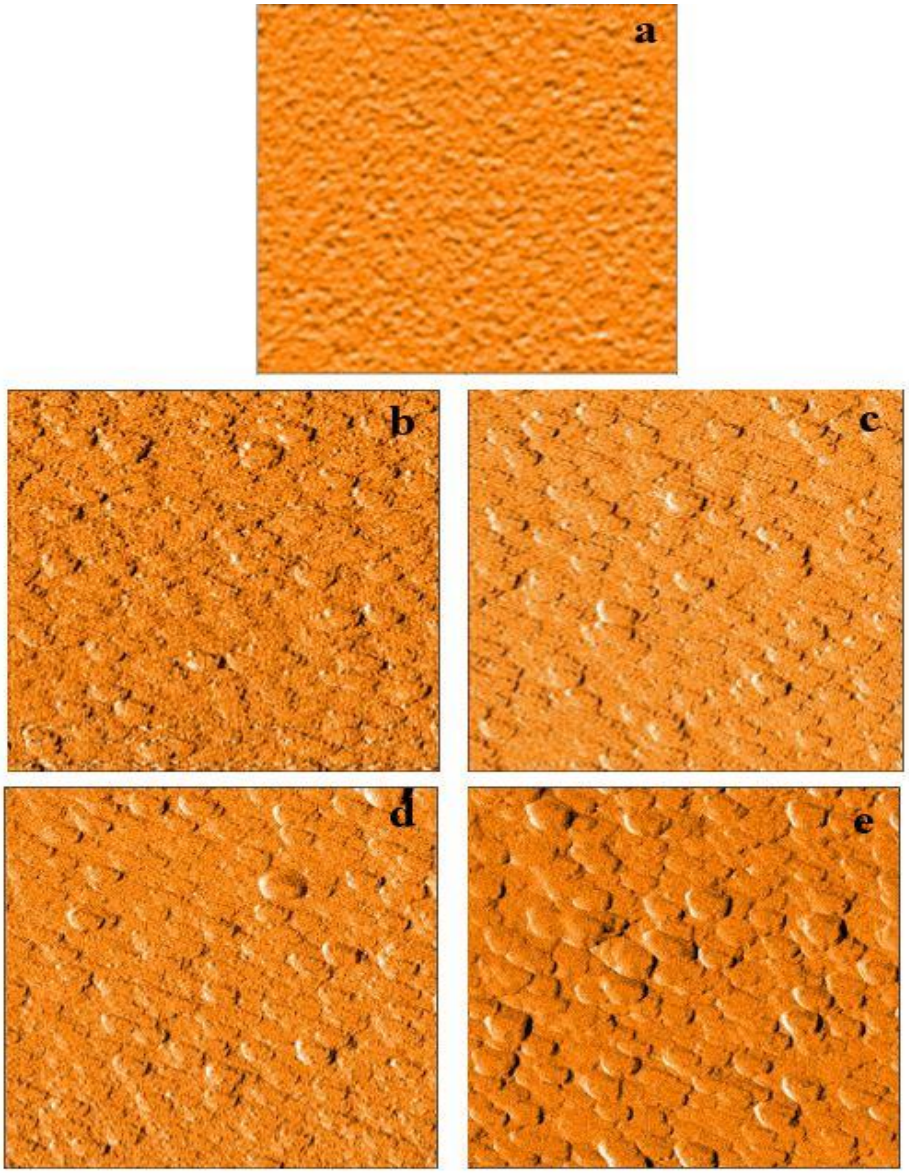

Figure 5.16: 2D AFM images of Zr-Ni_3Al films **(a)** 0 W Zr **(b)** 10 W Zr **(c)** 20 W Zr **(d)** 30 W Cr **(e)** 40 W Zr

The surface topography of Ni_3Al and Zr-Ni_3Al coatings is characterized using atomic force microscopy (AFM). An area of 50 x 50 μm^2 at 10 different spots of the deposited samples have been scanned to calculate the surface roughness (rms) whereas an area of 10 x 10 μm^2 and 5 x 5 μm^2 was scanned to reveal the 2D and 3D surface topography of each coating. The 2D and 3D AFM images of the synthesized coatings have been shown in **figure 5.16 and figure 5.17** respectively.

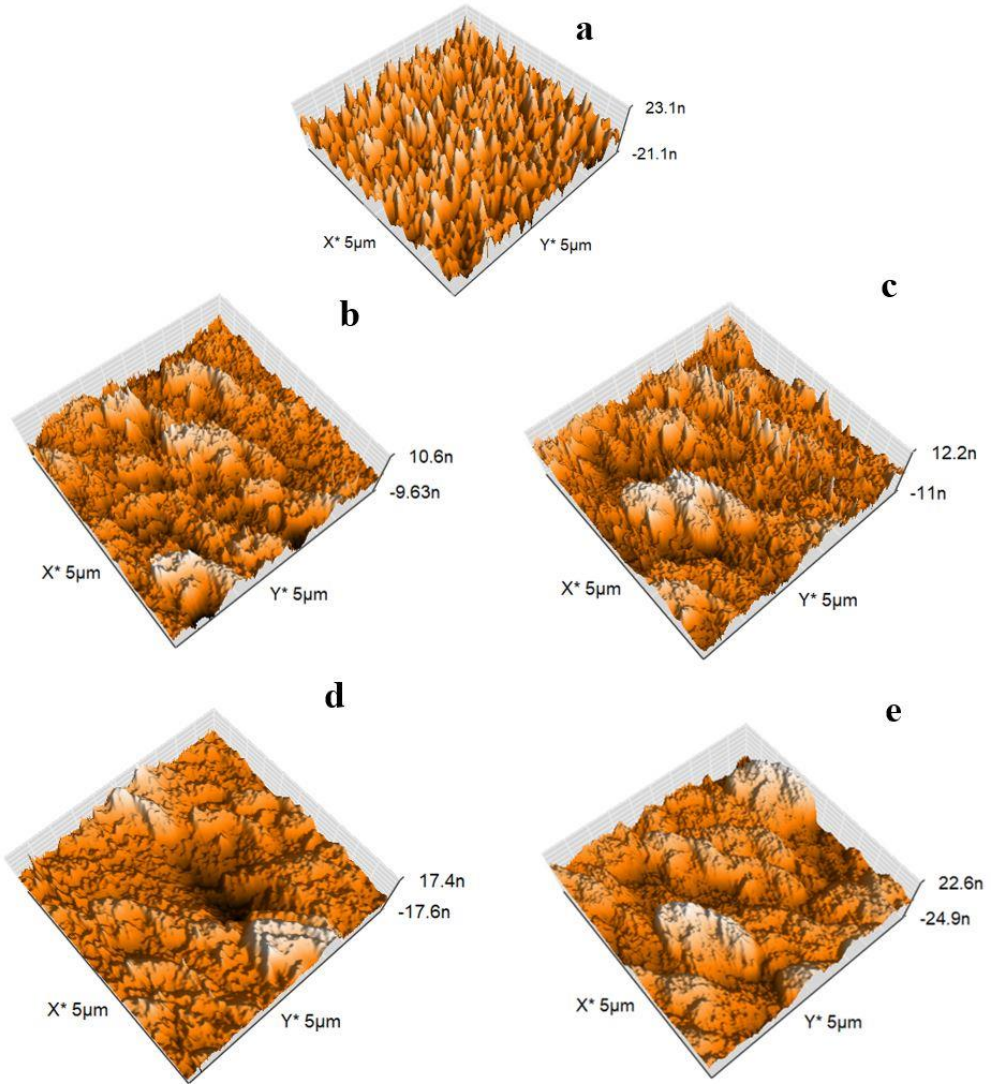

Figure 5.17: 3D AFM images of Zr-Ni_3Al films **(a)** 0 W Zr **(b)** 10 W Zr **(c)** 20 W Zr **(d)** 30 W Cr **(e)** 40 W Zr

From **figure 5.17**, it can be observed that the film deposited with 0 W Zr showed a large number of homogeneously distributed equiaxed pyramid

like dense asperities. With increase in the percentage of Zr content in the Ni_3Al matrix, the pyramid structured asperities undergo a transformation into large dome-like structures due to clustering of crystallites. The continuous and progressive development of these dome-like structures degrade the microstructure of the deposited films that can be observed in FE-SEM images (**figure 5.13**). This degradation is attributed to the increased void fraction within the coatings. The surface roughness of the coatings calculated using the inbuilt software in AFM has been reported in **table 5.4**. The minimum and maximum surface roughness of 7.2 nm and 13.6 nm has been observed for 0 W Zr and 40 W Zr respectively.

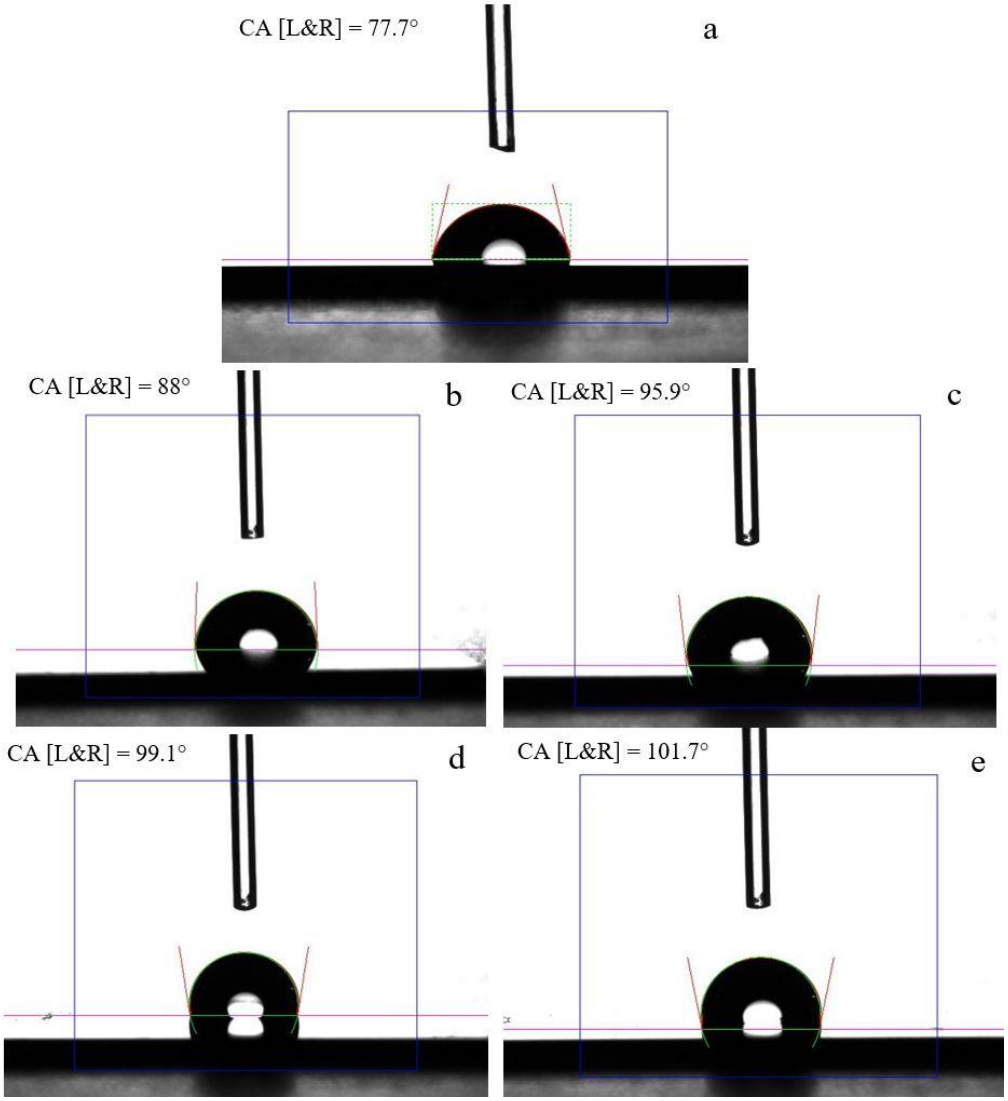

Figure 5.18: Contact angles of Zr-Ni_3Al films as a function of Zr enrichment **(a)** 0 W Zr **(b)** 10 W Zr **(c)** 20 W Zr **(d)** 30 W Cr **(e)** 40 W Zr

The wettability of the deposited Zr-Ni_3Al films has been studied using Drop shape analyzer at room temperature in terms of contact angles. The evaluation of contact angles between the distilled water and deposited surface is carried out on drop shape analyzer in steady state conditions. The results of the measurements have been displayed in **figure 5.18**.

From the figure, it can be observed that the Ni_3Al coating synthesized with 0 W Zr showed the minimum value of contact angle which increases with rise in percentage of Zr in Ni_3Al matrix. This could be the result of continuous rise in the surface roughness of the coating as the presence of the high intensity of the surface asperities and large number of void fractions decreases the interaction of water droplets with the deposited surface [100]. This is because the large volume of air is trapped between the surface asperities and water droplets and hence the surface interaction of water is decreased resulting in increasing the hydrophobic property of the film. The minimum and maximum value of 77.3° and 101.7° has been recorded for 0 W Zr and 40 W Zr films respectively.

A quasi-static, depth-controlled nanoindentation was performed to calculate the mechanical properties in terms of modulus and hardness at room temperature. The indentation was performed at 10 different places of deposited surface to calculate the average values of Young's modulus and hardness as shown in **figure 5.19**. From the figure it can be perceived that the hardness of the film decreases with rise in the concentration of Zr in the host Ni_3Al matrix. This is because of the generation of higher percentage of porosity due to grain coarsening which lead to the distortion of the microstructure. It has been reported in literature that the mechanical properties are highly governed by grain size and grain growth mechanism [88].

Figure 5.20 shows the relationship between hardness and inverse square root of grain size. From the figure it is observed that the hardness of the film is directly proportional to the inverse square root of grain size indicating that the hardness of the film decreases with increase in grain size following the classical Hall-Petch relation. This indicates that the hardness of the film decreases with enhancement in grain size following the dislocation pileup

model. Moreover, the value of R^2 is close to 1 (R^2 = 0.94) which suggests that the regression line fits the data well resulting in a high value of H-P coefficient [slope = 136.5109 ± 20.5064 GPa ($nm^{1/2}$)].

From **figure 5.19**, it is also observed that the evolution of Young's modulus also follows the same trend as that of hardness. It has been reported in literature that along with the Hall-Petch mechanism, the mechanical properties of Ni_3Al in bulk and thin film form are highly influenced by the formation of stable ordered intermetallic $L1_2$ phase of FCC structure [88], [97], [103].

However, in our case, with increasing the Zr content in the Ni_3Al film, a subsequent and continuous shift in XRD peak of (111) plane towards the lower angle is observed (**figure 5.12**) which states that the stable $L1_2$ phase of Ni_3Al is distorted resulting in degrading the mechanical properties of the deposited films.

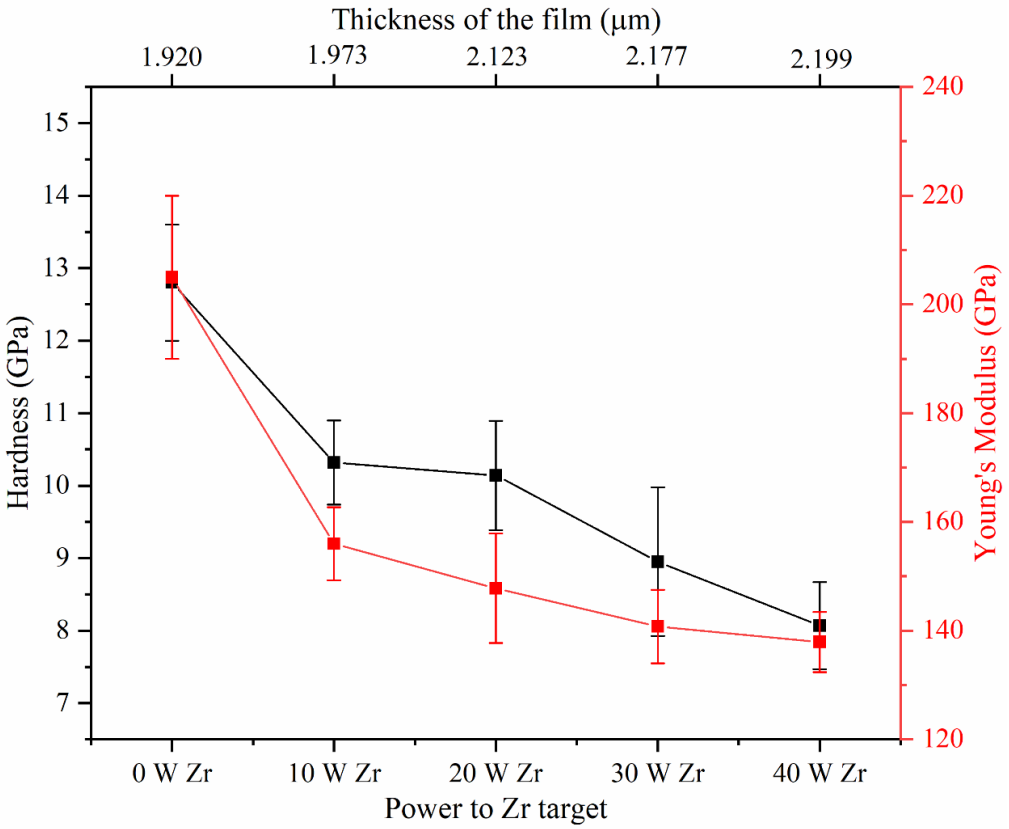

Figure 5.19: Hardness and Young's modulus of Zr-Ni_3Al films as a function of power to Zr target

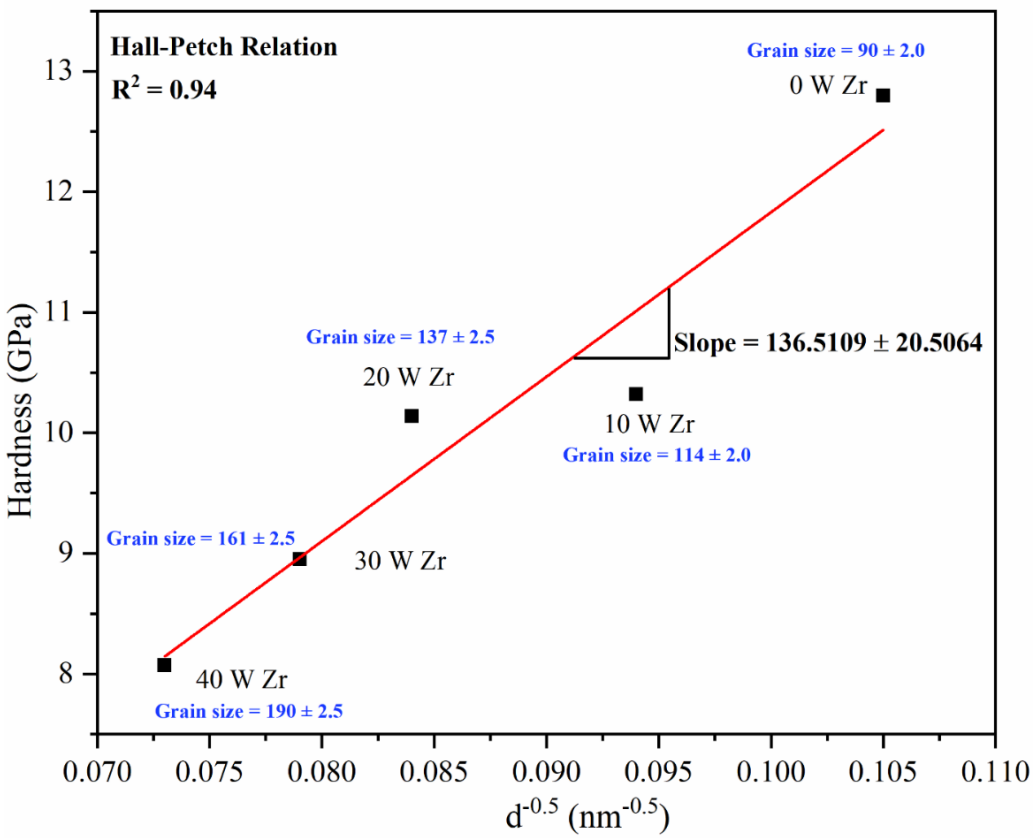

Figure 5.20: Hall-Petch relationship in Ni_3Al and Zr-Ni_3Al films

The load versus displacement curve of Zr-Ni_3Al films have been plotted in **figure 5.21.** The figure shows a depth control loading and unloading process with a maximum and minimum load of 2.82 mN and 1.95 mN for 0 W Zr and 40 W Zr films respectively. Both elastic and plastic deformation can be perceived during loading for all the deposited films whereas only elastic deformation is observed during the unloading process. It can be observed that 0 W Zr films showed a permanent deformation depth of 25 nm whereas the Ni_3Al film enriched with 10 W Zr and 20 W Zr have showed the permanent deformation depth of 55 nm. The maximum deformation depth of 58 nm is shown by the film deposited with 30 W Zr and 40 W Zr content. This shows that the 0 W Zr film exhibits a better rate of elastic recovery as compared to other films. This continuous and subsequent increase in permanent deformation suggests that the film gets soften by enriching Zr in Ni_3Al matrix resulting in decreasing the overall hardness of the film. Moreover, from the figure, it can be observed that to penetrate a constant depth during nanoindentation for all the films, the maximum applied load has been recorded

for 0 W Zr film suggesting that the film is harder as compared to other deposited films with Zr enrichment. Same kind of results have been observed by several research groups when they doped Ni_3Al films in form of multilayer films. However, a very limited literature has been reported so far in case in synthesizing and characterizing doped Ni_3Al films in alloy form. In this study the maximum and minimum hardness and Young's modulus of (12.8 ± 0.8 GPa), (205 ± 15 GPa) and (8.07 ± 0.6 GPa), (137 ± 5.5 GPa) has been observed for 0 W Zr and 40 W Zr coatings respectively.

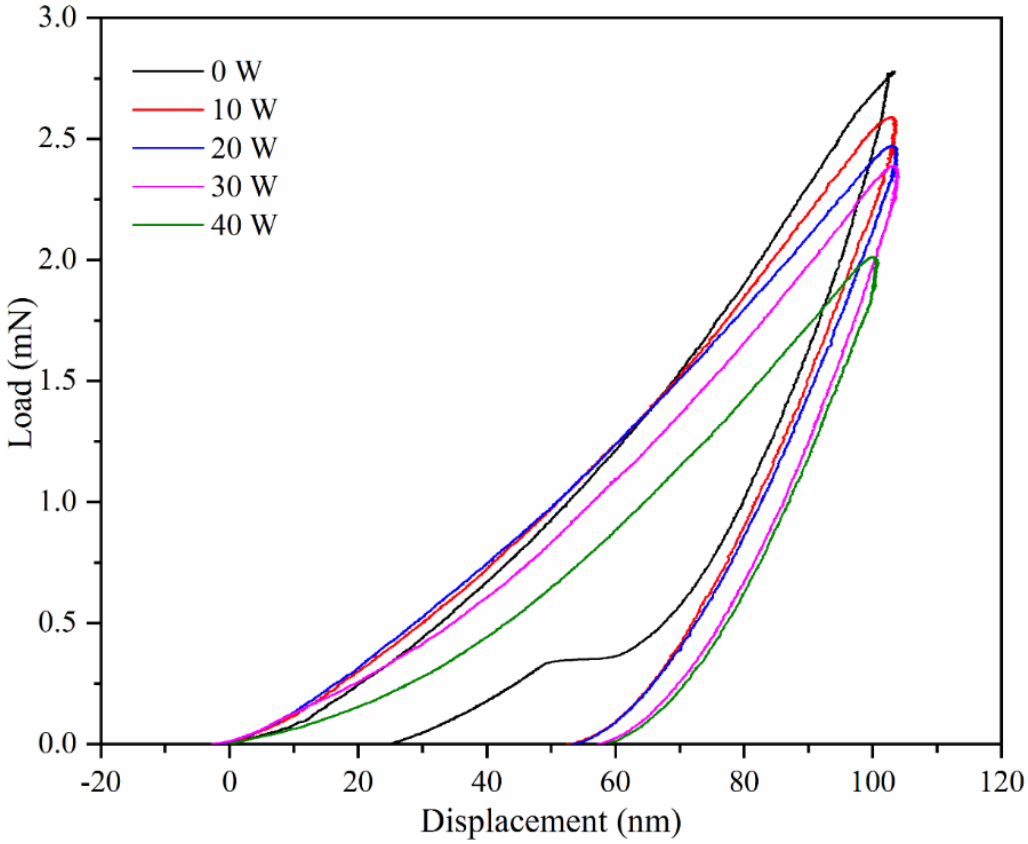

Figure 5.21: Load versus displacement graph of Zr-Ni_3Al films

5.2.4 CONCLUSION

Alloy Ni_3Al films with the variation of Zr content have been synthesized using Magnetron sputtering at a substrate temperature of 400℃. The chemical composition, surface morphology, and mechanical properties of the deposited coatings have been investigated. The results of EDS the increase in

concentration of Zr in host Ni_3Al with increase in power to Zr target. The XRD spectra of the coatings shows a preferred orientation of (111) plane which also corresponds to the standard ordered-intermetallic $L1_2$ structure of Ni_3Al. NO peak corresponding to Zr is observed. However, a continuous shift in XRD peak towards the lower angle is observed. It has been found that the enrichment of Zr in host Ni_3Al has resulted in enlargement of grains which contributed to the generation of porosity and increased surface roughness. The largest grain size (190 ± 2.5), highest percentage of porosity (13.6%) and highest roughness (13.6 nm) have been observed for Ni_3Al films enriched with 40 W Zr content. The highest hardness and Young's modulus of (12.8 ± 0.8 GPa) and (205 ± 15 GPa) has been observed for 0 W Zr coatings. The results of water drop shape analysis reflected an increase in the value of contact angle with increase in Zr content in the Ni_3Al matrix. The maximum contact angle of 101.7° has been recorded for 40 W Zr coatings.

CHAPTER 6

SYNTHESIS AND CHARACTERIZATION OF OXIDATION-RESISTANT PROPERTIES OF DC-CO-SPUTTERED DOPED Ni_3Al FILMS

6.1 DC MAGNETRON CO-SPUTTERED Cr-Ni_3Al FILMS

In this section, the evolution of phase, microstructure, adhesion and resistance to oxidation at high temperatures of Ni_3Al and Cr-Ni_3Al films have been explored and discussed in detail. The films were synthesized over INCONEL-718 at a substrate temperature of 400℃ via DC magnetron co-sputtering process. The evolution of phase, microstructure, surface morphology and adhesion of the deposited films have been characterized using XRD, FESEM, AFM and nanoindentation respectively. A high-temperature oxidation test was carried out in open air using a split furnace and weighing balance.

6.1.1 INTRODUCTION

Transition metal nitride coatings are well-established coatings that provide protection to the parent material in terms of improved tribological and mechanical properties [233]–[235]. These films have been broadly used in aerospace, marine industries and various structural and decorative applications [162], [163], [196], [236]. However, these nitrides didn't prove themselves the best candidate for their use at elevated temperatures. Over the last five decades, the continuous demands for materials for their applications at high-temperature attracted the eyes of researchers toward bulk nickel superalloy. Ni-superalloy has shown excellent thermal stability without losing much in high-temperature strength. However, for application at high temperatures like in gas turbine blades and jet engines, these material experiences cyclic and mechanical loads along with corrosion and oxidation attacks [186]. In order to protect these materials from cyclic attacks, NiAl and Ni_3Al-based coatings have been extensively researched in the last two decades. These coatings possess excellent corrosion and oxidation resistance properties even at elevated temperatures of 900℃. In particular, polycrystalline intermetallic Ni_3Al-based coatings have been recognized for their use at elevated temperatures as they exhibit extraordinary properties like corrosion and oxidation resistance, creep and fatigue resistance, stability at elevated temperature, improved stiffness, tribological and mechanical properties. Ni_3Al intermetallic compounds show brittle properties at ambient temperature. However, researchers have doped host Ni_3Al films with different materials

like Boron, Palladium, Zirconium and Chromium to overcome the brittle fracture at room temperature and improve the mechanical strength too [79], [86], [237]. It has been reported that the Ni_3Al films in the form of alloy or multilayered structure have shown the hardness in the range of 4 to 14 GPa whereas the coatings are also able to protect the material from being drastically oxidized at 900℃. Research has been done by several groups to enhance the hardness of the Ni_3Al films by synthesizing them in multilayer films followed by annealing at different temperatures. In our previous work, alloy Ni-rich Ni_3Al films were fabricated using DC magnetron sputtering where we observed that the Ni_3Al films deposited over heated silicon at 400℃ exhibited highest hardness of nearly 13 GPa. It has been stated in literature that there are several factors like the microstructure of the film, the dopants used, the $L1_2$ phase formed and the deposition technique which influences the properties of Ni_3Al based thin film coatings. Several studies reflect that Ni_3Al-based coatings with $L1_2$ structure are able to protect the material from being oxidized at elevated temperatures [86], [238]. This is because the Ni_3Al film is able to form the layer of Al_2O_3 which prevents the parent material from oxidation attacks. Rahman *et al.,* [186] deposited NiAl thin film on Superni-718 substrate using co-sputtering process and tested them against the cyclic oxidation at 900℃ for 50 cycles where each cycle involved 60 minutes of heating and 30 minutes of cooling in air. The outcomes of the research showed that the coating deposited at 350℃ showed the best oxidation-resistant properties because of the formation of oxidation-resistant oxide layers of Al_2O_3 and Cr_2O_3. Xing *et al.,* [86] deposited Ni_3Al and Cr/Ni_3Al multilayered coatings via magnetron sputtering over heated substrate at 400℃. They examined the mechanical properties of the film at ambient temperature where the studies for oxidation was carried out at 900℃, 1000℃ and 1100℃. They observed a gradual fall in the hardness of the deposited coatings whereas the modulus improved with increase in the concentration of Cr. The results of the oxidation test disclosed that the Cr/Ni_3Al films were able to protect the parent material from being oxidized even at 1100℃ and showed better resistance to oxidation than pure Ni_3Al films. Khakpour *et al.,* [239] synthesized Zr-doped aluminide coatings over Inc-738 substrate using pack cementation. They used

$ZrOCl_{2.8}H_2O/NH_4Cl$ powder as activators, 30% Al-Cr as compound and Al_2O3 and Al as filler materials. The cyclic oxidation test was carried out at 1100℃ for maximum of 50 cycles where individual cycle involved 60 minutes of heating followed by weight change measurements after 10 minutes of cooling. They found that the films modified by Zr showed improved oxidation-resistant properties as compared to undoped coatings. There are some studies reported in literature reflecting the effect of substrate temperatures, the chemical composition, dopants and variation in deposition parameters on oxidation-resistant properties of pure Ni_3Al or multilayered Ni_3Al based thin films but not even single research in literature elucidates the consequence of using dopant in the host Ni_3Al films in alloy form. This research reflects the effect of Cr enrichment on surface morphology and oxidation-resistant properties of Ni_3Al coatings deposited in alloy form

6.1.2 EXPERIMENTAL DETAILS

6.1.2.1 Synthesis of Ni_3Al and Cr-Ni_3Al films

Ni_3Al and Cr-Ni_3Al films were deposited over Inconel-718 using custom-designed DC magnetron sputtering (Excel Instruments, India) and co-sputtering respectively at substrate temperature of 400℃. The substrates were prepared in the dimension of (10 x 10 x 3) mm and polished with different grit sized SiC papers from 500 to 2500 grits and then polished with 0.25µm sized diamond paste. Further, they were cleaned in acetone via ultrasonication and air-dried prior to clamping to the substrate holder in vacuum chamber. The elemental composition of the substrate has been indexed in **table 6.1.** Both Ni_3Al (99.99%) and Cr (99.99%) sputter targets (2 inches dia & 2 mm thick) were placed in respective sputtering guns at a confocal arrangement of 30° apart from each other. The chamber was evacuated at a base pressure of 3 x 10^{-6} mbar to eradicate the impurities from the chamber walls and substrates. Argon (purity 99.999%) as a process gas was inserted in the chamber and the sputtering pressure of 3 x 10^{-2} mbar was maintained throughout the experiment. The substrate holder was rotated at a speed of 15 rpm to ensure the homogeneous deposition of the film. A pre-sputtering for ten minutes was performed to eradicate the impurities from the surface of both the sputter

targets while the actual sputtering was performed for 60 minutes. The Ni_3Al target was supplied with a constant DC power of 250 W while the DC power to the Cr target was varied as 0 W, 10 W, 20 W and 30 W to vary the Cr content in host Ni_3Al film. Four samples with different content of Cr were deposited namely 0 W Cr, 10 W Cr, 20 W Cr and 30 W Cr. During the experiment all the sputtering parameters were carefully monitored and kept constant. The parameters of deposition of Cr-Ni_3Al coatings are indexed in **table 6.2**.

Table 6.1: Elemental composition of INCONEL-718

Elements	Ni	Cr	Fe	Nb	Mo	Ti	Al	Mn	Si	Co	S	C
Composition (wt%)	53.293	17.4	19.7	4.8	3.25	0.96	0.5	0.03	0.03	0.01	0.007	0.02

Table 6.2: Sputtering parameters for depositing Zr-Ni_3Al films with variation in Zr content

Targets	Cr & Ni_3Al
Substrates	Inconel-718
Base pressure	3×10^{-6} mbar
Sputtering gas	Argon (30 sccm)
Sputtering pressure	3×10^{-2} mbar
Sputtering power (Ni_3Al)	250 W DC
Sputtering power (Cr)	**0 W, 10 W, 20 W and 30 W**
Substrate temperature	400°C
Deposition time	60 minutes

6.1.2.2 Characterization details

XRD measurements were performed on Bruker D8 ADVANCE ECO at ambient temperature with CuKα = 0.154 nm to identify the different phases of the substrate and deposited films before and after the oxidation test. The tests were conducted in the 2-theta range of 20 to 80 degrees with a scan rate of 0.02°/sec. The surface topography and the microstructural morphology of the coatings were characterized using atomic force microscopy (NaioAFM, Nanosurf, Switzerland) and FESEM (Nova NanoSEM 450, FEI) respectively

at room temperature. The elemental composition of the deposited films was characterized using EDS (Ametek) attached to the FESEM setup.

The adhesion strength of the coatings was characterized via a nano indenter (hysteron) scratch test at ambient temperature. A diamond Berkovich tip was used to scratch the deposited films in the edge forward direction with a scratch speed of 0.66 µm/sec. The applied progressive load was continuously increased from 0 µN to 1750 µN to scratch a distance of 10 µm.

Cyclic oxidation was performed at 900℃, 1000℃ and 1100℃ for 30 cycles to investigate the kinetics of oxidation in actual aggressive conditions. Each cycle consisted of 60 minutes of heating and 30 minutes of cooling followed by weight gain/loss measurements. The mirror-finished uncoated substrate and deposited Ni_3Al and Cr-Ni_3Al films were exposed to high temperatures in the open-air environment. The samples were placed in an alumina boat and were heated in a Split furnace (City Instruments, India). The samples cooled down to room temperature after 30 minutes of cooling in air and then weight change along with spallation (if any) after each cycle was measured using weighing balance (Sartorius, readability-0.01 mg) to articulate the kinetics of oxidation. The oxidized samples after the completion of 30 cycles at individual temperatures were characterized using XRD, FESEM, AFM and EDX to study the phase formation, microstructural changes, surface topography and elemental composition respectively.

6.1.3 RESULTS AND DISCUSSION

The Inconel-718 substrate upon mirror finishing showed dark silver color whereas the deposited Ni_3Al and Cr-Ni_3Al films showed black color. After 30 cycles of oxidation at 900℃, the substrate changed to dark brown whereas the Cr-Ni_3Al deposited samples showed a mix color of blue and green. With the rise in oxidation temperature the color of the uncoated and coated samples changed to dark black and black respectively. The change in colors of the samples after oxidation at different temperatures indicates the formation of different oxide layers on the surface of the material.

Figure 6.1 reflects the XRD spectra of Inconel-718 and as-deposited Ni_3Al and Cr-Ni_3Al films. It is observed that the Inconel-718 showed a major diffraction peak of Ni at 43.86° (111), 50.97° (200) and 74.98° (220). The 0 W Cr sample showed major diffraction peak at 44.26° (111), 51. 4° (200) and 75.42° (220) of FCC structure. These diffraction peaks are also in accord with the standard intermetallic $L1_2$ structure of Ni_3Al positioned at 44.11° (111), 51.39° (200) and 75.64° (220) [86]. With increase in the concentration of Cr in the samples, a continuous and subsequent shift in XRD spectra towards the lower angle is observed. The shift in the prominent peak of Ni_3Al and Cr-Ni_3Al (111) is shown in **figure 6.2**. This shift could be the result of the presence of microstrain in the film as larger Cr atoms (128 pm) replace smaller Ni (124 pm) from the host Ni_3Al matrix. The value of strain in Ni_3Al and Cr-Ni_3Al calculated using **equation 5.1, Chapter 5**, is shown in **table 6.3.** The substrate (Inconel-718) showed the preferred orientation of Ni (111) whereas all the deposited Ni_3Al and Cr-Ni_3Al films possessed a common preferred orientation of Ni_3Al (111) texture. **Figure 6.3** shows the XRD spectra of substrates, Ni_3Al and Cr-Ni_3Al films oxidized at various temperatures. From **figure 6.3 (a)** it can be seen that the XRD spectrum of oxidized substrate showed the preferred orientation of NiO (200) followed by low-intensity peak of Ni (111) and Ni (220) whereas the deposited Cr-Ni_3Al films showed the preferred orientation of Ni_3Al (111). The XRD spectrum of the substrate also shows different oxide peaks of Cr_2O_3 and Fe_2O_3. The spectra of the substrate and the coatings confirm that the substrate along with the deposited films gets oxidized however an additional peak of Al_2O_3 is observed in Ni_3Al and Cr-Ni_3Al films. From **figure 6.3 (b)** and **figure 6.3 (c)** it is seen that substrate showed the high-intensity peak of NiO (200) as a result of oxidation at 1000℃ and 1100℃. With increase in the oxidation temperature, the evolution of NiO (220) and Fe_2O_3 (110) is observed. This indicates that the substrates are more prone to oxidation at 1000℃ and 1100℃. However, the presence of XRD peaks of Cr_2O_3 and Al_2O_3 in oxidized Cr-Ni_3Al films confirms the presence of respective oxide layers protecting the surface from being drastically oxidized.

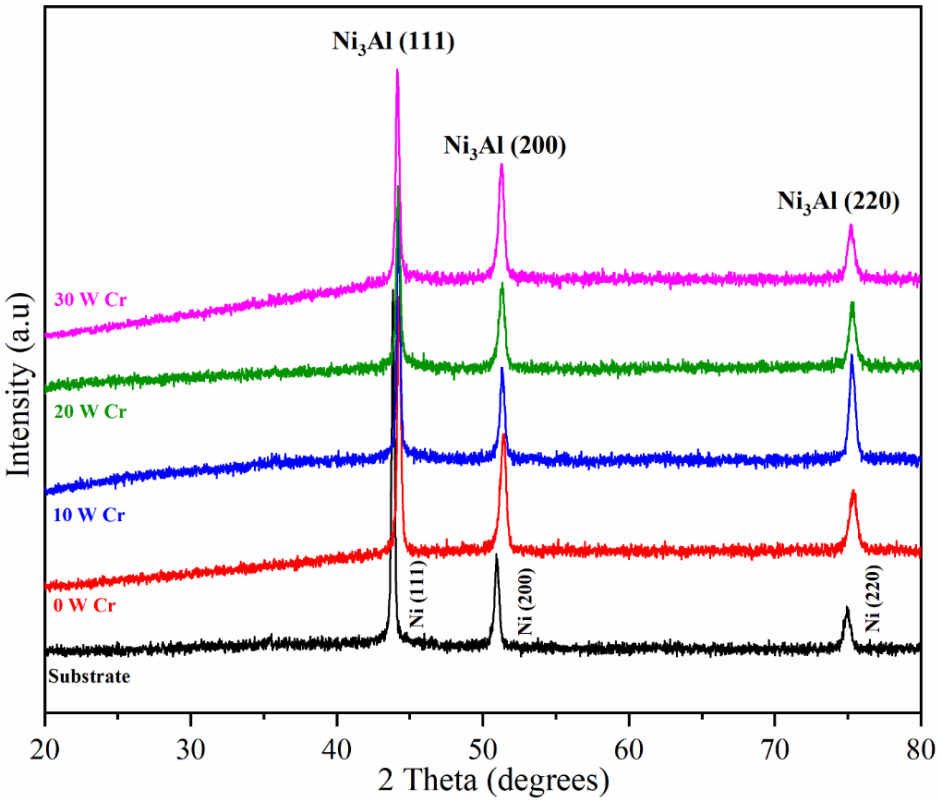

Figure 6.1: XRD Spectra of substrate, Ni_3Al and Cr-Ni_3Al films

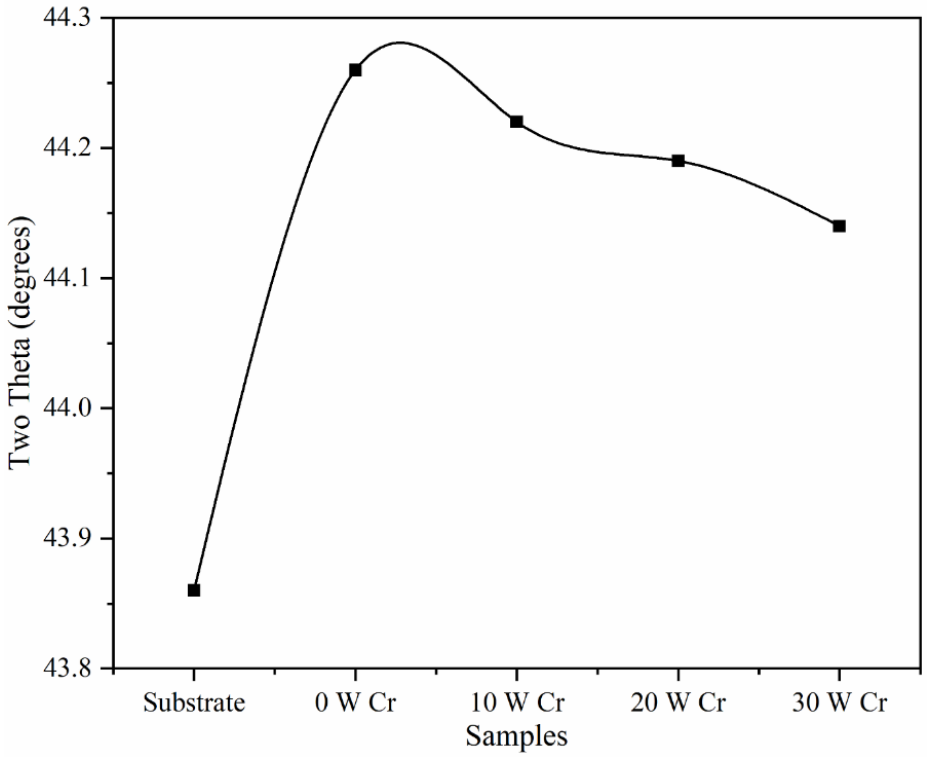

Figure 6.2: Peak shift in the prominent peak (111) of XRD Spectra of Ni_3Al and Cr-Ni_3Al films

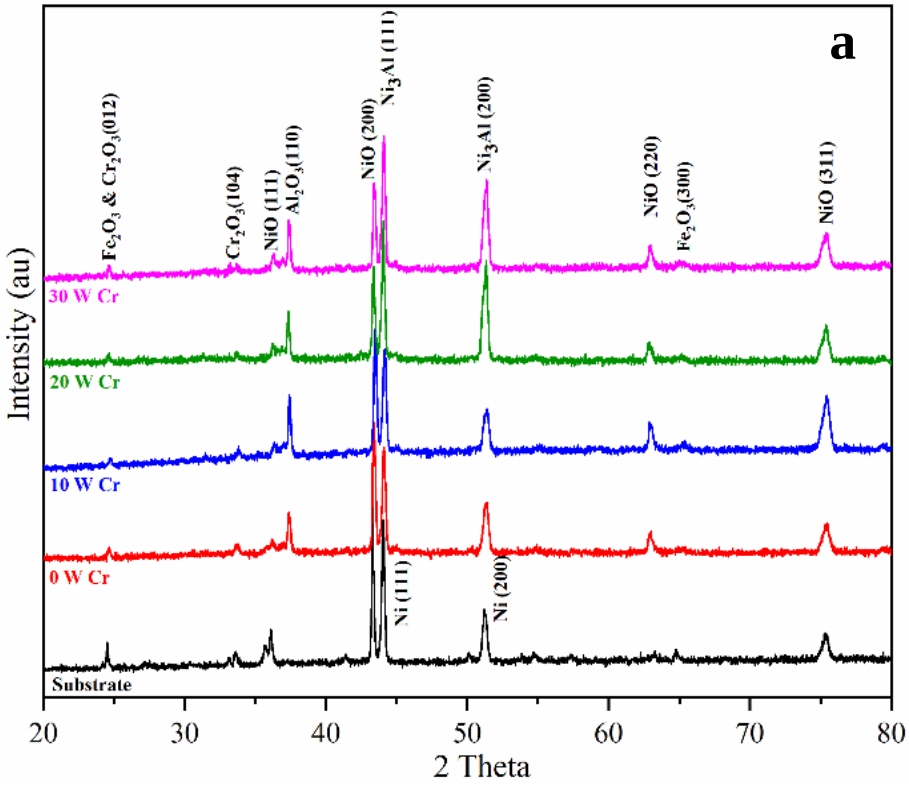

Figure 6.3 (a): XRD spectra of the oxidized substrate, Ni_3Al and Cr-Ni_3Al films at 900 ℃

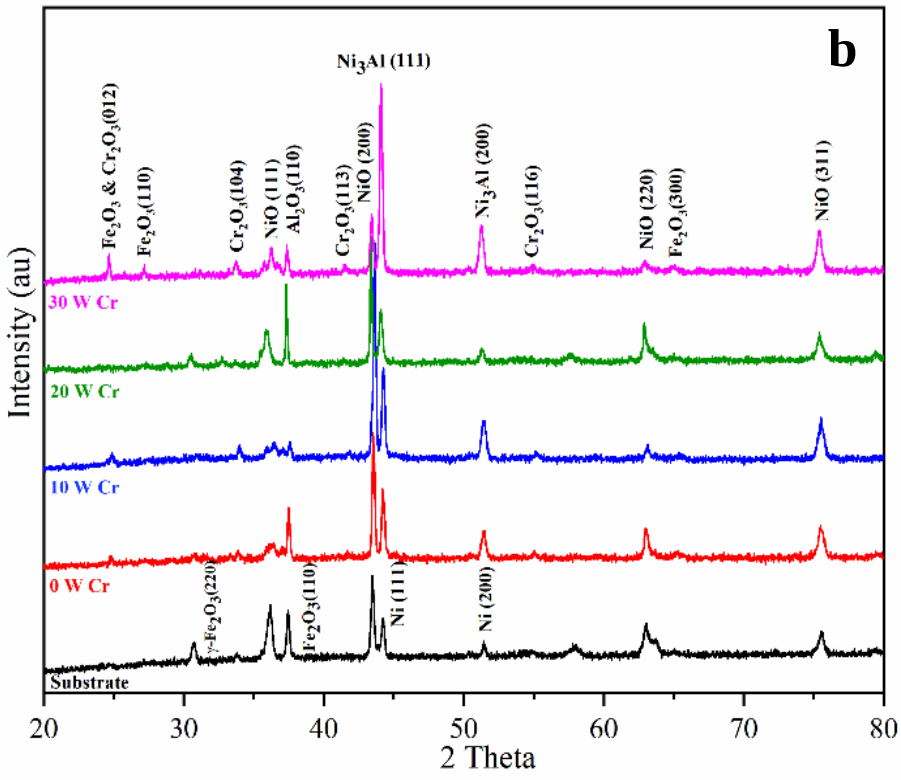

Figure 6.3 (b): XRD spectra of the oxidized substrate, Ni_3Al and Cr-Ni_3Al films at 1000 ℃

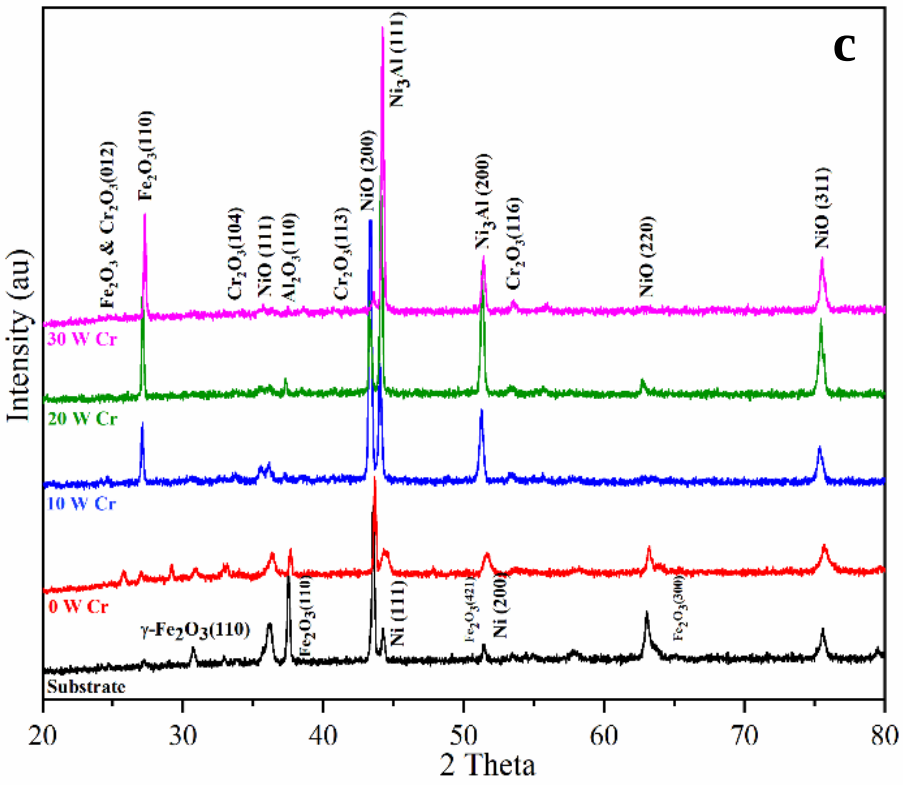

Figure 6.3 (c): XRD spectra of the oxidized substrate, Ni_3Al and Cr-Ni_3Al films at 1100 ℃

Table 6.3: Calculated grain size, porosity, surface roughness and microstrain in Cr-Ni_3Al films

SN	Sample	Cr (%)	Grain size (nm)	Porosity (%)	Roughness (nm)	Strain
1	Substrate	17.4	NA	NA	17.00 ± 0.50	0.00283
2	0 W Cr	0.00	88 ± 2.5	9.10	16.16 ± 0.50	0.00348
3	10 W Cr	1.10	84 ± 2.5	8.76	15.50 ± 0.50	0.00354
4	20 W Cr	2.30	78 ± 1.5	8.19	13.70 ± 0.50	0.00363
5	30 W Cr	5.70	71 ± 1.5	7.66	12.40 ± 0.50	0.00379

Figure 6.4 reflects the microstructure of synthesized Ni_3Al and Cr-Ni_3Al coatings. From the figure it can be observed that the films possessed equisized densely packed grains reflecting a smooth homogeneous surface. However, the film with 0 W Cr or 10 W Cr shows the higher percentage of pores over the surface which decreases with increase in Cr content in the film.

This led to a decrease in surface roughness as the presence of void fraction decreased.

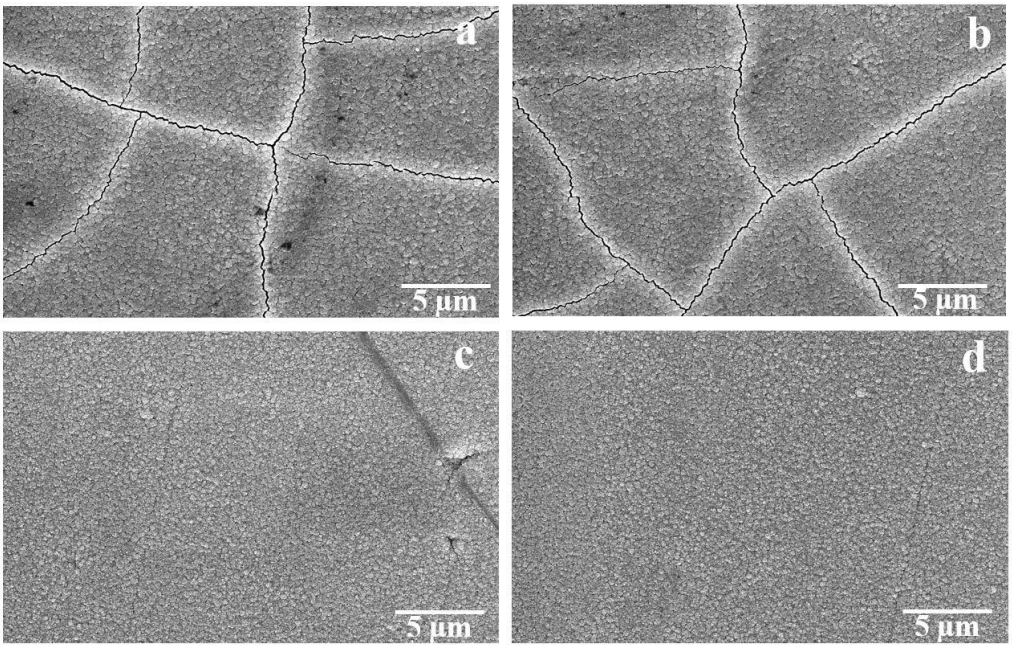

Figure 6.4: FESEM images of Cr-Ni_3Al films **(a)** 0 W Cr **(b)** 10 W Cr **(c)** 20 W Cr **(d)** 30 W Cr

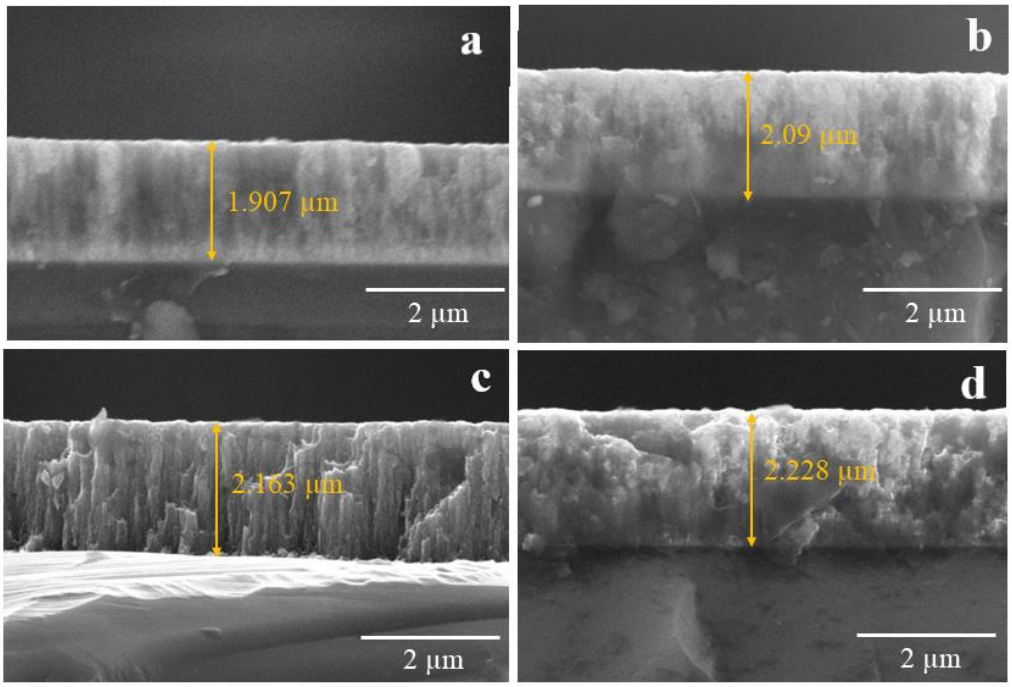

Figure 6.5: Cross-sectional thickness of deposited films **(a)** 0 W Cr **(b)** 10 W Cr **(c)** 20 W Cr **(d)** 30 W Cr

Image J software was used to calculate the grain size and porosity in the film from the FESEM images. Results revealed that the 0 W Cr possesses the maximum percentage of porosity (9.10 %) and the highest value of the grain size (88 ± 2.5) nm whereas the 30 W Cr possesses the lowest percentage of porosity (7.66 %) and least value of grain size (71 ± 1.5 nm). The cross-sectional thickness of the films is displayed in **figure 6.5**. The thickness of the film increased with increase in the Cr content with the evidence of the formation of columnar grains that grow with respect to increase in the deposition time and Cr content.

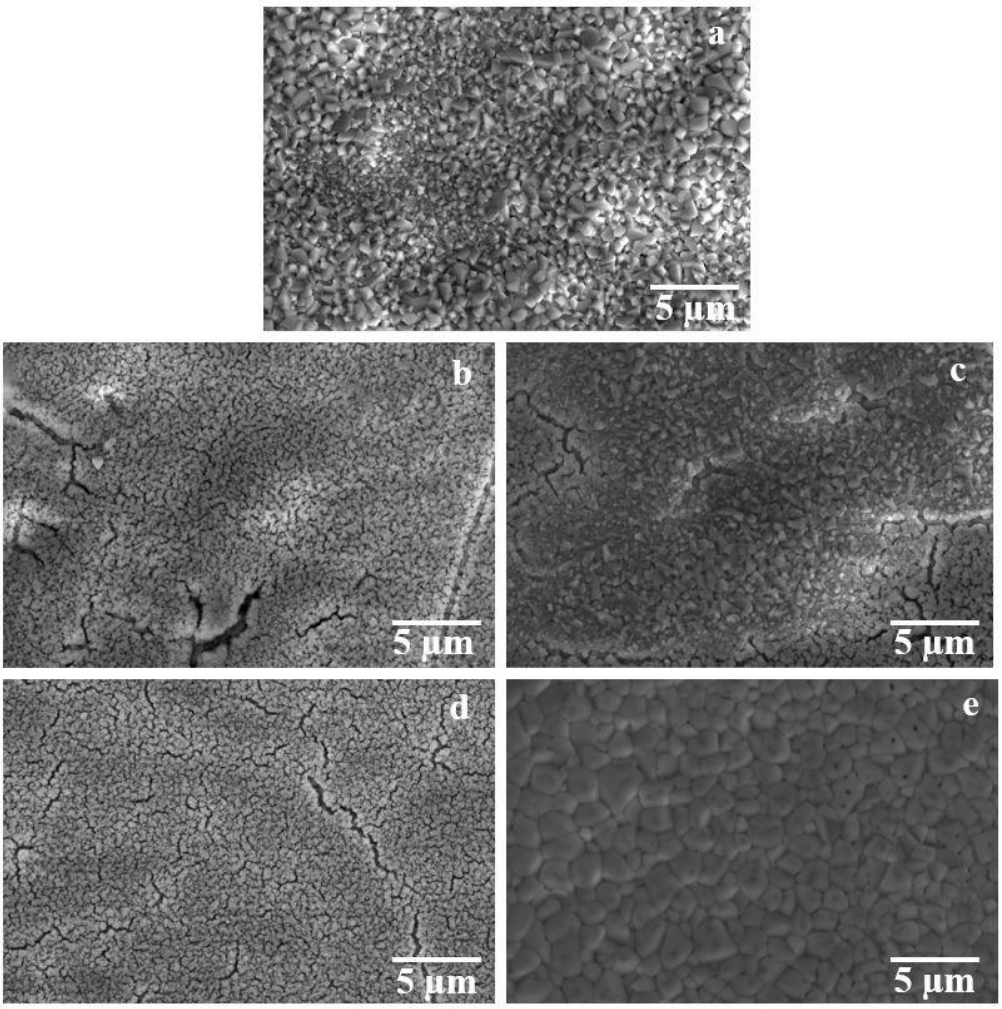

Figure 6.6: FESEM images of oxidized samples at 900°C **(a)** Substrate **(b)** 0 W Cr **(c)** 10 W Cr **(d)** 20 W Cr **(c)** 30 W Cr

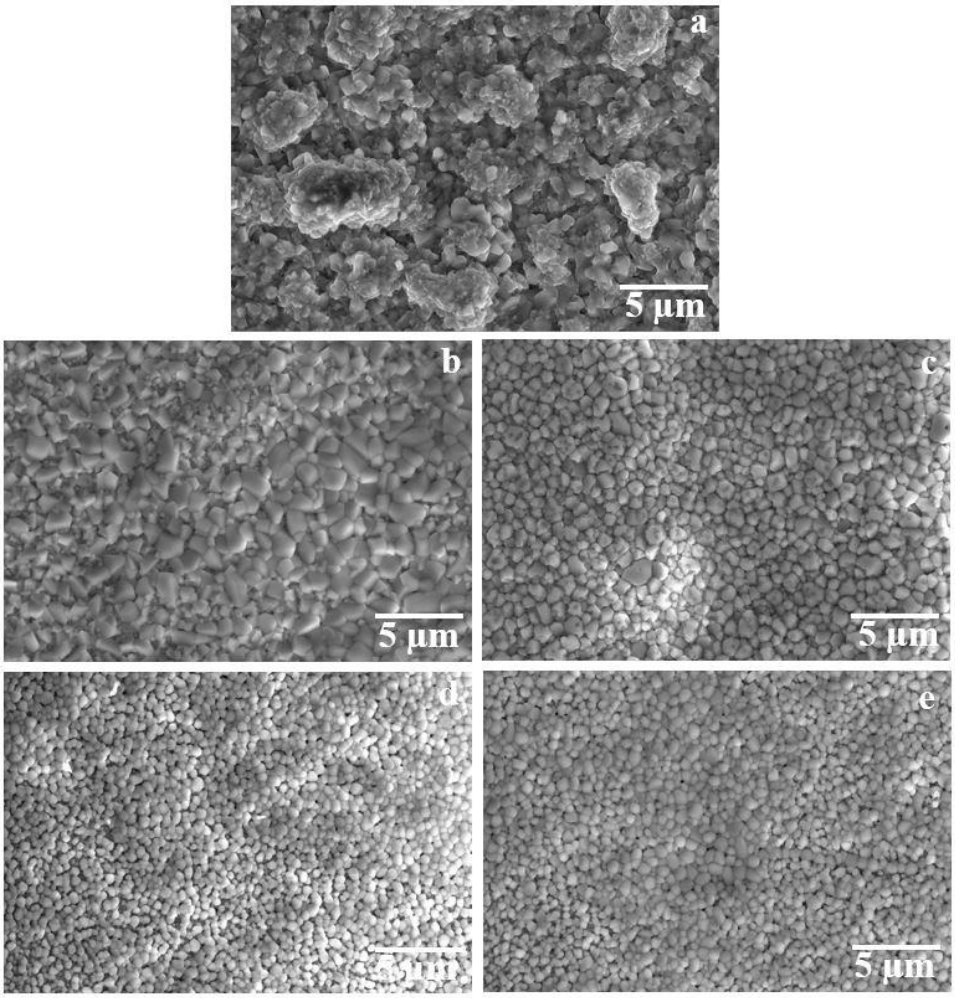

Figure 6.7: FESEM images of oxidized samples at 1000℃ **(a)** Substrate **(b)** 0 W Cr **(c)** 10 W Cr **(d)** 20 W Cr **(e)** 30 W Cr

The microstructure of the substrates and deposited films oxidized at 900℃, 1000℃ and 1100℃ have been shown in **figure 6.6**, **figure 6.7** and **figure 6.8** respectively. Furthermore, the elemental composition of the film after oxidation at various temperatures has been indexed in **table 6.4**. The microstructure of the substrate oxidized at various temperatures displays the existence of nano cracks and pores as a result of spallation of the oxidation layers from the surface of the substrate. At oxidation temperature of 900℃ **(figure 6.6)**, the 0 W Cr film showed the presence of microcracks which further decreased with increase in Cr concentration and finally disappeared in 30 W Cr film with the formation of compact integrity of larger grains. Increase in the percentage of Al as shown in **table 6.4**, indicates the formation of a high percentage of Al_2O_3 oxide layer which prevents the substrate from being

drastically oxidized at 900℃. Furthermore, at an oxidation temperature of 1000℃, the EDS data shows a smaller amount of Al as compared to that of 900℃. This indicates a higher rate of oxidation which results in the development of a larger volume of pores in the microstructure of the substrate and the deposited film as displayed in **figure 6.7**.

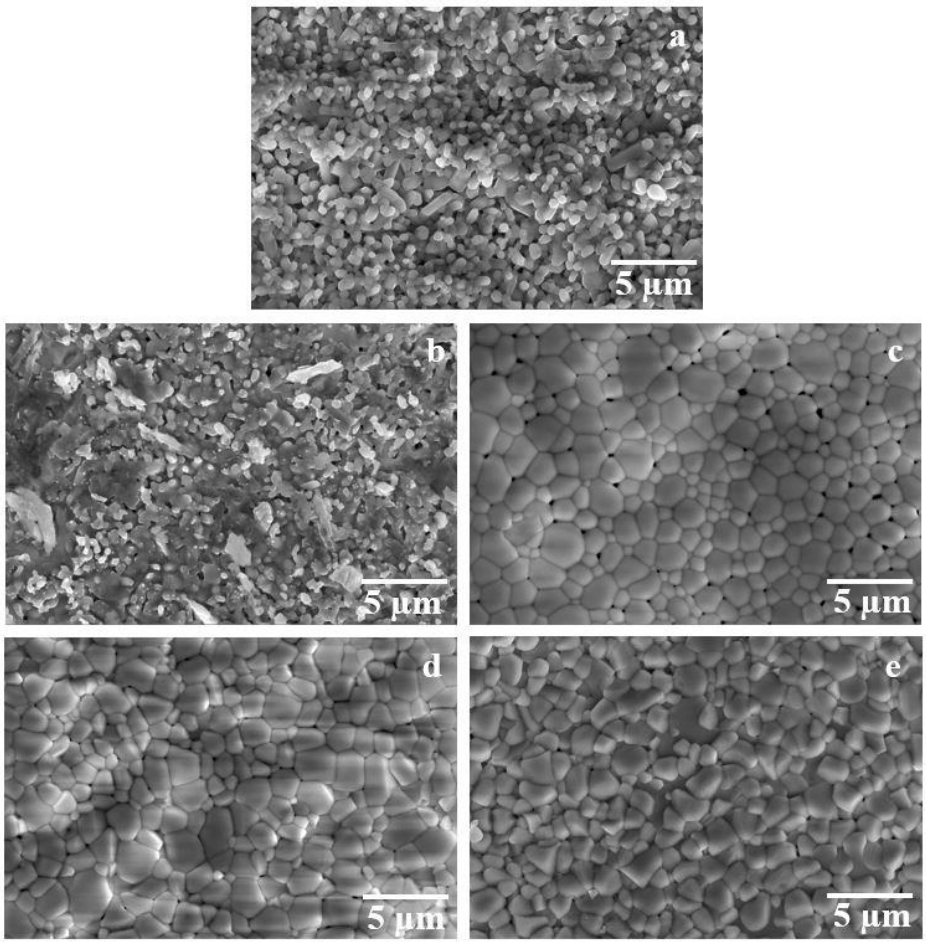

Figure 6.8: FESEM images of oxidized samples at 1100℃ **(a)** Substrate **(b)** 0 W Cr **(c)** 10 W Cr **(d)** 20 W Cr **(e)** 30 W Cr

However, it is found that the grain size of the film decreases with rise in the concentration of Cr when oxidized at the temperature of 1000℃. The substrate and 0 W Cr film showed a higher rate of spallation with maximum percentage of cracks and pores when oxidized at 1100℃ **(figure 6.8)**. This could be the result of the formation of low percentage of protective Al_2O_3 and Cr_2O_3 layers as there is a continuous spallation of oxidation layers followed by further oxidation. 10 W Cr films showed less spalled structures with visible micro pores promoting oxidation that disappears in 20 W Cr and 30 W Cr.

Table 6.4: EDS results of substrate and Cr-Ni_3Al films oxidized at different temperatures

Elements	Oxidized at 900°C				Oxidized at 1000°C				Oxidized at 1100°C			
	0 W Cr	10 W Cr	20 W Cr	30 W Cr	0 W Cr	10 W Cr	20 W Cr	30 W Cr	0 W Cr	10 W Cr	20 W Cr	30 W Cr
OK (at%)	51.12	50.27	45.63	41.66	53.87	43.98	43.35	39.31	74.14	47.45	48.97	54.22
AlK (at%)	2.55	3.33	10.32	13.23	0.72	1.96	4.69	5.30	1.21	0.58	0.86	1.78
CrK (at%)	0.5	1.89	3.46	3.60	0.62	3.48	3.15	4.61	1.3	2.17	2.06	2.90
NiK (at%)	45.83	44.51	40.58	41.51	44.79	50.58	48.81	50.78	23.36	49.81	48.12	41.11

The surface topography and the surface properties of substrate and as-deposited Ni_3Al and Cr-Ni_3Al films have been shown in **figure 6.9**. An area of 50 x 50 μm^2 was scanned in contact mode using a cantilever probe of AFM to analyze and calculate the surface topography and roughness (rms) of the deposited coatings. From **figure 6.9 (a)** it can be seen that the substrate showed a unidirectional arrangement of surface asperities as a result of surface polishing. The as-deposited Ni_3Al **figure 6.9 (b)** and Cr enriched Ni_3Al films **figure 6.9 (c, d, e)** showed almost similar surface topography consisting of unidirectional orientation of hill-type nano asperities. However, with rise in concentration of Cr in the host Ni_3Al matrix, the surface roughness (rms) of the coating decreases as indexed in **table 6.3**. The surface topography of the deposited coatings degraded as a result of high-temperature oxidation as shown in **figure 6.10**. This is because of the absorption of oxygen in the film that promotes the formation of dome-shaped larger asperities which are non-uniformly distributed over the deposited surface. The results of AFM reveal that the surface roughness of the Ni_3Al and Cr-Ni_3Al coatings increases with rise in oxidation temperature. However, the surface roughness declines as a result of increase in Cr content in host Ni_3Al alloy films. The values of surface roughness of the oxidized substrates and films have been tabulated in **table 6.5.**

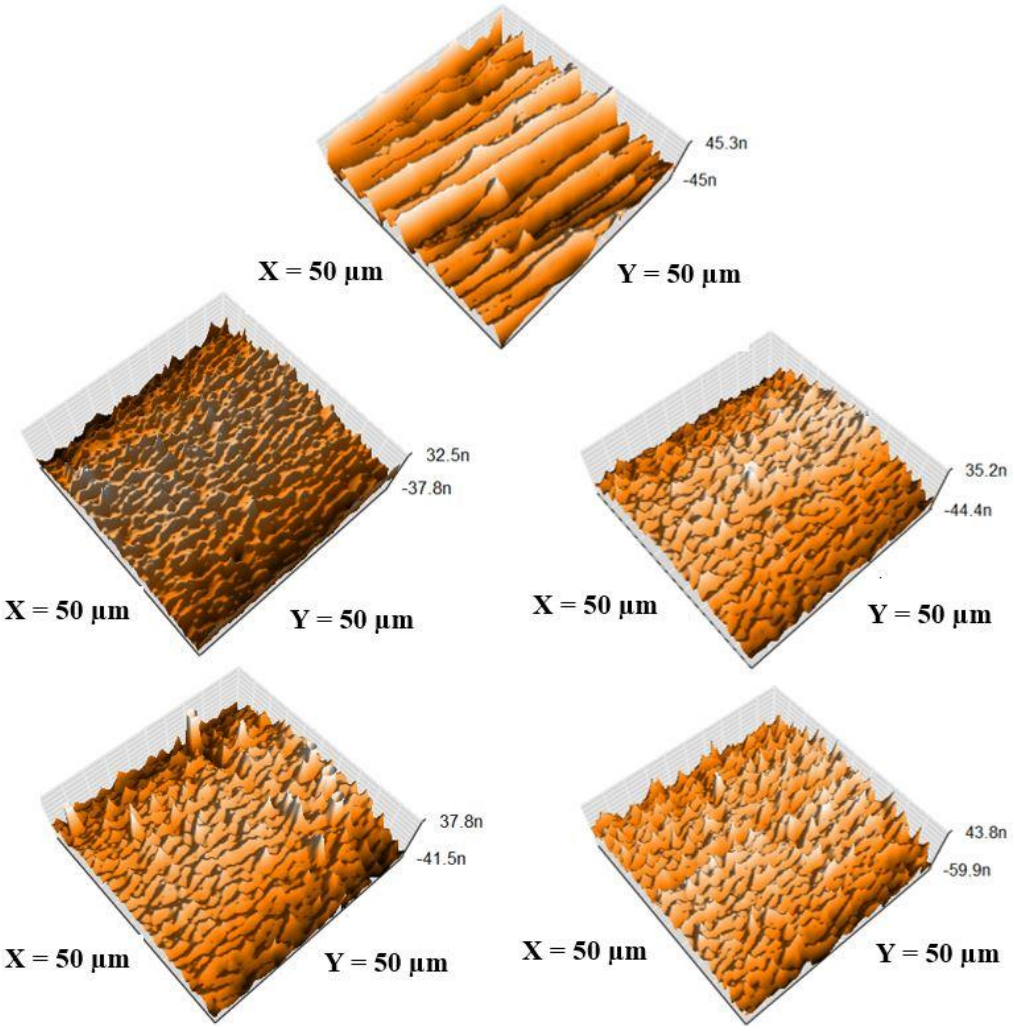

Figure 6.9: 3D AFM images of substrate as-deposited Cr-Ni_3Al films **(a)** Substrate **(b)** 0 W Cr **(c)** 10 W Cr **(d)** 20 W Cr **(e)** 30 W Cr

Table 6.5: Surface roughness of oxidized Ni_3Al and Cr-Ni_3Al films

SN	Sample	Surface roughness of as-deposited films (nm)	Surface roughness after oxidation at 900°C (nm)	Surface roughness after oxidation at 1000°C (nm)	Surface roughness after oxidation at 1100°C (nm)
1.	Substrate	17.00 ± 0.50	139 ± 2.0	291 ± 5.0	484 ± 8.0
2.	0 W Cr	16.16 ± 0.50	125 ± 2.0	253 ± 5.0	305 ± 5.0
3.	10 W Cr	15.50 ± 0.50	72 ± 1.5	179 ± 3.0	241 ± 4.0
4.	20 W Cr	13.70 ± 0.50	26 ± 1.0	117 ± 1.5	122 ± 1.5
5.	30 W Cr	12.40 ± 0.50	21 ± 1.0	55 ± 1.5	84 ± 1.5

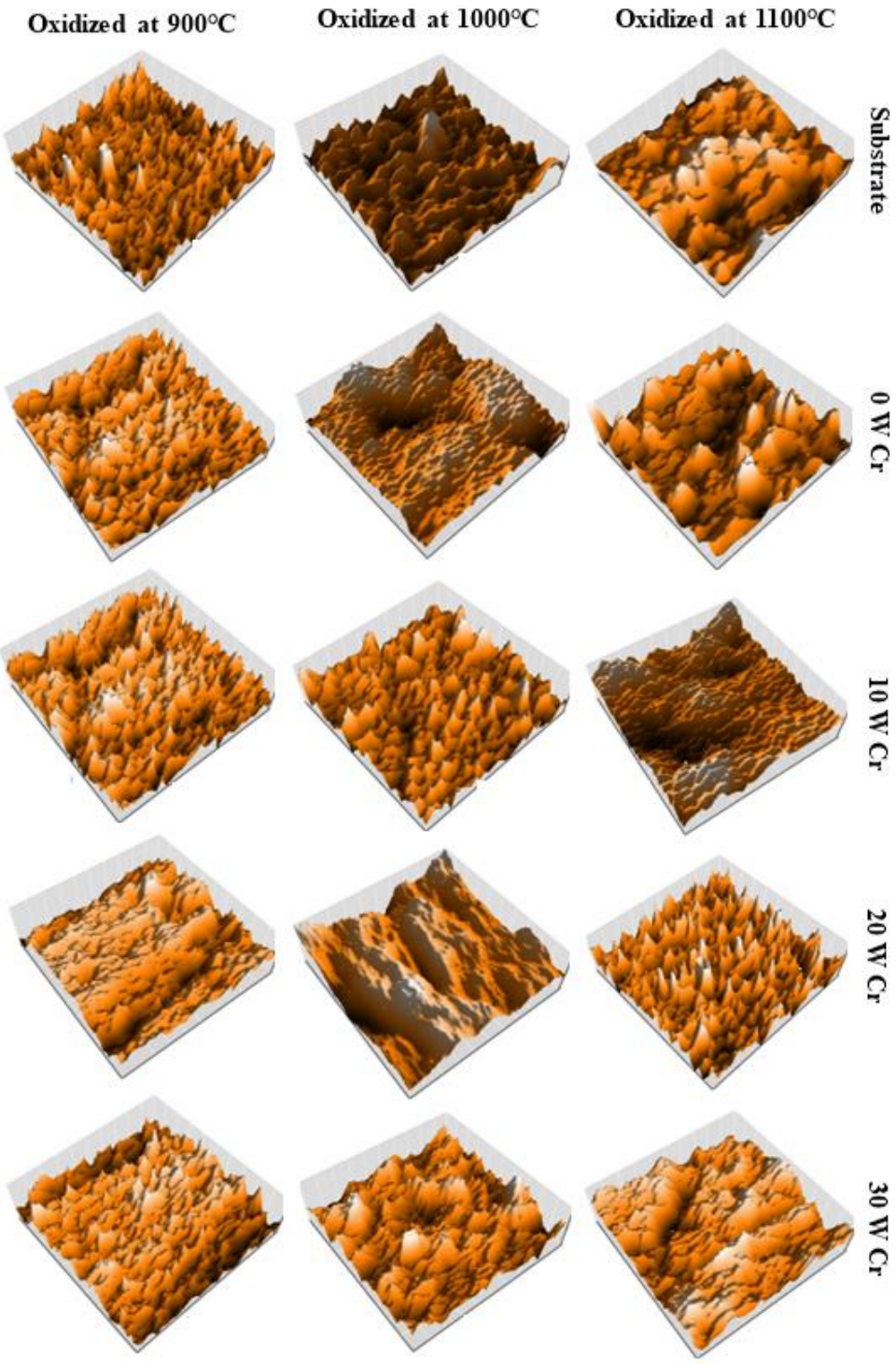

Figure 6.10: 3D AFM images of Substrate, Ni_3Al and Cr-Ni_3Al films oxidized at different temperatures

Nanoindentation was used to study the adhesive properties of Ni_3Al and Cr-Ni_3Al films at room temperature. The relation between the normal load and friction coefficient is plotted in **figure 6.11.**

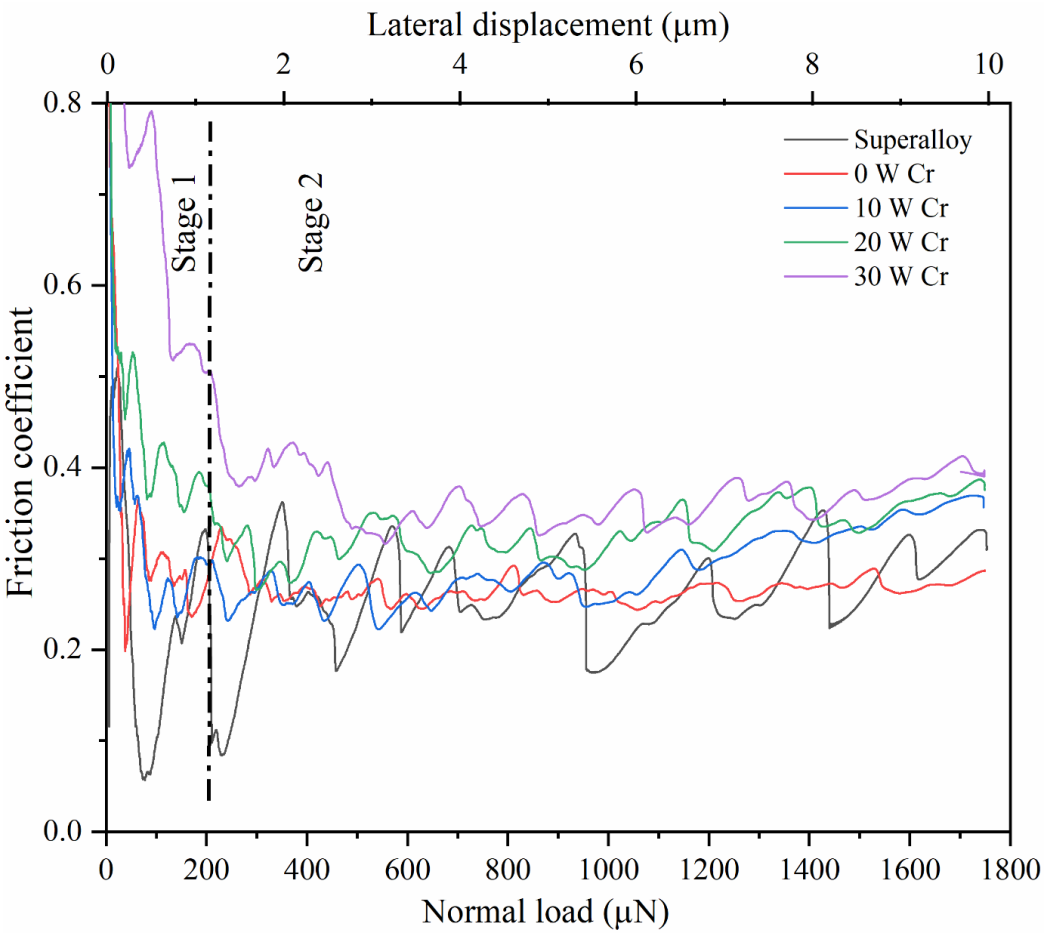

Figure 6.11: Relationship between normal load and friction coefficient of the substrate, Ni_3Al and Cr-Ni_3Al films

From the **figure 6.11** it can be seen that all the synthesized coatings along with the substrate showed a high coefficient of friction with a high amplitude of vibrations in stage 1. This could be the result of high resistance to deformation during the initial loading of indentation in stage 1. This is evidence of the formation of microcracks at the edges of the scratch line cavity. Furthermore, with an increase in progressive load beyond 200 μN, a constant coefficient of friction with low amplitude of vibrations is observed indicating the formation of microcracks at the edges of the scratch cavity. The high amplitude of vibration in the substrate throughout the scratch length indicates formation of larger cracks resulting in the high rate of variations in coefficient of friction. However, it can be seen that with rise in concentration of Cr in host Ni_3Al, the coefficient of friction increases. This shows that the rate of delamination

declines with rise in concentration of Cr in the Ni_3Al film. Hence the adhesion strength of the Ni_3Al films increases with increase in the Cr concentration.

The results of weight change per unit area versus the number of cycles as a result of oxidation have been plotted in **figure 6.12** to understand the kinetics of oxidation**.**

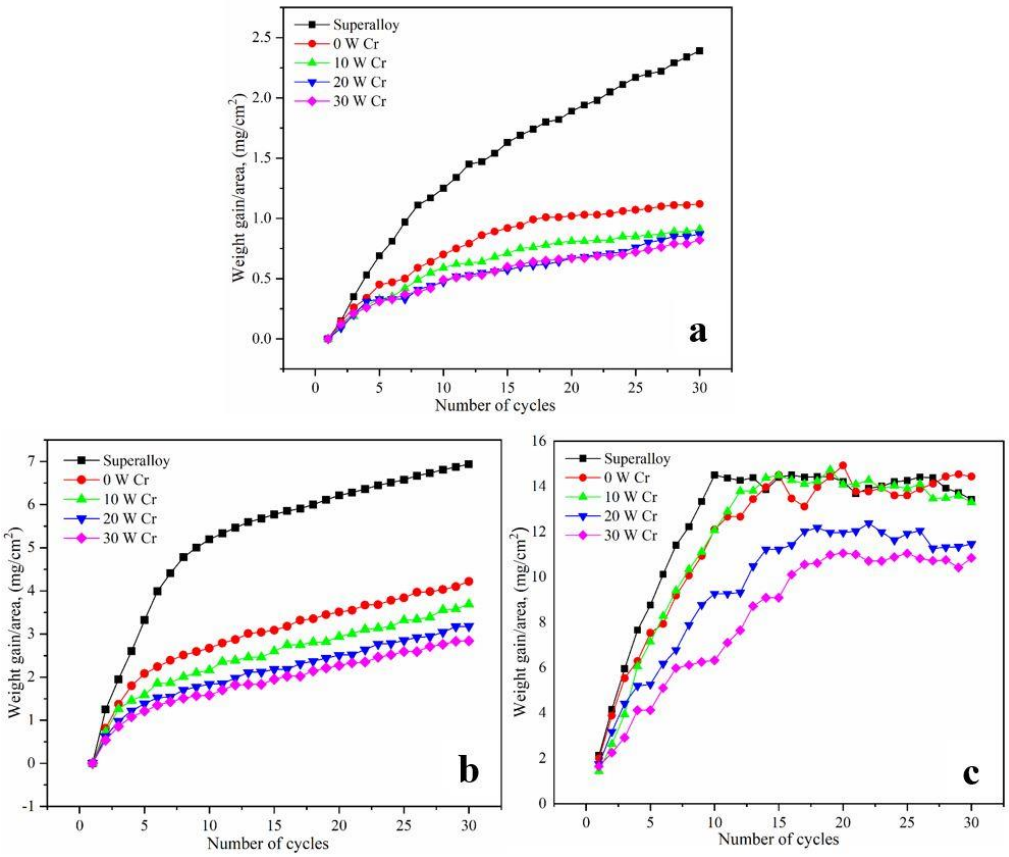

Figure 6.12: Weight gain/area versus number of cycles **(a)** Cr-Ni_3Al oxidized at 900°C **(b)** Cr-Ni_3Al oxidized at 1000°C **(c)** Cr-Ni_3Al oxidized at 1100°C

From **figure 6.12 (a)**, it is found that the substrate is more prone to oxidation at 900°C under cyclic oxidation. However, a subsequent and continuous decrease in weight gain is observed as result of increase in Cr content in the film indicating a slow rate of oxidation. This could be the result of the formation of oxide layers over the deposited films. The same kind of result in terms of weight gain is observed for the substrate and films oxidized at 1000°C as shown in **figure 6.12 (b).** A continuous weight gain by the substrate shows a linear pattern up to 10 cycles whereas 0 W Cr and 10 W Cr showed

the increment in weight gain up to 14 cycles when oxidized at 1100℃ as shown in **figure 6.12 (c).** A discontinuity in the weight gain and weight loss is observed after the 10^{th} cycle for the bare substrate, and the 14^{th} cycle for 0 W Cr and 10 W Cr films. The drop in weight is due to the removal of the oxidized layer from the surface of the substrate and the peeling of the thin film due to the edge effect [240]. However, the appearance of the fresh surface at higher temperatures leads to further oxidation resulting in weight gain. The oxidation kinetic curves of the substrate and deposited films oxidized at different temperatures have been shown in **figure 6.13**. The square of weight change per unit area for the substrate and films oxidized at 900℃ showed a linear trend of weight gain with respect to time. This is because of the slow rate of oxidation as the chemical reaction between the oxygen and the metal is slow. This could be the result of the formation of the compact integrity of adherent protective oxide layers of Cr_2O_3 and Al_2O_3 which prohibits the diffusion of oxygen to the surface [86]. The films oxidized at 1000℃ have also shown a similar trend except the weight gain by the substrate is prominent up to 1^{st} half of the cycles. However, the results of the square of weight change per unit area for the substrate and films oxidized at 1100℃ is close to a linear trend up to 10 cycles of oxidation beyond which a discontinuity in weight change is observed as shown in **figure 6.14**. This discontinuity could be the result of extreme diffusion of oxygen which accelerates the chemical reaction and penetrates through the oxide layers to react with the metal surface leading to a rise in the rate of oxidation. This high rate of oxidation further leads to the development of another oxidation layer that contributes to further oxidations and thus results in spalling of the oxide layer. A sudden weight loss observed after 10 cycles for both the substrate and deposited films at 1100℃ is because of the removal of the oxide layers from the surface. The results conclude that the change in square of weight per unit area at 900℃, 1000℃ and 1100℃ reflects parabolic characteristics of oxidation kinetics. The values of the parabolic rate constant (K_p) of the substrate and Cr-Ni_3Al films calculated from the slope of the linear regression fitted line have been mentioned in **table 6.6**. It is observed that the value of the parabolic rate constant (K_p) increases with rise in the oxidation temperature indicating a high

rate of continuous oxidation. However, it decreases with increase in Cr concentration in the films [186].

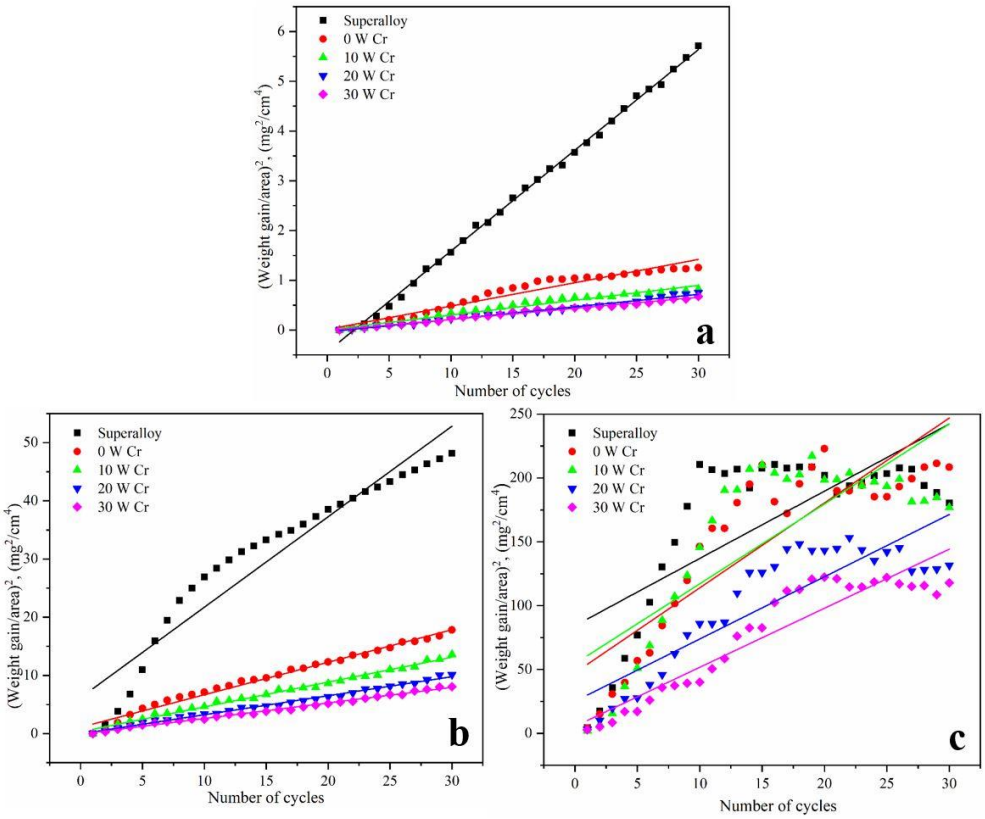

Figure 6.13: Parabolic characteristics of oxidation kinetics **(a)** Cr-Ni_3Al oxidized at 900°C **(b)** Cr-Ni_3Al oxidized at 1000°C **(c)** Cr-Ni_3Al oxidized at 1100°C

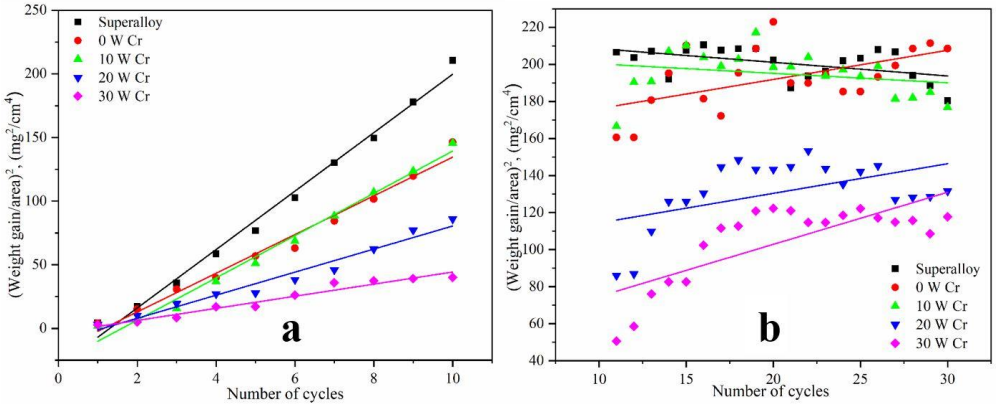

Figure 6.14: Parabolic characteristics of oxidation kinetics **(a)** Cr-Ni_3Al oxidized at 1100°C up to 10 cycles **(b)** Cr-Ni_3Al oxidized at 1100°C from 11 to 30 cycles.

Table 6.6: Parabolic rate constant of substrate and deposited Cr-Ni_3Al films

SN	Samples	Parabolic rate constant (K_p)		
		900°C	**1000°C**	**1100°C**
1	Substrate	0.20247 ± 0.00164	1.55476 ± 0.08745	5.26812 ± 0.93944
2	0 W Cr	0.04691 ± 0.00202	0.55889 ± 0.01284	6.65231 ± 0.71215
3	10 W Cr	0.02975 ± 0.00106	0.42651 ± 0.00741	6.25606 ± 0.90077
4	20 W Cr	0.0252 ± 0.00094	0.32682 ± 0.0055	4.87686 ± 0.50187
5	30 W Cr	0.02233 ± 0.00082	0.26719 ± 0.00413	4.62594 ± 0.33453

6.1.4 CONCLUSION

Ni_3Al and Cr-Ni_3Al coatings were synthesized using DC magnetron sputtering. The phase formation, microstructure, surface topography and oxidation kinetics of the substrate and deposited coatings have been studied. The results of the XRD spectrum showed the preferred orientation of Ni_3Al (111) for Ni_3Al and Cr-Ni_3Al films where as a preferred orientation of Ni (111) has been shown for substrate. The XRD spectra of Cr-Ni_3Al films showed a peak shift towards lower degree of angle with increase in Cr content in host Ni_3Al. Results of FESEM showed the presence of microcracks in 0 W Cr and 10 W Cr which decreases with increase in Cr content in host Ni_3Al films. Accordingly, the AFM results reflected a subsequent and continuous decline in the surface roughness of the coating. The maximum and minimum roughness values of 16.16 ± 0.50 nm and 12.40 ± 0.50 nm have been obtained for 0 W Cr and 30 W Cr respectively. The results of the scratch test showed that with increase in Cr concentration in Ni_3Al film, the adhesion strength between the deposited film and substrate increases. The deposited films and the substrate were exposed to high temperatures experiencing the actual cyclic attack of oxidation. Results of the tests revealed that all the films along with the substrate oxidized at high temperatures. However, the presence of Cr and the development of Al_2O_3 and Cr_2O_3 layer at high temperatures protects the superalloy from being drastically oxidized. It is found that, with rise in oxidation temperature, the value of the parabolic rate constant (K_p) increases indicating a higher rate of oxidation. It decreases with an increase in concentration of Cr indicating a lower rate of oxidation. The results of cyclic

oxidation and parabolic rate constant reveal that the superalloy and the films have a tendency to continuous oxidation. 30 W Cr has shown the slowest rate of oxidation among all the Cr-Ni_3Al at all tested oxidation temperatures.

6.2 DC MAGNETRON CO-SPUTTERED Zr-Ni_3Al FILMS

In this section, the evolution of phase, microstructure, adhesion and high-temperature oxidation resistance properties of Ni_3Al and Zr-Ni_3Al films have been explored and discussed in detail using the same characterization techniques discussed in ***SECTION 6.1.***

6.2.1 INTRODUCTION

In the last two decades transition metal-based coatings have been widely explored by several researchers in order to achieve enhanced properties in terms of hardness, wear resistance, fatigue and creep resistance along with thermal stability [13], [20], [226], [241]–[244]. These coatings have been used in automobile, aerospace, microchip, MEMS and marine industries [13], [20], [163], [226], [241]–[248]. However, the demand for coatings for their application at high temperatures has attracted the eyes of researchers toward Ni based coatings especially NiAl and Ni_3Al coatings. Several researchers have fabricated Ni_3Al-based coatings in multilayer form and found that these films possess high-temperature oxidation resistant properties with enhanced durability [68], [86], [89].

Yavorska *et al.,* [249] deposited Zr-doped NiAl coatings on pure nickel substrate using the chemical vapor deposition method. They observed that the better oxidation test of Zr-Nial coating was achieved when the atomic percent of Zr was less than 1 at % in the film. Khakpour *et al.,* [239] deposited pure aluminide and Zr-doped aluminide coatings on Inc-738 using a pack aluminizing process where they used NH_4Cl as an activator. They found that the Zr-doped aluminide coating showed better resistance against oxidation as compared to pure aluminide coatings. Yovorska *et al.,* [230] deposited Zr-doped aluminide coatings on M247 and M200 superalloys using the chemical vapor deposition method. They proclaimed that the addition of Zr in aluminide coatings improved the oxidation resistance properties of superalloys.

However, there is very limited literature reported so far explaining the oxidation-resistant properties of doped Ni_3Al films in alloy form. This work reports the synthesis and characterization of Ni_3Al and Zr doped Ni_3Al films

in alloy form for their microstructural, adhesive and high-temperature oxidation resistant properties.

6.2.2 EXPERIMENTAL DETAILS

6.2.2.1 Synthesis of Ni_3Al and Zr-Ni_3Al films

Ni_3Al and Zr-Ni_3Al films were deposited on Inconel-718 substrate using DC magnetron sputtering and co-sputtering respectively. The deposition process and the parameters of deposition were kept constant as discussed in **section 6.1.2.1** except the use of Zr target at the place of Cr to synthesize the Zr-Ni_3Al films namely 0 W Zr, 10 W Zr, 20 W Zr and 30 W Zr. The parameters of deposition of Zr-Ni_3Al films have been shown in **table 6.7**.

Table 6.7: Sputtering parameters for depositing Zr-Ni_3Al films with variation in Zr content

Targets	Zr & Ni_3Al
Substrates	Inconel-718
Base pressure	3×10^{-6} mbar
Sputtering gas	Argon (30 sccm)
Sputtering pressure	3×10^{-2} mbar
Sputtering power (Ni_3Al)	250 W DC
Sputtering power (Zr)	**0 W, 10 W, 20 W and 30 W**
Substrate temperature	400°C
Deposition time	60 minutes

6.2.2.2 Characterization details

The Ni_3Al and Zr-Ni_3Al films deposited on the Inconel-718 substrate were characterized to investigate the evolution of phase, microstructure, surface topography, adhesion and high-temperature oxidation resistance properties. The characterization techniques and the testing parameters for Ni_3Al and Zr-Ni_3Al films were the same as discussed in **section 6.1.2.2**.

6.2.3 RESULTS AND DISCUSSION

The Inconel-718 in its initial state reflected a dark brown color which upon polishing showed a dark silver color whereas the as-deposited Zr-Ni_3Al films were black in color. Upon oxidation at various temperatures, the color of the substrate and coatings changed simultaneously. The color of the substrate changed from dark silver to dark brown whereas the deposited films 0 W Zr, 10 W Zr, 20 W Zr and 30 W Zr changed to light greenish blue, moderate blue, dark blue and dark brown after oxidation at 900℃ respectively. With rise in oxidation temperature, the substrate and the deposited coatings changed to light dark which finally converted into dark black when oxidized at 1100℃.

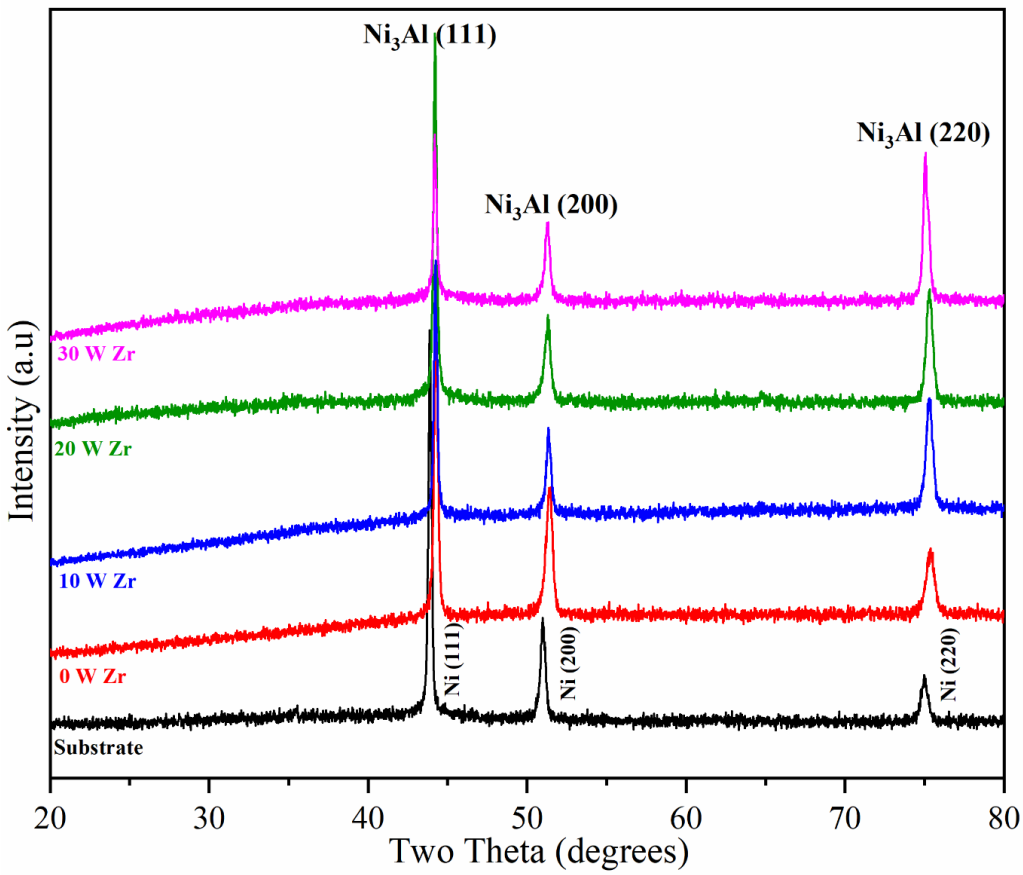

Figure 6.15: XRD Spectra of as-deposited Ni_3Al and Zr-Ni_3Al films

Figure 6.15 reflects the XRD spectra of Inconel-718 and as-synthesized Ni_3Al and Zr-Ni_3Al films. The spectrum of substrate showed the preferred orientation of Ni (111) at 43.86° followed by low intensity peak of Ni (200) at 50.97° and Ni (220) at 74.98° whereas the spectrum of 0 W Zr showed the prominent peak of Ni_3Al (111) at 44.26° followed by Ni_3Al (200) at 51.4° and

Ni_3Al (220) at 75.42° of FCC structure. These peaks of 0 W Zr are in accord with the standard intermetallic ordering of $L1_2$ FCC structure at 44.11° (111), 51.39° (200) and 75.64° (220). However, the spectra of Zr-Ni_3Al films showed the preferred orientation of (111) texture, but a continuous shift in all the XRD peaks towards the lower angle is seen as a result of rise in concentration of Zr in the Ni_3Al matrix (**figure 6.16)**. This could be the result of the generation of microstrain within the film as the larger Zr (160 pm) replaces the smaller Ni (124 pm) from the host Ni_3Al matrix. The value of strain in Ni_3Al and Zr-Ni_3Al calculated using **equation 1, Chapter 5**, is shown in **table 6.8.**

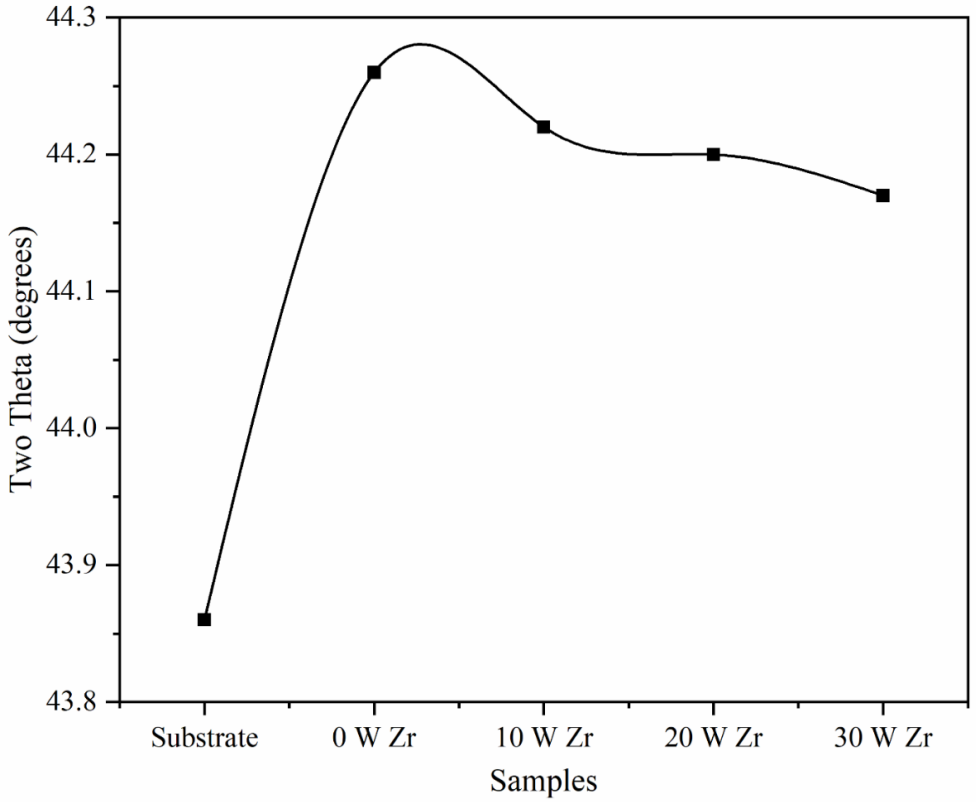

Figure 6.16: Peak shift in the prominent peak (111) of XRD Spectra of Ni_3Al and Zr-Ni_3Al films

The evolution of phases in XRD spectra of the oxidized substrate and films has been shown in **figure 6.17.** XRD spectra of substrate and 0 W Zr reflect the prominent peak of NiO (200) when oxidized at 900℃ as shown in **figure 6.17 (a)**. However, with increase in Zr content in the film, the preferred

orientation of the Zr-Ni_3Al films changed to Ni_3Al (111) for 10 W Zr 20 W Zr and 30 W Zr followed by low-intensity peaks of Ni_3Al (200), NiO, Al_2O_3, Cr_2O_3 and Fe_2O_3. The spectra of substrate and 10 W Zr film oxidized at 1000℃ showed the preferred orientation of NiO (200) texture whereas the 20 W Zr and 30 W Zr films showed the preferred orientation of Ni_3Al (111) texture. **Figure 6.17 (c)** reflects the spectra of the substrate and films oxidized at 1100℃. The spectra of the substrate showed the preferred orientation of NiO (200) and high-intensity peak of Fe_2O_3 which indicates that the substrate is more prone to oxidation at 1100℃. However, 10 W Zr and 20 W Zr showed the preferred orientation of Ni_3Al (111) indicating the existence of adherent Ni_3Al film on the substrate but the evolution of Fe_2O_3 indicated the presence of an oxidation layer as a result of peeling due to edge effect. The evolution of Al_2O_3 on the oxidized film and Cr_2O_3 peak at the edges of 30 W Zr shows evidence of the existence of oxide layers that protects the substrate from being drastically oxidized.

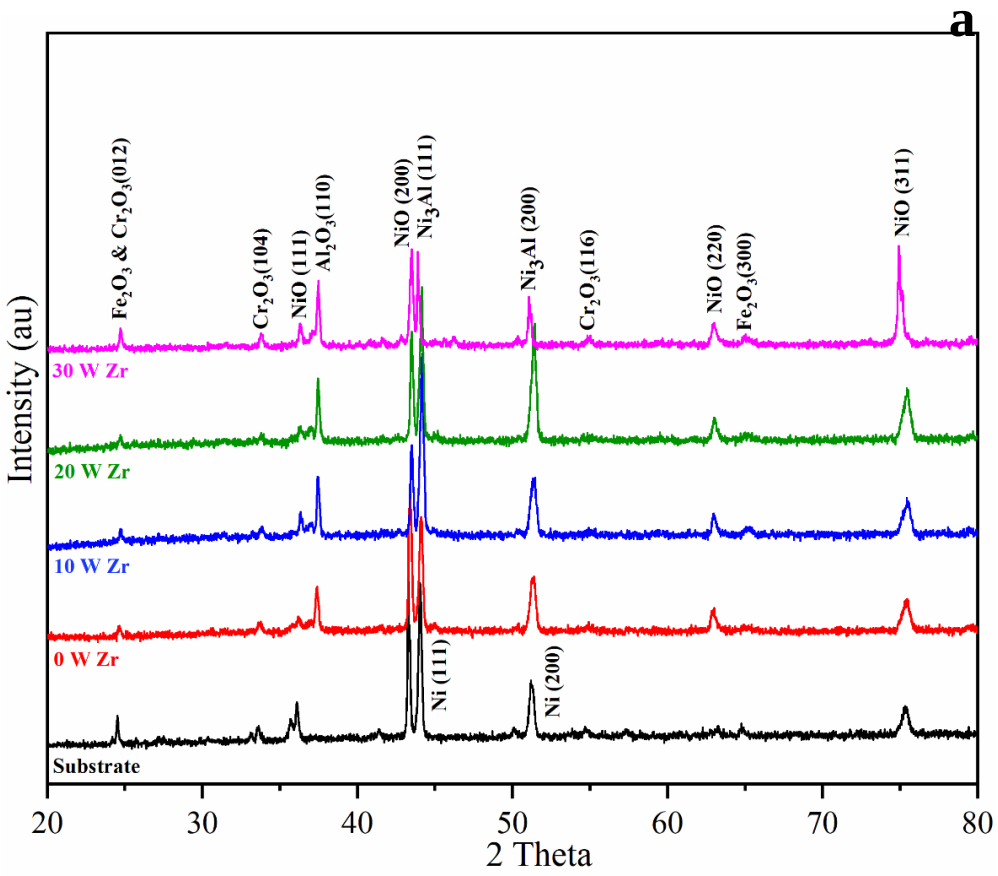

Figure 6.17 (a): XRD spectra of Ni_3Al and Zr-Ni_3Al films oxidized at 900℃

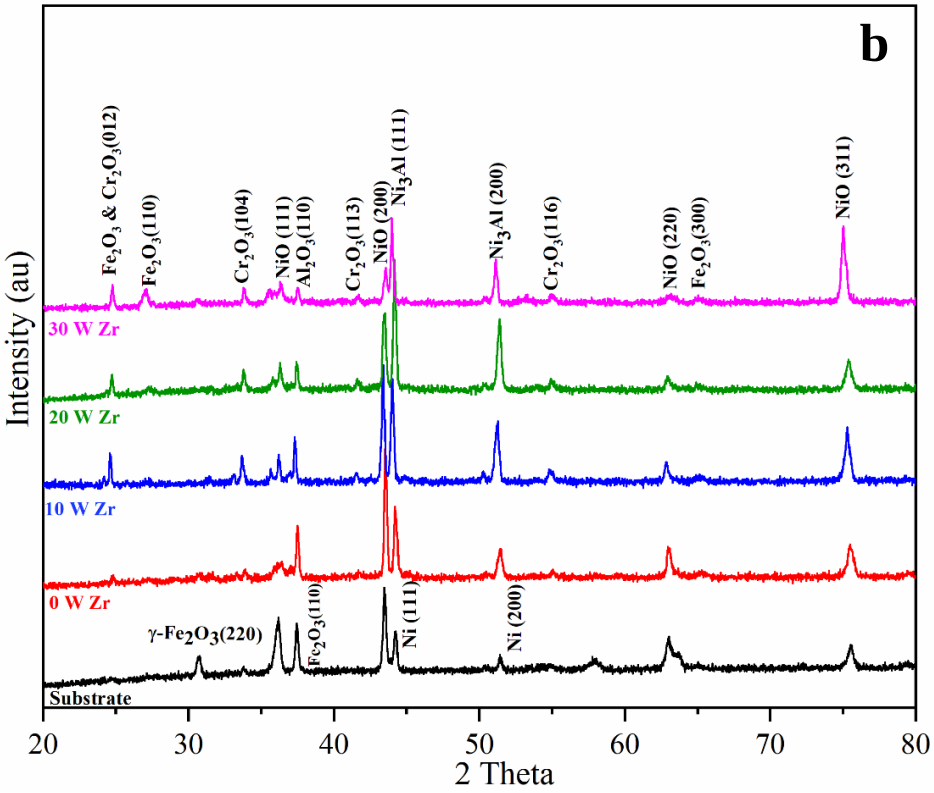

Figure 6.17 (b): XRD spectra of Ni_3Al and Zr-Ni_3Al films oxidized at 1000°C

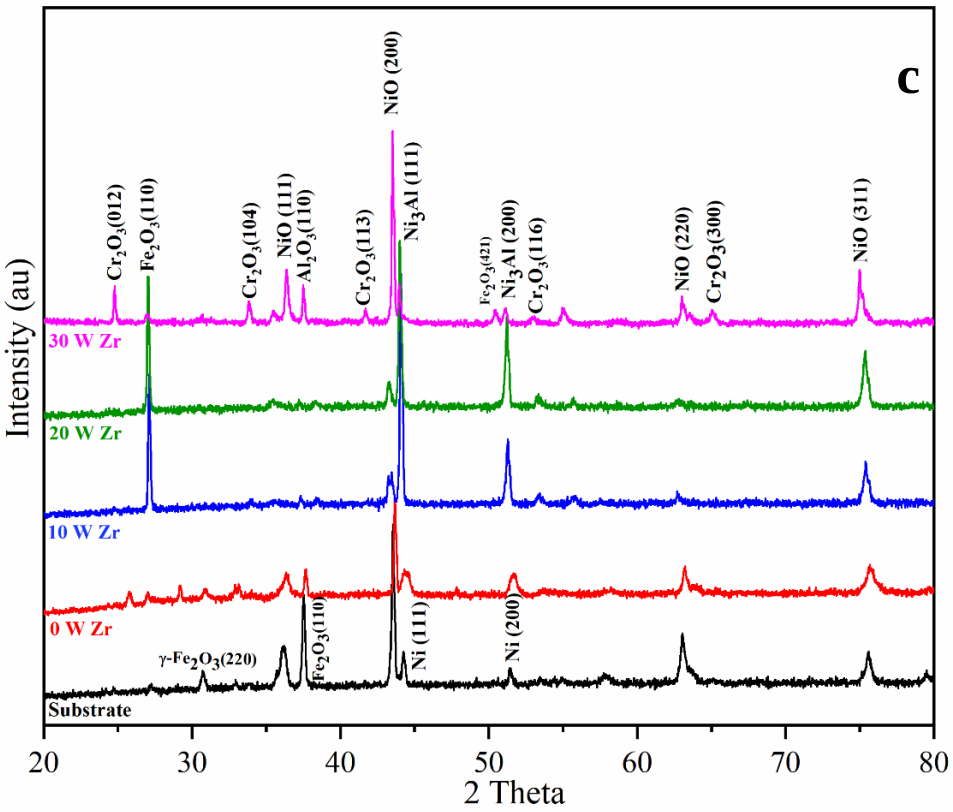

Figure 6.17 (c): XRD spectra of Ni_3Al and Zr-Ni_3Al films oxidized at 1100°C

Table 6.8: Calculated grain size, porosity, surface roughness and microstrain in Zr-Ni_3Al films

SN	Sample	Zr (%)	Grain size (nm)	Porosity (%)	Roughness (nm)	Strain
1	Substrate	0.0	NA	NA	17.00 ± 0.50	0.00283
2	0 W Zr	0.0	88.0 ± 2.5	9.12	16.16 ± 0.50	0.00345
3	10 W Zr	0.65	85.1 ± 2.5	8.89	15.17 ± 0.50	0.00352
4	20 W Zr	1.02	83.6 ± 2.5	8.42	14.36 ± 0.50	0.00359
5	30 W Zr	1.20	79.4 ± 1.5	8.21	13.12 ± 0.50	0.00364

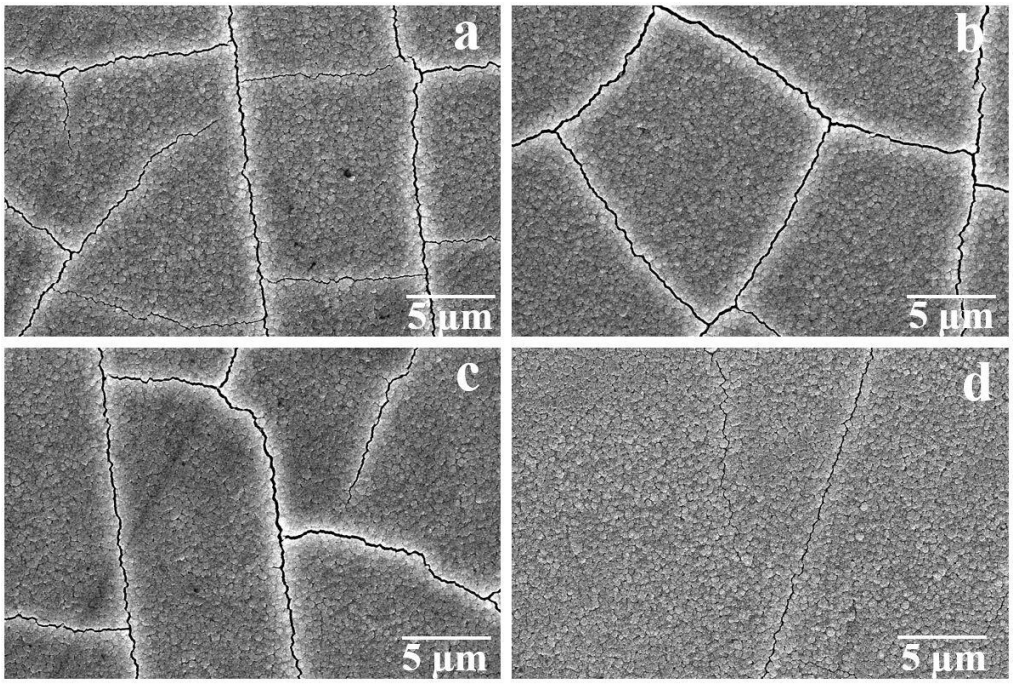

Figure 6.18: FESEM images of Zr-Ni_3Al films **(a)** 0 W Zr **(b)** 10 W Zr **(c)** 20 W Zr **(d)** 30 W Zr

The microstructure of Ni_3Al and Zr-Ni_3Al films characterized using FESEM is shown in **figure 6.18**. From the figure it is observed that 0 W Zr, 10 W Zr and 20 W Zr films possessed higher percentage of pores throughout the surface. However, it decreases with increase in Zr concentration in the Ni_3Al matrix resulting in the evolution of smooth surface morphology and structure which contributes in lowering the surface roughness of the synthesized coatings. Irrespective of the presence of microcracks, the synthesized coatings reflect the densely packed grains showing the homogeneous structure of the coating.

To calculate the average grain size and percentage of porosity in the film, Image J software was used. For this purpose, FESEM images were used in the software. Results showed that the Ni_3Al film with 0 W Zr showed the maximum percentage of cracks and porosity (9.12 %) along with the highest value of grain size (88.0 ± 2.5 nm).

The cross-sectional images of the Zr-Ni_3Al coatings are displayed in **figure 6.19**. It is observed that the thickness of the coating increases with rise in the concentration of Zr with the evidence of the formation of columnar grains during the grain growth.

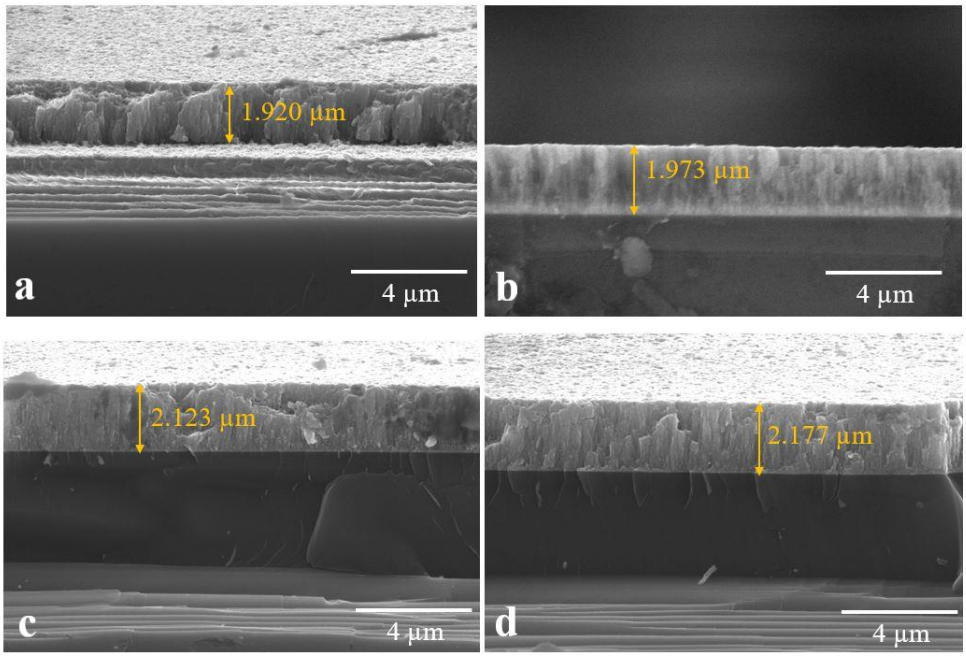

Figure 6.19: Cross-sectional thickness of deposited films **(a)** 0 W Zr **(b)** 10 W Zr **(c)** 20 W Zr **(d)** 30 W Zr

Microstructures of the deposited films oxidized at 900°C, 1000°C and 1100°C have been shown in **figure 6.20**, **figure 6.21** and **figure 6.22.** The corresponding results of elemental composition has been indexed in **table 6.9**.

The microstructure of the substrate oxidized at 900°C shows that the surface of the substrate has spalled more as compared to the surface of the synthesized coatings. Moreover, the surface spallation of substrate increases with increase in oxidation temperature to 1100°C resulting in the formation of a larger percentage of microcracks and pores. However, 10 W Zr, 20 W Zr and 30 W

Zr films oxidized at 900℃ also show the presence of microcracks and pores but they possessed tightly packed grains. The rise in the concentration of Al in Zr-Ni_3Al coatings after oxidation at 900℃ is evidence of the formation of the Al_2O_3 layer which protects the material from being drastically oxidized.

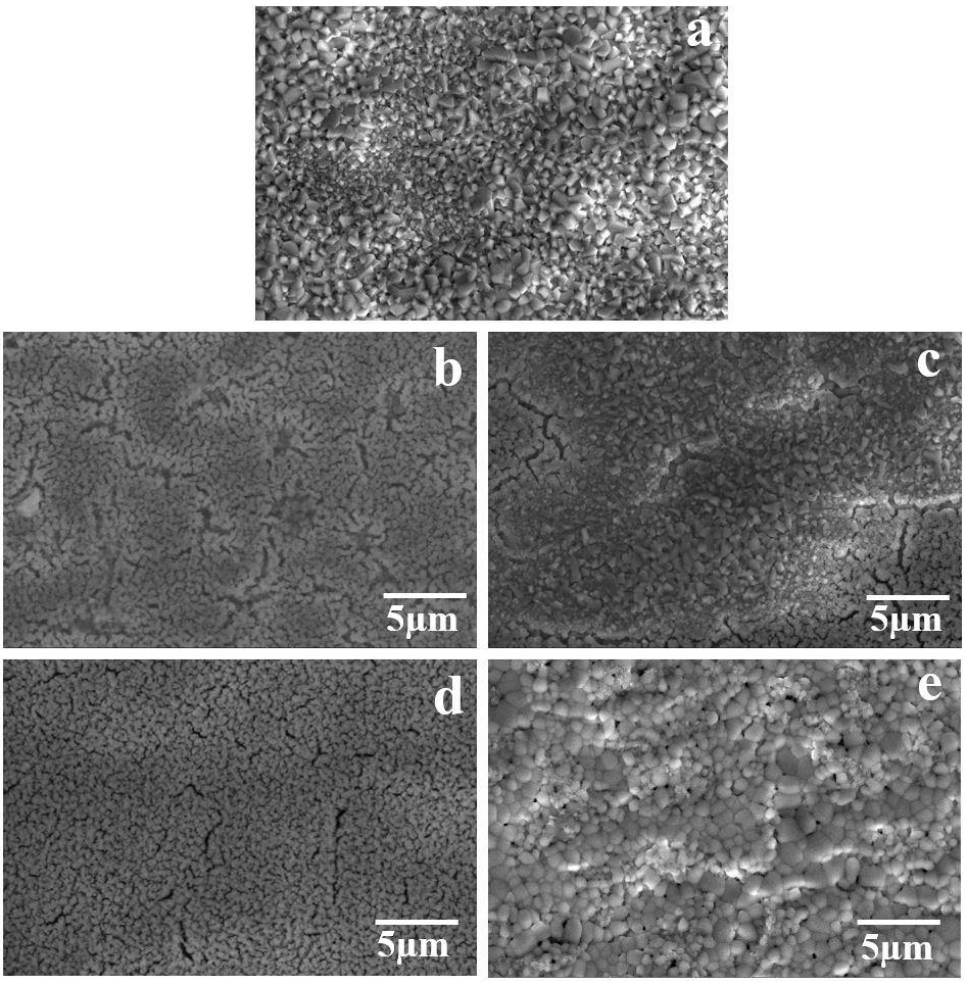

Figure 6.20: FESEM images of oxidized samples at 900℃ **(a)** Substrate **(b)** 0 W Zr **(c)** 10 W Zr **(d)** 20 W Zr **(e)** 30 W Zr

Furthermore, with the rise in oxidation temperature up to 1000℃, the concentration of Al decreases **(Table 6.9)** resulting in the formation of a small fraction of Al_2O_3 layers as compared to 900℃. This could be the result of the high rate of oxidation as oxygen reacts with the metal surface at a faster rate. From **figure 6.21,** it can be observed that there is a continuous decrease in spallation of the deposited surface with the evolution of packed microstructure when the percentage of Zr in Ni_3Al was increased up to 30 W Zr. However,

with increase in the Zr concentration in Ni_3Al films, the grain size of the film oxidized at 1000℃ also decreased resulting in the formation of less percentage of microcracks and porosity.

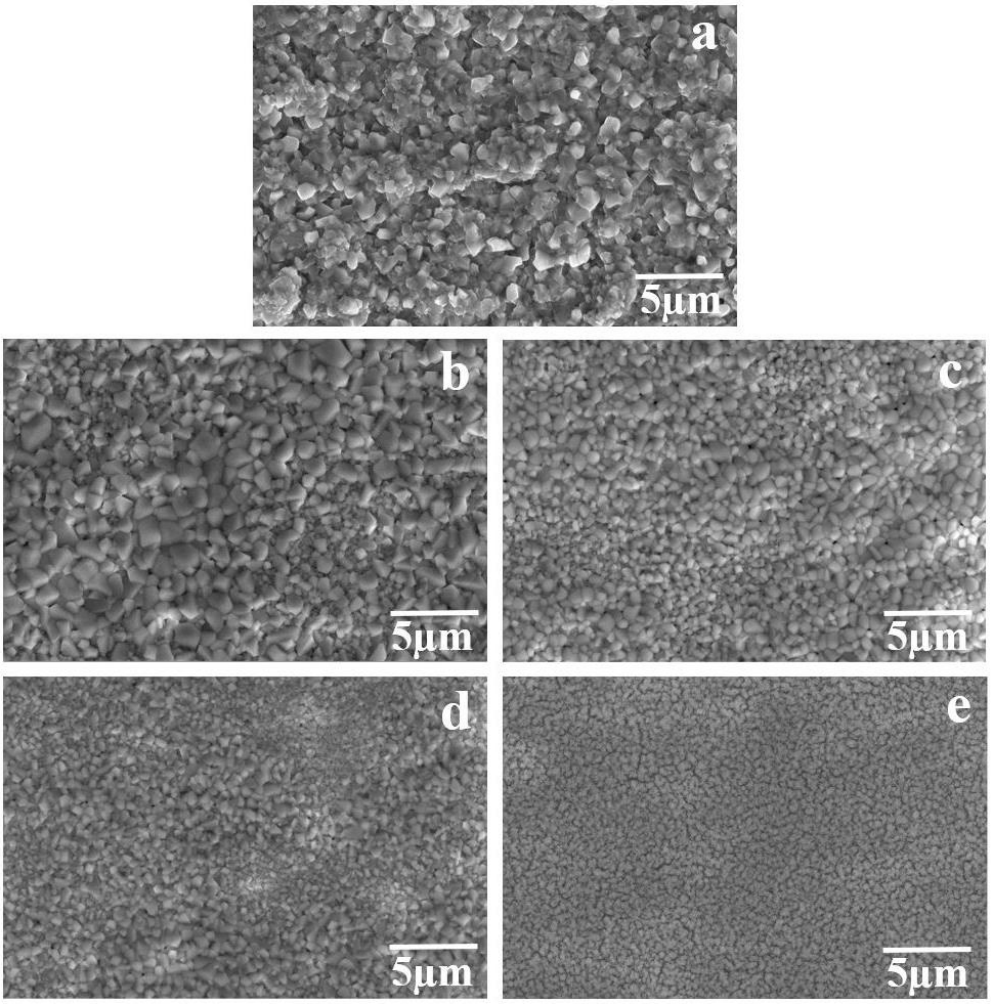

Figure 6.21: FESEM images of oxidized samples at 1000℃ **(a)** Substrate **(b)** 0 W Zr **(c)** 10 W Zr **(d)** 20 W Zr **(e)** 30 W Zr

The substrate, 0 W Zr, 10 W Zr, and 20 W Zr samples oxidized at 1100℃ show a larger number of pores due to the clustering of grains on the surface as a result of the high rate of oxidation as shown in **figure 6.22**. This could be the result of the peeling of the oxide layers from the surface because of the high rate of diffusion of oxygen with the metal surface. The film with 30 W Zr oxidized at 1100℃ showed compact integrity of grains with a smaller percentage of pores which is evident from the low oxidation rate as compared to the substrate and other deposited films oxidized at 1100℃.

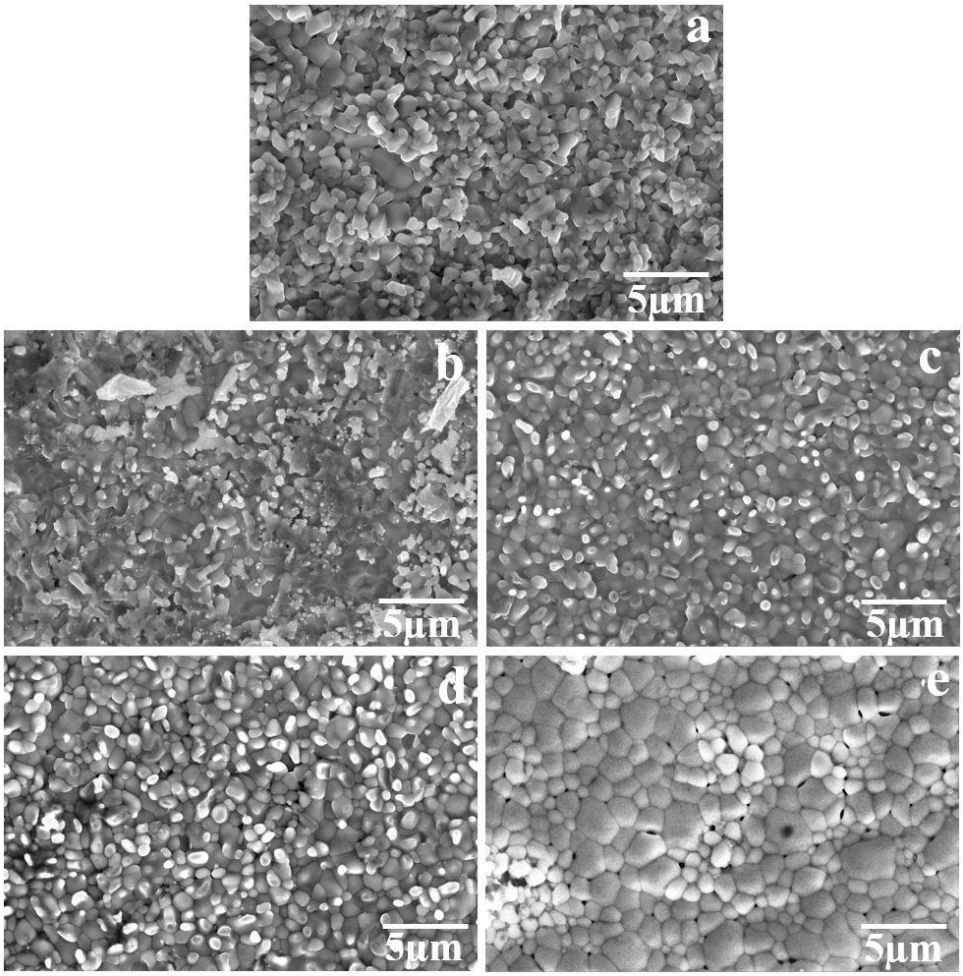

Figure 6.22: FESEM images of oxidized samples at 1100°C **(a)** Substrate **(b)** 0 W Zr **(c)** 10 W Zr **(d)** 20 W Zr **(e)** 30 W Zr

Table 6.9: EDS results of substrate and Zr-Ni_3Al films oxidized at different temperatures

Elements	Oxidized at 900°C				Oxidized at 1000°C				Oxidized at 1100°C			
	0 W Zr	**10 W Zr**	**20 W Zr**	**30 W Zr**	**0 W Zr**	**10 W Zr**	**20 W Zr**	**30 W Zr**	**0 W Zr**	**10 W Zr**	**20 W Zr**	**30 W Zr**
OK (at%)	51.12	49.30	50.73	42.37	53.87	48.29	50.85	59.15	74.14	51.13	81.24	76.27
AlK (at%)	2.55	2.57	9.70	11.50	0.72	1.30	5.60	8.06	1.21	0.51	1.62	1.82
ZrK (at%)	0.5	0.10	0.40	1.06	0.62	0.47	0.37	0.05	1.3	0.60	0.42	0.30
NiK (at%)	45.83	48.03	39.17	45.14	44.79	49.94	43.17	32.73	23.36	47.77	16.72	21.61

The AFM 3D images showing the surface topography of the substrate, Ni_3Al and Zr-Ni_3Al films have been shown in **figure 6.23**. To analyze the surface

topography and roughness of the coating, an area of 50 x 50 μm^2 was scanned using the cantilever probe of AFM in contact mode. The surface roughness (rms) of the substrate and synthesized coating was calculated using the inbuilt software in the setup. The surface topography of the polished substrate showed a long chain of unidirectional asperities. The Ni_3Al and Zr-Ni_3Al films also consisted of the nano asperities which are non-continuously aligned with the formation of nano hills and valleys. The results of the AFM showed that the enrichment of Zr in the host Ni_3Al matrix reduced the surface roughness of the coating. The maximum and the minimum surface roughness of 16.16 ± 0.5 nm and 13.12 ± 0.5 nm was observed for 0 W Zr and 30 W Zr respectively. The results of the surface roughness have been indexed in **table 6.8**.

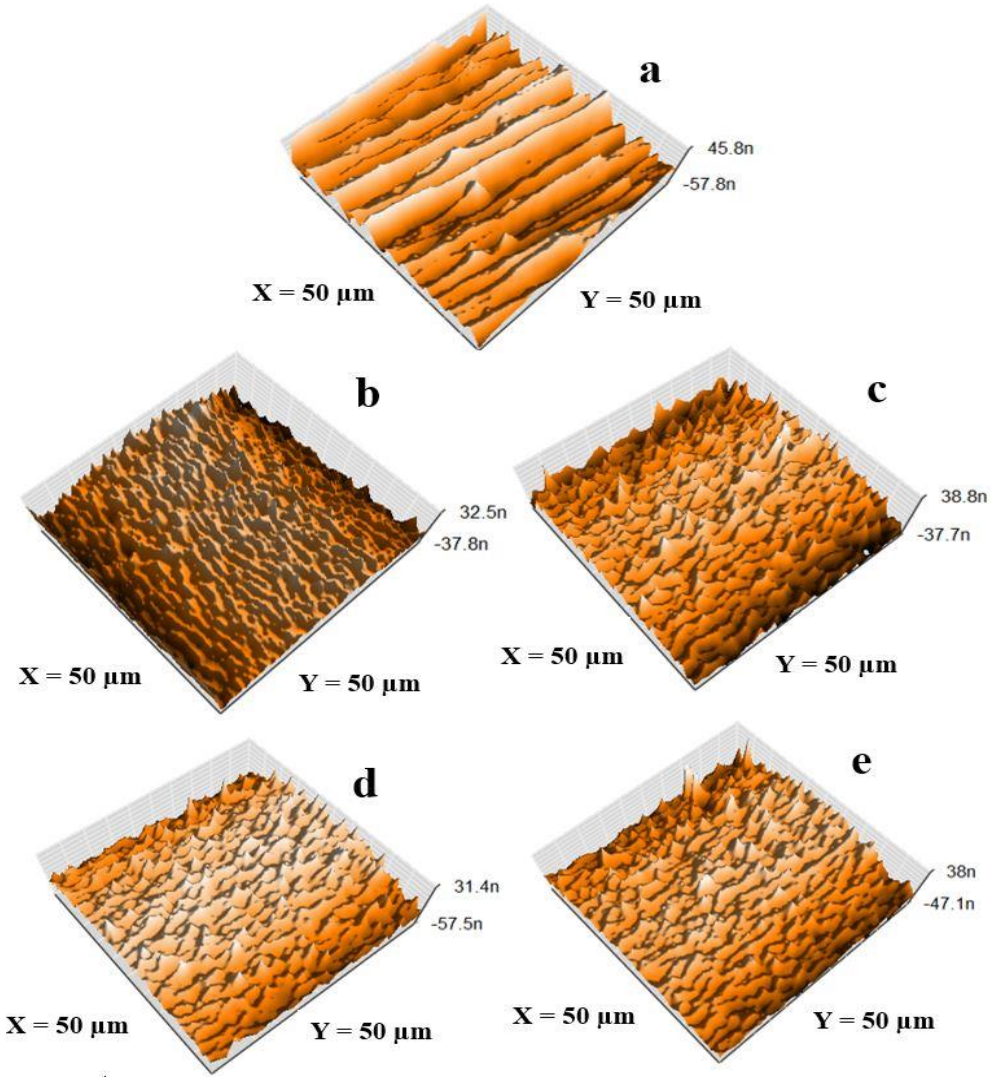

Figure 6.23: 3D AFM images of as-deposited Zr-Ni_3Al films (a) 0 W Zr (b) 10 W Zr (c) 20 W Zr (d) 30 W Zr

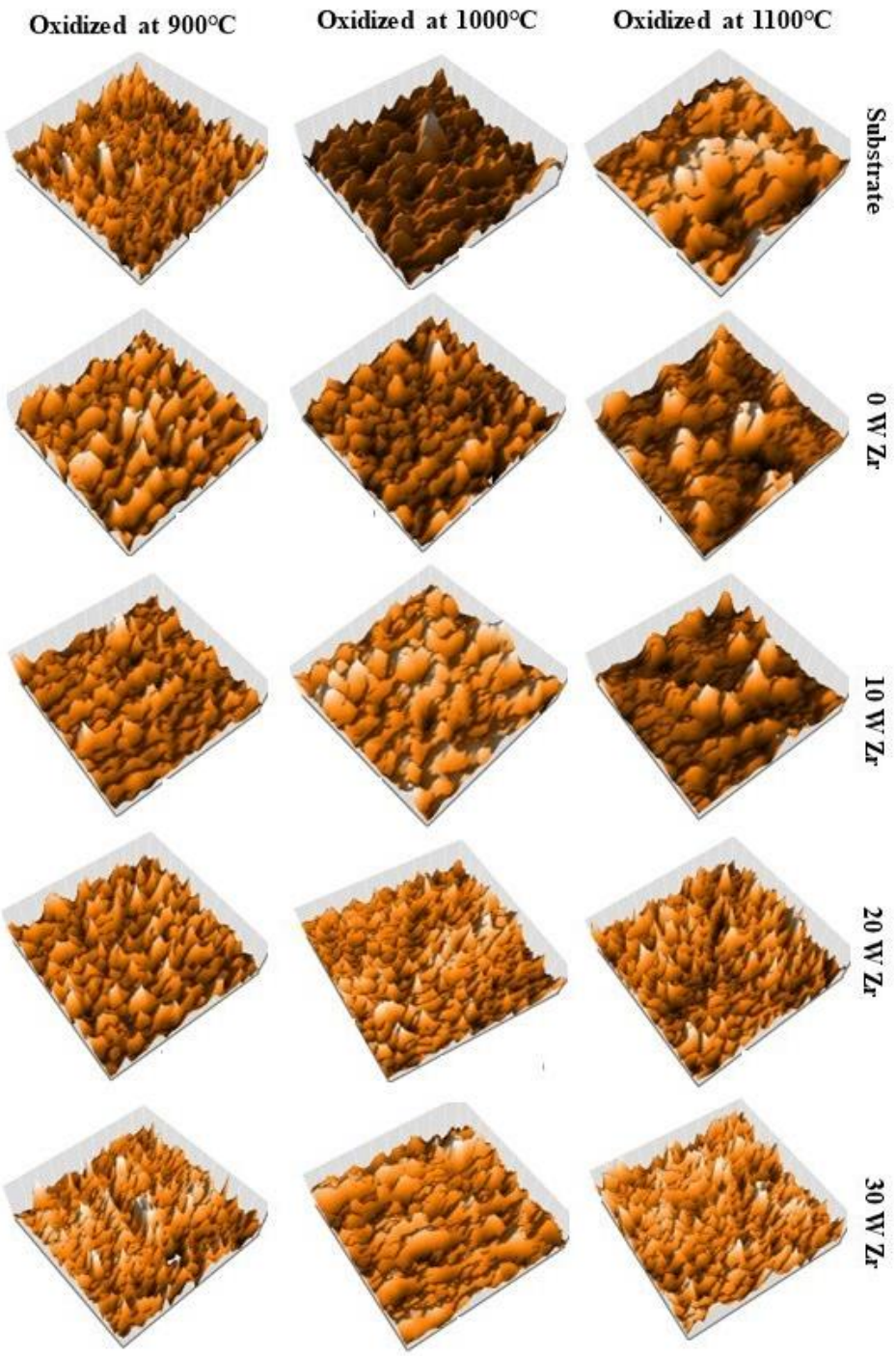

Figure 6.24 3D AFM images of Substrate, Ni_3Al and Zr-Ni_3Al films oxidized at different temperatures

The surface topography of the substrates, Ni_3Al and Zr-Ni_3Al films oxidized at different elevated temperatures has been shown in **figure 6.24**. From the figure it can be observed that the surface of the oxidized films showed larger and broader asperities as compared to the as-deposited films **(figure 6.23)**

because of the cyclic oxidation attacks. The enhancement in the dimension of the surface asperities results in increasing the roughness of the oxidized coatings. This could be the reason for the formation of non-uniformly distributed dome shapes larger hills and valleys resulting from the absorption of oxygen in the film. The results of AFM reflected that the surface roughness of the film increases continuously with increase in the oxidation temperature. However, a subsequent and gradual decline in the surface roughness of the coating has been observed with Zr enrichment in the host Ni_3Al matrix. The results of the surface roughness (rms) of the coating after the cyclic oxidation test have been indexed in **table 6.10**.

Table 6.10: Surface roughness of oxidized Ni_3Al and Zr-Ni_3Al films

SN	Sample	Surface roughness of as-deposited films (nm)	Surface roughness after oxidation at 900°C (nm)	Surface roughness after oxidation at 1000°C (nm)	Surface roughness after oxidation at 1100°C (nm)
1.	Substrate	17.00 ± 0.50	139 ± 2.0	291 ± 5.0	484 ± 8.0
2.	0 W Zr	16.16 ± 0.50	129 ± 2.0	283 ± 5.0	359 ± 5.0
3.	10 W Zr	15.17 ± 0.50	108 ± 1.5	214 ± 3.0	263 ± 4.0
4.	20 W Zr	14.36 ± 0.50	45 ± 1.0	128 ± 1.5	134 ± 1.5
5.	30 W Zr	13.12 ± 0.50	29 ± 1.0	56 ± 1.5	115 ± 1.5

To investigate the adhesive strength of Ni_3Al and Zr-Ni_3Al films, nanoindentation was used to perform the scratch test at room temperature. **Figure 6.25** shows the relationship between the friction coefficient and normal load. It is observed that the substrates and deposited films shows a high coefficient of friction having a high amplitude of vibrations during stage 1. This could be the result of the resisting force against the deformation of the substrate and deposited film during the initial stage of loading. The high amplitude in friction force indicates the formation of microcracks at the edges of the scratch cavity. Furthermore, the amplitude of vibration decreases for substrate and deposited films in stage 2 as compared to stage 1. It is evident from the constant coefficient of friction in stage 2 that there is a continuous formation of microcracks at the edges of the scratch cavity. However, it can be seen that the substrate shows a continuous vibration of higher amplitude

throughout the scratch length. This indicates the formation of larger cracks with continuous and progressive delamination. From the figure it can be observed that the coefficient of friction increases with rise in Zr content in the host Ni_3Al matrix which suggests that the rate of delamination declines with rise in Zr content. Hence, it can be said that the adhesive strength of Ni_3Al film increases with rise in the Zr content.

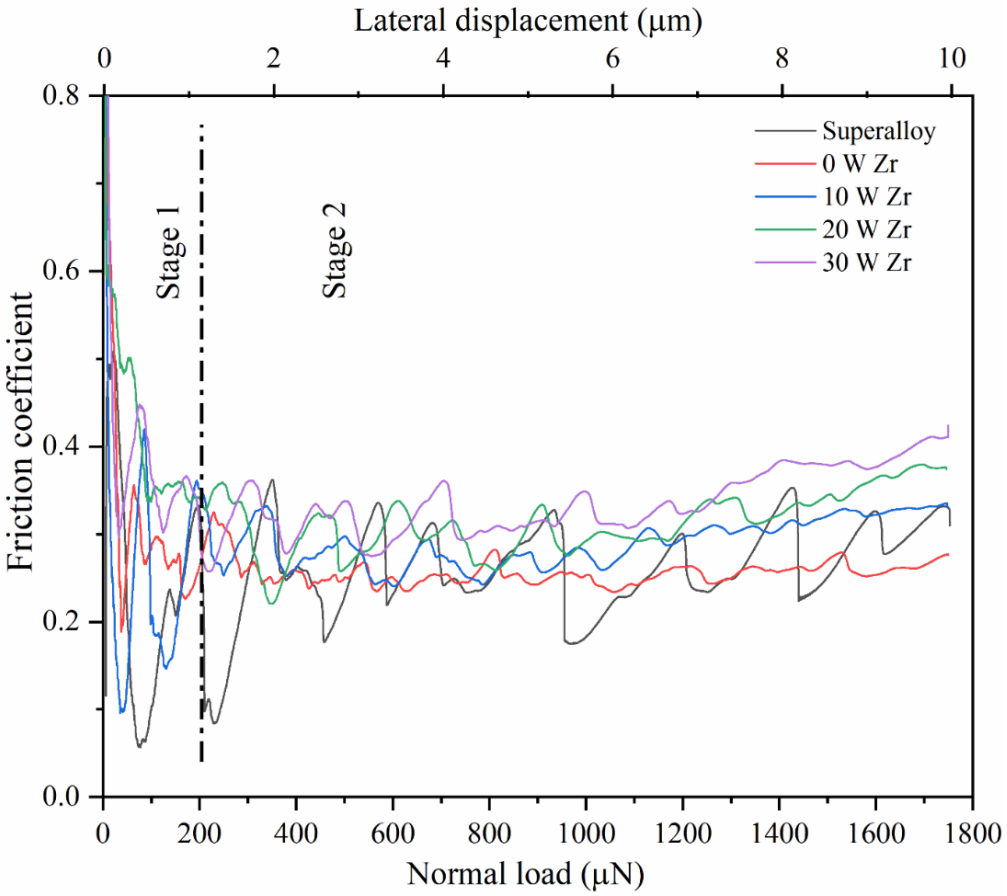

Figure 6.25: Relationship between normal load and friction coefficient of the substrate, Ni_3Al and Zr-Ni_3Al films

The weight change per unit area versus cycle time was calculated to measure and understand the kinetics of oxidation. The results of the oxidation test performed at various temperatures are demonstrated in **figure 6.26**. From the figure, it can be observed the substrate is more prone to oxidation. However, the results of weight gain per unit area versus time indicated that the Ni_3Al and Zr-Ni_3Al films were able to protect the surface from being drastically oxidized

showing a slow rate of oxidation as compared to substrate when oxidized at 900℃ **[figure 6.26 (a)]**.

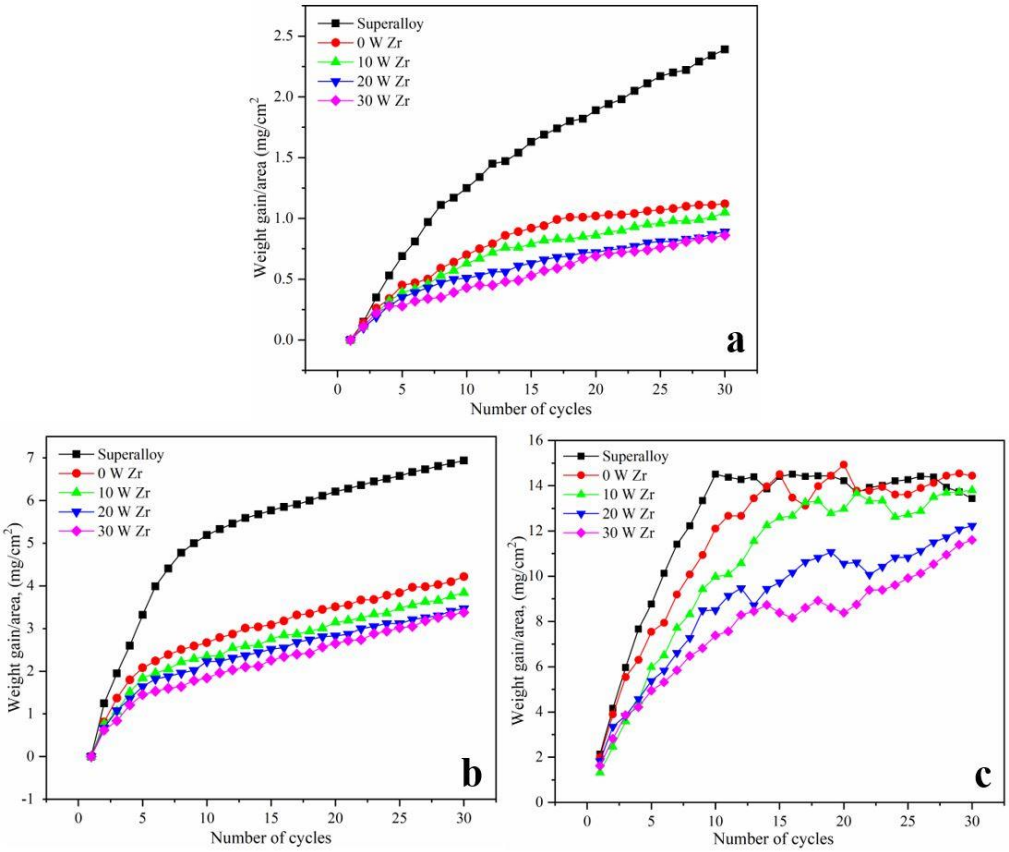

Figure 6.26: Weight gain/area versus number of cycles **(a)** Zr-Ni_3Al oxidized at 900℃ **(b)** Zr-Ni_3Al oxidized at 1000℃ **(c)** Zr-Ni_3Al oxidized at 1100℃

A subsequent and continuous increase in weight gain is observed in all the films and substrates when oxidized at 1000℃ showing a high rate of oxidation as compared to 900℃ **[Figure 6.26 (b)]**. The results of oxidation in terms of weight change for the substrate and films oxidized at 1100℃ showed a linear increment in weight gain in case of substrate up to 9^{th} cycles after which a discontinuity in weight change is observed. The discontinuity in weight change in 0 W Zr, 10 W Zr, 20 W Zr and 30 W Zr is seen after the 10^{th}, 11^{th}, 13^{th} and 16^{th} cycles of oxidation ℃ respectively **[Figure 6.26 (c)]**. This sudden fall in the weight change is due to the removal of the oxide layer from the surface and the pilling of the film from the edges of the substrate as a result of the higher rate of oxidation. However, the exposure of the fresh surface after removal of the oxide layer further leads to oxidation, and thus a

weight gain is observed as a result. **Figure 6.27** shows the parabolic oxidation kinetic curves of substrates and deposited films oxidized at different temperatures. The square of weight change per unit area versus cycle time for the substrate and deposited films oxidized at 900℃ showed a linear trend of weight gain with respect to time. This indicates continuous oxidation over time. However, the rate of oxidation in deposited films is lower as compared to bare substrate because of the slow rate of chemical reaction between oxygen and the surface of the substrate (Inconel-718) **[figure 6.27 (a)]**. This could be the result of higher surface integrity of the developed adherent protective oxide layers of Al_2O_3 which forbids the continuous diffusion of oxygen into the surface. The rate of oxidation in terms of weight gain per unit area at 1000℃ is higher in the substrate and deposited films when compared to the rate of oxidation at 900℃. However, the substrate is found to be more prone to oxidation in the first half of the cycles as shown in **figure 6.27 (b)**. **Figure 6.27 (c)** shows the parabolic kinetics of oxidation of the substrate and the deposited films oxidized at 1100℃. The results of the square of weight change per unit area versus cycle time show that the substrate and films are prone to linear oxidation up to a few initial cycles after which a discontinuity in weight change is observed **(figure 6.28)**. This is because of the higher rate of oxidation resulting in continuous mass loss and further mass gain as a result of exposure of the new surface. Moreover, the high rate of oxidation led to the extreme diffusion of oxygen which accelerates the chemical reaction, and oxygen penetrates through the oxide layers and reacts with the newly exposed surface of the substrate and films. The higher rate of oxidation within the film again leads to the formation of a new oxidation layer that contributing to further oxidations. This results in the spalling of the oxide layer with the increase in cycle time resulting in weight loss of the film. The results of the weight gain per unit area versus cycle time and the square of weight gain per unit area versus cycle time indicate parabolic kinetics of continuous oxidation with different rates at different temperatures.

The parabolic rate constant (K_p) of the substrate and deposited Zr-Ni_3Al films oxidized at different temperatures have been mentioned in **table 6.11**. It can be

seen that the value of the parabolic rate constant (K_p) increases with increase in oxidation temperature indicating a high rate of continuous oxidation. However, it decreases with increase in Zr concentration in the film.

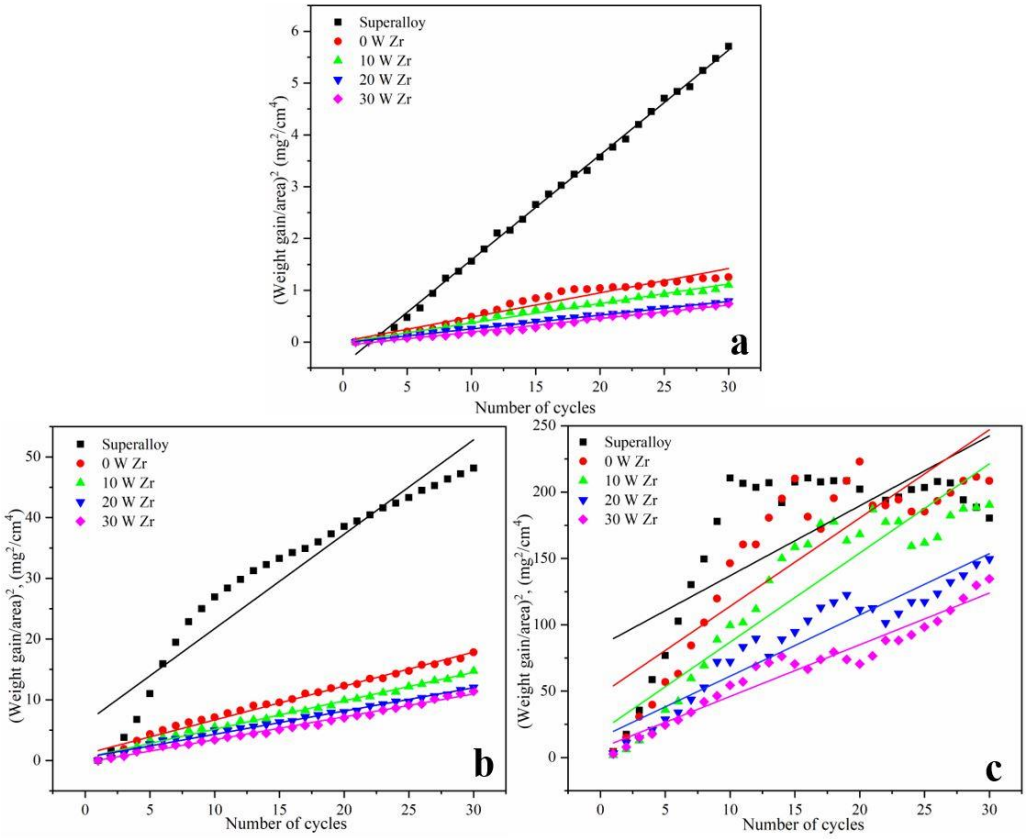

Figure 6.27: Parabolic characteristics of oxidation kinetics **(a)** Zr-Ni_3Al oxidized at 900°C **(b)** Zr-Ni_3Al oxidized at 1000°C **(c)** Zr-Ni_3Al oxidized at 1100°C

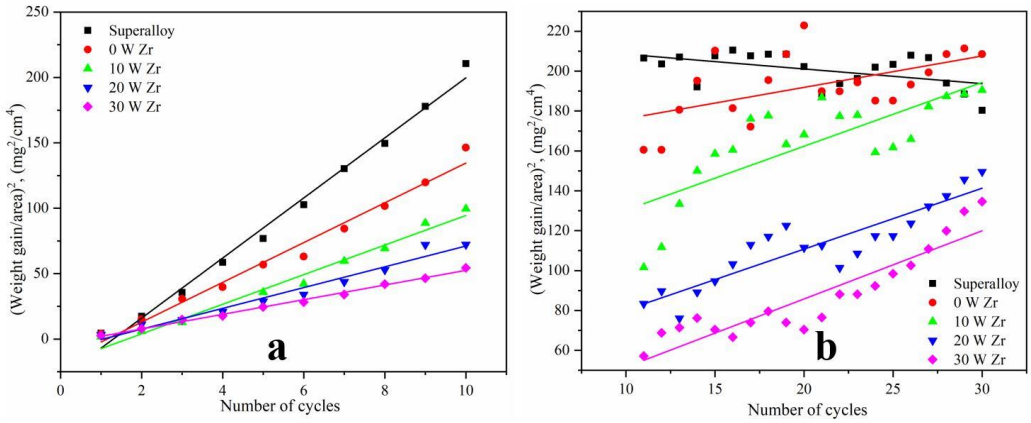

Figure 6.28: Parabolic characteristics of oxidation kinetics **(a)** Zr-Ni_3Al oxidized at 1100°C up to 10 cycles **(b)** Zr-Ni_3Al oxidized at 1100°C from 11 to 30 cycles.

Table 6.11: Parabolic rate constant of substrate and deposited Zr-Ni_3Al films

SN	Samples	Parabolic rate constant (K_p)		
		900°C	**1000°C**	**1100°C**
1	Substrate	0.20247 ± 0.00164	1.55476 ± 0.08745	5.26812 ± 0.93944
2	0 W Zr	0.04691 ± 0.00202	0.55889 ± 0.01284	6.65231 ± 0.71215
3	10 W Zr	0.03771 ± 9.79341	0.46904 ± 0.00869	6.71871 ± 0.52311
4	20 W Zr	0.02668 ± 3.54024	0.38346 ± 0.00729	4.61715 ± 0.26627
5	30 W Zr	0.02597 ± 5.78706	0.37619 ± 0.00618	3.89496 ± 0.17152

6.2.4 CONCLUSION

Zr-Ni_3Al coatings were successively synthesized using DC magnetron co-sputtering at the substrate temperature of 400°C. The formation of different phases, surface topography and microstructure were characterized using XRD, AFM and FESEM respectively. The results of XRD spectra showed that the substrate possessed the preferred orientation of Ni (111) followed by Ni (200) and (220) whereas the as-deposited Zr-Ni_3Al coatings showed the preferred orientation of Ni_3Al (111) followed by a low-intensity peak of (200) and (220) texture. Furthermore, with the increase in the concentration of Zr in host Ni_3Al, a subsequent and continuous shift in XRD spectra towards the lower angle has been observed. The microstructure of 0 W Zr, 10 W Zr and 20 W Zr films possess a larger percentage of microcracks which decreased in 30 W Zr coating. Accordingly, the results of AFM showed a gradual decline in the surface roughness of the film with increase in the Zr content in the Ni_3Al matrix. Additionally, the adhesive strength of the Zr-Ni_3Al films was enhanced when Zr was enriched in the host Ni_3Al matrix. The results of cyclic oxidation at high temperatures reveal that all the deposited films and substrates were oxidized at 900°C, 1000°C and 1100°C. However, a slow rate of oxidation was observed at exposure temperature of 900°C which increases with rise in oxidation temperature. Moreover, the rate of oxidation decreases with increase in concentration of Zr content in Ni_3Al film. The value of the parabolic rate constant for all the deposited films oxidized at different temperatures reveals that the substrate is more prone to oxidation and the

Ni_3Al coating enriched with Zr is capable of protecting the superalloy from being drastically oxidized at higher temperatures.

CONCLUSION AND FUTURE PROSPECTS

CONCLUSION

The main objective of this research was to synthesize different kinds of Ni_3Al-based thin films using magnetron sputtering and to investigate their microstructural, mechanical and oxidation resistant properties using different characterization tools and techniques. In addition, this study reports the comparison of sputtering parameters and use of dopants that influences the properties of the film.

Ni_3Al and doped Ni_3Al-based alloy coatings were deposited over silicon (100) and Inconel-718 substrates using DC magnetron sputtering and co-sputtering process respectively. The evolution of different phases, surface topography, surface morphology and elemental composition were studied using XRD, AFM, FE-SEM and EDS respectively. Nanoindentation was used to investigate the hardness, Young's modulus and adhesive strength of the deposited films whereas the oxidation test was performed at 900℃, 1000℃ and 1100℃.

Synthesis and characterization of different Ni_3Al-based coatings with varying sputtering parameters and use of different concentration of dopants have been mentioned in **table 7.1**.

Table 7.1: Hardness, Young's modulus, and oxidation resistant properties of Ni_3Al-based coating with respect to varying sputtering parameters

Experiment	**Sputtering parameters**	**Substrate**	**Hardness**	**Young's modulus**	**Oxidation resistant test**
Experiment 1	**Variation in substrate temperature**				
Ni_3Al alloy films	RT	Si (100)	7.4 ± 2.6	92.1 ± 14.3	NA
	200℃		7.9 ± 1.8	102.2 ± 14.5	
	400℃		**12.8 ± 0.8**	**205 ± 15**	
	600℃		4.06 ± 0.6	74.8 ± 9.6	

Experiment 2	**Variation in Ni concentration with variation in power to Ni target**	**Substrate**	**Hardness**	**Young's modulus**	**Oxidation resistant test**
Ni_3Al and Ni-rich Ni_3Al alloy films	0 W Ni (79.2 at % of Ni)	Si (100)	**12.8 ± 0.8**	**205.3 ± 15**	NA
	25 W Ni (83.6 at % of Ni)		10.05 ± 1.4	165.3 ± 20.9	
	50 W Ni (85.1 at % of Ni)		7.66 ± 0.70	181.2 ± 12.2	
	100 W Ni (86.7 at % of Ni)		2.69 ± 0.74	90.7 ± 14.5	
Experiment 3	**Variation in Cr concentration with variation in power to Cr target**	**Substrate**	**Hardness**	**Young's modulus**	**Oxidation resistant test**
Cr-Ni_3Al alloy films	0 W Cr (0.00 at % of Cr)	Si (100)	**12.7 ± 0.8**	**206 ± 15**	NA
	10 W Cr (1.07 at % of Cr)		12.08 ± 1.3	148 ± 19	
	20 W Cr (2.25 at % of Cr)		9.21 ± 0.53	138 ± 5.2	
	30 W Cr (5.71 at % of Cr)		8.21 ± 0.57	130 ± 9.5	
	40 W Cr (7.31 at % of Cr)		7.0 ± 0.51	129 ± 5.6	
Experiment 4	**Variation in Zr concentration with variation in power to Zr target**	**Substrate**	**Hardness**	**Young's modulus**	**Oxidation resistant test**
	0 W Zr (0.00 at % of Zr)		**12.8 ± 0.8**	**205 ± 15**	

Zr-Ni_3Al alloy films	10 W Zr (0.65 at % of Zr)	Si (100)	10.3 ± 0.58	156 ± 6.7	NA
	20 W Zr (1.02 at % of Zr)		10.1 ± 0.75	147.8 ± 10.0	
	30 W Zr (1.20 at % of Zr)		8.95 ± 1.02	140.7 ± 6.7	
	40 W Zr (1.51 at % of Zr)		8.07 ± 0.6	137.9 ± 5.5	
Experiment 5	**Variation in Cr concentration with variation in power to Cr target**	**Substrate**	**Hardness**	**Young's modulus**	**Oxidation resistant test**
Cr-Ni_3Al alloy films	0 W Cr (0.00 at % of Cr)	Inconel-718	NA	NA	**30 W Cr** with at % of Cr showed the best oxidation resistant properties at 900°C
	10 W Cr (1.10 at % of Cr)				
	20 W Cr (2.30 at % of Cr)				
	30 W Cr (5.70 at % of Cr)				
Experiment 6	**Variation in Zr concentration with variation in power to Zr target**	**Substrate**	**Hardness**	**Young's modulus**	**Oxidation resistant test**
Zr-Ni_3Al alloy films	0 W Zr (0.00 at % of Zr)	Inconel-718	NA	NA	**30 W Zr** with at % of Zr showed the best oxidation resistant properties at 900°C
	10 W Zr (0.65 at % of Zr)				
	20 W Zr (1.02 at % of Zr)				
	30 W Zr (1.20 at % of Zr)				

From the results of the experiments, it is observed that the alloy Ni_3Al films deposited at 400℃ without doping has shown the maximum hardness and Young's modulus of 12.85 ± 0.8 GPa and 205 ± 15 GPa respectively. The addition of Ni, Cr and Zr in the host Ni_3Al matrix resulted in degradation of microstructure which in return decreases the hardness and Young's modulus. However, the microstructure of Cr-Ni_3Al and Zr-Ni_3Al alloy films gets improved when deposited on Ni-Superalloy. Results of the oxidation test reveal that the all the deposited films were oxidized at each studied temperature. However, the substrate was found to be more prone to oxidation. The results of weight change per unit area versus cycle time and parabolic rate constant of oxidation kinetics confirm that the substrate and films were oxidized at high temperature but Cr-Ni_3Al and Zr-Ni_3Al alloy films are capable of protecting the superalloy from being drastically oxidized.

FUTURE PROSPECTS

Based on the present work and available literature in the field of synthesizing and characterizing Ni_3Al-based coatings, following scope of work are recommended for future work.

1. The effect of sputtering pressure on microstructural, mechanical and tribological properties are still to be investigated for both alloy and multilayer form of Ni_3Al based coatings.
2. The effect of sputtering power and thus the film thickness on the microstructural, mechanical and tribological properties are to be investigated.
3. The substrate-target distance can be optimized to achieve better results.
4. There is a large scope to dope host Ni_3Al matrix in alloy and multilayer form using other transition metals and high entropy alloys.
5. The corrosion test of Ni_3Al-based coatings can be investigated in different corrosive and marine environments.

REFERENCES

[1] S. O. Mbam, S. E. Nwonu, O. A. Orelaja, U. S. Nwigwe, and X.-F. Gou, "Thin-film coating; historical evolution, conventional deposition technologies, stress-state micro/nano-level measurement/models and prospects projection: a critical review," *Mater. Res. Express*, vol. 6, no. 12, p. 122001, Dec. 2019, doi: 10.1088/2053-1591/ab52cd.

[2] E. Jackson, "Opticks: or a treatise of the reflections, refractions, inflections and colours of light.," *Am. J. Ophthalmol.*, vol. 15, no. 1, p. 66, 1932, doi: 10.1016/s0002-9394(14)77324-6.

[3] P. Redhead, "History of vacuum devices," *Cern Eur. Organ. Nucl. Res.*, pp. 281–290, 1999.

[4] R. Ramesh and N. A. Spaldin, "Multiferroics: Progress and prospects in thin films," *Nanosci. Technol. A Collect. Rev. from Nat. Journals*, vol. 3, pp. 20–28, 2009, doi: 10.1142/9789814287005_0003.

[5] P. Joshi, A. A. Gesawat, and K. Singh, "Development and characterization of Ti-Nb-N coatings on stainless steel using reactive DC magnetron sputtering," vol. 4, no. 16, pp. 1059–1068, 2015.

[6] S. Steel *et al.*, "Enhancement of the Corrosion Resistance of 304 Stainless Steel by Cr–N and Cr(N,O) Coatings," pp. 17–20, 2018, doi: 10.3390/coatings8040132.

[7] S. K. Mishra and S. Kumari, "Development of hard and optically transparent Al-Si-N nanocomposite coatings," no. January, 2016, doi: 10.1002/sia.5954.

[8] P. Gao, Q. Guo, Y. Xing, and Y. Guo, "Structural, Mechanical, and Tribological Properties of Hard Coatings," *Coatings*, vol. 13, no. 2, pp. 2–6, 2023, doi: 10.3390/coatings13020325.

[9] M. Ge, J. Zhu, R. Zhang, and C. Wang, "Current status of hard coating research," *J. Comput. Electron. Inf. Manag.*, vol. 10, no. 1, pp. 68–71, 2023, doi: 10.54097/jceim.v10i1.5754.

[10] W. Cheng, J. Wang, X. Ma, P. Liu, P. K. Liaw, and W. Li, "A review on microstructures and mechanical properties of protective nano-

multilayered films or coatings," *J. Mater. Res. Technol.*, vol. 27, pp. 2413–2442, 2023, doi: 10.1016/j.jmrt.2023.10.012.

[11] S. Ranganatha and T. V. Venkatesha, "Studies on the preparation and properties of electroless Ni-W-P alloy coatings and its nano-MoS 2 composite," *Phys. Scr.*, vol. 85, no. 3, 2012, doi: 10.1088/0031-8949/85/03/035601.

[12] J. L. Cao, K. L. Choy, H. L. Sun, H. Q. Li, D. Teer, and M. D. Bao, "Syntheses of nano-multilayered TiN/TiSiN and CrN/CrSiN hard coatings," *J. Coatings Technol. Res.*, vol. 8, no. 2, pp. 283–288, 2011, doi: 10.1007/s11998-010-9275-0.

[13] G. S. Fox-Rabinovich, K. Yamamoto, S. C. Veldhuis, A. I. Kovalev, L. S. Shuster, and L. Ning, "Self-adaptive wear behavior of nano-multilayered TiAlCrN/WN coatings under severe machining conditions," *Surf. Coatings Technol.*, vol. 201, no. 3–4, pp. 1852–1860, 2006, doi: 10.1016/j.surfcoat.2006.03.010.

[14] M. Nordin, R. Sundström, T. I. Selinder, and S. Hogmark, "Wear and failure mechanisms of multilayered PVD TiN/TaN coated tools when milling austenitic stainless steel," *Surf. Coatings Technol.*, vol. 133–134, pp. 240–246, 2000, doi: 10.1016/S0257-8972(00)00933-6.

[15] I. M. B. Navinsek, P.Panjan, "Title of the 114083th document," vol. 97, pp. 182–191, 1997.

[16] S. Zhang and W. Zhu, "TiN coating of tool steels: a review," *J. Mater. Process. Tech.*, vol. 39, no. 1–2, pp. 165–177, 1993, doi: 10.1016/0924-0136(93)90016-Y.

[17] R. P. Van Hove, I. N. Sierevelt, B. J. Van Royen, and P. A. Nolte, "Titanium-Nitride Coating of Orthopaedic Implants: A Review of the Literature," *Biomed Res. Int.*, vol. 2015, 2015, doi: 10.1155/2015/485975.

[18] D. Seneviratne, G. N. Nielson, S. Takahashi, G. Barbastathis, and H. L. Tuller, "On the use of titanium nitride as structural material for nano-electro-mechanical systems (NEMS)," *2005 5th IEEE Conf. Nanotechnol.*, vol. 1, no. July, pp. 138–141, 2005, doi: 10.1109/NANO.2005.1500712.

[19] R. Sanjinés, P. Hones, and F. Lévy, “Hexagonal nitride coatings: Electronic and mechanical properties of V2N, Cr2N and δ-MoN,” *Thin Solid Films*, vol. 332, no. 1–2, pp. 225–229, 1998, doi: 10.1016/S0040-6090(98)00991-2.

[20] L. Aissani, M. Fellah, and C. Nouveau, “Structural Mechanical and Tribological Behavior of Reactive Sputtered Cr-N and Cr-V-N Films,” *Diffus. Found.*, vol. 18, pp. 27–34, 2018, doi: 10.4028/www.scientific.net/df.18.27.

[21] J. W. Du, L. Chen, J. Chen, and Y. Du, “Mechanical properties, thermal stability and oxidation resistance of TiN/CrN multilayer coatings,” *Vacuum*, vol. 179, p. 109468, 2020, doi: 10.1016/j.vacuum.2020.109468.

[22] W. J. Tomlinson and G. R. Wilson, “The oxidation of electroless Ni-B and Ni-P coatings in air at 800 to 1000°C,” *J. Mater. Sci.*, vol. 21, no. 1, pp. 97–102, 1986, doi: 10.1007/BF01144705.

[23] G. Bertrand, H. Mahdjoub, and C. Meunier, “A study of the corrosion behaviour and protective quality of sputtered chromium nitride coatings,” *Surf. Coatings Technol.*, vol. 126, no. 2–3, pp. 199–209, 2000, doi: 10.1016/S0257-8972(00)00527-2.

[24] K. V Madhuri, *10. Thermal protection coatings of metal oxide powders*. INC, 2020.

[25] “The fundamentals of chemical vapour deposition,” vol. 12, pp. 1285–1306.

[26] S. Senapati and P. Maiti, *9. Emerging bio-applications of two-dimensional nanoheterostructure materials*. INC, 2020.

[27] M. Klaus, C. Genzel, and H. Holzschuh, “Residual stress depth profiling in complex hard coating systems by X-ray diffraction,” *Thin Solid Films*, vol. 517, no. 3, pp. 1172–1176, 2008, doi: 10.1016/j.tsf.2008.05.018.

[28] M. B. Tahir, M. Rafique, M. S. Rafique, T. Nawaz, M. Rizwan, and M. Tanveer, *Chapter 8 - Photocatalytic nanomaterials for degradation of organic pollutants and heavy metals*. Elsevier Inc., 2020.

[29] K. Reichelt and X. Jiang, “I1,” vol. 191, pp. 91–126, 1990.

[30] H. G. Prengel, W. R. Pfouts, and A. T. Santhanam, “State of the art in hard coatings for carbide cutting tools,” *Surf. Coatings Technol.*, vol. 102, no. 3, pp. 183–190, 1998, doi: 10.1016/S0257-8972(96)03061-7.

[31] Z. G. Zhang *et al.*, “Influence of Ni content on the structure and properties of Cr-Ni-N coatings prepared by direct current magnetron sputtering,” *Thin Solid Films*, vol. 517, no. 11, pp. 3304–3309, 2009, doi: 10.1016/j.tsf.2009.01.014.

[32] J. Kopac, M. Sokovic, and S. Dolinsek, “Tribology of coated tools in conventional and HSC machining,” *J. Mater. Process. Technol.*, vol. 118, no. 1–3, pp. 377–384, 2001, doi: 10.1016/S0924-0136(01)00974-8.

[33] Y. Yang, W. Yao, and H. Zhang, “Phase constituents and mechanical properties of laser in-situ synthesized TiCN/TiN composite coating on Ti-6Al-4V,” *Surf. Coatings Technol.*, vol. 205, no. 2, pp. 620–624, 2010, doi: 10.1016/j.surfcoat.2010.07.058.

[34] M. A. Gharavi *et al.*, “materials Synthesis and characterization of single-phase epitaxial Cr 2 N thin films by reactive magnetron sputtering,” 2018, doi: 10.1007/s10853-018-2914-z.

[35] Y. X. Ou, H. Chen, Z. Y. Li, J. Lin, W. Pan, and M. K. Lei, “Microstructure and tribological behavior of TiAlSiN coatings deposited by deep oscillation magnetron sputtering,” *J. Am. Ceram. Soc.*, vol. 101, no. 11, pp. 5166–5176, 2018, doi: 10.1111/jace.15769.

[36] S. Yadav and S. K. Mishra, “Analysis of Hardness of Nano-Composite (TiSiBC) Coated SS 304 sheet,” vol. v, pp. 1–4.

[37] E. Santecchia *et al.*, “Investigation of the Temperature-Related Wear Performance of Hard Nanostructured Coatings Deposited on a S600 High Speed Steel,” pp. 7–10, doi: 10.3390/met9030332.

[38] R. Hauert and J. Patscheider, “From alloying to nanocomposites - Improved performance of hard coatings,” *Adv. Eng. Mater.*, vol. 2, no. 5, pp. 247–259, 2000, doi: 10.1002/(SICI)1527-2648(200005)2:5<247::AID-ADEM247>3.0.CO;2-U.

[39] S. Paldey and S. C. Dee, “Single layer and multilayer wear resistant coatings of (Ti , Al) N : a re v iew,” vol. 342, pp. 58–79, 2003.

[40] M. Sundar, A. M. Kamara, P. T. Mativenga, and L. Li, “Synthesis of TiAlN based coating on mild steel substrate using combined laser/sol-gel technique,” *Surf. Coatings Technol.*, vol. 204, no. 16–17, pp. 2539–2545, 2010, doi: 10.1016/j.surfcoat.2010.01.037.

[41] P. Li *et al.*, “Int . Journal of Refractory Metals and Hard Materials Microstructure , mechanical and thermal properties of TiAlN / CrAlN multilayer coatings,” *RMHM*, pp. 1–7, 2013, doi: 10.1016/j.ijrmhm.2013.01.020.

[42] W. Tillmann, F. Hoffmann, and T. Sprute, “Tribological and mechanical properties of Ti/TiAlN/TiAlCN nanoscale multilayer PVD coatings deposited on AISI H11 hot work tool steel,” *Appl. Surf. Sci.*, 2014, doi: 10.1016/j.apsusc.2014.03.026.

[43] Y. Long, J. Zeng, D. Yu, and S. Wu, “Microstructure of TiAlN and CrAlN coatings and cutting performance of coated silicon nitride inserts in cast iron turning,” *Ceram. Int.*, vol. 40, no. 7 PART A, pp. 9889–9894, 2014, doi: 10.1016/j.ceramint.2014.02.083.

[44] I. N. Reddy, A. Dey, N. S. S. Anoop, and P. Bera, “Corrosion Behaviour of Sputtered Alumina Thin Films,” *J. Inst. Eng. Ser. D*, 2015, doi: 10.1007/s40033-015-0072-x.

[45] D. G. Sangiovanni, M. Sahul, M. Truchlý, and P. Kú, “Acta Materialia Toughness enhancement in highly NbN-alloyed Ti-Al-N hard coatings Mari a san Pla Tom a,” vol. 121, 2016, doi: 10.1016/j.actamat.2016.08.084.

[46] F. F. Komarov, V. M. Konstantinov, A. V. Kovalchuk, S. V. Konstantinov, and H. A. Tkachenko, “The effect of steel substrate pre-hardening on structural, mechanical, and tribological properties of magnetron sputtered TiN and TiAlN coatings,” *Wear*, vol. 352–353, pp. 92–101, 2016, doi: 10.1016/j.wear.2016.02.007.

[47] S. Paskvale, M. Remškar, and M. Čekada, “Author ’ s Accepted Manuscript,” *Wear*, 2016, doi: 10.1016/j.wear.2016.01.020.

[48] A. Almotairi, A. Warkentin, and Z. Farhat, “Mechanical damage of hard chromium coatings on 416 stainless steel,” *EFA*, 2016, doi: 10.1016/j.engfailanal.2016.04.011.

[49] Z. Lei, Y. Liu, F. Ma, Z. Song, and Y. Li, *Abstract*. Elsevier Ltd, 2016.

[50] X. Sui *et al.*, “Improved toughness of layered architecture TiAlN / CrN coatings for titanium high speed cutting,” *Ceram. Int.*, no. December, pp. 0–1, 2017, doi: 10.1016/j.ceramint.2017.12.210.

[51] C. S. Kumar and S. K. Patel, “PT SC,” *Surf. Coat. Technol.*, 2017, doi: 10.1016/j.surfcoat.2017.12.048.

[52] S. Kaushal, D. Gupta, and H. Bhowmick, “On Development and Wear Behavior of Microwave- Processed Functionally Graded Ni-SiC Clads on SS-304 Substrate,” *J. Mater. Eng. Perform.*, 2017, doi: 10.1007/s11665-017-3110-z.

[53] M. Gong, J. Chen, X. Deng, and S. Wu, “PT,” *Int. J. Refract. Met. Hard Mater.*, 2017, doi: 10.1016/j.ijrmhm.2017.08.003.

[54] S. C. Vettivel, R. Jegan, J. Vignesh, and S. Suresh, “Surface characteristics and wear depth profile of the TiN , TiAlN and AlCrN coated stainless steel in dry sliding wear condition,” *Surfaces and Interfaces*, vol. 6, pp. 1–10, 2017, doi: 10.1016/j.surfin.2016.10.008.

[55] C. He *et al.*, “Microstructure , mechanical and corrosion properties of TiN / Ni nanomultilayered films,” *Rare Met.*, 2018, doi: 10.1007/s12598-018-1154-3.

[56] P. Mahato, S. K. Mishra, N. Chandra, and P. Banerjee, “An International Conference on Tribology , Enhancement of the Mechanical and Tribological Performance of Stainless Steel 304 by Ti-based Nanocomposite Coatings Deposited by PVD Method,” no. December, 2018.

[57] M. Szala, M. Walczak, K. Pasierbiewicz, and M. Kamiński, “Cavitation Erosion and Wear Mechanisms of AlTiN and TiAlN Films Deposited on Stainless Steel Substrate,” no. Ciwc, pp. 1–15, 2019.

[58] B. Abdallah, M. Kakhia, and W. Alsadat, “Deposition of TiN and TiAlVN thin films by DC magnetron sputtering Composition , corrosion and mechanical study,” 2019, doi: 10.1108/IJSI-10-2019-0105.

[59] E. Contreras, J. Cortínez, R. Talamantes, A. Hurtado, and M. Gómez, “Surface & Coatings Technology Microstructure , mechanical and

tribological performance of nanostructured TiAlTaN- (TiAlN / TaN) n coatings : Understanding the e ff ect of quaternary / multilayer volume fraction," *Surf. Coat. Technol.*, vol. 377, no. July, p. 124875, 2019, doi: 10.1016/j.surfcoat.2019.07.086.

[60] J. Alyones, M. Salameh, and B. Abdallah, "Investigation of Pressure Effect on Structural , Mechanical Properties and Corrosion Performance of CrN Thin Films," pp. 2–8, 2019.

[61] S. Fryska, S. Justyna, and J. Baranowska, "Structure and mechanical properties of chromium nitride / S-phase composite coatings deposited on 304 stainless steel," vol. 676, no. January, pp. 144–150, 2019, doi: 10.1016/j.tsf.2019.01.046.

[62] Y. Wang *et al.*, "Applied Surface Science Improvement in the tribocorrosion performance of CrCN coating by multilayered design for marine protective application," *Appl. Surf. Sci.*, vol. 528, no. June, p. 147061, 2020, doi: 10.1016/j.apsusc.2020.147061.

[63] D. Kazlauskas, V. Jankauskas, and S. Tuˇ, "Metal WC-Co Tools with TiAlN and CrN PVD Coatings for Processing Solid Oak Wood," 2020.

[64] A. Awan *et al.*, "Corrosion and wear behavior of TiN PVD," vol. 34, no. 8, 2020, doi: 10.1007/s12206-020-0714-2.

[65] D. V Mejía, A. M. Echavarría, J. A. Calder, and G. B. G, "Microstructural and electrochemical properties of TiAlN (Ag , Cu) nanocomposite coatings for medical applications deposited by dc magnetron sputtering," vol. 828, 2020, doi: 10.1016/j.jallcom.2020.154396.

[66] P. S. Kevin, A. Tiwari, S. Seman, S. Ali, B. Mohamed, and R. Jayaganthan, "Erosion-Corrosion Protection Due to Cr 3 C 2 -NiCr Cermet Coating on Stainless Steel," pp. 1–17, 2020.

[67] N. Li, M. Wang, G. Zheng, P. Li, Y. Li, and G. Chen, "Ni 2 Al 3 intermetallic coating: microstructure and mechanical properties," *Adv. Mater. Process. Technol.*, vol. 4, no. 2, pp. 255–261, 2018, doi: 10.1080/2374068X.2017.1414996.

[68] C. Zhang *et al.*, "Enhancement of high-temperature strength of Ni-based films by addition of nano-multilayers and incorporation of W,"

Acta Mater., vol. 133, pp. 55–67, 2017, doi: 10.1016/j.actamat.2017.05.037.

[69] E. E. Kornienko *et al.*, "Effect of plasma spraying regimes on structure and properties of Ni3Al coatings," *Thermophys. Aeromechanics*, vol. 23, no. 6, pp. 919–927, 2016, doi: 10.1134/S0869864316060147.

[70] N. K. Mahto, R. Tyagi, and S. K. Sinha, "Synergistic effect of Ag and WS2 on high temperature tribological performance of Ni3Al based composites," *Tribol. Int.*, vol. 183, no. January, p. 108408, 2023, doi: 10.1016/j.triboint.2023.108408.

[71] N. Li, M. Wang, G. Zheng, Y. Li, and G. Chen, "Composition distribution and electrochemical behavior of an Ni2Al3 coating on Q235 steel," *Metals (Basel).*, vol. 6, no. 3, pp. 17–23, 2016, doi: 10.3390/met6030058.

[72] J. Li *et al.*, "Fabrication of stable Ni–Al4Ni3–Al2O3 superhydrophobic surface on aluminum substrate for self-cleaning, anti-corrosive and catalytic performance," *J. Mater. Sci.*, vol. 53, no. 2, pp. 1097–1109, 2018, doi: 10.1007/s10853-017-1569-5.

[73] N. K. Mahto, R. Tyagi, S. K. Sinha, and M. Kaur, "Evaluation of lubrication potential of Ni3Al-WS2-Cu-doped hBN self-lubricating hybrid composites," *Tribol. Int.*, vol. 189, no. July, p. 108898, 2023, doi: 10.1016/j.triboint.2023.108898.

[74] R. Mao and D. Xiang, "Preparing W-Ni3Al alloy at low sintering temperature by adding MoO3: Microstructure, mechanical properties, and salt spray corrosion," *J. Alloys Compd.*, vol. 956, p. 170306, 2023, doi: 10.1016/j.jallcom.2023.170306.

[75] H. Liu, M. M. Xu, S. Li, Z. B. Bao, S. L. Zhu, and F. H. Wang, "Improving cyclic oxidation resistance of Ni3Al-based single crystal superalloy with low-diffusion platinum-modified aluminide coating," *J. Mater. Sci. Technol.*, vol. 54, pp. 132–143, 2020, doi: 10.1016/j.jmst.2020.05.007.

[76] Y. Cao, A. M. Mohamed, S. Moshtaghi, M. Taheri, and M. J. Torkamany, "Investigation of creep behavior of Ni3Al-base superalloy by small punch creep," *Vacuum*, vol. 187, no. October 2020, p. 110101,

2021, doi: 10.1016/j.vacuum.2021.110101.

[77] M. Zagula-Yavorska, J. Morgiel, J. Romanowska, and J. Sieniawski, “Nanoparticles in zirconium-doped aluminide coatings,” *Mater. Lett.*, vol. 139, pp. 50–54, 2015, doi: 10.1016/j.matlet.2014.09.128.

[78] T. H. Chuang, “The mutual effects of boron, zirconium and aluminium on grain boundary segregation in Ni3Al intermetallic compounds,” *Mater. Sci. Eng. A*, vol. 141, no. 2, pp. 169–178, 1991, doi: 10.1016/0921-5093(91)90767-H.

[79] Y. Gu, D. Lin, and J. Guo, “Ductilization of Ni3Al by alloying with zirconium,” *Scr. Mater.*, vol. 35, no. 5, pp. 609–613, 1996, doi: 10.1016/1359-6462(96)00187-X.

[80] X. Xiao *et al.*, “Tuning the microstructure and mechanical properties in nanocrystalline Cr coatings by sputtering power,” *Mater. Sci. Eng. A*, vol. 844, no. April, p. 143204, 2022, doi: 10.1016/j.msea.2022.143204.

[81] M. Mirzaaghaei, M. Enayati, and M. Ahmadi, “Fabricating the Tribological Properties and Investigating of Ni 3 Al-MoS 2 Composite Coating,” vol. 9, no. 1, pp. 21–30, 2021.

[82] M. Mirzaaghaei, M. H. Enayati, and M. Ahmadi, “Investigating the Morphology and Build of Cu-Ni3Al-MoS2 Composite Coating by Physical Vapor Deposition Method شه,” vol. 19, no. 1, pp. 67–77, 2017.

[83] M. Mirzaaghaei, M. H. Enayati, and M. Ahmadi, “The Tribological Properties of Cu-Ni 3 Al-Mos 2 Composite Coating Deposited by Magnetron Sputtering,” vol. 4, no. 4, pp. 37–45, 2016.

[84] E. C. Patterson and L. L. Henry, “Magnetoresistance measurements on boron-doped and undoped Ni3Al thin films,” *Mater. Res. Soc. Symp. - Proc.*, vol. 648, pp. 1–4, 2001, doi: 10.1557/proc-648-p3.24.

[85] C. Mei, S. Patu, S. Changxu, and S. Jianian, “Effects of B+ and Cr+ ion implantation on the oxidation of Ni3Al,” *J. Mater. Sci.*, vol. 28, no. 20, pp. 5508–5513, 1993, doi: 10.1007/BF00367822.

[86] Y. Y. Xing, B. Dai, X. H. Wei, Y. J. Ma, and M. Wang, “Enhancement of high-temperature oxidation resistance and mechanical properties of Ni3Al thin films by inserting ultrathin Cr layers,” *Vacuum*, vol. 101, pp. 107–112, 2014, doi: 10.1016/j.vacuum.2013.07.040.

[87] S. Tixier, P. Böni, and H. Van Swygenhoven, “Hardness enhancement of sputtered Ni3Al/Ni multilayers,” *Thin Solid Films*, vol. 342, no. 1, pp. 188–193, 1999, doi: 10.1016/S0040-6090(98)01495-3.

[88] R. Banerjee, G. . Thompson, P. . Anderson, and H. . Fraser, “Sputter deposited nanocrystalline Ni-25Al alloy thin films and Ni/Ni3Al multilayers,” *Thin Solid Films*, vol. 424, no. 1, pp. 93–98, Jan. 2003, doi: 10.1016/S0040-6090(02)00924-0.

[89] C. Zhang *et al.*, “Enhancement of hardness and thermal stability of W-doped Ni3Al thin films at elevated temperature,” *Mater. Des.*, vol. 111, pp. 575–583, 2016, doi: 10.1016/j.matdes.2016.09.039.

[90] S. B. Mishra, K. Chandra, and S. Prakash, “Studies on erosion-corrosion behaviour of plasma sprayed Ni 3 Al coating in a coal-fired thermal power plant environment at 540°C,” *Anti-Corrosion Methods Mater.*, vol. 64, no. 5, pp. 540–549, Sep. 2017, doi: 10.1108/ACMM-11-2015-1592.

[91] W. H. Xu, X. K. Meng, C. S. Yuan, A. H. W. Ngan, K. L. Wang, and Z. G. Liu, “Synthesis and mechanical property evaluation of Ni/Ni3Al microlaminates,” *Mater. Lett.*, vol. 46, no. 5, pp. 303–308, 2000, doi: 10.1016/S0167-577X(00)00192-0.

[92] H. Van Swygenhoven, P. Bijni, F. T. Division, and C.- Villigen, “Nanostructured N & Al Produced Sputtering By Magnetron,” vol. 6, no. 95, pp. 0–3, 1995.

[93] H. P. Ng, X. K. Meng, and A. H. W. Ngan, “An investigation into the fabrication and properties of Ni3Al thin coatings on nickel substrates,” *Scr. Mater.*, vol. 39, no. 12, pp. 1737–1742, 1998, doi: 10.1016/S1359-6462(98)00388-1.

[94] X. K. Meng, H. Vehoff, and A. H. W. Ngan, “Hard multilayered thin films of metal-intermetallic Ni/Ni3Al,” *J. Mater. Res.*, vol. 15, no. 12, pp. 2595–2597, 2000, doi: 10.1557/JMR.2000.0371.

[95] W. H. Xu, X. K. Meng, A. H. W. Ngan, X. Y. Chen, and Z. G. Liu, “Fabrication of Ni-Al thin film by PLD and properties of Ni3Al thin coatings,” *Mater. Lett.*, vol. 44, no. 5, pp. 314–318, 2000, doi: 10.1016/S0167-577X(00)00051-3.

[96] R. Banerjee, G. . Thompson, P. . Anderson, and H. . Fraser, “Sputter deposited nanocrystalline Ni-25Al alloy thin films and Ni/Ni3Al multilayers,” *Thin Solid Films*, vol. 424, no. 1, pp. 93–98, Jan. 2003, doi: 10.1016/S0040-6090(02)00924-0.

[97] R. Banerjee, “Hardness of sputter deposited nanocrystalline Ni3Al thin films,” *Mater. Lett.*, vol. 61, no. 2, pp. 609–612, 2007, doi: 10.1016/j.matlet.2006.05.023.

[98] M. V. Fedorischeva, V. P. Sergeev, N. A. Popova, and E. V. Kozlov, “Temperature effect on microstructure and mechanical properties of the nano-structured Ni3Al coating,” *Mater. Sci. Eng. A*, vol. 483–484, no. 1-2 C, pp. 644–647, 2008, doi: 10.1016/j.msea.2007.03.108.

[99] F. Azarmi, X. W. Tangpong, and T. Chandanayaka, “Investigation on mechanical properties of cold sprayed Ni-Ni3Al composites,” *Surf. Eng.*, vol. 31, no. 11, pp. 832–839, 2015, doi: 10.1179/1743294414Y.0000000384.

[100] S. K. Tiwari *et al.*, “Synthesis and characterization of sputter-deposited Ni-rich Ni3Al hard coatings,” *J. Alloys Compd.*, vol. 926, p. 166802, 2022, doi: 10.1016/j.jallcom.2022.166802.

[101] C. Sun, S. A. Maloy, K. Baldwin, Y. Wang, and J. A. Valdez, “Phase Stability of Ni/Ni3Al Multilayers Under Thermal Annealing and Irradiation,” *Jom*, vol. 72, no. 11, pp. 3995–4001, 2020, doi: 10.1007/s11837-020-04377-0.

[102] C. Zhang, K. Feng, Z. Li, F. Lu, J. Huang, and Y. Wu, “Applied Surface Science Microstructure and mechanical properties of sputter deposited Ni / Ni 3 Al multilayer films at elevated temperature,” *Appl. Surf. Sci.*, vol. 378, pp. 408–417, 2016, doi: 10.1016/j.apsusc.2016.04.027.

[103] C. Zhang, K. Feng, Z. Li, F. Lu, J. Huang, and Y. Wu, “Microstructure and mechanical properties of sputter deposited Ni/Ni 3 Al multilayer films at elevated temperature,” *Appl. Surf. Sci.*, vol. 378, pp. 408–417, 2016, doi: 10.1016/j.apsusc.2016.04.027.

[104] X. K. Meng, H. Shen, H. Vehoff, S. Mathur, and A. H. W. Ngan, “Fractography, elastic modulus, and oxidation resistance of Novel

metal-intermetallic Ni/Ni<inf>3</inf>Al multilayer films," *J. Mater. Res.*, vol. 17, no. 4, 2002, doi: http://hdl.handle.net/10722/42408.

[105] W. N. Sharpe, B. Yuan, and R. L. Edwards, "A new technique for measuring the mechanical properties of thin films," *J. Microelectromechanical Syst.*, vol. 6, no. 3, pp. 193–198, 1997, doi: 10.1109/84.623107.

[106] K. Zweibel, "Thin Films: Past, Present, Future," *Prog. Photovoltaics Res. Appl.*, vol. 3, no. 5, pp. 279–293, 1995, doi: 10.1002/pip.4670030503.

[107] N. Kaiser, "Review of the Fundamentals of Thin-Film Growth.pdf," vol. 41, no. 16, 2002.

[108] J. M. Lackner and W. Waldhauser, *Inorganic PVD and CVD coatings in medicine - A review of protein and cell adhesion on coated surfaces*, vol. 24, no. 5. 2010.

[109] K. Lukaszkowicz, "Review of Nanocomposite Thin Films and Coatings Deposited by PVD and CVD Technology," *Nanomaterials*, no. Cvd, 2011, doi: 10.5772/25799.

[110] P. Mulheran and J. Blackman, "Capture zones and scaling in homogeneous thin-film growth," *Phys. Rev. B - Condens. Matter Mater. Phys.*, vol. 53, no. 15, pp. 10261–10267, 1996, doi: 10.1103/PhysRevB.53.10261.

[111] R. Ishihara and F. C. Voogt, "Heterogeneous nucleation in excimer-laser melted Si thin-films," *Solid State Phenom.*, vol. 80–81, pp. 163–168, 2001, doi: 10.4028/www.scientific.net/ssp.80-81.163.

[112] D. Zacher, O. Shekhah, C. Wöll, and R. A. Fischer, "Thin films of metal–organic frameworks," *Chem. Soc. Rev.*, vol. 38, no. 5, pp. 1418–1429, 2009, doi: 10.1039/b805038b.

[113] N. T. K. Thanh, N. Maclean, and S. Mahiddine, "Mechanisms of Nucleation and Growth of Nanoparticles in Solution," vol. 3, no. 1, 2013.

[114] J. O. and G. C. Edgar Alfonso, "Thin Film Growth Through Sputtering Technique," *J. Electron. Mater.*, vol. 23, no. 7, pp. 11–12, 1977, [Online]. Available: http://www.mtixtl.com/tech-articles/Thin Film

Deposition (Thermal-evaporation).pdf.

[115] “The growth will be described by the critical nucleus size r * and the critical energy barrier Δ G * according to the following expressions:,” [Online]. Available: https://www.google.com/url?sa=i&url=https%3A%2F%2Fwww.engr.colostate.edu%2FECE581%2Ffall07%2FTwo%2520dimensional%2520structures.pdf&psig=AOvVaw0kIiSqRqBn1TrnQeLCKDVS&ust=1667570509504000&source=images&cd=vfe&ved=0CA4QjhxqFwoTCOjTnLGWkvsCFQAAAAAdAAAAABAI.

[116] S. Swann, “Magnetron sputtering,” *Phys. Technol.*, vol. 19, no. 2, pp. 67–75, 1988, doi: 10.1088/0305-4624/19/2/304.

[117] J. Musil, “Low-pressure magnetron sputtering,” *Vacuum*, vol. 50, no. 3–4, pp. 363–372, 1998, doi: 10.1016/s0042-207x(98)00068-2.

[118] R. K. Waits, “Planar Magnetron Sputtering.,” *J Vac Sci Technol*, vol. 15, no. 2, pp. 179–187, 1978, doi: 10.1116/1.569451.

[119] D. G. Constantin, M. Apreutesei, R. Arvinte, A. Marin, O. C. Andrei, and D. Munteanu, “Magnetron Sputtering Technique Used for Coatings Deposition ; Technologies and Applications,” *7th Int. Conf. Mater. Sci. Eng.*, vol. 12, no. January, pp. 24–26, 2011, [Online]. Available: https://www.researchgate.net/publication/267686049.

[120] I. V. Svadkovski, D. A. Golosov, and S. M. Zavatskiy, “Characterisation parameters for unbalanced magnetron sputtering systems,” *Vacuum*, vol. 68, no. 4, pp. 283–290, 2002, doi: 10.1016/S0042-207X(02)00385-8.

[121] S. K. Habib, A. Rizk, and I. A. Mousa, “Physical parameters affecting deposition rates of binary alloys in a magnetron sputtering system,” *Vacuum*, vol. 49, no. 2, pp. 153–160, 1998, doi: 10.1016/s0042-207x(97)00158-9.

[122] J. Epp, *X-Ray Diffraction (XRD) Techniques for Materials Characterization*. Elsevier Ltd, 2016.

[123] B. R. Rehani, P. B. Joshi, K. N. Lad, and A. Pratap, “Crystallite size estimation of elemental and composite silver nano-powders using XRD principles,” *Indian J. Pure Appl. Phys.*, vol. 44, no. 2, pp. 157–161,

2006.

[124] “(+Cos 20),” *Structure*, pp. 526–531, 1974.

[125] P. A. Rundquist, P. Photinos, S. Jagannathan, and S. A. Asher, “Dynamical Bragg diffraction from crystalline colloidal arrays,” *J. Chem. Phys.*, vol. 91, no. 8, pp. 4932–4941, 1989, doi: 10.1063/1.456734.

[126] A. Richel, N. P. Johnson, and D. W. McComb, “Observation of Bragg reflection in photonic crystals synthesized from air spheres in a titania matrix,” *Appl. Phys. Lett.*, vol. 76, no. 14, pp. 1816–1818, 2000, doi: 10.1063/1.126175.

[127] F. T. L. Muniz, M. A. R. Miranda, C. Morilla Dos Santos, and J. M. Sasaki, “The Scherrer equation and the dynamical theory of X-ray diffraction,” *Acta Crystallogr. Sect. A Found. Adv.*, vol. 72, no. 3, pp. 385–390, 2016, doi: 10.1107/S205327331600365X.

[128] A. L. Patternson, “Scherrer Formula.pdf,” *Physical review*, vol. 56. p. 978, 1939.

[129] K. He, N. Chen, C. Wang, L. Wei, and J. Chen, “Method for Determining Crystal Grain Size by X-Ray Diffraction,” *Cryst. Res. Technol.*, vol. 53, no. 2, pp. 1–6, 2018, doi: 10.1002/crat.201700157.

[130] A. Monshi, M. R. Foroughi, and M. R. Monshi, “Modified Scherrer Equation to Estimate More Accurately Nano-Crystallite Size Using XRD,” *World J. Nano Sci. Eng.*, vol. 02, no. 03, pp. 154–160, 2012, doi: 10.4236/wjnse.2012.23020.

[131] M. Abd Mutalib, M. A. Rahman, M. H. D. Othman, A. F. Ismail, and J. Jaafar, *Scanning Electron Microscopy (SEM) and Energy-Dispersive X-Ray (EDX) Spectroscopy*. Elsevier B.V., 2017.

[132] B. Cenozoic, “Book Review,” vol. 17, no. 1982, pp. 171–172, 1991.

[133] C. X-rays, “Analytical Electron Microscopy for Materials Science,” *Mater. Today*, vol. 6, no. 1, p. 38, 2003, doi: 10.1016/s1369-7021(03)00133-0.

[134] R. A. Waldo, M. C. Militello, and S. W. Gaarenstroom, “Quantitative thin-film analysis with an energy-dispersive x-ray detector,” *Surf. Interface Anal.*, vol. 20, no. 2, pp. 111–114, 1993, doi:

10.1002/sia.740200204.

[135] V. D. Hodoroaba, *Energy-dispersive X-ray spectroscopy (EDS)*, no. X. Elsevier Inc., 2019.

[136] K. Sakai, "Atomic Force Microscope (AFM)," *Meas. Tech. Pract. Colloid Interface Phenom.*, vol. 56, no. 9, pp. 51–57, 2019, doi: 10.1007/978-981-13-5931-6_8.

[137] D. Johnson, N. Hilal, and W. R. Bowen, *Basic Principles of Atomic Force Microscopy*. Elsevier Ltd, 2009.

[138] M. R. McCraw, B. Uluutku, and S. D. Solares, "Linear Viscoelasticity: Review of Theory and Applications in Atomic Force Microscopy," *Reports Mech. Eng.*, vol. 2, no. 1, pp. 151–179, 2021, doi: 10.31181/rme200102156m.

[139] M. Guilizzoni, "Drop shape visualization and contact angle measurement on curved surfaces," *J. Colloid Interface Sci.*, vol. 364, no. 1, pp. 230–236, 2011, doi: 10.1016/j.jcis.2011.08.019.

[140] P. B. Welzel, C. Rauwolf, O. Yudin, and K. Grundke, "Influence of aqueous electrolytes on the wetting behavior of hydrophobic solid polymers - Low-rate dynamic liquid/fluid contact angle measurements using axisymmetric drop shape analysis," *J. Colloid Interface Sci.*, vol. 251, no. 1, pp. 101–108, 2002, doi: 10.1006/jcis.2002.8356.

[141] P. Letellier, A. Mayaffre, and M. Turmine, "Drop size effect on contact angle explained by nonextensive thermodynamics. Young's equation revisited," *J. Colloid Interface Sci.*, vol. 314, no. 2, pp. 604–614, 2007, doi: 10.1016/j.jcis.2007.05.085.

[142] D. Y. Kwok and A. W. Neumann, *Contact angle measurement and contact angle interpretation*, vol. 81, no. 3. 1999.

[143] H. L. Kornberg and H. A. Krebs, "© 1957 Nature Publishing Group," *Gr. Nat. Publ.*, vol. 180, pp. 756–757, 1957.

[144] G. M. P. W.C. Oliver, "An improved techniques for determining Hardness and elastic modulus using," *J. Mater.*, vol. 7. pp. 1564–1583, 1992.

[145] R. He *et al.*, "Studies on mechanical properties of thermoelectric materials by nanoindentation," *Phys. Status Solidi Appl. Mater. Sci.*,

vol. 212, no. 10, pp. 2191–2195, 2015, doi: 10.1002/pssa.201532045.

[146] B. A. Galanov and S. N. Dub, “Critical comments to the Oliver–Pharr measurement technique of hardness and elastic modulus by instrumented indentations and refinement of its basic relations,” *J. Superhard Mater.*, vol. 39, no. 6, pp. 373–389, 2017, doi: 10.3103/S1063457617060016.

[147] X. Li and B. Bhushan, “A review of nanoindentation continuous stiffness measurement technique and its applications,” *Mater. Charact.*, vol. 48, no. 1, pp. 11–36, 2002, doi: 10.1016/S1044-5803(02)00192-4.

[148] S. Zak, C. O. W. Trost, P. Kreiml, and M. J. Cordill, “Accurate measurement of thin film mechanical properties using nanoindentation,” *J. Mater. Res.*, vol. 37, no. 7, pp. 1373–1389, 2022, doi: 10.1557/s43578-022-00541-1.

[149] K. Liu *et al.*, “Comparison of shale fracture toughness obtained from scratch test and nanoindentation test,” *Int. J. Rock Mech. Min. Sci.*, vol. 162, no. November 2022, p. 105282, 2023, doi: 10.1016/j.ijrmms.2022.105282.

[150] A. Günen, K. M. Döleker, M. E. Korkmaz, M. S. Gök, and A. Erdogan, “Characteristics, high temperature wear and oxidation behavior of boride layer grown on nimonic 80A Ni-based superalloy,” *Surf. Coatings Technol.*, vol. 409, no. January, 2021, doi: 10.1016/j.surfcoat.2021.126906.

[151] D. He, H. Guan, X. Sun, and X. Jiang, “Manufacturing, structure and high temperature corrosion of palladium-modified aluminide coatings on nickel-base superalloy M38,” *Thin Solid Films*, vol. 376, no. 1–2, pp. 144–151, 2000, doi: 10.1016/S0040-6090(00)01198-6.

[152] J. Cao, J. Zhang, R. Chen, Y. Ye, and Y. Hua, “High temperature oxidation behavior of Ni-based superalloy GH202,” *Mater. Charact.*, vol. 118, pp. 122–128, 2016, doi: 10.1016/j.matchar.2016.05.013.

[153] D. Li *et al.*, “High temperature oxidation behavior of Ni-based superalloy Nimonic95 and the effect of pre-oxidation treatment,” *Vacuum*, vol. 194, no. June, p. 110582, 2021, doi: 10.1016/j.vacuum.2021.110582.

[154] M. S. Kabir, P. Munroe, Z. Zhou, and Z. Xie, “Structure and mechanical properties of graded Cr/CrN/CrTiN coatings synthesized by close field unbalanced magnetron sputtering,” *Surf. Coatings Technol.*, vol. 309, pp. 779–789, 2017, doi: 10.1016/j.surfcoat.2016.10.087.

[155] P. L. Tam, Z. F. Zhou, P. W. Shum, and K. Y. Li, “Structural, mechanical, and tribological studies of Cr-Ti-Al-N coating with different chemical compositions,” *Thin Solid Films*, vol. 516, no. 16, pp. 5725–5731, 2008, doi: 10.1016/j.tsf.2007.07.127.

[156] G. Xian, J. Xiong, H. Zhao, H. Fan, Z. Li, and H. Du, “Evaluation of the structure and properties of the hard TiAlN-(TiAlN/CrAlSiN)-TiAlN multiple coatings deposited on different substrate materials,” *Int. J. Refract. Met. Hard Mater.*, vol. 85, no. May, p. 105056, 2019, doi: 10.1016/j.ijrmhm.2019.105056.

[157] Q. Li, F. Q. Jiang, Y. X. Leng, R. H. Wei, and N. Huang, “Microstructure and tribological properties of Ti(Cr)SiCN coating deposited by plasma enhanced magnetron sputtering,” *Vacuum*, vol. 89, no. 1, pp. 168–173, 2013, doi: 10.1016/j.vacuum.2012.03.053.

[158] A. F. Rousseau *et al.*, “Microstructural and tribological characterisation of a nitriding/TiAlN PVD coating duplex treatment applied to M2 High Speed Steel tools,” *Surf. Coatings Technol.*, vol. 272, pp. 403–408, 2015, doi: 10.1016/j.surfcoat.2015.03.034.

[159] L. A. Dobrzański, K. Lukaszkowicz, and A. Zarychta, “Mechanical properties of monolayer coatings deposited by PVD techniques,” vol. 20, no. 9, pp. 423–426, 2007.

[160] M. Athmani, A. AL-Rjoub, D. Cavaleiro, A. Chala, A. Cavaleiro, and F. Fernandes, “Microstructural, mechanical, thermal stability and oxidation behavior of TiSiN/CrVxN multilayer coatings deposited by D.C. reactive magnetron sputtering,” *Surf. Coatings Technol.*, vol. 405, p. 126593, 2021, doi: 10.1016/j.surfcoat.2020.126593.

[161] F. Pei, H. J. Liu, L. Chen, Y. X. Xu, and Y. Du, “Improved properties of TiAlN coating by combined Si-addition and multilayer architecture,” *J. Alloys Compd.*, vol. 790, pp. 909–916, 2019, doi: 10.1016/j.jallcom.2019.03.248.

[162] P. Li *et al.*, “Microstructure, mechanical and thermal properties of TiAlN/CrAlN multilayer coatings,” *Int. J. Refract. Met. Hard Mater.*, vol. 40, pp. 51–57, 2013, doi: 10.1016/j.ijrmhm.2013.01.020.

[163] D. A. Delisle and J. E. Krzanowski, “Surface morphology and texture of TiAlN/CrN multilayer coatings,” *Thin Solid Films*, vol. 524, pp. 100–106, 2012, doi: 10.1016/j.tsf.2012.09.073.

[164] R. Hollerweger *et al.*, “Controlling microstructure , preferred orientation , and mechanical properties of Cr-Al-N by bombardment and alloying with Ta,” no. March, 2016, doi: 10.1063/1.4941533.

[165] X. Bai, W. Zheng, T. An, and Q. Jiang, “Effects of deposition parameters on microstructure of CrN/Si 3N4 nanolayered coatings and their thermal stability,” *J. Phys. Condens. Matter*, vol. 17, no. 41, pp. 6405–6413, 2005, doi: 10.1088/0953-8984/17/41/011.

[166] L. Jiahong and K. Dejun, “Characteristics and Tribological Behaviors of TiAlN/Cr-Ni Composite Coatings at Elevated Temperatures,” *J. Mater. Eng. Perform.*, vol. 28, no. 11, pp. 7075–7085, 2019, doi: 10.1007/s11665-019-04429-w.

[167] A. Mège-Revil, P. Steyer, J. Fontaine, J. F. Pierson, and C. Esnouf, “Oxidation and tribo-oxidation of nanocomposite Cr-Si-N coatings deposited by a hybrid arc/magnetron process,” *Surf. Coatings Technol.*, vol. 204, no. 6–7, pp. 973–977, 2009, doi: 10.1016/j.surfcoat.2009.06.039.

[168] A. Buranawong and N. Witit-Anun, “Structure and oxidation behavior CrN thin films deposited using DC reactive magnetron sputtering,” *Key Eng. Mater.*, vol. 798 KEM, pp. 122–127, 2019, doi: 10.4028/www.scientific.net/KEM.798.122.

[169] E. Contreras Romero, J. Cortínez Osorio, R. Talamantes Soto, A. Hurtado Macías, and M. Gómez Botero, “Microstructure, mechanical and tribological performance of nanostructured TiAlTaN-(TiAlN/TaN)n coatings: Understanding the effect of quaternary/multilayer volume fraction,” *Surf. Coatings Technol.*, vol. 377, no. July, p. 124875, 2019, doi: 10.1016/j.surfcoat.2019.07.086.

[170] K. Taweesup, P. Visuttipitukul, N. Yongvanich, and G. Lothongkum,

"Corrosion behavior of Ti-Cr-N coatings on tool steel substrates prepared using DC magnetron sputtering at low growth temperatures," *Surf. Coatings Technol.*, vol. 358, pp. 732–740, 2019, doi: 10.1016/j.surfcoat.2018.11.082.

[171] J. Li *et al.*, "Cyclic oxidation behavior of Ni3Al-basedsuperalloy," *Vacuum*, vol. 169, no. September, 2019, doi: 10.1016/j.vacuum.2019.108938.

[172] S. Tixier, P. Böni, and H. Van Swygenhoven, "Hardness enhancement of sputtered Ni 3 Al/Ni multilayers," *Thin Solid Films*, vol. 342, no. 1–2, pp. 188–193, Mar. 1999, doi: 10.1016/S0040-6090(98)01495-3.

[173] J. Çermák and I. Stloukal, "Low-temperature tracer diffusion of nickel in Ni3Al intermetallic," *Scr. Mater.*, vol. 36, no. 4, pp. 433–437, 1997, doi: 10.1016/S1359-6462(96)00400-9.

[174] C. L. Chang, C. S. Huang, and J. Y. Jao, "Microstructural, mechanical and wear properties of Cr-Al-B-N coatings deposited by DC reactive magnetron co-sputtering," *Surf. Coatings Technol.*, vol. 205, no. 8–9, pp. 2730–2737, 2011, doi: 10.1016/j.surfcoat.2010.10.023.

[175] Y. Huang, M. J. Aziz, J. W. Hutchinson, A. G. Evans, R. Saha, and W. D. Nix, "Comparison of mechanical properties of Ni3Al thin films in disordered FCC and ordered L12 phases," *Acta Mater.*, vol. 49, no. 14, pp. 2853–2861, 2001, doi: 10.1016/S1359-6454(01)00094-5.

[176] H. S. Akkera, N. N. K. Reddy, and M. C. Sekhar, "Thickness dependent structural and electrical properties of magnetron sputtered nanostructured CrN thin films," *Mater. Res.*, vol. 20, no. 3, pp. 712–717, 2017, doi: 10.1590/1980-5373-MR-2016-0786.

[177] P. De Almeida, R. Schäublin, A. Almazouzi, M. Victoria, and F. Lévy, "Microstructure and growth modes of stoichiometric NiAl and Ni3Al thin films deposited by r.f.-magnetron sputtering," *Thin Solid Films*, vol. 368, no. 1, pp. 26–34, 2000, doi: 10.1016/S0040-6090(00)00854-3.

[178] R. Banerjee, J. P. Fain, P. M. Anderson, and H. L. Fraser, "Influence of crystallographic orientation and layer thickness on fracture behavior of Ni/Ni3Al multilayered thin films," *Scr. Mater.*, vol. 44, no. 11, pp. 2629–2633, 2001, doi: 10.1016/S1359-6462(01)00966-6.

[179] E. A. Sperling, R. Banerjee, G. B. Thompson, J. P. Fain, P. M. Anderson, and H. L. Fraser, “Processing and microstructural characterization of sputter-deposited Ni/Ni3Al multilayered thin films,” *J. Mater. Res.*, vol. 18, no. 4, pp. 979–987, 2003, doi: 10.1557/JMR.2003.0134.

[180] S. Zhu, Q. Bi, J. Yang, W. Liu, and Q. Xue, “Ni3Al matrix high temperature self-lubricating composites,” *Tribol. Int.*, vol. 44, no. 4, pp. 445–453, 2011, doi: 10.1016/j.triboint.2010.11.016.

[181] G. Prévot, D. Schmaus, and S. Le Moal, “Epitaxial alloyed films out of the bulk stability domain: Surface structure and composition of Ni3Al and NiAl films on a stepped Ni(1 1 1) surface,” *Surf. Sci.*, vol. 604, no. 9–10, pp. 770–778, 2010, doi: 10.1016/j.susc.2010.01.025.

[182] H. P. Ng and A. H. W. Ngan, “An in situ transmission electron microscope investigation into grain growth and ordering of sputter-deposited nanocrystalline Ni3Al thin films,” *J. Mater. Res.*, vol. 17, no. 8, pp. 2085–2094, 2002, doi: 10.1557/JMR.2002.0308.

[183] H. P. ng and A. H. W. Ngan, “Metal-to-insulator transition in sputter deposited 3Ni/Al thin films,” *J. Appl. Phys.*, vol. 88, no. 5, pp. 2609–2616, 2000, doi: 10.1063/1.1286773.

[184] C.-C. Wu and F.-B. Wu, “Microstructure and mechanical properties of magnetron co-sputtered Ni–Al coatings,” *Surf. Coatings Technol.*, vol. 204, no. 6–7, pp. 854–859, Dec. 2009, doi: 10.1016/j.surfcoat.2009.09.019.

[185] R. Banerjee, G. B. Thompson, G. B. Viswanathan, and H. L. Fraser, “Unexpected nanoscale phase separation in sputter-deposited Ni-25 at. % Al thin films,” *Philos. Mag. Lett.*, vol. 82, no. 11, pp. 623–640, 2002, doi: 10.1080/0950083021000036076.

[186] A. Rahman, R. Jayaganthan, S. Prakash, V. Chawla, and R. Chandra, “High temperature oxidation behavior of nanostructured Ni-Al coatings on superalloy,” *J. Alloys Compd.*, vol. 472, no. 1–2, pp. 478–483, 2009, doi: 10.1016/j.jallcom.2008.04.091.

[187] X. Yang, X. Peng, and F. Wang, “Size effect of Al particles on the structure and oxidation of Ni/Ni3Al composites transformed from

electrodeposited Ni-Al films," *Scr. Mater.*, vol. 56, no. 6, pp. 509–512, 2007, doi: 10.1016/j.scriptamat.2006.11.016.

[188] Q. Wu, S. Li, Y. Ma, and S. Gong, "Study on behavior of NiAl coating with different Ni/Al ratios," *Vacuum*, vol. 93, pp. 37–44, 2013, doi: 10.1016/j.vacuum.2013.01.001.

[189] S. Tixier, P. Böni, and H. Van Swygenhoven, "Structural coherence of sputtered Ni3Al/Ni multilayers," *J. Vac. Sci. Technol. A Vacuum, Surfaces, Film.*, vol. 16, no. 4, pp. 2429–2436, 1998, doi: 10.1116/1.581362.

[190] M. V. Fedorishcheva, V. P. Sergeev, O. V. Sergeev, and E. V. Kozlov, "Structure and mechanical properties of intermetallic magnetron-sputtered coating based on the Ni-Al system," *Bull. Russ. Acad. Sci. Phys.*, vol. 73, no. 7, pp. 988–991, 2009, doi: 10.3103/S1062873809070399.

[191] S. Zhang, Y. Fu, H. Du, X. T. Zeng, and Y. C. Liu, "Magnetron sputtering of nanocomposite (Ti, Cr)CN/DLC coatings," *Surf. Coatings Technol.*, vol. 162, no. 1, pp. 42–48, 2003, doi: 10.1016/S0257-8972(02)00561-3.

[192] C. Leyens, J. W. Van Liere, M. Peters, and W. A. Kaysser, "Magnetron-sputtered Ti-Cr-Al coatings for oxidation protection of titanium alloys," *Surf. Coatings Technol.*, vol. 108–109, no. 1–3, pp. 30–35, 1998, doi: 10.1016/S0257-8972(98)00574-X.

[193] J. Jin, Z. Zhu, and D. Zheng, "Influence of Ti content on the corrosion properties and contact resistance of CrTiN coating in simulated proton exchange membrane fuel cells," *Int. J. Hydrogen Energy*, vol. 42, no. 16, pp. 11758–11770, 2017, doi: 10.1016/j.ijhydene.2017.02.014.

[194] A. Y. Adesina, Z. M. Gasem, and A. M. Kumar, "Electrochemical evaluation of the corrosion protectiveness and porosity of vacuum annealed CrAlN and TiAlN cathodic arc physical vapor deposited coatings," *Mater. Corros.*, vol. 70, no. 9, pp. 1601–1616, 2019, doi: 10.1002/maco.201810715.

[195] S. Sharifi Malvajerdi, A. Sharifi Malvajerdi, M. Ghanaatshoar, M. Habibi, and H. Jahdi, "TiCrN-TiAlN-TiAlSiN-TiAlSiCN multi-layers

utilized to increase tillage tools useful lifetime," *Sci. Rep.*, vol. 9, no. 1, pp. 1–12, 2019, doi: 10.1038/s41598-019-55677-8.

[196] Y. X. Xu *et al.*, "Effect of CrN addition on the structure, mechanical and thermal properties of Ti-Al-N coating," *Surf. Coatings Technol.*, vol. 235, pp. 506–512, 2013, doi: 10.1016/j.surfcoat.2013.08.010.

[197] S. Sveen, J. M. Andersson, R. M'Saoubi, and M. Olsson, "Scratch adhesion characteristics of PVD TiAlN deposited on high speed steel, cemented carbide and PCBN substrates," *Wear*, vol. 308, no. 1–2, pp. 133–141, 2013, doi: 10.1016/j.wear.2013.08.025.

[198] Y. C. Pan, T. H. Chuang, and Y. D. Yao, "Long-term oxidation behaviour of Ni3Al alloys with and without chromium additions," *J. Mater. Sci.*, vol. 26, no. 22, pp. 6097–6103, 1991, doi: 10.1007/BF01113890.

[199] Z. Zhang, B. Gleeson, K. Jung, L. Li, and J. C. Yang, "A diffusion analysis of transient subsurface γ′-Ni 3Al formation during β-NiAl oxidation," *Acta Mater.*, vol. 60, no. 13–14, pp. 5273–5283, 2012, doi: 10.1016/j.actamat.2012.06.021.

[200] D. Kourtidou *et al.*, "Deposition of Ni-Al coatings by pack cementation and corrosion resistance in high temperature and marine environments," *Corros. Sci.*, vol. 148, pp. 12–23, 2019, doi: 10.1016/j.corsci.2018.11.003.

[201] "PROCESSING, MICROSTRUCTURE, AND FRACTURE BEHAVIOR OF NICKEL! NICKEL ALUMINIDE MULTILAYERED THIN FILMS R. Banerjee, J. P. Fain, G. B. Thompson, P. M. Anderson, and H. L. Fraser Department of Materials Science and Engineering, The Ohio State University, Col," vol. 594, pp. 19–24, 2000.

[202] F. Lang and T. Narita, "Improvement in oxidation resistance of a Ni3Al-based superalloy IC6 by rhenium-based diffusion barrier coatings," *Intermetallics*, vol. 15, no. 4, pp. 599–606, 2007, doi: 10.1016/j.intermet.2006.10.042.

[203] "31_443.pdf." .

[204] G. Heydari, E. Thormann, M. Järn, E. Tyrode, and P. M. Claesson,

"Hydrophobic surfaces: Topography effects on wetting by supercooled water and freezing delay," *J. Phys. Chem. C*, vol. 117, no. 42, pp. 21752–21762, 2013, doi: 10.1021/jp404396m.

[205] J. Niu, W. Wang, S. Zhu, and F. Wang, "The scaling behavior of sputtered Ni 3Al coatings with and without Pt modification," *Corros. Sci.*, vol. 58, pp. 115–120, 2012, doi: 10.1016/j.corsci.2012.01.008.

[206] S. K. Tiwari, A. U. Rao, A. S. Kharb, A. K. Chawla, and D. K. Avasthi, "A review of mechanical and tribological properties of Ni 3 Al-based coatings-synthesis and high-temperature behavior," *Phys. Scr.*, vol. 98, no. 7, p. 72001, 2023, doi: 10.1088/1402-4896/acd81c.

[207] A. U. Rao, S. K. Tiwari, M. S. Goyat, and A. K. Chawla, "Recent developments in magnetron-sputtered silicon nitride coatings of improved mechanical and tribological properties for extreme situations," *J. Mater. Sci.*, vol. 58, no. 24, pp. 9755–9804, Jun. 2023, doi: 10.1007/s10853-023-08575-4.

[208] K. Gong, H. Luo, D. Feng, and C. Li, "Wear of Ni3Al-based materials and its chromium-carbide reinforced composites," *Wear*, vol. 265, no. 11–12, pp. 1751–1755, 2008, doi: 10.1016/j.wear.2008.04.038.

[209] D. Lee, "An investigation of thermal aging effects on the mechanical properties of a Ni3Al-based alloy by nanoindentation," *J. Alloys Compd.*, vol. 480, no. 2, pp. 347–350, 2009, doi: 10.1016/j.jallcom.2009.02.014.

[210] S. Zhu, Q. Bi, J. Yang, and W. Liu, "Influence of Cr content on tribological properties of Ni3Al matrix high temperature self-lubricating composites," *Tribol. Int.*, vol. 44, no. 10, pp. 1182–1187, 2011, doi: 10.1016/j.triboint.2011.05.014.

[211] S. Kang and J. H. Selverian, "Effect of active metal coatings on the mechanical properties of silicon nitride-based ceramics," *J. Mater. Sci.*, vol. 28, no. 20, pp. 5514–5520, Oct. 1993, doi: 10.1007/BF00367823.

[212] M. Diserens, J. Patscheider, and F. Lévy, "Mechanical properties and oxidation resistance of nanocomposite TiN-SiNx physical-vapor-deposited thin films," *Surf. Coatings Technol.*, vol. 120–121, pp. 158–165, 1999, doi: 10.1016/S0257-8972(99)00481-8.

[213] J. Duszczyk, J. Zhou, L. Marvina, and L. Z. Zhuang, “In-situ reactive synthesis of the Ni3Al intermetallic compound and subsequent diffusion bonding with different steels for surface coating,” *J. Mater. Sci.*, vol. 34, no. 16, pp. 3937–3950, 1999, doi: 10.1023/A:1004639210093.

[214] S. A. Serna *et al.*, “Synthesis and Characterization of a Ni3Al Intermetallic Modified with Copper Atoms via Powder Metallurgy,” *J. Mater. Eng. Perform.*, vol. 30, no. 3, pp. 1906–1913, 2021, doi: 10.1007/s11665-021-05541-6.

[215] C. Yan, Y. Kang, L. Kong, and S. Zhu, “Tribological Properties of Ni3Al Matrix Composite Sliding Against Si3N4, SiC and Al2O3 at Elevated Temperatures,” *J. Mater. Eng. Perform.*, vol. 26, no. 1, pp. 168–176, 2017, doi: 10.1007/s11665-016-2456-y.

[216] T. Chandanayaka and F. Azarmi, “Investigation on the effect of reinforcement particle size on the mechanical properties of the cold sprayed Ni-Ni3Al composites,” *J. Mater. Eng. Perform.*, vol. 23, no. 5, pp. 1815–1822, 2014, doi: 10.1007/s11665-014-0941-8.

[217] A. N. Filippin *et al.*, “Ni-Al-Cr superalloy as high temperature cathode current collector for advanced thin film Li batteries,” *RSC Adv.*, vol. 8, no. 36, pp. 20304–20313, 2018, doi: 10.1039/c8ra02461h.

[218] M. Nastasi, L. S. Hung, and J. W. Mayer, “Phase formation by ion beam mixing in Ni/Al, Pd/Al, and Pt/Al bilayers,” *Appl. Phys. Lett.*, vol. 43, no. 9, pp. 831–833, 1983, doi: 10.1063/1.94511.

[219] I. Stloukal, J. Čermák, J. Růžičková, and A. Pokorná, “Iron grain boundary diffusion in pure and in Cr, Fe and Zr-doped Ni3Al alloys,” *Intermetallics*, vol. 7, no. 1, pp. 33–38, 1999, doi: 10.1016/S0966-9795(98)00008-9.

[220] K. Aoki, K. Ishikawa, and T. Masumoto, “Ductilization of Ni3Al by alloying with boron and substitutional elements,” *Mater. Sci. Eng. A*, vol. 192–193, no. PART 1, pp. 316–323, 1995, doi: 10.1016/0921-5093(94)03213-0.

[221] Heryanto, B. Abdullah, D. Tahir, and Mahdalia, “Quantitative analysis of X-Ray diffraction spectra for determine structural properties and

deformation energy of Al, Cu and Si," *J. Phys. Conf. Ser.*, vol. 1317, no. 1, 2019, doi: 10.1088/1742-6596/1317/1/012052.

[222] N. H. Astuti, N. A. Wibowo, and M. R. S. S. N. Ayub, "The Porosity Calculation of Various Types of Paper Using Image Analysis," *J. Pendidik. Fis. Indones.*, vol. 14, no. 1, pp. 46–51, 2018, doi: 10.15294/jpfi.v14i1.9878.

[223] D. Wu, J. Zhang, J. C. Huang, H. Bei, and T. G. Nieh, "Grain-boundary strengthening in nanocrystalline chromium and the Hall-Petch coefficient of body-centered cubic metals," *Scr. Mater.*, vol. 68, no. 2, pp. 118–121, 2013, doi: 10.1016/j.scriptamat.2012.09.025.

[224] W. Zhang *et al.*, "Experimental study on the thickness-dependent hardness of SiO2 thin films using nanoindentation," *Coatings*, vol. 11, no. 1, pp. 1–12, 2021, doi: 10.3390/coatings11010023.

[225] R. Wang, J. Deng, Z. Zhang, and D. Ge, "Microstructure and tribological properties of Ni3Al matrix micro-laminated films deposited by electrohydrodynamic atomization," *Appl. Surf. Sci.*, vol. 606, no. September, p. 154918, 2022, doi: 10.1016/j.apsusc.2022.154918.

[226] C. H. Lin, Y. Z. Tsai, and J. G. Duh, "Effect of grain size on mechanical properties in CrAlN/SiNx multilayer coatings," *Thin Solid Films*, vol. 518, no. 24, pp. 7312–7315, 2010, doi: 10.1016/j.tsf.2010.04.100.

[227] X. K. Meng, H. Vehoff, and A. H. W. Ngan, "Hard multilayered thin films of metal–intermetallic Ni/Ni 3 Al," *J. Mater. Res.*, vol. 15, no. 12, pp. 2595–2597, Dec. 2000, doi: 10.1557/JMR.2000.0371.

[228] J.-H. Lee, B. Choe, Z. Lee, and H. Kim, "Effect of zirconium in two phase (NiAl + Ni3Al) alloy," *Scr. Mater.*, vol. 40, no. 7, pp. 853–857, Mar. 1999, doi: 10.1016/S1359-6462(99)00004-4.

[229] Y. F. Li, J. T. Guo, L. Z. Zhou, and H. Q. Ye, "Effect of recrystallization on room-temperature mechanical properties of Zr-doped Ni3Al alloy," *Mater. Lett.*, vol. 58, no. 12–13, pp. 1853–1856, 2004, doi: 10.1016/j.matlet.2003.11.018.

[230] M. Zagula-Yavorska, M. Pytel, J. Romanowska, and J. Sieniawski, "The Effect of Zirconium Addition on the Oxidation Resistance of

Aluminide Coatings," *J. Mater. Eng. Perform.*, vol. 24, no. 4, pp. 1614–1625, 2015, doi: 10.1007/s11665-015-1421-5.

[231] X. Zhang, M. Watanabe, and S. Kuroda, "Effects of residual stress on the mechanical properties of plasma-sprayed thermal barrier coatings," *Eng. Fract. Mech.*, vol. 110, pp. 314–327, 2013, doi: 10.1016/j.engfracmech.2013.08.016.

[232] A. S. Ebner *et al.*, "Grain boundary segregation in Ni-base alloys: A combined atom probe tomography and first principles study," *Acta Mater.*, vol. 221, p. 117354, 2021, doi: 10.1016/j.actamat.2021.117354.

[233] D. T. Quinto, G. J. Wolfe, and P. C. Jindal, "High Temperature microhardness of hard coatings produced by physical and chemical vapor deposition," *Thin Solid Films*, vol. 153, no. 1–3, pp. 19–36, 1987, doi: 10.1016/0040-6090(87)90166-0.

[234] H. L. Sun, Z. X. Song, D. G. Guo, F. Ma, and K. W. Xu, "Microstructure and mechanical properties of nanocrystalline tungsten thin films," *J. Mater. Sci. Technol.*, vol. 26, no. 1, pp. 87–92, 2010, doi: 10.1016/S1005-0302(10)60014-X.

[235] M. W. Reedy, T. J. Eden, J. K. Potter, and D. E. Wolfe, "Erosion performance and characterization of nanolayer (Ti,Cr)N hard coatings for gas turbine engine compressor blade applications," *Surf. Coatings Technol.*, vol. 206, no. 2–3, pp. 464–472, 2011, doi: 10.1016/j.surfcoat.2011.07.063.

[236] J. Zheng, J. Hao, X. Liu, Q. Gong, and W. Liu, "Surface & Coatings Technology A thick TiN / TiCN multilayer fi lm by DC magnetron sputtering," *Surf. Coat. Technol.*, vol. 209, pp. 110–116, 2012, doi: 10.1016/j.surfcoat.2012.08.045.

[237] A. Chiba, S. Hanada, and S. Watanabe, "Ductilization of Ni3Al by macroalloying with Pd," *Acta Metall. Mater.*, vol. 39, no. 8, pp. 1799–1805, 1991, doi: 10.1016/0956-7151(91)90148-T.

[238] A. M. Venezia, C. M. Loxton, and J. A. Horton, "Temperature and pressure effects for oxygen adsorption and oxidation of Ni3Al alloyed with chromium and zirconium," *Surf. Sci.*, vol. 225, no. 1–2, pp. 195–205, 1990, doi: 10.1016/0039-6028(90)90438-E.

[239] I. Khakpour, R. Soltani, and M. H. Sohi, “Microstructure and High Temperature Oxidation Behaviour of Zr-Doped Aluminide Coatings Fabricated on Nickel-based Super Alloy,” *Procedia Mater. Sci.*, vol. 11, pp. 515–521, 2015, doi: 10.1016/j.mspro.2015.11.011.

[240] H. Liu and W. Chen, “Porosity-dependent cyclic-oxidation resistance at 850 °C of annealed Ni-Al-based coatings via electroplating,” *Surf. Coatings Technol.*, vol. 202, no. 16, pp. 4019–4027, 2008, doi: 10.1016/j.surfcoat.2008.02.015.

[241] A. Fabrizi *et al.*, “Oxidation Behaviour and Thermal Stability of Nanocomposited Ti-Al-Si-B-N and Ti-Cr-B-N Coatings,” *Mater. Sci. Forum*, vol. 604–605, pp. 19–28, 2008, doi: 10.4028/www.scientific.net/msf.604-605.19.

[242] J. Lin *et al.*, “Structure and properties of selected (Cr-Al-N, TiC-C, Cr-B-N) nanostructured tribological coatings,” *Int. J. Refract. Met. Hard Mater.*, vol. 28, no. 1, pp. 2–14, 2010, doi: 10.1016/j.ijrmhm.2009.07.012.

[243] J. Zheng, J. Hao, X. Liu, Q. Gong, and W. Liu, “Applied Surface Science TiN / TiCN multilayer films modified by argon plasma treatment,” *Appl. Surf. Sci.*, vol. 280, pp. 764–771, 2013, doi: 10.1016/j.apsusc.2013.05.058.

[244] J. Xu, K. Hattori, Y. Seino, and I. Kojima, “Microstructure and properties of CrN y Si 3 N 4 nano-structured multilayer films,” vol. 414, pp. 239–245, 2002.

[245] N. E. Beliardouh, K. Bouzid, C. Nouveau, B. Tlili, and M. J. Walock, “Tribological and electrochemical performances of Cr/CrN and Cr/CrN/CrAlN multilayer coatings deposited by RF magnetron sputtering,” *Tribol. Int.*, vol. 82, no. PB, pp. 443–452, 2015, doi: 10.1016/j.triboint.2014.03.018.

[246] C. M. Koller *et al.*, “Thermal stability and oxidation resistance of arc evaporated TiAlN, TaAlN, TiAlTaN, and TiAlN/TaAlN coatings,” *Surf. Coatings Technol.*, vol. 259, no. PC, pp. 599–607, 2014, doi: 10.1016/j.surfcoat.2014.10.024.

[247] M. S. Cfubms, P. V Kiryukhantsev-korneev, Z. S. Amankeldina, A. N.

Sheveyko, and S. Vorotilo, “applied sciences E ff ect of Boron and Oxygen on the Structure and Properties of Protective Decorative Cr – Al – Ti – N Coatings Deposited by Closed Field Unbalanced,” no. Cvd, 2019.

[248] C. Lo and A. Ferna, “Magnetron sputtering of Cr (Al) N coatings : Mechanical and tribological study,” vol. 200, pp. 192–197, 2005, doi: 10.1016/j.surfcoat.2005.02.105.

[249] M. Zagula-Yavorska, J. Sieniawski, and J. Romanowska, “Oxidation behaviour of zirconium-doped NiAl coatings deposited on pure nickel,” *Arch. Mater. Sci. Eng.*, vol. 58, no. 2, pp. 250–254, 2012.

LIST OF PUBLICATIONS

1.	**Tiwari, S.K.**, Rao, A.U., Chawla, V., Dubey, P., Saxena, V., Chawla, A.K. and Avasthi, D.K., 2022. Synthesis and characterization of sputter-deposited Ni-rich Ni_3Al hard coatings. ***Journal of Alloys and Compounds***, 926, p.166802. Doi: https://doi.org/10.1016/j.jallcom.2022.166802
2.	**Tiwari, S.K.,** Rao, A.U., Kharb, A.S., Chawla, A.K. and Avasthi, D.K., 2023. A review of mechanical and tribological properties of Ni_3Al-based coatings-synthesis and high-temperature behavior. ***Physica Scripta.*** Doi: https://doi.org/10.1088/1402-4896/acd81c
3.	**Tiwari, S.K.,** Rao, A.U., Kharb, A.S., Chawla, V., Sardana, N., Avasthi, D.K. and Chawla, A.K., 2023. Investigation of mechanical and microstructural properties of sputter-deposited Zr-Ni3Al coatings. ***Journal of Vacuum Science & Technology A, 41(6).*** Doi: https://doi.org/10.1116/6.0003022
4.	**Tiwari, S.K.,** Rao, A.U., Kharb, A.S., Chawla, V., Pandey, J.K., Saxena, V., Sardana, N., Avasthi, D.K. and Chawla, A.K., 2023. Microstructural and Mechanical Properties of Cr-Ni_3Al Alloy Films Synthesized by Magnetron Sputtering. ***Journal of Materials Engineering and Performance***, pp.1-10. Doi: https://doi.org/10.1007/s11665-023-08894-2

SIMILARITY INDEX

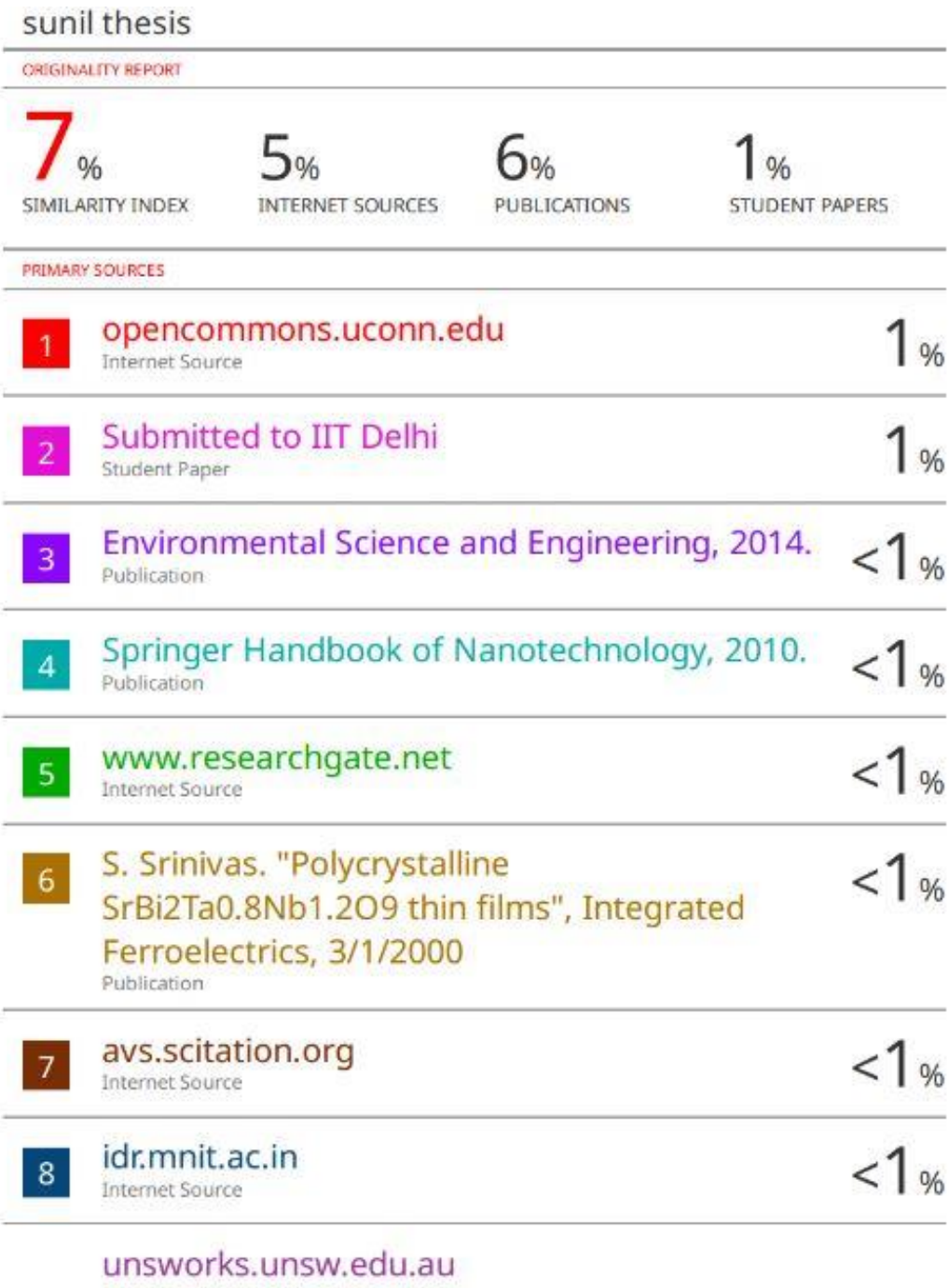

sunil thesis

ORIGINALITY REPORT

7%	5%	6%	1%
SIMILARITY INDEX	INTERNET SOURCES	PUBLICATIONS	STUDENT PAPERS

PRIMARY SOURCES

1	opencommons.uconn.edu Internet Source	1%
2	Submitted to IIT Delhi Student Paper	1%
3	Environmental Science and Engineering, 2014. Publication	<1%
4	Springer Handbook of Nanotechnology, 2010. Publication	<1%
5	www.researchgate.net Internet Source	<1%
6	S. Srinivas. "Polycrystalline SrBi2Ta0.8Nb1.2O9 thin films", Integrated Ferroelectrics, 3/1/2000 Publication	<1%
7	avs.scitation.org Internet Source	<1%
8	idr.mnit.ac.in Internet Source	<1%

unsworks.unsw.edu.au